To the Graduate Council:

I am submitting herewith a dissertation written by Kyonsuku Min entitled "Rheology, Phase Morphology and Processing of Polymer Blends." I have examined the final copy of this dissertation and recommend that it be accepted in partial fulfillment of the requirements for the degree of Doctor of Philosophy, with a major in Polymer Engineering.

James L. White, Major Professor

We have read this dissertation
and recommend its acceptance:

Accepted for the Council:

The Graduate School

RHEOLOGY, PHASE MORPHOLOGY AND PROCESSING OF POLYMER BLENDS

A Dissertation

Presented for the

Doctor of Philosophy

Degree

The University of Tennessee, Knoxville

Kyonsuku Min

March 1984

© 1984

KYONSUKU MIN

All Rights Reserved

To my father and mother,

who sacrificed for my higher education.

ACKNOWLEDGEMENTS

The author is indebted to the many persons who have been of assistance in various ways to make this investigation possible.

First of all, sincere appreciation goes to Professor James L. White, the author's adviser through her graduate study at The University of Tennessee. Professor White has always provided helpful guidance and patient encouragement in all aspects of the author's graduate work.

Appreciation is also extended to Professor J. F. Fellers for his encouragement, helpful comments, and suggestions.

The author is also grateful to all faculty members and student colleagues who have given useful suggestions and discussions. The author thanks Mr. B. L. McGill for his help in her study of Scanning Electron Microscopy.

Financial support for this study was provided by the National Science Foundation.

ABSTRACT

The development of phase morphology, rheological properties, and processing behavior of mechanical blends of a polystyrene (PS) and three different high density polyethylenes (PE), high density polyethylene and nylon 6 (N6), high density polyethylene and polycarbonate were studied. Phase morphologies were determined by scanning-electron microscopy for: (a) products prepared in a screw extruder/static mixer system, (b) samples removed from a cone-plate viscometer, (c) extrudates from capillary dies, (d) melt spun fibers, and (d) biaxially stretched films. Disperse phase dimensions were measured. The values varied from 1-5μ in the products from static mixers. The dimensions of the dispersed phase in the blend products from the cone-plate and capillary die were of the same order. The melt spun fibers exhibited disperse phase dimensions as low as 0.35μ. Polystyrene was extracted from the blend fibers to produce small diameter, PE fibrils, or mini-fibers.

Both initial melts and the blends were rheologically characterized. The shear viscosity η and principal normal stress difference N_1 exhibit maxima and minima when plotted as a function of composition. The phenomena were interpreted using the observed two-phase morphologies, i.e., droplets, lamellae, and fibers. An attempt was made to predict the observed dependence using hydrodynamic theories of dispersed two-phase liquids. Studies of elongational

flow indicated that the PE/PS blend behavior was similar to the characteristic of pure PE whose failure was due to ductile necking.

The characteristics of extrudates and isothermal and non-isothermal melt spinning behavior of the PE/PS blends were investigated. Wide-angle x-ray diffraction studies have been carried out on blend fibers and the orientation of the crystalline polyethylene regions determined as a function of process conditions. This orientation decreases rapidly with addition of polystyrene when the melt spun filaments are compared at the same spinline stress.

The characteristics of biaxially stretched films of PE/PS blends were studied. The dispersed phase was stretched biaxially and have the appearance of multi-layered sheets.

TABLE OF CONTENTS

CHAPTER		PAGE
I.	INTRODUCTION	1
II.	LITERATURE SURVEY	3
	A. Thermodynamics of Polymer Blends	3
	A.1. General Criteria	3
	A.2. The Entropy of Mixing	5
	A.3. ΔH_m: the Solubility Parameter	7
	B. Stratified Two-Phase Flow of Polymer Melts	10
	B.1. Newtonian Fluids	10
	B.2. Non-Newtonian Fluids	12
	C. Mixing and Dispersion Process	14
	C.1. Types of Mixers	14
	C.2. Screw Extruders and Theory of Mixing	14
	C.3. Motionless Mixer	15
	D. Interfacial Phenomena in Disperse Liquids or Melts	20
	D.1. The Breakup and Instability of Newtonian Fluids	20
	D.2. The Breakup and Instability of Non-Newtonian Fluids	24
	E. Modes of Two-Phase Morphology of Blends	28
	F. Rheological Properties of Two-Phase Fluids	31
	F.1. Viscosity of Newtonian Liquid Mixtures	31
	F.2. Principal Normal Stress Difference in Newtonian Fluid Emulsions	38
	F.3. Principal Normal Stress Difference in Polymer Melt Blends	39
	F.4. Elongational Viscosities of Polymer Blends	39
III.	MATERIALS AND EXPERIMENTAL PROCEDURE	41
	A. Materials	41
	B. Sample Preparation (Blending)	41
	C. Experimental Procedure	43
	C.1. Steady Shear Flow Measurements	43
	C.2. Elongational Flow Measurement	46
	C.3. Extrudate Swell Measurement	50
	C.4. Melt Spinning Under Non-Isothermal Conditions	50
	C.5. Melt Spinning Instability Under Isothermal Conditions	52
	C.6. Formation of Oriented Films	54

CHAPTER PAGE

C.7. Wide-Angle X-Ray Diffraction 54
C.8. Scanning Electron Microscopy (SEM) 59

IV. BLEND PHASE MORPHOLOGY AND ITS VARIATION IN RHEOMETERS 60

A. Extrudates from Screw Extruder/Static Mixer System 60
A.1. Results 60
A.2. Discussion 76
B. Morphology of Samples Sheared in a Cone-Plate Rheometer 81
B.1. Results 81
B.2. Discussion 87
C. Capillary Extrudate 87
C.1. Results 87
C.2. Discussion 108
D. Fibrillation in Flow Through the Capillary 120
D.1. Results 120
D.2. Discussion 131

V. RHEOLOGICAL PROPERTIES OF BLENDS 135

A. Shear Viscosity 135
A.1. Results 135
A.2. Discussion 139
B. First Normal Stress Difference 153
B.1. Results 157
B.2. Discussion 157
C. Elongational Flow 166
C.1. Shrinkage 167
C.2. Elongational Viscosity 167
C.3. Elongation to Break 197

VI. PROCESSING STUDIES OF POLYMER MELT BLENDS 204

A. Extrudate Swell 204
A.1. Results 204
A.2. Discussion 209
B. Melt Spinning 213
B.1. Structure Development 213
B.2. Draw Resonance During Isothermal Melt Spinning 226
C. Mini-Fibers 231
C.1. Results 231
C.2. Discussion 231
D. The Character of the Dispersed Phase in Biaxially Stretched Blended Films 253

CHAPTER PAGE

D.1. Results 253
D.2. Discussion 262

VII. CONCLUSIONS AND RECOMMENDATIONS 265

A. Conclusions 265
B. Recommendations 268

LIST OF REFERENCES 269

VITA 280

LIST OF TABLES

TABLE		PAGE
II-1.	Range of Experimental Values of Solubility Parameter	9
II-2.	Typical Examples of Compatible and Incompatible Polymer Blends	11
III-1.	Materials	42
III-2.	Composition and Temperature of Blends Investigated	44
IV-1.	The Dimensions of Discrete Phase of PE-2/PS Blends Prepared in a Screw Extruder and Koch Static Mixer	68
IV-2.	The Dimensions of the Discrete Phase of PE/PS Blends Prepared in a Screw Extruder and Koch Static Mixer	69
IV-3.	Comparisons of Morphologies from Different Investigators (HDPE-PS)	77
IV-4.	Comparison of the Discrete Phase Size of PE-2/PS, PE-2/N6, PE-2/PC Blends at 240°C	82
IV-5.	The Dimensions of Discrete Phase of PE-2/PS Blends Stressed in a Cone-Plate	88
IV-6.	The Influence of Extrusion Conditions on Discrete Phase Size Extrudated from Capillary (PE-2/PS)	102
IV-7.	The Influence of Extrusion Conditions on Discrete Size Extrudates from Capillary (PE-3/PS)	103
IV-8.	The Influence of Extrusion Conditions on Discrete Size Extrudates from Capillary (PE-1/PS)	104
IV-9.	The Influence of Extrusion Conditions on Discrete Size Extruded from Capillary	114
IV-10.	The Viscosity Ratio $\eta_{dispersed}/\eta_{matrix}$ and $\kappa/\eta_m\dot{\gamma}d_w$ on the Fibrillation	132

TABLE PAGE

V-1. Summary of Maximum Elongational Viscosity for PE, PS and PE/PS Blends 196

V-2. Comparison of Elongation to Break ($\ln L_B/\ln L_o$) for PE/PS Blends 201

V-3. Comparison of Elongation to Break ($\ln L_B/\ln L_o$) with Tanaka's Data 202

VI-1. Draw Resonance of Isothermal Melt Spinning 229

VI-2. The Influence of Drawdown Ratios on the Dimensions of Mini-Fibers of PE/PS, 10/90, 70/30, 50/50, 30/70 and 90/10 Blend Melt Spun Fibers 249

VI-3. The Influence of Drawdown Ratios on the Dimensions of Mini-Fibers of PE/PS, 10/90 and 90/10 Blend Melt Spun Fibers 250

LIST OF FIGURES

FIGURE		PAGE
II-1.	The Free Energy of Mixing Diagrams for Binary Mixture	4
II-2.	Photographs and Schematic View of (a) (b) Ross ISG Mixing Elements; (c) Kenics Mixer Elements; (d) Koch Mixer Elements	18
II-3.	Tracing of Droplets in Shearing Flow with Various Viscosity Ratios: and Increasing Shear Rates: (a) $\lambda < 0.2$; (b) $0.03 \leq \lambda \leq 2.2$; (c) $0.03 \leq \lambda \leq 2.2$; (d) $\lambda \geq 3.8$	22
II-4.	Schematic Representation of Droplet-Fiber Transformation	27
II-5.	Schematic Models of Two-Phase Flow: (a) Lamellae Parallel to the Applied Shear Stress; (b) Lamellae Perpendicular to the Applied Shear Stress; (c) Separating Planes Parallel to the Applied Shear Stress	33
III-1.	Schematic Diagram of Elongational Rheometer	47
III-2.	Schematic Diagram of the Isothermal Melt Spinning	51
III-3.	Schematic Diagram of the Non-Isothermal Melt Spinning	53
III-4.	Flat-Film Technique Arrangement	55
III-5.	Angular Coordinates of a Pole on a Spherical Projection	56
IV-1.	SEM Microphotographs of Fracture Surfaces of PE-2/PS Blends Prepared in Screw Extruder and Koch Static Mixer: (a) 90/10; (b) 70/30; (c) 50/50; (d) 30/70; (e) 10/90	61
IV-2.	SEM Microphotographs of Fracture Surfaces of PE-2/PS Blends Prepared in a Screw Extruder and Koch Static Mixer: (a) 90/10; (b) 70/30; (c) 50/50; (d) 30/70; (e) 10/90	62

FIGURE PAGE

IV-3. SEM Microphotographs of Fracture Surfaces of PE-1/PS Blends Prepared in a Screw Extruder and Koch Static Mixer: (a) 90/10; (b) 70/30; (c) 50/50; (d) 30/70; (e) 10/90 63

IV-4. SEM Microphotographs of Fracture Surfaces of PE-3/PS Blends Prepared in a Screw Extruder and Koch Static Mixer: (a) 90/10; (b) 70/30; (c) 50/50; (d) 30/70; (e) 10/90 64

IV-5. SEM Microphotographs of Extracted Cross-Sections of PE-3/PS (A) and PE-1/PS (B) Blends: (a) 70/30; (b) 50/50; (c) 30/70; (d) 70/30; (e) 50/50; (f) 30/70 65

IV-6. The Comparison of Discrete Phases of Different Polyethylenes 70

IV-7. SEM Microphotographs of PE-2/PS/SES Blends Prepared in Screw Extruder and Koch Static Mixer: (a) 50/50/5 at 180°C; (b) 50/50/5 at 240°C; (c) 50/50/50 at 180°C . . . 72

IV-8. SEM Microphotographs of PE-2/N6 Blends Prepared in a Screw Extruder and Koch Static Mixer: (a) 90/10; (b) 70/30; (c) 50/50; (d) 30/70; (e) 10/90 73

IV-9. SEM Microphotographs of PE-2/PC Blends Prepared in a Screw Extruder and Koch Static Mixer: (a) 70/30; (b) 50/50; (c) 30/70 74

IV-10. The Comparison of Discrete Phase Sizes of PE-2/PS, PE-2/N6 and PE-2/PC 75

IV-11. Viscosity, η, as a Function of Shear Rate for Polyethylene and Polystyrene at Two Different Temperatures 78

IV-12. Viscosity, η, as a Function of Shear Rate for Different Polyethylenes at 180°C 79

IV-13. Viscosity, η, as a Function of Shear Rate for Polystyrene-2 (PE-2), Nylon 6 (N6) and Polycarbonate (PC) . 80

IV-14. SEM Microphotographs of PE-2/PS Blends Stressed in a Cone-Plate: (i) 90/10; (ii) 70/30; (iii) 50/50; (iv) 30/70; (v) 10/90 83

FIGURE PAGE

IV-15. SEM Microphotographs of PE-2/PS-70/30 Blend Extrudates as a Function of Die Wall Shear Rate $32Q/\pi D^3$: (a) 12.2 sec^{-1}; (b) 69.6 sec^{-1} 89

IV-16. SEM Microphotographs of PE-2/PS-50/50 Blend Extrudates as a Function of Die Wall Shear Rate $32Q/\pi D^3$: (a) 2.0 sec^{-1}; (b) 11.0 sec^{-1}; (c) 70.8 sec^{-1} 90

IV-17. SEM Microphotographs of PE-2/PS-10/90 Blend Extrudates as a Function of Die Wall Shear Rate $32Q/\pi D^3$: (a) 2.6 sec^{-1}; (b) 13.0 sec^{-1}; (c) 60.0 sec^{-1} 91

IV-18. SEM Microphotographs of PE-3/PS-90/10 Blend Extrudates as a Function of Die Wall Shear Rate $32Q/\pi D^3$: (a) 2.2 sec^{-1}; (b) 11.2 sec^{-1}; (c) 55.2 sec^{-1} 92

IV-19. SEM Microphotographs of PE-3/PS-70/30 Blend Extrudates as a Function of Die Wall Shear Rate $32Q/\pi D^3$: (a) 2.4 sec^{-1}; (b) 11.7 sec^{-1}; (c) 56.8 sec^{-1} 93

IV-20. SEM Microphotographs of PE-3/PS-50/50 Blend Extrudates as a Function of Die Wall Shear Rate $32Q/\pi D^3$: (a) 2.0 sec^{-1}; (b) 11.6 sec^{-1}; (c) 54.5 sec^{-1} 94

IV-21. SEM Microphotographs of PE-3/PS-30/70 Blend Extrudates as a Function of Die Wall Shear Rate $32Q/\pi D^3$: (a) 2.0 sec^{-1}; (b) 10.6 sec^{-1}; (c) 61.8 sec^{-1} 95

IV-22. SEM Microphotographs of PE-3/PS-10/90 Blend Extrudates as a Function of Die Wall Shear Rate $32Q/\pi D^3$: (a) 2.5 sec^{-1}; (b) 12.1 sec^{-1}; (c) 69.0 sec^{-1} 96

IV-23. SEM Microphotographs of PE-1/PS-90/10 Blend Extrudates as a Function of Die Wall Shear Rate $32Q/\pi D^3$: (a) 2.2 sec^{-1}; (b) 11.7 sec^{-1}; (c) 58.6 sec^{-1} 97

IV-24. SEM Microphotographs of PE-1/PS-70/30 Blend Extrudates as a Function of Die Wall Shear Rate $32Q/\pi D^3$: (a) 2.3 sec^{-1}; (b) 11.4 sec^{-1}; (c) 61.8 sec^{-1} 98

FIGURE PAGE

IV-25. SEM Microphotographs of PE-1/PS-50/50 Blend Extrudates as a Function of Die Shear Wall Rate $32Q/\pi D^3$: (a) 2.5 sec^{-1}; (b) 12.4 sec^{-1}; (c) 67.2 sec^{-1} 99

IV-26. SEM Microphotographs of PE-1/PS-30/70 Blend Extrudates as a Function of Die Wall Shear Rate $32Q/\pi D^3$: (a) 2.6 sec^{-1}; (b) 12.9 sec^{-1}; (c) 83.9 sec^{-1} 100

IV-27. SEM Microphotographs of PE-1/PS-10/90 Blend Extrudates as a Function of Die Wall Shear Rate $32Q/\pi D^3$: (a) 2.6 sec^{-1}; (b) 12.9 sec^{-1}; (c) 72.9 sec^{-1} 101

IV-28. Mean Dimension of Discrete Phase in PE-2/PS Blends as a Function of Die Wall Shear Stress (σ_{12}) 105

IV-29. Mean Dimension of Discrete Phase in PE-1/PS Blends as a Function of Die Wall Shear Stress (σ_{12}) 106

IV-30. Mean Dimension of Discrete Phase in PE-3/PS as a Function of Die Shear Stress (σ_{12}) 107

IV-31. SEM Microphotographs of PE-2/N6-70/30 Blend Extrudate as a Function of Die Wall Shear Rate: (a) 2.4 sec^{-1}; (b) 11.7 sec^{-1}; (c) 62.7 sec^{-1} 109

IV-32. SEM Microphotographs of PE-2/N6-30/70 Blend Extrudate as a Function of Wall Shear Rate: (a) 2.2 sec^{-1}; (b) 10.6 sec^{-1}; (c) 56.0 sec^{-1} 110

IV-33. SEM Microphotographs of PE-2/PC-70/30 Blend Extrudate as a Function of Die Wall Shear Rate: (a) 2.2 sec^{-1}; (b) 11.3 sec^{-1}; (c) 56.0 sec^{-1} 111

IV-34. SEM Microphotographs of PE-2/PC-30/70 Blend Extrudate as a Function of Die Wall Shear Rate: (a) 2.2 sec^{-1}; (b) 10.9 sec^{-1}; (c) 56.0 sec^{-1} 112

IV-35. Mean Dimension of Discrete Phase in (a) PE-2/N6 and (b) PE-2/PC Blends as a Function of Die Shear Stress (σ_{12}) 113

IV-36. SEM Microphotographs of PE-1/N6-50/50 Blend Extrudate as a Function of Die Wall Shear Rate: (a) 2.1 sec^{-1}; (b) 10.9 sec^{-1}; (c) 57.1 sec^{-1} 115

FIGURE PAGE

IV-37. SEM Microphotographs of PE-2/PC-50/50 Blend Extrudate as a Function of Die Wall Shear Rate: (a) 2.3 sec^{-1}; (b) 12.0 sec^{-1}; (c) 57.4 sec^{-1} 116

IV-38. The Scheme of Types of Dispersion 118

IV-39. The Comparisons of the Discrete Phase Size as a Function of the Dimensionless Parameter ($\sigma_{12}d/\kappa$) 121

IV-40. SEM Microphotographs of Longitudinal Sections of PE-2/PS-70/30 Blend Extrudates as a Function of Die Wall Shear Rate: (a) 2.3 sec^{-1}; (b) 12.2 sec^{-1}; (c) 69.6 sec^{-1} 122

IV-41. SEM Microphotographs of Longitudinal Sections of PE-2/PS-50/50 Blend Extrudates as a Function of Die Wall Shear Rate: (a) 2.0 sec^{-1}; (b) 11.0 sec^{-1}; (c) 70.8 sec^{-1} 123

IV-42. SEM Microphotographs of Longitudinal Sections of PE-2/PS-10/90 Blend Extrudates as a Function of Die Wall Shear Rate: (a) 2.2 sec^{-1}; (b) 12.2 sec^{-1}; (c) 52.8 sec^{-1} 124

IV-43. SEM Microphotographs of Longitudinal Sections of PE-1/PS-10/90 Blend Extrudates as a Function of Viscosity Ratio: η_d/η_m: (a) 0.81; (b) 0.56; (c) 0.42 125

IV-44. SEM Microphotographs of Longitudinal Sections of PE-1/PS-90/10 Blend Extrudates as a Function of Viscosity ratio η_d/η_m: (a) 1.93; (b) 1.51; (c) 1.38 126

IV-45. SEM Microphotographs of Longitudinal Cross Section of PE-3/PS-10/90 Blend Extrudates as a Function of Viscosity Ratio: η_d/η_m: (a) 0.45; (b) 0.37; (c) 0.27 127

IV-46. SEM Microphotographs of Longitudinal Sections of PE-3/PS-90/10 Blend Extrudates as a Function of Viscosity Ratio: η_d/η_m: (a) 2.22; (b) 2.71; (c) 3.66 128

IV-47. SEM Microphotographs of Longitudinal Sections of PE-2/PS-90/10 Blend Extrudates as a Function of Viscosity Ratio: η_d/η_m: (a) 1.93; (b) 1.51; (c) 1.38 129

FIGURE PAGE

IV-48. SEM Microphotographs of Longitudinal Cross Section of PE-2/PS-10/90 Blend Extrudates as a Function of Viscosity Ratio: η_d/η_m: (a) 0.52; (b) 0.66; (c) 0.72 130

IV-49. Schematic Representation of Droplet-Fiber Transformation 134

V-1. Shear Viscosity Versus Shear Rate for PE-2/PS Blends . . 136

V-2. Shear Viscosity Versus Shear Rate for PE-1/PS Blends . . 137

V-3. Shear Viscosity Versus Shear Rate for PE-3/PS Blends . . 138

V-4. Shear Viscosity Versus Shear Rate for PE-2/N6 Blends . . 140

V-5. Shear Viscosity Versus Shear Rate for PE-2/PC Blends . . 141

V-6. Composition Dependence of Viscosity of Blends of PE-2/PS as a Function of Shear Rate 142

V-7. Composition Dependence of Viscosity of PE-2/PS Blends as a Function of Shear Stress 143

V-8. Composition Dependence of Viscosity of PE-3/PS Blends as a Function of Shear Stress 144

V-9. Composition Dependence of Viscosity of PE-1/PS Blends as a Function of Shear Stress 145

V-10. Composition Dependence of Viscosity of PE-1/PS, PE-2/PS and PE-3/PS Blends at a Fixed Shear Stress . . . 146

V-11. Composition Dependence of Viscosity of PE-2/N6 Blends as a Function of Shear Stress 149

V-12. Composition Dependence of Viscosity of PE-2/PC Blends as a Function of Shear Stress 151

V-13. Comparison of Viscosity-Composition Dependence with Theoretical Prediction 152

V-14. Comparison of Observed Composition Dependence with Theoretical Predictions and Morphologies at Low Shear Stress 154

V-15. Comparison of Observed Composition Dependence with Theoretical Predictions and Morphologies at High Shear Stresses 155

FIGURE PAGE

V-16. Comparison of Observed Composition Dependence with Theoretical Predictions 156

V-17. First Normal Stress Difference (N_1) as a Function of Shear Stress (σ_{12}) for Polyethylenes and Polystyrene . . 158

V-18. First Normal Stress Difference (N_1) as a Function of Shear Stress (σ_{12}) for PE-2/PS Blends 159

V-19. First Normal Stress Difference (N_1) as a Function of Shear Stress (σ_{12}) for PE-1/PS 160

V-20. First Normal Stress Difference (N_1) as a Function of Shear Stress (σ_{12}) for PE-3/PS 161

V-21. Comparison of the Composition Dependence of Viscosity and First Normal Stress for PE-2/PS at Various Shear Stress Blends 162

V-22. Comparison of the Composition Dependence of First Normal Stress Difference and Morphology for PE-2/PS Blends at Various Shear Stresses 163

V-23. Comparison of the Composition Dependence of Viscosity and First Normal Stress Difference for PE-1/PS Blends at Various Shear Stresses 164

V-24. Comparison of the Composition Dependence of Viscosity and First Normal Stress Differences for PE-3/PS Blends at a Fixed Shear Stress 165

V-25. Composition Dependence of Shrinkage for PE-1, 2, 3/PS Blends 168

V-26. Transient Elongational Viscosity ($\chi(t)$) as a Function of Elongation Rate and Time (t) for Polystyrene 169

V-27. Transient Elongational Viscosity ($\chi(t)$) as a Function of Elongation Rate and Time (t) for Polystyrene (PE-2) 170

V-28. Transient Elongational Viscosity ($\chi(t)$) as a Function of Elongation Rate and Time (t) for PE-2/PS-90/10 Blend 171

V-29. Transient Elongational Viscosity ($\chi(t)$) as a Function of Elongation Rate and Time (t) for PE-2/PS-70/30 Blend 172

FIGURE PAGE

V-30. Transient Elongational Viscosity ($\chi(t)$) as a Function of Elongation Rate and Time (t) for PE-2/PS-50/50 Blend 173

V-31. Transient Elongational Viscosity ($\chi(t)$) as a Function of Elongation Rate and Time (t) for PE-2/PS-30/70 Blend 174

V-32. Transient Elongational Viscosity ($\chi(t)$) as a Function of Elongation Rate and Time (t) for PE-2/PS-10/90 Blend 175

V-33. Transient Elongational Viscosity ($\chi(t)$) as a Function of Elongation Rate and Time (t) for High Density Polyethylene (PE-1) 176

V-34. Transient Elongational Viscosity ($\chi(t)$) as a Function of Elongation Rate and Time (t) for PE-1/PS-90/10 Blend 177

V-35. Transient Elongational Viscosity ($\chi(t)$) as a Function of Elongation Rate and Time (t) for PE-1/PS-70/30 Blend 178

V-36. Transient Elongational Viscosity ($\chi(t)$) as a Function of Elongation Rate and Time (t) for PE-1/PS-50/50 Blend 179

V-37. Transient Elongational Viscosity ($\chi(t)$) as a Function of Elongation Rate and Time (t) for PE-1/PS-30/70 Blend 180

V-38. Transient Elongational Viscosity ($\chi(t)$) as a Function of Elongation Rate and Time (t) for PE-1/PS-10/90 Blend 181

V-39. Transient Elongational Viscosity ($\chi(t)$) as a Function of Elongation Rate and Time (t) for High Density Polyethylene (PE-3) 182

V-40. Transient Elongational Viscosity ($\chi(t)$) as a Function of Elongation Rate and Time (t) for PE-3/PS-90/10 Blend 183

V-41. Transient Elongational Viscosity ($\chi(t)$) as a Function of Elongation Rate and Time (t) for PE-3/PS-70/30 Blend 184

FIGURE PAGE

V-42. Transient Elongational Viscosity ($\chi(t)$) as a Function of Elongation Rate and Time (t) for PE-3/PS-50/50 Blend 185

V-43. Transient Elongational Viscosity ($\chi(t)$) as a Function of Elongation Rate and Time (t) for PE-3/PS-30/70 Blend 186

V-44. Transient Elongational Viscosity ($\chi(t)$) as a Function of Elongation Rate and Time (t) for PE-3/PS-10/90 Blend 187

V-45. Maximum Elongational Viscosity (χ) as a Function of Elongation Rate ($\dot{E}$) for PE-2/PS Blends 189

V-46. Maximum Elongational Viscosity (χ) as a Function of Elongation Rate ($\dot{E}$) for PE-3/PS Blends 190

V-47. Maximum Elongational Viscosity (χ) as a Function of Elongation Rate ($\dot{E}$) for PE-3/PS Blends 191

V-48. Reduced Elongational Viscosity ($\chi/3\eta_0$) as a Function of Elongation Rate ($\dot{E}$) for PE-2/PS Blends 193

V-49. Reduced Elongational Viscosity ($\chi/3\eta_0$) as a Function of Elongation Rate ($\dot{E}$) for PE-1/PS Blends 194

V-50. Reduced Elongational Viscosity ($\chi/3\eta_0$) as a Function of Elongation Rate ($\dot{E}$) for PE-3/PS Blends 195

V-51. Elongation to Break ($\ln L_B/\ln L_0$) as a Function of Elongation Rate ($\dot{E}$) for PE-2/PS Blends 198

V-52. Elongation to Break ($\ln L_B/\ln L_0$) as a Function of Elongation Rate ($\dot{E}$) for PE-1/PS Blends 199

V-53. Elongation to Break ($\ln L_B/\ln L_0$) as a Function of Elongation Rate ($\dot{E}$) for PE-3/PS Blends 200

VI-1. Extrudate Swell (B) as a Function of Shear Stress (σ_{12}) for PE-1, 2, 3 and PS 205

VI-2. Extrudate Swell (B) as a Function of Shear Stress (σ_{12}) for PE-2/PS Blends 206

VI-3. Extrudate Swell (B) as a Function of Shear Stress (σ_{12}) for PE-1/PS Blend 207

FIGURE PAGE

VI-4. Extrudate Swell (B) as a Function of Shear Stress (σ_{12}) for PE-3/PS Blend 208

VI-5. Composition Dependence of Extrudate Swell (B) for PE-2/PS Blends 210

VI-6. Composition Dependence of Extrudate Swell (B) for PE-1/PS Blends 211

VI-7. Composition Dependence of Extrudate Swell (B) for PE-3/PS Blends 212

VI-8. 2θ Scan for Polyethylene (PE-2), Polystyrene (PS) and PE-2/PS Blend Melt Spun Fibers 215

VI-9. WAX Film Patterns for Polyethylene (PE-2), Polystyrene and PE-2/PS Blend Melt Spun Fibers 216

VI-10. WAX Film Patterns for Polyethylene (PE-2) and PE-2/PS Blend Melt Spun Fibers with Different Melt Draw Ratios: (a) 0; (b) 18.8; (c) 37.6; (d) 75.4; (e) .161; (f) 0; (g) 18.8; (h) 75.4; (i) 161 217

VI-11. Herman-Stein Orientation Factors f_a, f_b and f_c as a Function of Spinline Stress for PE-2 219

VI-12. Herman-Stein Orientation Factors f_a, f_b and f_c as a Function of Spinline Stress for PE-2/PS-90/10 Blend . . 220

VI-13. Herman-Stein Orientation Factors f_a, f_b and f_c as a Function of Spinline Stress for PE-2/PS-70/30 Blend . . 221

VI-14. Herman-Stein Orientation Factors f_a, f_b and f_c as a Function of Spinline Stress 222

VI-15. Herman-Stein Orientation Factors f_a, f_b and f_c as a Function of Spinline Stress for PE-2/PS-30/70 Blend . . 223

VI-16. Herman-Stein Orientation Factors f_a, f_b and f_c as a Function of Spinline Stress for PE-2/PS-10/90 Blend . . 224

VI-17. Composition Dependence of Herman's Orientation Factors for PE-2/PS Blends at a Fixed Spinline Stress 225

VI-18. Diameter Fluctuations of PE-2, PS and PE-2/PS-50/50 Blend Under the Isothermal Melt Spinning after Onset . . 227

FIGURE PAGE

VI-19. Diameter Fluctuations of PE-2/PS-50/50 Blend for Stable and Unstable Conditions 228

VI-20. Toluene Extracted PE-2/PS Blend Melt Spun Fibers at Drawdown Ratio V_L/V_0 = 215 232

VI-21. Toluene Extracted Various PE/PS-10/90 Blend Melt Spun Fibers at Drawdown Ratio V_L/V_0 = 18.8 233

VI-22. SEM Microphotographs of PE-2/PS-90/10 Blend Melt Spun Fibers with Different Drawdown Ratios: (a) 1; (b) 18.8; (c) 37.6; (d) 56.6; (e) 75.4 234

VI-23. SEM Microphotographs of PE-2/PS-50/50 Blend Melt Spun Fibers with Different Drawdown Ratios: (a) 1; (b) 18.8; (c) 37.6; (d) 56.6 236

VI-24. SEM Microphotographs of PE-2/PS-30/70 Blend Melt Spun Fibers with Different Drawdown Ratios: (a) 7; (b) 37.6 238

VI-25. SEM Microphotographs of PE-2/PS-10/90 Blend Melt Spun Fibers with Different Drawdown Ratios: (a) 1; (b) 37.6; (c) 56.6 239

VI-26. SEM Microphotographs of PE-1/PS-90/10 Blend Melt Spun Fibers with Different Drawndown Ratios: (a) 1; (b) 18.8; (c) 37.6; (d) 56.6; (e) 75.4 240

VI-27. SEM Microphotographs of PE-1/PS-90/10 Blend Melt Spun Fibers with Different Drawdown Ratios: (a) 1; (b) 18.8; (c) 37.6 242

VI-28. SEM Microphotographs of PE-3/PS-10/90 Blend Melt Spun Fibers with Different Drawdown Ratios: (a) 1; (b) 18.8; (c) 37.6; (d) 56.6; (e) 75.4 244

VI-29. SEM Microphotographs of PE-3/PS-90/10 Blend Melt Spun Fibers with Different Drawdown Ratios: (a) 1; (b) 18.8; (c) 37.6; (d) 75.4 246

VI-30. Comparison of Affine-Deformation of Mini-Fibers of PE-2/PS Blend Melt Spun Fibers 251

VI-31. Comparison of Affine-Deformation of Mini-Fibers of PE-1, 2 and 3/PS-90/10 and -10/90 Blend Melt Spun Fibers 252

FIGURE PAGE

VI-32. SEM Microphotographs of PE-1/PS-90/10 Blend Melt Spun Fibers 254

VI-33. SEM Microphotographs of Biaxially Stretched Films of PE-2/PS-90/10 Blend with Different Stretching Ratios 255

VI-34. SEM Microphotographs of Biaxially Stretched Films of PE-2/PS-70/30 Blend with Different Stretching Ratios 256

VI-35. SEM Microphotographs of PE-2/PS-90/10 Blend with Different Stretching Ratios 257

VI-36. SEM Microphotographs of Biaxially Stretched Films of PE-2/PS-30/70 Blend with Different Stretching Ratios . . 259

VI-37. SEM Microphotographs of Biaxially Stretched Films of PE-2/PS-10/90 Blend with Different Stretching Ratios . . 261

VI-38. Schematic Representation of Biaxial Deformation of Discrete Phase of PE-2/PS Blend Films 263

CHAPTER I

INTRODUCTION

It is of technological importance to combine different polymers to form alloys (or polyblends). Such systems are designed to improve mechanical properties, solvent resistance, and processability. Such a procedure has economical advantages, as blending is obviously cheaper than developing a new polymer with a new chemical structure. Blends of different elastomers have been used for many years (Patents as early as 1846 discuss natural rubber gutta perutea blends.). Perhaps the first major commercial two-phase polymer systems were modified polystyrenes in which a dispersed rubber phase was added for impact resistance. These systems are produced by polymerizing styrene monomer containing a dissolved rubber (4). Commercially useful alloys, including thermoplastic elastomers, are produced by mechanical melt mixing of existing polymers.

Polymer blends can be characterized in their phase behavior as being either compatible or incompatible. Incompatible blends possess two-phase dispersion morphologies which are produced by the flow fields of different mixing devices. The morphology of two-phase polymer blends would appear dependent on the chemical nature of the two polymers, their melt rheological properties, and the flow history. The morphology of the two phases largely governs the mechanical properties such as the tensile strength, toughness, and

impact strength. There have been no serious studies of the influence of structural and processing variables on blend morphology or processability.

In this dissertation, the relationship between polymer component chemical character and rheological properties on the morphology properties and processing behavior blends are investigated. The melt rheological properties and processing of the blends will be investigated as a function of composition. The development of a general quantitative perspective of this area is sought. The polymers chosen for investigation are polyethylene (PE), polystyrene (PS), nylon 6 (N6), and polycarbonate (PC). Blends will be formed by mechanically mixing these polymers together at various binary compositions. These systems were chosen because they have:

1. Variability in polarity.
2. The availability of many different commercial grades of polyethylene and the dependence of the viscosity of polystyrene on temperature which allows one to obtain regular variations in rheological properties.
3. The solubility of polystyrene, nylon 6, and polycarbonate in solvents allowing them to be readily extracted to.
4. The general chemical stability of the polymers involved.

CHAPTER II

LITERATURE SURVEY

A. THERMODYNAMICS OF POLYMER BLENDS

A.1. General Criteria

Polymer blends can be characterized by their phase behavior as being either compatible or incompatible. Incompatible blends show multiple phases. Each phase of a completely incompatible blend contains an essentially pure blend component, whereas the phases of partially incompatible blends may contain some of each component in the blend. Finally, blends can also be found which are completely compatible and have only one phase.

The rules governing compatible behavior of polymer blends are best understood in a thermodynamic context through the Gibbs free energy of mixing, ΔG_m (38)(120). As shown in Figure II-1, ΔG_m for a binary mixture can vary with composition in several ways. Complete compatibility exists only if

$$\Delta G_m < 0$$

$$\frac{\partial^2 G_m}{\partial \phi_2^2} > 0 \qquad \text{(II-1)}$$

These criteria are met by curve B for all compositions. Blends described by curve A violate equation (II-1) and are completely

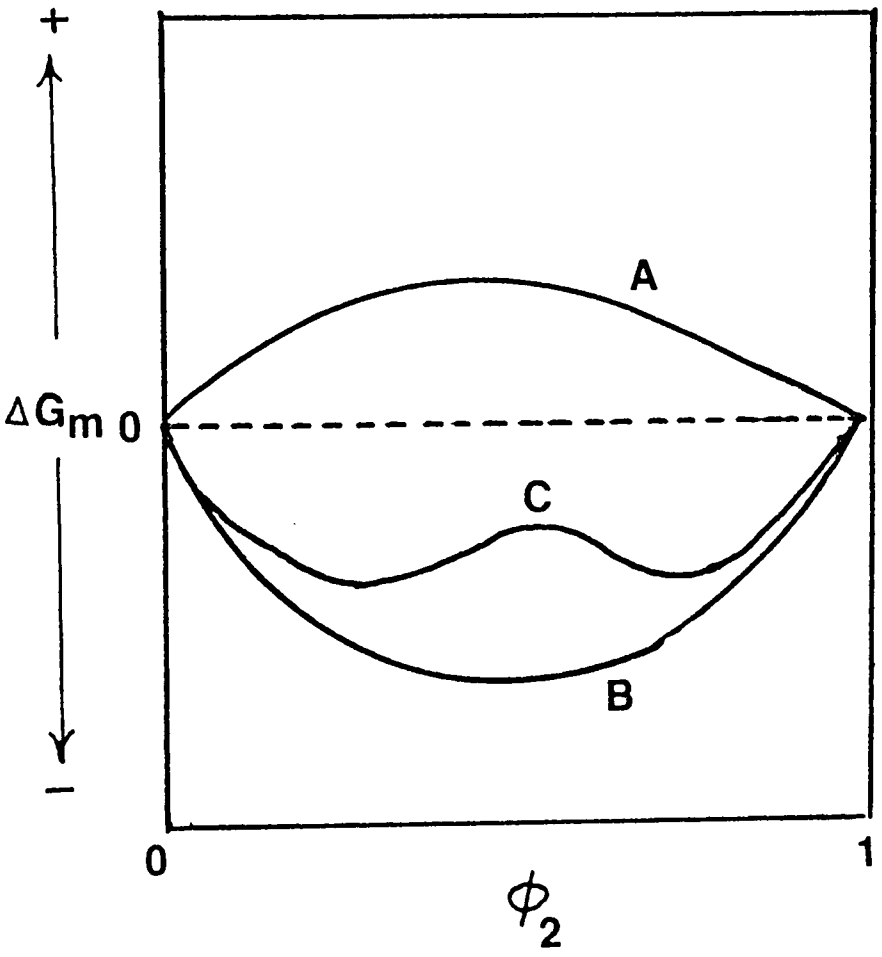


Figure II-1. The free energy of mixing diagrams for binary mixture.

incompatible. A system described by curve C is partially compatible at equilibrium. A single phase can be formed at compositions to the left and right of the minima of curve C. However, two phases will be formed with compositions given by the minima when mixtures are prepared at overall concentrations in the center range.

A.2. The Entropy of Mixing

The free energy of mixing can be described in terms of enthalpic and entropic contributions.

$$\Delta G_m = \Delta H_m - T(\Delta S_m^{(c)} + \Delta S_m^{(e)}) \qquad \text{(II-2)}$$

where: ΔH_m is the heat of mixing;
$\Delta S_m^{(c)}$ is the combinatorial entropy of mixing;
$\Delta S_m^{(e)}$ is the excess entropy of mixing.

For a binary solution of small molecules which mix randomly the value of $\Delta S_m^{(c)}$ per mole is:

$$\Delta S_m^{(c)} = -R[N_1 \ln X_1 + N_2 \ln X_2] \qquad \text{(II-3)}$$

where: X_i is the mole fraction and N_i the number of moles of species i of the mixture.

Flory (36)(37)(38)(39) and Huggins (68)(69)(70), following suggestions of Meyer (101) developed expressions to describe the combinatorial entropy of mixing of polymer chains with solvents (or other polymer chains) on a lattice of fixed volume. They obtained

$$\Delta S_m^{(c)} = -k\left[\frac{X_1}{V_1} \ln\phi_1 + \frac{X_2}{V_2} \ln\phi_2\right] \qquad \text{(II-4a)}$$

where V_i is the molar volume of species i. The total free energy of mixing is given by

$$\Delta G_m = \Delta H_m + RT(X_1 \ln\phi_1 + X_2 \ln\phi_2) - T\Delta S_m^{(e)} \qquad \text{(II-4b)}$$

Flory (39) has generalized this to solutions of polydisperse polymers. Scott (139) and Tompa (169) applied the Flory-Huggins theory of polymer solution thermodynamics to the mixing of the two polymer components. Because of the high molecular weights of commercially important polymers, V_i, which is proportional to molecular weight, is very large, and $S_m^{(c)}$ for polymer mixtures is virtually zero. Paxton and others (116) report that as the molecular weights of polymers decrease and the ΔS_m term increases, compatibility becomes greater. These results have profound consequences regarding the general miscibility of polymer blends since it suggests that $\Delta G_m < 0$ only when $\Delta H_m < 0$ or $\Delta S_m^{(e)} > 0$.

Little is presently known about the excess entropy of mixing, $\Delta S_m^{(e)}$, except that it can result from "equation of state" effects associated with volume changes on mixing (120). Prigogine (120), Flory (40), and many others have developed a partition function whose lattice energy is related to volume to the equation of state effects.

Flory's lattice concept is limited, as it does not predict the volume changes. Because of the very small combinatorial entropy of mixing, the excess entropy due to the volume change could play an important role in overall thermodynamic behavior, even though one would expect its magnitude to be quite small because volume changes on mixing are typically less than 1 percent. To the extent this phenomenon is general and that $\Delta S_m^{(e)}$ is proportional to ΔV_m, the excess entropy contribution to ΔG_m will be positive and, therefore, tend to lead to blend incompatibility.

A.3. ΔH_m: the Solubility Parameter

Scatchard (134) and Hildebrand (65) have investigated how ΔH_m is related to the interaction energy. The entropy of mixing is primarily dependent on the energy change associated with nearest neighbor contacts during mixing. This is a good approximation and is independent of molecular weight. The polymer segments should interact via dispersive or Van der Waals type bonding between segments. Hildebrand suggested that the heat of mixing can be estimated using the solubility parameters of pure components δ_i. These are defined as cohesive energy density

$$\delta_i = \sqrt{E_i/V_i} \ (\text{cal/cm}^3)^{\frac{1}{2}} \qquad \text{(II-5)}$$

where: E_i is the molar cohensive energy;

V_i is the molar volume.

The heat of mixing has the form:

$$\Delta H_m = V(\delta_1 - \delta_2)^2 \phi_1 \phi_2 \qquad \text{(II-6)}$$

Several general methods are available for determining the solubility parameter of a substance. These include internal pressure methods (109)(110)(112), swelling (96), heats of solution, chromatography, solution behavior (144) and/or extrapolation (197) from correlation with surface tension (65), refractive index (16)(80), etc. It has been found that δ_i has additive properties which can be calculated using group contributions. Small (143) was one of the first to give methods estimate corrections for dipole effects, hydrogen bonding and ionic interactions. It is important to note that equation (II-4b) always predicts a positive entropy of mixing when $\delta_1 \simeq \delta_2$. More recent studies have been made by Hoy (66), Konstan and Feairheller (81), and Van Krevelen (177). Data for solubility parameters of polymers are rather poor and unreliable. Typically reported solubility parameters for polymers are listed in Table II-1.

Flory (39) has expressed the heat of mixing

$$\Delta H_m = \frac{\chi_{12} RT}{V} \phi_1 \phi_2 \qquad \text{(II-7)}$$

where χ_{12} is the interaction parameter and ϕ_1 and ϕ_2 are volume fraction.

The Flory-Huggins interaction parameter was supposed to be independent of concentration, temperature, and molecular weight. Experimentally, this is found not to be the case proposed on

Table II-1. Range of experimental values of solubility parameter

Polymer	δ_i*
Polyethylene	8.25
Polypropylene	7.55
Poly(vinyl chloride)	9.55
Poly(methyl methacrylate)	8.9
Polystyrene	9.0
Polyacrylonitrile	12.7
Poly(ethylene terephthalate)	10.7
Polyamide (Nylon 6-6)	13.0
Polyamide (Polycaprolactan)	9.34
Cellulose acetate butyrate	8.90

*Small, P.A., J. Appl. Chem. 3, 71 (1953).

empirical specific function of temperature for interaction parameter. Further considerations are given by McMaster (99) and Patterson (115).

Polymer pairs with chemical structures capable of specific interactions have exothermic or negative heats of mixing (28)(29)(60)(110)(113)(114)(120)(143). Experimental data for those interactions has been represented empirically in the form (11):

$$\Delta H_m = B\phi_1\phi_2 = \frac{\chi RT}{V}\phi_1\phi_2 \qquad \text{(II-8)}$$

where B or equivalently χ are negative and express the magnitude of the observed exotherm. This leads to compatibility. Table II-2 shows typical compatible and incompatible polymer pairs. Barlow and Paul (11) showed examples of probable specific interaction pairs. For example, Polyvinyl Chloride/Polyether may be hydrogen bond formation (114)(203), and Polycarbonate/Polyether may have n-π complex formation, and Poly-ρ-Phenylene Oxide/PS may have π-π complex formation (28)(29)(186)(187).

B. STRATIFIED TWO-PHASE FLOW OF POLYMER MELTS

B.1. Newtonian Fluids

Theoretical and experimental studies of stratified laminar two-phase flows of viscous liquids in channels has been undertaken by Russel and Charles (132) and Charles and Redburger (22), Gemmel and Epstin (45), and Yu and Sparrow (201) during the past few decades. They note that large pressure gradient reductions are obtained by the addition of a small amount of water to crude oil

Table II-2. Typical examples of compatible and incompatible polymer blends

	Methods of Compatibility Determination	Reference
Compatible Pairs		
PS-Poly(2,6 dimethyl-1,4-phyenylene)	Dynamic mechanical calorimetric, rheological	(120)(152)
Isotactic PS-PPO	T_g, T_m depression	(188)
PS-Poly(vinylmethy ether)	Calorimetric, nuclear magnetic resonance	(7)(8) (110)
PS-Polystyrene-co-acrylonitrile	Dynamic mechanical, Cloud-point curve	(99)(140)
PVC-Pol(ε-caprolactone)	Dynamic mechanical Crystallization kinetics	(150)
	Small angle x-ray	(77)
PVC-Syndiotactic Poly-methylene methacrylate (PMMA)	Dynamic mechanical	(138)
Incompatible Pairs		
PS-PE	Scanning electron microscopy	(9)(10)(35)(62) (63)
	Rheological	(97)(149)(151)
PS-PVC	SEM, Dynamic mechanical	(82)
PE-Polypropylene (PP)	Crystallization kinetics	(142)
PS-PMMA	Transmission electron microscopy (TEM)	(174)
N6-PE	Polarized light microscopy	(61)
N6-PP	SEM, Wide angle x-ray	(90)

flowing through a pipeline. This fact resulted in the reduction of pumping cost without decreasing flow rate (23)(73). Charles et al. (21) have shown that pressure losses in two-phase stratified flow of water and high viscosity crude oil were lower than those predicted from solution of the Navier-Stokes equations presuming a constant flat interface shape. This was variously explained by turbulence at the interface leading to emulsification of oil (22) and the meniscus. Charles and Lilleleht (23) found interface curvature between flowing oil and water at the wall of rectangular conduit and concluded that it depended upon previous flow conditions. Yu and Sparrow (207) observed that oil-water stratified flow systems exhibited curved interfaces and that the extent of interface curvature increased with flow rate. Encapsulation has been found by Everage (33) in other Newtonian liquid systems. Many researchers have predicted velocity profiles in two phase flow of Newtonian fluids for specified interface shape (22)(23)(33)(34)(45)(64)(145)(190).

B.2. Non-Newtonian Fluids

The pioneering studies of stratified bicomponent polymer melt flow through the capillary and the accompanying problems of the interface configuration were those of Southern and Ballman (145)(146). They made extensive studies of distortion of interface shape on melt viscosity ratio using polystyrenes of different molecular weight distribution. The interface shape dependency on the viscosity ratio in stratified bicomponent flow has been clearly demonstrated. Lower viscosity component wrapped around the high viscosity polymer as well as

for Newtonian fluids and led to encapsulation. Interface curvature increased with increased capillary L/D ratio and with viscosity ratio. Southern and Ballman observed that this was consistent with the idea of a reversible interface motion necessary for pressure drop equalization. They noted that relative extent of extrudate swell has relatively very little effect on the degree of interface wrap-around. They concluded the difference in the magnitude of the laminar shear viscosity between the two melt phases causes the interface rearrangement. Experiments by Han (48), Lee and White (85), and Everage (33) also lend support. Mechanistic arguments for this view are given by Maclean (94), Everage (33)(34), and White and Lee (85), who concluded that the higher the viscosity ratio the system had, the greater the level of encapsulation.

Han et al. (48)(51)(57)(58)(202) derived the velocity profile and flow rate for multilayer flow in a slit die and concentric flow in a circular pipe by the use of the power law. Uhland (175) also analyzed the two-phase flow in a circular pipe using a power law viscosity function. He showed that thickness is a function of volume ratio, viscosity ratio, power law index, and temperature profile. Maclean (98) and Everage (33) determined the velocity profile and interface configuration in stratified bicomponent tube flow through hypothesizing a principle of minimum viscous dissipation. Lee and White (85) analyzed this using hydrodynamic lubrication theory.

Schrenk (137) and Han et al. (48)(78) have described interfacial instability of multilayer coextrusion in a slit die.

Li (88)(89) initiated the theory of interfacial instability in viscoelastic fluids. Khan and Han (78) have studied the phenomena of interfacial instability of two second-order fluids in a slit die theoretically and have reported that interfacial instability is influenced by the viscosity ratio, relative elastic behavior, and depth ratio.

C. MIXING AND DISPERSION PROCESS

C.1. Types of Mixers

Mixing of polymers was first carried out extensively in the rubber industry but has since become a major plastic processing operation. Typical examples of mixing processes include the mixing of ethylene-propylene terpolymer into polypropylene in a Banbury mixer and blending of polyolefines in an extruder.

C.2. Screw Extruders and Theory of Mixing

Screw extruders may be divided into single screw and twin screw apparatus. The single screw extruder was developed as forming machine rubber and plastic materials. It functions as a mixing machine because of the shearing deformation which the mixture is subjected to. A conventional screw extruder consists of three basic stages through which the material being processed moves. First of all, there is a "hopper" into which the initial solid compound is charged and which serves the purpose of containing the material and feeding it to the succeeding stage. The second stage of the extruder consists of a rotating screw inside a smooth barrel. The screw takes

up the material fed from the hopper and conveys it down the length of the barrel while melting it. The final stage of the extruder is a die which takes up the melt from the screw and shapes it.

Theoretical analysis of the flow of fluids in a screw feeding a die were first carried out and published by Rowell and Finlayson (130). Carley, Mallouk, and McKelvey (19) presumed that the polymer responded as a Newtonian fluid as it moved through the extruder screw and applied Rowell and Finlayson's theory. Tadmor (155), Klein, and Marshall (150)(157) developed a theory of the melting zone.

There have been studies of the mixing process in mixing in the metering region of a screw extruder (105)(147). For a constant volume system, the reduction in striation thickness is related to the creation of new interfacial area, which, in turn, is related to the shear strain of the fluid and orientation of the interface. The amount of shear received by an element of liquid in the channel was calculated by Mohr et al. (105) as the sum of the products of shear rate and residence time for each part of the flow path. The predictions of Mohr et al. have been confirmed in experiments by Maddock (95).

C.3. Motionless Mixer

Motionless mixers represent ingenious designs, through which one may rearrange the flow field and reshuffle streams in such a way that the interfacial area increases appreciably and predictably every time the fluid mixture flows through a repetitive mixing element making up a motionless mixer. Although the exact mixing pattern is

specific to the particular type of the motionless mixer used, it is generally true that the interfacial area between the major and minor components is increased in two ways: by shear or extensional flow and splitting and recombining fluid stream. There are three different types of motionless mixers (139). These are the Ross ISG (Interfacial Surface Generator), the Kenics Static Mixer, and the Koch Mixer.

The Ross ISG (Figure II-2(a), (b)) has four circular holes which form a line perpendicular to that formed by the exit holes in each element. This is achieved by drilling the exit obliquely with respect to the axis of the element and in such a way that an outside entrance has an inside exit, thus achieving radial mixing. On the other hand, a tetrahedral space is formed between two consecutive elements. The four streams from the first element join together in this space, creating new interfaces (strains). The flow that occurs in the tetrahedral spaces is divergent-covergent in nature and results in an effective stretching of the interfacial area elements. In this stretched state, the fluid is divided into four streams by the holes of the second element where radial redistribution will occur again. The net result of the fluid stream combination and flow is a four-fold increase of the number of striations N_s. Following the fluid through consecutive elements, one can easily show that the relation between N_s and the number of elements E is

$$N_s = 4^E \qquad \text{(II-9)}$$

The Koch Mixer (Figure II-2(d)) has mixing elements which are round, rectangular, or otherwise shaped assembly containing a large number of parallel, corrugated metal sheets. The corrugation angle of adjacent layers in the element is reversed with respect to the mixer axis. The streams entering the mixing cell are rearranged due to extensional and shearing forces and subsequently divided into new streams, each of which leaves the mixing cell in a different direction. Both streams upon arriving at the next corrugation intersection are again rearranged and divided into two new streams, each of which in turn departs in a new direction for further rearranging and subdivision. The length of the corrugation is usually equal to the diameter of the housing. The number of layers generated by Koch static mixing elements is given by

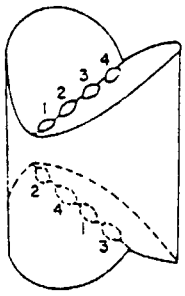
$$S = \frac{m}{2} (2m)^{E-1} \qquad \text{(II-10)}$$

where m = the number of corrugated plates per element.

The Kenics Static Mixer consists of helical elements fixed within a tubular housing. Consecutive helices are of opposite sense. They are welded together so that the adjacent edges are perpendicular to each other. The fluid is thus split every time it leaves one element and enters the next. Within each element the fluid flows in two semicircular helical channels where the flow field consists of a combination of down-channel and significant cross-channel velocity components. During each splitting, the number of striations is doubled, leading to a relationship given by



(a)



(b)

Figure II-2. Photographs and schematic view of (a) (b) Ross ISG mixing elements; (c) Kenics mixer elements; (d) Koch mixer elements.



(c)



(d)

Figure II-2 (continued)

$$N_s = 2^E \qquad \text{(II-11)}$$

where E is the number of elements.

Han and Kim (54) and Van Oene (179)(180) used a Kenics static mixer with a screw extruder to get better uniform dispersion of PE-PS blend. Shimomura, Spruiell, and White (142) and Liang et al. (90) used a Koch static mixer with a screw extruder for PP-PE blends and PP-N6 blends, respectively.

D. INTERFACIAL PHENOMENA IN DISPERSE LIQUIDS OR MELTS

D.1. The Breakup and Instability of Newtonian Fluids

Fundamental studies of mechanisms of mixing and dispersion in two-phase Newtonian fluids have a long history. In 1932, Taylor (160)(161) provided the first theoretical analysis and experiments on the breakup of elongated droplets suspended in deforming liquids. He solved the creeping motion equation for an undeformed, neutrally buoyant, fluid drop, with the outside and inside pressure balanced by interfacial tension. He showed that in steady shear flow, the drop becomes ellipsoidal. He interpreted the deformation of droplets in terms of a shape parameter D

$$D = \frac{L - B}{L + B} \qquad \text{(II-12)}$$

Here, L is the length, and B is the height of the deformed drops. The deformation, D, depends only upon the two dimensionless parameters λ and k

$$D = k \cdot \frac{(19\lambda + 16)}{(16\lambda + 16)} \qquad \text{(II-13)}$$

$$\lambda = \frac{\eta_1}{\eta_2} \qquad \text{(II-14)}$$

and

$$k = \frac{\dot{\gamma} a \eta_2}{\kappa} \qquad \text{(II-15)}$$

where κ is the interfacial tension of the 1-2 interface, η_1 and η_2 are the viscosities of the dispersed and the medium phases, respectively, a is the particle radius, and $\dot{\gamma}$ is the magnitude of the local shear rate. The product $\dot{\gamma}\eta_2$ represents the local shear stress.

According to Taylor, breakup would occur when interfacial tension forces, tending to maintain the drop shape, could no longer balance the external forces tending to burst the droplets. The critical deformation is given by D = 0.5. The precision of the experimental results were limited by the approximate character of the measurements of κ, the interfacial tension. In 1959, Bartok and Mason (13)(14) found a linear variation of D with $\dot{\gamma}a$ for several systems, but κ was unknown. Rumscheidt and Mason (131) found that the mechanisms of breakup of drops at high values of D were found to vary with λ and to be different for shear and hyperbolic flow with known κ values. They classified four distinct modes of behavior which were dependent mainly upon λ. This is illustrated in Figure II-3. Karam and Bellinger (76) experimentally investigated the effects of λ, κ, and a on breakup of Newtonian droplets on uniform shear flow. They reported that there is a range of viscosity ratios, outside of which

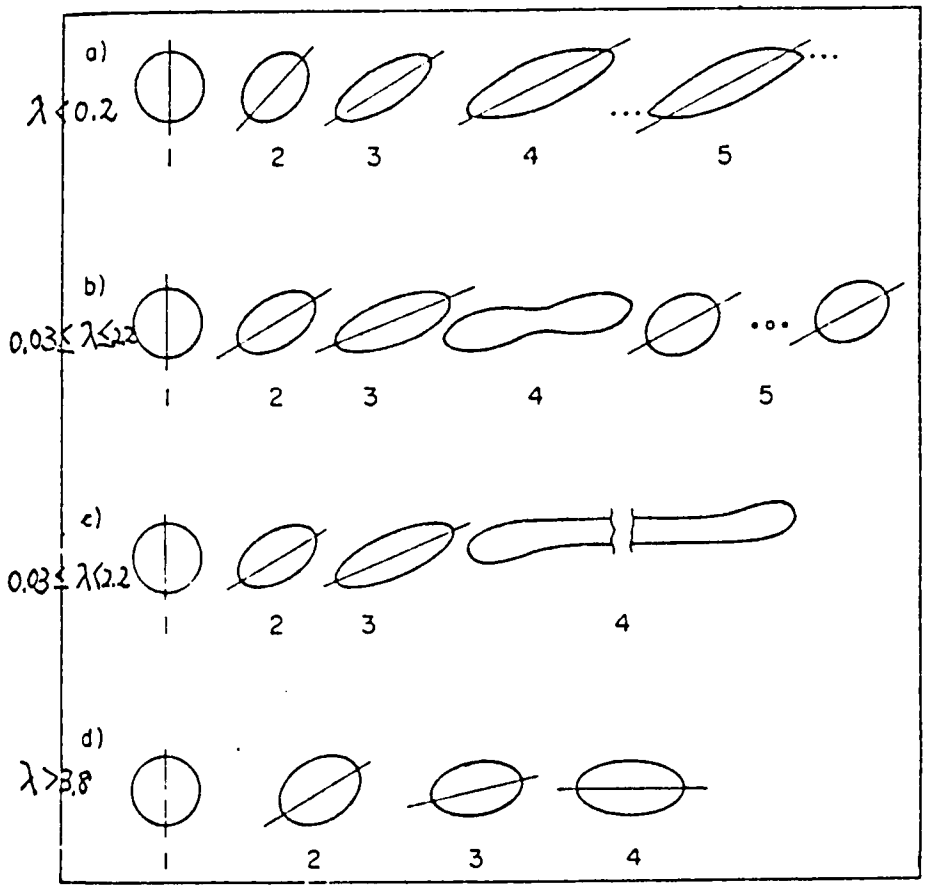


Figure II-3. Tracing of droplets in shearing flow with various viscosity ratios: and increasing shear rates: (a) $\lambda < 0.2$; (b) $0.03 \leq \lambda \leq 2.2$; (c) $0.03 \leq \lambda \leq 2.2$; (d) $\lambda \geq 3.8$.

droplet breakup will not occur, and that breakup occurs only when the viscosity ratio lies in the range of 0.2-1.0.

In the 1970's, Torza, Cox, and Mason (170) reported that the mechanism of droplet breakup depends more on the rate of increase in shear rate than viscosity ratio. They have found, from their experimental study in uniform shear flow, that the rate of increase in shear rate $\dot{\gamma}$ influences both the value of $\dot{\gamma}\eta_2$ and the mode of breakup, and that the product of $\dot{\gamma}\eta_2$ and droplet radius "a" stays nearly constant for a given viscosity ratio in the range of 0.3-0.6. Breakup did not occur at all when the viscosity ratio was greater than 3.0, which is in agreement with the result of Karam and Bellinger (76). They observed that at high shear rates, the droplet is pulled out into a long threadlike form which eventually becomes varicose and breaks up into a series of smaller droplets (Mode b) in Figure II-3), and that big viscous drops were more easily pulled out into liquid threads (Mode e) than small and inviscid drops. The burst was independent of a and η_1 at very low $\frac{d\dot{\gamma}}{dt}$ and occurred in Mode B_1 (Figure II-3). They mentioned that the dependence of drop burst upon $\frac{d\dot{\gamma}}{dt}$ could be explained by considering the relaxation time $\tau = \frac{a\eta_2}{K}$, and indicating large and viscous drops readjust their shapes more slowly than small and inviscid drops so that high rates of increasing $\dot{\gamma}$ stretched the spheroidal drops directly into threads which had no time to relax but broke up into many drops similar to Rayligh instabilities (122)(123).

Droplet breakup is a transient phenomenon. Therefore, any theoretical attempt to understand this phenomenon requires the

solution of unsteady-state equations of motion. The instability of a droplet is governed by the local flow conditions and the rheological and interfacial properties of the fluids involved. Tomotika (167)(168) was the first to carry out a hydrodynamic stability analysis explaining Taylor's experimental observation (160)(161). Tomotika assumed a uniform rate of strain imposed on a liquid cylinder, having a uniform cross-section initially, and showed from his analysis that, if the ratio of viscosities of the two fluids is neither zero nor infinity, the maximum instability (i.e., droplet breakup) always occurs at a certain definite value of wavelength of the assumed initial disturbance. More recently, Mikami et al. (102) extended Tomotika's analysis to predict the time of breakup and the size of broken droplets in steady extensional flow.

D.2. The Breakup and Instability of Non-Newtonian Fluids

D.2-1. Theoretical works. Following a suggestion of Cox (27), Van Oene (178) has emphasized the stabilizing effect of viscoelasticity. He argued that important parameters responsible for the formation of spheres, ribbons, or elongated filament morphologies in a matrix were particle size "a," interfacial tension "κ," and difference in the viscoelastic properties of the two phases. He introduced a relationship between the second normal stress difference and the apparent interfacial tension from thermodynamic considerations. He concluded that elastic effect will depend on the particle size and will tend to be dominant polymer melt blends.

Chin and Han (24)(25) presented both theoretical and experimental studies of the phenomenon of droplet breakup and determined effect of elasticity for a criterion of droplet breakup. They linearized the equation of motion for a system which obeyed a viscoelastic constitutive equation based on Jeffery's model. They concluded that when either the droplet phase or suspending medium, or both, were viscoelastic fluids, the fluid elasticity should play an important role in the occurrence of recoil and most likely in the occurrence of droplet breakup. They suggested that the system parameters were effective on the breakup and instability with the viscosity ratio λ, other parameter ratio, $\frac{\eta_0 \dot{\gamma} a}{\kappa}$, and ratios of relaxation terms of the two phases $\frac{\tau_1}{\tau_2}$. Both the dispersed fluid elasticity and Weissenberg number, $\tau\dot{\gamma}$, and medium elasticity are reported as stabilizing.

D.2-2. Experimental works. Hydrodynamic breakup of a particular phase structure gives rise to single droplets. Recent experimental studies of Han and Funatsu (50) on the stability of single droplet of polymer solutions have shown that dispersion can be obtained by successively developing elongated filaments in converging flow as in a die entrance and then breaking these up in a succeeding diverging flow. They have shown that the stable continuous threads would be observed in flow if the ratio of droplets viscosity to the medium viscosity is greater than or equal to 3-4. If it is smaller or equal to 3, breakup of the droplets would occur in flow.

Extensive studies of breakup and instability of dispersed droplets in two-phase melt systems have been carried out by Vinogradov and his coworkers (1)(172)(173)(181). They find by mixing pellets of polyoxymethylene (POM) and a copolyamide, a fine series of ultra-thin POM fibers is obtained. It would appear that these filaments are formed in elongational flow in the die (Figure II-4(a)). They concluded that the magnitude of shear stress is the important determining factor in the process of fibrillation if the viscosity ratio is close to unity. Similar conditions yielded thin fibers in polyoxymethylene and Ethylene Vinyl Acetate Copolymer blends. They mentioned that the deformability of the drop was determined by two parameters: the ratio (λ) of the viscosity of the emulsified liquid to the viscosity of the medium and the ratio of the interfacial tension (κ) to the product of the shear stress and the radius of the particle ($\bar{a}$); i.e., $\frac{\kappa}{a\bar{a}} = \frac{\kappa}{a\eta\dot{\gamma}}$. If the value is $K > 1$, surface phenomena will play a substantial part in the deformation for submicron drops. For drops larger than a micron with $K << 1$, the deformability becomes a function of the ratio of the viscosities of the melts only. They observed that at large $\lambda(\frac{\eta_1}{\eta_2})$ values drop deformation in the extrudate was insignificant; i.e., no fiber formation took place.

Van Oene (178) has noted that the transition from the drop to fiber in polyethylene-polystyrene blend was observed when the viscosities of the dispersed phase and dispersion medium were the same, and if both the viscosity ratio and the interfacial parameters are small, both phases will be deformed as a continuum. Alle and

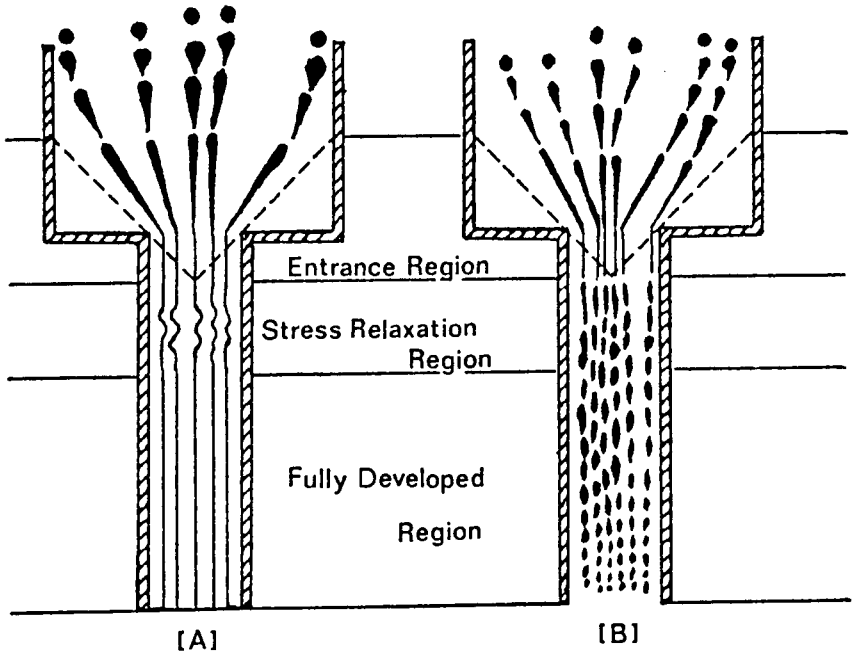


Figure II-4. Schematic representation of droplet-fiber transformation.

Lynagae-Jorgensen's (3) experimental results coincided with Vinogradov and his coworkers' fibrillation results and summarized two possible cases for the drop-fiber transition or drop-breakup of two-phase molten polymer systems shown in Figure II-4(a), (b):

Case 1: When the dispersed phase is more viscous than the continuous phase and is present in minor or equal amounts, the droplets are elongated at the entrance region. The elongated droplets snap back in a stress relaxation region and form randomly distributed "fibrils" of thin continuous layers parallel to flow direction in developed flow region as shown in Figure II-4(a).

Case 2: When the dispersed phase is less viscous than matrix phase and is present in minor amounts, the droplets are elongated in the entrance region. These elongated droplets either recoil or break up into smaller droplets in the stress relaxation region and form fine and uniform dispersion of smaller droplets in the developed flow region as shown in Figure II-4(b).

E. MODES OF TWO-PHASE MORPHOLOGY OF BLENDS

Since the development of Kato's osmium stain technique (1960), the morphology of rubber modified plastic and block copolymers and graft copolymers has been studied by various investigators. These

include High Impact Polystyrene (HIPS), Acrylonitrile-Butadiene Styrene copolymer (ABS), polyvinyl chloride-natural rubber (PVC-NBR), and High Impact Polyvinyl Chloride (HIPVC) by Transmission Electron Microscopy (TEM) (98). They observed two-phase structure with rubber phases appearing as sea-island.

Various other methods have been applied to observe phase morphology such as scanning electron microscopy, polarized light microscopy, phase contrast microscopy, and interference optical microscopy. The samples have been prepared for observation by etching (removal of soluble phases) and thin sections have been made by microtome and fracture surfaces broken in liquid nitrogen. The structures observed are summarized by Heikens et al. (62)(63), Martuscelli et al. (97), and Sperling (147), who classified the phase morphologies observed into four general categories:

1. Ribbons and lamellae (stratified structure);
2. Rods and fibrils;
3. Droplets;
4. Co-continuous phases.

Van Oene (178)(180) for PS-PE, PS-PMMA, Martuscelli et al. (97) for PP-PE and PE-PS, Vinogradov and his coworkers (1)(172) (173)(181) for POM-Copolyamide and POM-Ethylene-Vinyl Acetrate copolymer (CEVAc), and Alle et al. (3) for PP-PE observed droplet-fibril transitions in capillary flow even when they used different pre-mixing devices. Vinogradov and coworkers observed that as the shear stress increased, the diameter of fibrils decreased to sub-microscopic dimensions.

The platelet-lamellae morphology (stratified structure) was observed by Vanoene (178)(180) for PE/PS - 10/90, 30/70 and Han et al. (52)(53) for PE/PS and PP/PS - 25/75, 50/50, 75/25, Hayashida et al. (61) for PE/PP, PE/N6 - 25/75, 50/50, 75/25 and White et al. (189) PE/PS - 50/50 for cross-sections perpendicular to the flow direction. At the lowest shear rate, the dispersed phase forms a lamellar morphology even though some fibrils with elliptical cross-section can be seen. As the shear rate increases, the lamellar morphology became dominant. At the highest rate, where the extrudate itself is severely distorted by melt fracture, the lamellar morphology persists, containing vortexlike swirls. The lamellar morphology is independent of the shear rate or shear stress and residence time and temperature. Hayashida et al. (61) explained this type morphology as being due to the extruder screw rotation because the number of vortices was greater when screw revolution rate was increased.
et al. (189) also observed the telescopic structure of PE-PS blends extruded from ram extruders.

Han and his coworkers (53)(54)(55) observed that the morphology of the PE-PS blends in ratio 25/75 and 50/50 was similar; both blends have polystyrene droplets dispersed in a continuous phase of HDPE. In 75/25 blends, the two components seem interlocked. This type of morphology was found to be independent of temperature.

In more recent works, Liang et al. (90) observed phase size growth of PP-N6 blends as a function of time under quiescent and mild deformation rate conditions. Fukushima et al. (43) have also observed this for PE-N6 systems.

F. RHEOLOGICAL PROPERTIES OF TWO-PHASE FLUIDS

F.1. Viscosity of Newtonian Liquid Mixtures

It has been tacitly assumed by the great majority of workers that when two liquids are mixed, the viscosity of mixture is normally a linear function of the composition. This was considered as early as 1876 in the work of Wijkander (194) and supported by Linebarger (1896) (91) for a mixture of miscible and chemically indifferent liquids.

Various empirical formulae have been proposed to represent viscosity-composition behavior in solutions. Experiments by Arrhenius on aqueous solutions of alcohols and other substances led him to propose a logarithmic rule as an empirical law. Reyer (124), Wagner (184), Launstein (83)(84), and Kanitz (75) have found that Arrhenius's logarithmic rule applies in various systems. According to Arrhenius, the viscosity η at temperature T of a mixture which contains in ϕ_1 of a liquid of viscosity η_1, ϕ_2 of one of viscosity η_2 at temperature τ is given by the equation

$$\eta = \eta_1^{\phi_1}\eta_2^{\phi_2}\eta_3^{\phi_3} \text{ ----}$$

$$\log \eta = \phi_1 \log \eta_1 + \phi_2 \log \eta_2 + \phi_3 \ln \eta_3 + \text{ ----} \qquad \text{(II-16)}$$

Thorpe and Rodger (163) were struck by the absence of linearity in the viscosity curves in the case of mixtures of benzene and chloroform and mixtures of carbon disulfide with benzene, toluene, ether, and acetic ether. Most of the viscosity-composition curves showed a minimum or a maximum.

In 1900, Lees (86) developed a theory based on the assumption that if the lamellae of viscous material are arranged parallel to the applied shear stress (Figure II-5(a)), the viscosity η of the mixture may be calculated using a volume averaged shear rate as follows

$$\dot{\gamma} = \phi_1\dot{\gamma}_1 + \phi_2\dot{\gamma}_2$$

$$\frac{\sigma_{12}}{\eta} = \phi_1 \frac{\sigma_{12}}{\eta_1} + \phi_2 \frac{\sigma_{12}}{\eta_2}$$

$$\frac{1}{\eta} = \frac{\phi_1}{\eta_1} + \frac{\phi_2}{\eta_2} \qquad \text{(II-17)}$$

If the lamellae of viscous material are arranged perpendicular to the appling shear stress (Figure II-5(b)), the viscosity η of mixture is argued to be

$$\eta = \phi_1\eta_1 + \phi_2\eta_2 + \text{----} \qquad \text{(II-18)}$$

In two systems of separating planes mutually perpendicular to each other, the viscosity of mixture η is given by (Figure II-5(c))

$$\log \eta = \phi_1 \log \eta_1 + \phi_2 \log \eta_2 + \phi_3 \log \eta_3 \qquad \text{(II-19)}$$

Lees compared many results of the viscosities of mixtures of water and alcohols or certain acids with these equations but was unable to obtain a satisfactory verification of any of these from the experimental results.

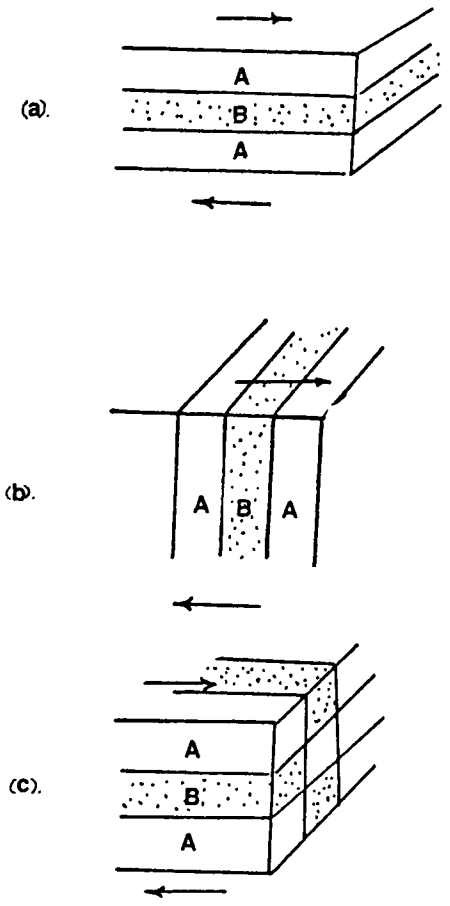


Figure II-5. Schematic models of two-phase flow: (a) lamellae parallel to the applied shear stress; (b) lamellae perpendicular to the applied shear stress; (c) separating planes parallel to the applied shear stress.

The basic hydrodynamic formulation for the viscosity of suspensions is that of Einstein (31)(32). Einstein based his formula on solution of the creeping flow equations for a Newtonian fluid containing suspended isolated rigid spheres (infinite dilution). He obtained

$$\eta = \eta_0 \left(1 + \frac{5}{2} \phi\right) \tag{II-20}$$

In 1911, Hadamard (47) showed that for a liquid sphere, the factor 2/3 in Stokes's law for the velocity of free fall must be replaced by

$$\frac{2\ \eta_0/3 + \eta'}{\eta_0 + \eta'}$$

Therefore

$$\eta = \eta_0 \left(1 + \frac{2\ \eta_0/3 + \eta'}{\eta_0 + \eta'} \phi\right) \tag{II-21}$$

where η' is the viscosity of the dispersed droplet and η_0 is the viscosity of the medium and ϕ is the concentration. Taylor (160) (161) modified Einstein's solution for shear flow of an isolated suspension of rigid spheres to an emulsion of spherical droplets of liquid of viscosity η' in a second liquid of viscosity η_0. He obtained

$$\eta = \eta_0 \left(1 + \frac{\eta_0 + \frac{5}{2} \eta'}{\eta_0 + \eta'} \phi\right) \tag{II-22}$$

In 1933, Richardson (125) made measurements on the behavior of emulsions when subjected to shear in a coaxial cylinder apparatus,

using water and benzene as the two components. He found that the viscosity increases rapidly with the concentration of the disperse phase, although the water-in-benzene emulsion breaks up when the water predominates in quantity over the second constituent. The trend of the curve for benzene-in-water resembles that of solid suspensions and suggests an exponential relation between apparent viscosity and concentrations. He introduced the logarithmic formula

$$\log \left(\frac{\eta}{\eta_o}\right) = \chi C \qquad \text{(II-23)}$$

where C is concentration and χ is the coefficient dependent on the emulsifying agent.

Leviton and Leighton (87) in 1936 observed that below the concentration corresponding to "close-packing," globule size has little influence on viscosity. On the other hand, later, Lyttleton and Traxler (93) found that a 60 percent asphalt emulsion was separated into two fractions. The one having greater uniformity of globule size was ten times more viscous than the other. Sumner (154) remarks that the more uniform the globule size, the lower is the volume concentration at which close-packing is reached, the greater is the hindrance to flow of the continuous medium at any given volume concentration. Richardson (126) investigated that in a falling sphere viscometer, the apparent viscosity of four 75 percent oil/water emulsions were measured and the larger size of drops and the broader the size distribution, the lower is the viscosity.

Leviton and Leighton (87), on the other hand, have found that emulsions of milk, i.e., fat globules in water, satisfy a modified Einstein-Taylor formula:

$$\log \eta/\eta_o = 2.5 \left(\frac{\eta' + 2\eta_o/3}{\eta' + \eta_o}\right)(\phi + \phi^{5/3} + \phi^{11/3}) \qquad \text{(II-24)}$$

At small values of ϕ, this becomes practically the same as Taylor's formula. Nawab and Mason (108) measured the viscosity of various emulsions, e.g., butylbenzoic acid in water, and found those data coincided with Taylor's equation.

More recently, Frankel and Acrivos (42) established a constitutive equation for dilute emulsions in steady shearing flow from hydrodynamic theory. Considering the deformation of the drop, they find

$$\begin{aligned} \underset{\sim}{P} + \Lambda \frac{D\underset{\sim}{P}}{Dt} = 2\eta_o \{1 + (\frac{5\lambda + 2}{2\lambda + 2})\phi\} \{\underset{\sim}{d} + \Lambda \frac{D\underset{\sim}{P}}{Dt}\} \\ + (\frac{\eta_o^2 a}{\sigma})\phi \{-\frac{1}{40}(\frac{19\lambda + 16}{\lambda + 1})^2 \frac{D\underset{\sim}{d}}{Dt} \\ + \frac{3(19\lambda + 16)(25\lambda^2 + 41\lambda + 4)}{140(\lambda + 1)^3} S_d (\underset{\sim}{d} \cdot \underset{\sim}{d})\} \end{aligned} \qquad \text{(II-25)}$$

where

$$\begin{aligned} S_d (\underset{\sim}{d} \cdot \underset{\sim}{d}) &= \frac{1}{2}[\underset{\sim}{d}^2 + (\underset{\sim}{d}^T)^2 - \frac{2}{3} \text{tr} (\underset{\sim}{d}^2)\underset{\sim}{I}] \\ \Lambda &= \frac{(2k + 3)(19\lambda + 16)}{40(\lambda + 1)} (\frac{\eta_o a}{\sigma}) \end{aligned} \qquad \text{(II-26)}$$

It can be shown that for steady shearing flow, the viscosity of the emulsion is given by

$$\eta = \frac{\eta_o}{1 + \Lambda^2\dot{\gamma}^2} \{1 + (\frac{5\lambda + 2}{2\lambda + 2})\ \phi + \Lambda\dot{\gamma}^2\ [(1 + \frac{5\lambda + 2}{2\lambda + 2}\ \phi)\ \Lambda - \frac{\eta_o a}{80\sigma}\ (\frac{19\lambda + 16}{\lambda + 1})^2]\} \tag{II-27}$$

Choi and Schowalter (26) also developed a constitutive equation of state for slightly concentrated emulsions. For steady flow,

$$(1 + h_1 \frac{D}{Dt})\ \underset{\sim}{P} = 2\eta_a\ (1 + h_2 \frac{D}{Dt})\ \underset{\sim}{d} \tag{II-28}$$

where

$$\eta_a = \eta_o\ [1 + \frac{5\lambda + 2}{2(\lambda + 1)}\ \phi + \frac{5(5\lambda + 2)^2}{8(\lambda + 1)^2}\ \phi^2] \tag{II-29}$$

$$h_1 = \frac{(19\lambda + 16)(2\lambda + 3)}{40(\lambda + 1)}\ (\frac{\eta_o a}{\sigma})\ [1 + \frac{5(19\lambda + 16)}{4(\lambda + 1)(2\lambda + 3)}\ \phi] \tag{II-30}$$

$$h_2 = \frac{(19\lambda + 16)(2\lambda + 3)}{40(\lambda + 1)}\ (\frac{\eta o^a}{\sigma})\ [1 + \frac{3(19\lambda + 16)}{4(\lambda + 1)(2\lambda + 3)}\ \phi] \tag{II-31}$$

The equations derived above by Choi and Schowalter take into account the interactions of neighboring droplets and the deformation of droplets in flow. The viscosity of the emulsion was found to be given the following expression

$$\eta = \frac{\eta_a\ (1 + h_1 h_2 \dot{\gamma}^2)}{1 + h_1^2 \dot{\gamma}^2} \tag{II-32}$$

Copolyamide (CPA), a copolymer of 44 percent caprolactom, 37 percent hexamethylene adipate, and 19 percent hexamethylene sebacote, shows clearly that the viscosity-composition relationship is extremely sensitive to the magnitude of the shear stress. Both maxima and minima are observed.

Liang et al. (90) measured the viscosities of polypropylene-nylon 6 blends at 230°C and found that the viscosities vs. concentration curves showed minima and maxima.

F.2. Principal Normal Stress Difference in Newtonian Fluid Emulsions

Theoretical considerations of normal stress differences based on the two-phase morphology of fluids was advanced from the studies of the emulsion. In 1970, Frankel and Acrivos (42) predicted the existence of oppositive normal stress difference of dilute emulsions in steady shearing flow theoretically in hydrodynamic theories of emulsions. Choi and Schowalter (26) also developed a constitutive equation for moderately concentrated emulsions in steady shearing flow and predicted the first normal stress difference consisting of two Newtonian liquids. More recently, Han and King (56) have observed normal stress differences in Newtonian fluid and non-Newtonian fluid emulsions. They found values of N_1/σ_{12} of order one. They note that both the Frankel-Acrivos model and the Choi-Schowalter model can predict at least qualitatively the first formal difference of emulsions of Newtonian liquids, i.e., low molecular weight polyisobutylenes and glycerin.

F.3. Principal Normal Stress Difference in Polymer Melt Blends

There is a lack of studies on the principal normal stress difference in polymer melt blends because of the limited measurements. Han and his coworkers (53)(54)(55) have measured the first normal stress difference using exit pressure for PE/PS blends. Han and Kim et al. (55) had determined the normal stress for PS/PMMA blends using a cone-plate rheometer. They found a minimum in the exit pressure was observed for the PE/PS-75/25 blend, which has an interlocked morphology. It was opposite to the composition dependence of the viscosity. Starita (149) noted that the normal force difference exhibited an opposite tendency to the viscosity vs. composition curves.

Liang et al. (90) measured the normal stress differences for polypropylene-nylon 6 systems using a cone-plate rheometer. Their data for normal stress differences are higher than those of the pure polymers at the same shear stress. These data show both a minimum and a maximum.

F.4. Elongational Viscosities of Polymer Blends

Han and Kim (53) have made an experimental study of melt spinning in order to investigate the spinnability and phase morphology of PE/PS blends. They showed that the apparent elongational viscosity decreases with elongational rate and that blends of PE/PS give rise to apparent elongational viscosities even lower than those of the pure components. They concluded that the apparent elongation viscosity goes through a minimum at a blending ratio of 75 percent of PS to 25 percent of HDPE.

Tanaka (158) reported the elongational viscosity of 50/50 PS/PE system at 180°C. They demonstrated that the characteristics of the 50/50 blend resembled those of HDPE.

CHAPTER III

MATERIALS AND EXPERIMENTAL PROCEDURE

A. MATERIALS

Four different types of polymers were used in this study: high density polyethylene (PE), polycarbonate (PC), polystyrene (PS), and Nylon-6 (N6). Three different polyethylenes of varying molecular weight were included. These are designed PE-1, PE-2, and PE-3. The characteristics of these samples are summarized in Table III-1.

Various blends of these polymers have been prepared. These are PE-1/PS, PE-2/PS, PE-3/PS, PE-2/N6, and PE-2/PC. the PE-2/PS system has been investigated at two temperatures. This allowed for the study of five separate PE/PS systems using different temperatures and polymers and, thus, the study of the viscosity ratio effect independent of changes in interfacial character.

In order to stabilize the blends produced, surface active compounds have been added in the blending operation. Styrene-Ethylene-Styrene copolymer (SES) was chosen as a surface active compound and added to PE-2/PS-50/50 blends.

B. SAMPLE PREPARATION (BLENDING)

All of the systems were mixed in a 3/4-inch Brabender screw extruder with a Koch static mixer. The PE-1/PS, PE-2/PS, and PE-3/PS samples were blended at 180°C. The PE-2/PS system was also mixed at

Table III-1. Materials

Polymers	δ^*	Commercial Designation	MI	M_w ,	M_w/M_n
Polyethylene PE-1		Chemplex 6003	0.3	83,092,	4.91
PE-2	8.25	Chemplex 6109	0.9	154,170,	6.28
PE-3		Chemplex 6060	6.0	109,417,	6.66
Polystyrene (PS)	9.0	Dow 678u	12.0	240,000,	3.0
Nylon-6(N6)	9.4	American Enka	-	45,000,	2.08
Polycarbonate (PC)		General Electric Type .940	-	-	
Styrene-Ethylene-Styrene Copolymer (SES)	-	Shell Co. (Kraton G)	-	-	

*Solubility parameter by Small, P. A., J. Appl. Chem., 3, 71 (1953).

240°C. The PE-2/N6 and PE-2/PC blends were prepared at 240°C. The PE-2/PS/SES system was produced at 180°C and 240°C. The composition and temperature of the blends investigated are shown in Table III-2.

C. EXPERIMENTAL PROCEDURE

C.1. Steady Shear Flow Measurements

Steady shear flow measurements were carried out in a Rheometrics Mechanical Spectrometer (Model RMS7200) at low shear rates. An Instron Capillary Rheometer was used in the higher shear rate range. Measurements were carried out at the temperature at which the blend was prepared, 180°C or 240°C.

The cone-and-plate geometry was used to measure the shear stress, σ_{12}, the first normal stress differences, N_1, and the viscosity η. The cone has a diameter of 2.5 cm and an angle of 0.1 radian. The shear stress and the first normal stress difference were determined by measuring the torque, T, and the thrust force, F. The viscosity, the shear stress, and the first normal stress difference were determined from the following equations (184)(189)

$$\dot{\gamma} = \frac{\Omega}{\alpha} \qquad \text{(III-1)}$$

$$\eta = \frac{\sigma_{12}}{\dot{\gamma}} = \frac{3T}{2\pi R^3 \dot{\gamma}} \qquad \text{(III-2)}$$

$$N_1 = \sigma_{11} - \sigma_{22} = \frac{2F}{\pi R^2} \qquad \text{(III-3)}$$

Table III-2. Composition and temperature of blends investigated

Systems	Temperature Studied	Compositions
PE-1/PS	180°C	90/10, 70/30, 50/50, 30/70, 10/90
PE-2/PS	180°C, 240°C	
PE-3/PS	180°C	
PE-2/N6	240°C	90/10, 70/30, 50/50, 30/70, 10/90
PE-2/PC	240°C	90/10, 70/30, 50/50, 30/70
PE-2/PS/SES	180°C, 240°C	50/50/5, 50/50/50

where Ω is the angular velocity of the cone, α is the cone angle, T is the torque, F is the thrust force, and R is the radius of the cone.

An Instron Capillary Rheometer was used to measure the shear viscosity at high shear rates. A close-fitting plunger was driven through the barrel at a constant speed extruding the melt through a capillary die fixed to the bottom of the barrel. By recording the plunger force from the load cell and the plunger speed, a total pressure drop and volumetric flow rate are obtained. The shear stress was measured through the pressure loss through a series of four capillary dies of diameter D, 1.47 mm and (length/diameter) (L/D) 10, 20, 30, and 40.

The pressure, P_{total}, was plotted as a function of die L/D and the die wall shear stress $(\sigma_{12})_w$ was determined from (184)(189)

$$P_{total} = P_{ends} + 4(\sigma_{12})_w \, L/D \qquad \text{(III-4)}$$

where P_{ends} is the sum of die entrance and exit pressure losses. The die wall shear rate was determined from Weissenberg's relationship (184)(189)

$$\dot{\gamma}_w = \frac{3n' + 1}{4n'} \quad \frac{32Q}{\pi D^3} \qquad \text{(III-5)}$$

where

$$n' = \frac{d \log (\sigma_{12})_w}{d \log 32Q/\pi D^3} \qquad \text{(III-6)}$$

where Q is the flow rate.

C.2. Elongational Flow Measurement

Elongational viscosity measurements were carried out at 180°C in the elongational viscometer shown in Figure III-1. The rheometer developed by Ide (71)(72) in our laboratory was modified by W. Minoshima, Y. Suetsugu, and H. Yamane. The changes are summarized in papers by Suetsugu and White (153) and Yamane and White (200).

The sample which lies in a silicone oil bath is clamped at one end and stretched with a double-gear shaped pair of vertical rollers. The force detecting system was an AC-operated, 50g force transducer. A tube block heater was set at the bottom of the silicone oil bath. The temperature was controlled by a proportional temperature controller. The temperature was measured with an iron-constantan thermocouple at a distance of 1 cm horizontally away from the sample. The temperature fluctuation was within $\pm$0.5°C at the maximum.

As noted above, the force was determined by an AC-operated force transducer (Schaevitz FtA-G-50). The maximum linear operation region of the force transducer is $\pm$50g. The displacement of the core due to the stretching force of 50g is very small in comparison with the 22-cm length of the sample. The force transducer was connected to a digital transducer readout (Schaevitz Model DTR-450) and to a recorder.

The gear-shaped rollers were designed to press the sample in between them. The radius of the rollers was 1.75 cm. The rollers were rotated by two 1/15-HP B and B motors (1.6 r.p.m. and 12 r.p.m.) controlled by a B and B controller. The elongational rates achieved were in the range 4.46×10^{-3} sec^{-1} to 7.50×10^{-1} sec^{-1}.

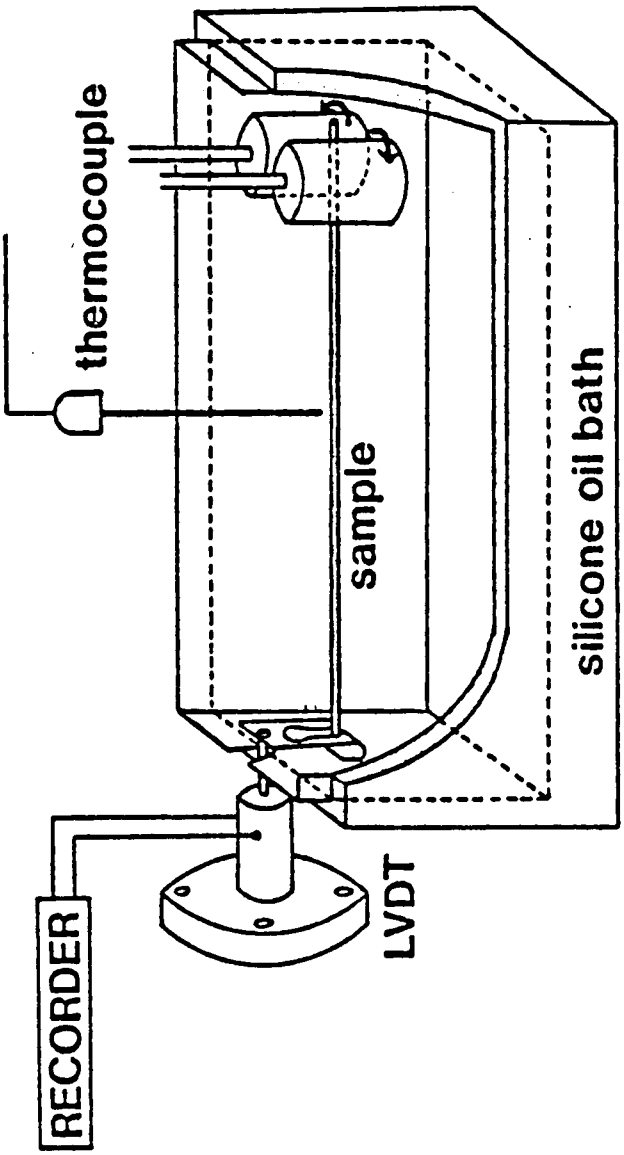


Figure III-1. Schematic diagram of elongational rheometer.

Rod-shaped samples were prepared by extrusion with a Brabender single screw extruder (C. W. Brabender Co., 3/4-inch diameter, and L/D = 10). Dies with a diameter of 1 mm were used for PE and PE/PS blends and 3 mm for PS. The screw speed was usually 8 r.p.m. One end of a rod-shaped sample was annealed and glued with a nut or a ring by quick-set epoxy. This side was inserted into the sample holder jointed to the force transducer through a narrow gap of cover glass. The other end of the sample was held between rollers.

The silicone oil used as the oil bath medium was Dow Corning, Fluid 200® (kinetic viscosity: 100 centistrokes at 25°C, density: 0.968 g/cm^3 at 25°C).

The samples were first annealed for 20 minutes at 180°C in the silicone oil bath to eliminate residual stress and orientation. The blends show especially large shrinkage. It was about 80 percent, and, therefore, the initial lengths of samples were prepared about 115 cm. The shrinkage cross-section at 180°C, A, was calculated from

$$A = \frac{L_o}{L}\frac{\rho_o}{\rho}A_o = \frac{1}{1+\int_{Tg}^{180}\alpha\,dT}\ \frac{1}{\rho}\ \frac{W}{L_o} \qquad \text{(III-7)}$$

where L is the length of a sample, ρ is the density, α is the linear thermal expansion coefficient of the filament. The symbols with and without subscript o are the values at room temperature, 25°C, and at 180°C, respectively. An average value of A was calculated from measurements of the samples. It was assumed in the calculation that the densities of filaments are constant during deformation, and that

the thermal expansions of filaments are due to both the matrix and the dispersed phase; that is,

$$\alpha = \phi\alpha_{PE} + (1 - \phi)\alpha_{PS} \qquad \text{(III-8)}$$

where ϕ is the volume fraction of high density polyethylene and α_{PS} is the thermal expansion coefficient of PS, equal to 5.55×10^{-4}/°C above Tg and 1.85×10^{-4}/°C below Tg. α_{PE} is the thermal expansion coefficient of PE, equal to 2.5×10^{-4}/°C over 115°C.

The filament was connected between the sample holder and the take-up rollers. After 20 minutes, the filament was stretched at a constant elongational rate. The elongational rate E is defined by

$$E = \frac{\partial V_1}{\partial \chi_1} = \frac{1}{L}\frac{dL}{dt} = \frac{V_L}{V} = \frac{R\Omega}{L} \qquad \text{(III-9)}$$

where, in this experiment, R - 1.75 cm, L = 22 cm, and Ω is the angular velocity of rollers. Under an assumption of uniform deformation, the tensile stress $\sigma_{11}(t)$ is

$$\sigma_{11} = \frac{F(t)}{A(t)} = \frac{F(t)}{A(0)} e^{Et} \qquad \text{(III-10)}$$

where F(t) is the total tensile force at t = t, and A(t) and A(0) are the cross-sectional area given by equation (III-7) at t = t and t = 0, respectively. The elongational viscosity $\chi(t)$ is defined by

$$\chi(t) = \frac{\sigma_{11}(t)}{E} \qquad \text{(III-11)}$$

The elongation to break was calculated from the time to failure. Since a cylinder deforms with time according to

$$L(t) = L(0)\, e^{Et} \qquad \text{(III-12)}$$

The elongation to break is

$$\ln \frac{L_B}{L_0} = Et_B \qquad \text{(III-13)}$$

where L_B and L_0 denote sample lengths at the time of failure and in the initial state, respectively.

C.3. Extrudate Swell Measurement

Extrudate swell measurements were carried out using an Instron Capillary Rheometer at 180°C. A die with L/D = 40.0 and diameter of 1.47 mm was used to obtain extrudate swell d/D or B. Extrudate emerging from dies were cut at distance 5 cm below the die exit. Extrudates directly cooled in the air were measured with a micrometer to determine the diameter. The room temperature data were normalized by 180°C by using a density factor $[\rho(20°C)/\rho(180°C)]^{1/3}$. The normal-normalized densities of blends were calculated using additivity of volume fractions

$$\left(\frac{1}{\rho}\right) = \phi_{PE}\left(\frac{1}{\rho_{PE}}\right) + \phi_{PS}\left(\frac{1}{\rho_{PS}}\right) \qquad \text{(III-14)}$$

C.4. Melt Spinning Under Non-Isothermal Conditions

Non-isothermal melt spinning experiments were carried out. The apparatus is shown in Figure III-2. The samples were extruded

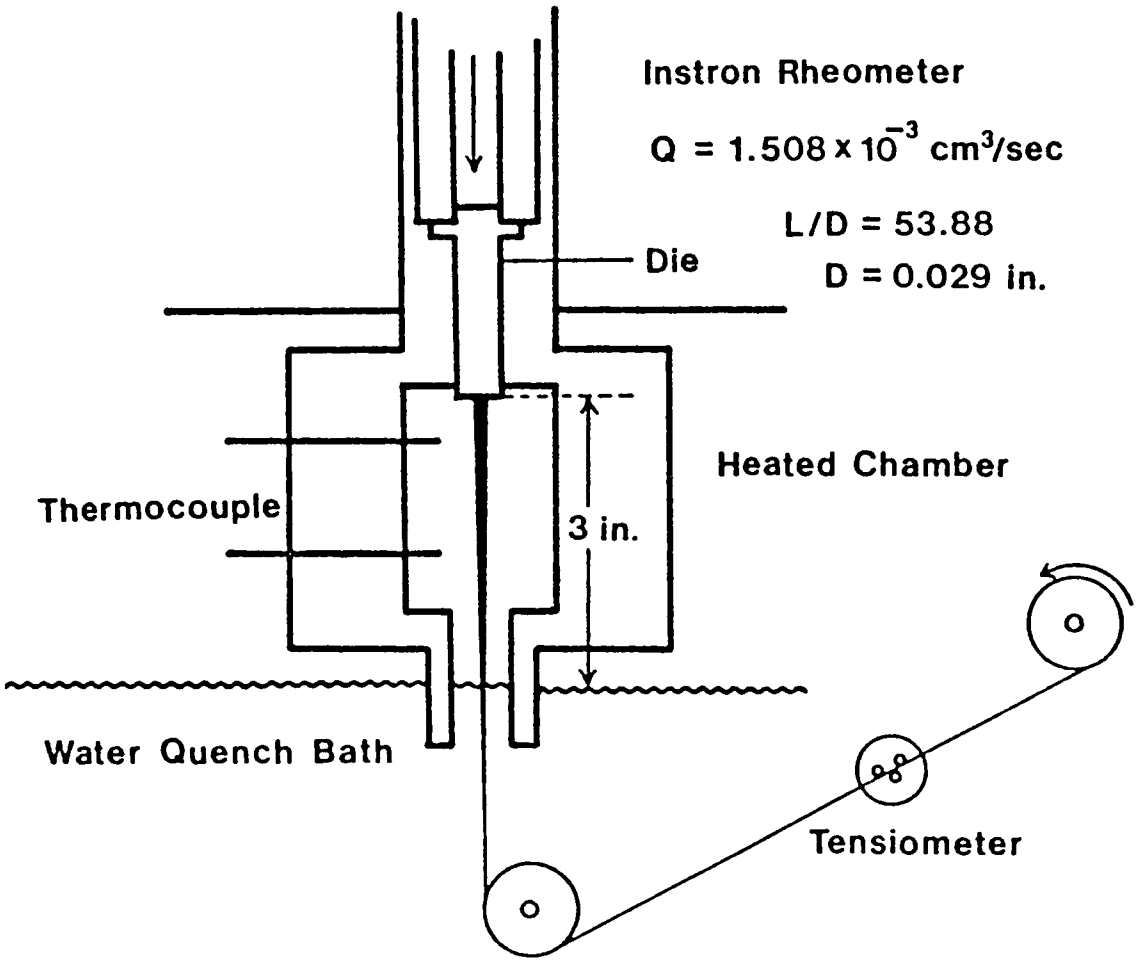


Figure III-2. Schematic diagram of the isothermal melt spinning.

through a die at 180°C into room air and then into an iced-water quench bath. The die used had a 0.058-inch diameter and a 40.0 L/D ratio. The flow rate was constant throughout the experiment at 1.508×10^{-3} cm^3/sec. The filament descended from the die into a water quench bath, passed around a roller and onto a take-up device with a take up speed 1-16 m/min. depending on drawdown ratio. The diameter of the take-up roll was 8.8 cm. The roll was driven by two types of 1/15-HP B and B motors having maximum speeds of 12 r.p.m. and 86 r.p.m. The spin path from the die exit to the water surface was always kept constant at 19.5 cm. The take-up speed was from 1 to 16 m/min. depending on drawdown ratio. Spinline tension was measured with a Rothschild tensionmeter and calibrated due to the presence of the teflon® rods and brittleness of these samples.

The diameter of the fiber taken up was measured using a thickness gauge.

C.5. Melt Spinning Instability Under Isothermal Conditions

Isothermal melt spinning experiments were carried out using the Instron Capillary Rheometer in order to measure the onset of draw resonance. The apparatus used is shown in Figure III-3. The polymer melt was extruded through a die of diameter of 0.058 inches and L/D ratio 27.6. The extrudate passed into a 1.0-inch inside diameter by 3-inch long heated chamber and then into a water quench bottle. Two sets of heaters were used to heat the chamber. Two thermocouples were located at 0.25 and 1.5 inches from the die exit, respectively, and were connected to temperature controllers. A

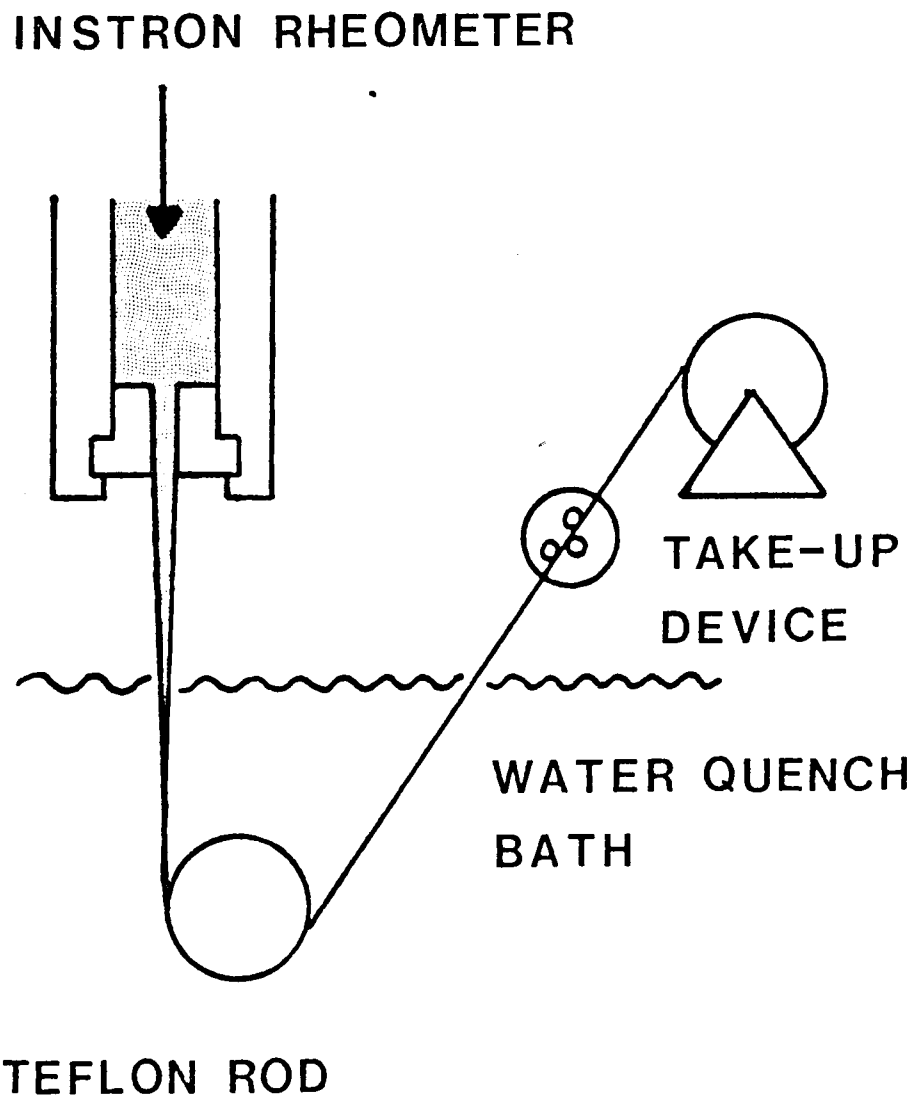


Figure III-3. Schematic diagram of the non-isothermal melt spinning.

take-up roll of diameter 8.8 cm was driven by a 1/15-HP B and B motor (12 r.p.m., maximum speed). A Rothschild tensionmeter (40g and 4 g full scale) was connected to a strip chart recorder (Model EV-205-11, Heath Co., Benton Harbor, Michigan) and a potentiometric amplifier (Model EV-200-01, Heath Co.). The flow rate was maintained at 1.508×10^{-3} cm^3/sec.

The fiber diameter was measured using a thickness gauge.

C.6. Formation of Oriented Films

The PE-2/PS blend samples were molded into sheets of dimension (8 x 8 x 0.152 inch) in a compression molding press at a temperature of 180°C. The sheets were placed in a T. M. Long Biaxial Tester (T. M. Long Co., Inc., Somerville, New Jersey) and equally biaxially stretched at rates of 600 percent of initial length per minute. After stretching the samples were quenched.

C.7. Wide-Angle X-Ray Diffraction

The orientation of crystalline regions of high density polyethylene were measured by wide-angle x-ray diffraction. Nickel-filtered CuKα radiation was used. The flat film technique was applied to the melt spun blend fibers (Figure III-4).

HDPE crystallizes to form an orthorhombic unit cell as first shown by Bunn (17). The uniaxial orientation of HDPE may be expressed in terms of the Hermans-Stein orientation factors for the three crystallographic axes (9) (Figure III-5). These are defined as follows:

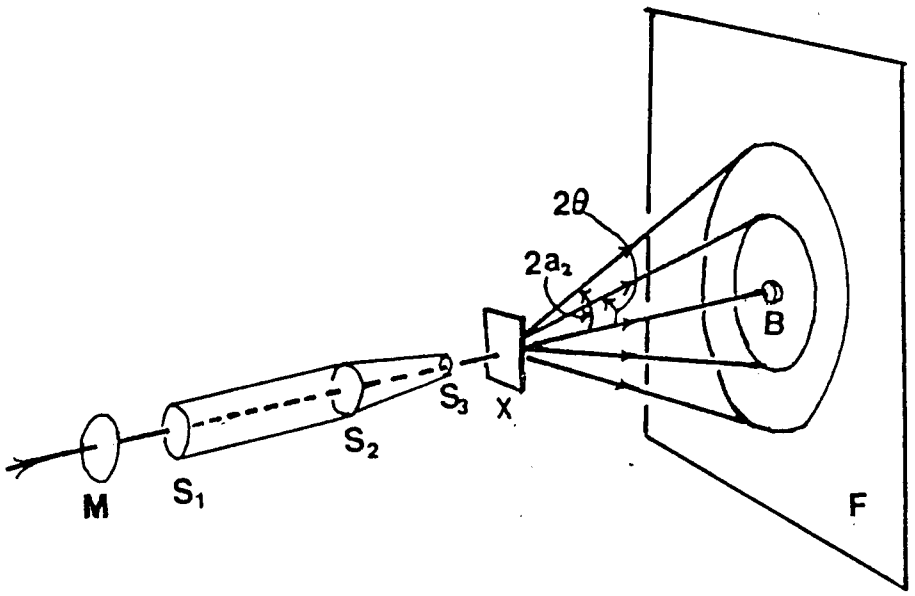


Figure III-4. Flat-film technique arrangement. M: filter; S_1, S_2, S_3: collimeter apertures; X: samples; B: beam stop; F: film.

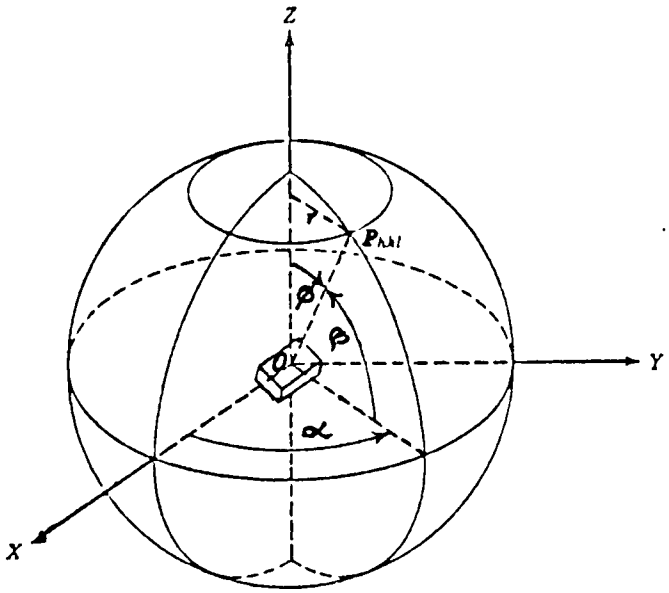


Figure III-5. Angular coordinates of a pole on a spherical projection.

$$f_j = \frac{\overline{3\cos^2\phi_j - 1}}{2} \qquad \text{(III-14)}$$

where ϕ_j is the angle between the fiber axis and j-crystallographic axis. For an orthorhombic unit cell, f_a, f_b, and f_c are interrelated by

$$f_a + f_b + f_c = 0. \qquad \text{(III-15)}$$

The strongest WAXS reflections for polyethylene are the 110, 200, and 020 reflections. The 020 reflection is weak in comparison to the others. Therefore, the 200 was used to obtain f_a directly and the f_b by Stein's expression (151)

$$\overline{\cos^2\phi_b} = \frac{\overline{\cos^2\phi_{110,1}} - 0.308\ \overline{\cos^2\phi_{200}}}{0.692} \qquad \text{(III-16)}$$

Finally, to obtain f_c, equation (III-15) was used.

The orientation factors were computed from intensity scans. The corrections applied to the intensity diffracted by each sample and recorded in the teletype include all the following: a) cosmic x-ray background, b) x-ray energy fluctuations, c) air scattering, d) sample absorption, and e) Lorentz-Polarization effects. The final expression for the corrected intensities after applying all of the above corrections to the recorded intensity is given by

$$I_C = (I_R - I_{CB})K - I_{air}\ \left(\frac{I_0^o}{I_{2\theta}}\right)\left(\frac{1}{L - P}\right) \qquad \text{(III-17)}$$

where I_R = recorded intensity, I_{CB} = average cosmic background intensity, I_{air} = intensity of air scattering. The absorption correction is negligible because the sample thickness is very small.

The amorphous background of PS overlapped on the amorphous peak of PE. The contribution of PS to the scattering will be dependent on the volume fraction of each specimen and on the intensities per unit volume diffracted by each of them. It is reasonable to assume $I_{total\theta}$ as given by

$$\begin{aligned} I_{total\theta} &= \phi I_{total\theta} + (1 - \phi) I_{total\theta} \\ &= I_{PEtotal} + I_{PStotal} \end{aligned} \qquad \text{(III-18)}$$

where ϕ is the volume fraction of PE

$$I_{total\theta} = I_{PE-c} + I_{PE-a} + I_{PStotal}$$

$$I_{PE-c} = I_{total\theta} - I_{PE-a} - I_{PStotal} \qquad \text{(III-19)}$$

$$I_{PE-c} = I_{total\theta} - I_{PE-a} - (1 - \phi) I_{PS}$$

where: I_{PE-c} is the intensity of crystalline region;

I_{PC-a} is the intensity of amorphous region;

I_{PS} is the intensity of pure polystyrene.

$I_{total\theta}$ and I_{PS} are known. I_{PE-a} may be estimated using the Gaussian distribution of the amorphous peak at 19.6° of polyethylene.

C.8. Scanning Electron Microscopy (SEM)

The SEM studies were carried out using an AMR model 900 high resolution scanning electron microscope (Advanced Metal Research Corporation, Burlington, Massachusetts). Fracture surfaces of extrudates from a screw extruder with a static mixer, as well as extrudates from capillary die and samples from the cone-plate rheometer, were prepared in liquid nitrogen (-160°C). A gold palladium alloy was applied to the surfaces of the sections. Some of the spun fibers were trimmed by a Microtone (A0820 American Optical) and PS extracted with toluene (80°C). The mini-fibers were observed after a gold palladium coating was placed on their surface.

CHAPTER IV

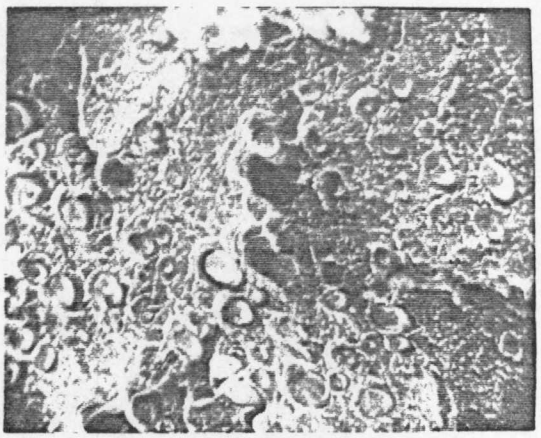
BLEND PHASE MORPHOLOGY AND ITS VARIATION IN RHEOMETERS

Experimental studies of the variation of phase morphology with melt processing conditions will be discussed here. We observed the phase morphology in: a) screw extruder with a static mixer, b) a cone-plate rheometer, and c) a ram extruder with a capillary die. The experiments were carried out at 180°C for the polyethylene-polystyrene system, at 240°C for the polyethylene-polycarbonate and polyethylene-nylon 6 systems. The characteristics of these materials are listed in Table III-1, page 42, Chapter III.

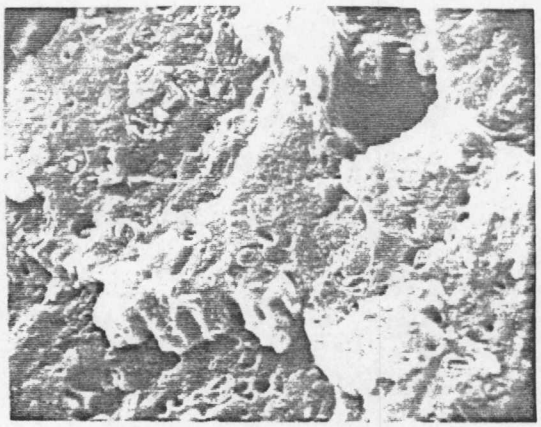
A. EXTRUDATES FROM SCREW EXTRUDER/STATIC MIXER SYSTEM

A.1. Results

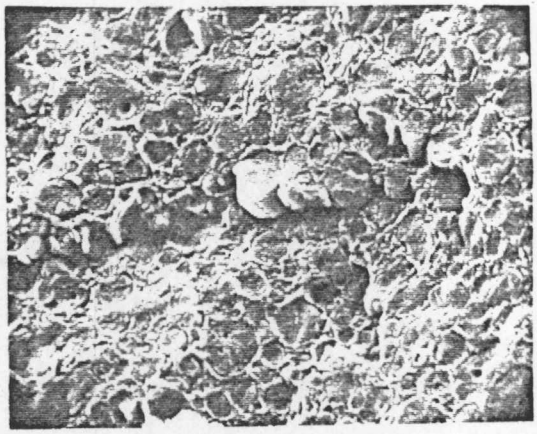
Extrudates from the static mixer were fractured in the liquid nitrogen (-160°C). SEM microphotographs of fracture surface of polyethylene-polystyrene blends are shown in Figures IV-1 through IV-4. Figure IV-5(A) and (B) show SEM microphotographs of extracted cross-sections of PE-1/PS and PE-2/PS blends. In the polyethylene (PE-2)-polystyrene systems processed at 180°C and 240°C, the PE/PS-90/10, 70/30, and 50/50 blends show polystyrene islands in a polyethylene sea. The PE/PS-30/70 and the PE/PS-10/90 show polyethylene islands in a polystyrene sea. The cross-sections of the discrete islands have dimensions of 1-5 microns depending on composition. The total phase



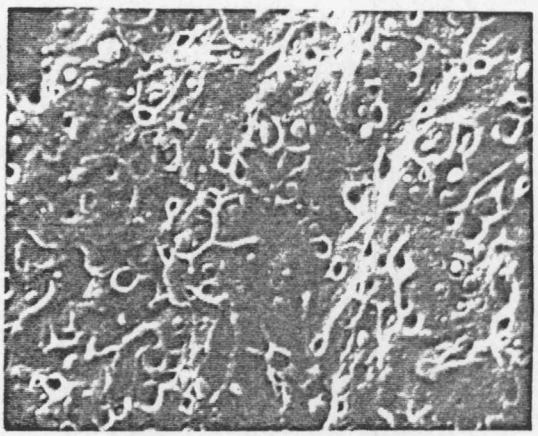
(a) PE90/PS10



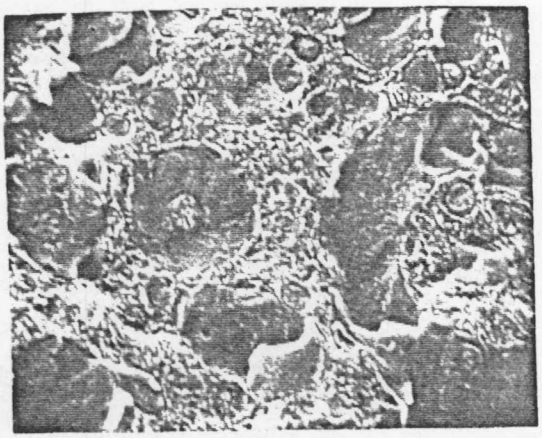
(d) PE30/PS70



(b) PE70/PS30



(e) PE10/PS90



(c) PE50/PS50

—20μ—

Temp. 180°C

Figure IV-1. SEM microphotographs of fracture surfaces of PE-2/PS blends prepared in screw extruder and Koch static mixer: (a) 90/10; (b) 70/30; (c) 50/50; (d) 30/70; (e) 10/90.

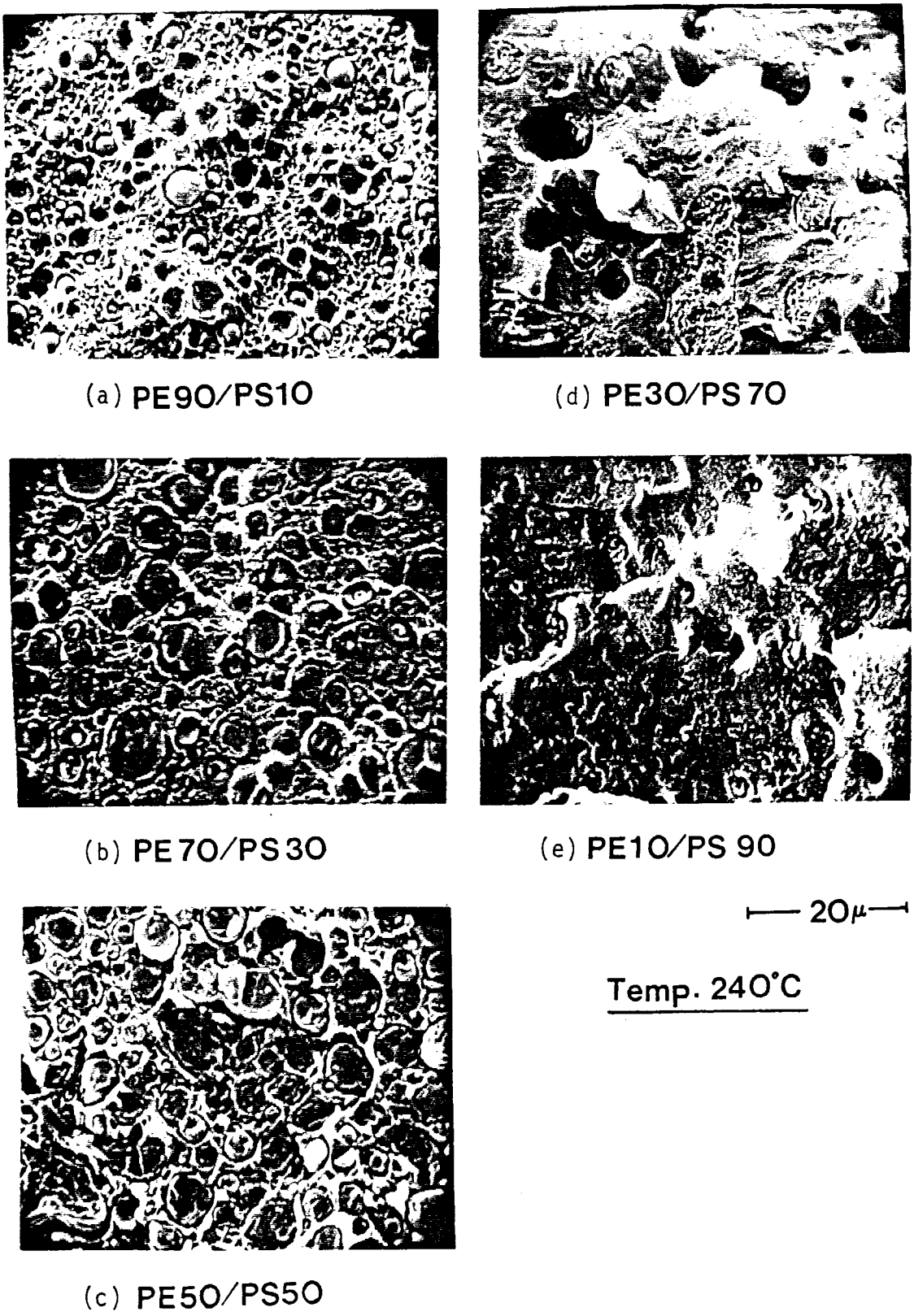
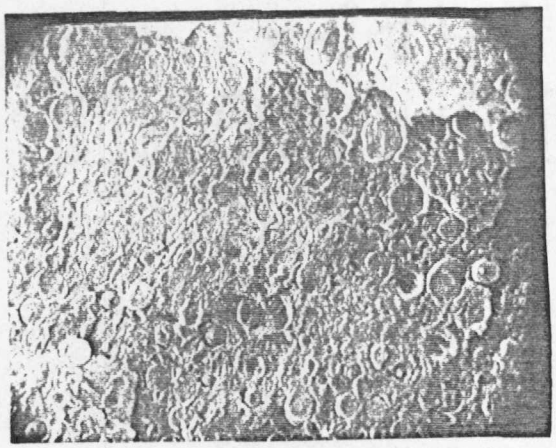
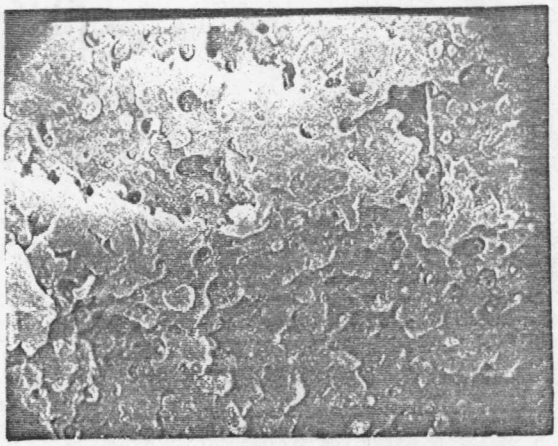


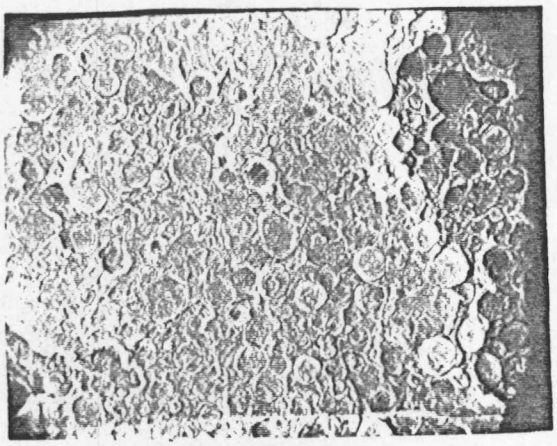
Figure IV-2. SEM microphotographs of fracture surfaces of PE-2/PS blends prepared in a screw extruder and Koch static mixer: (a) 90/10; (b) 70/30; (c) 50/50; (d) 30/70; (e) 10/90.



(a) PE 90/ PS10 —4μ—



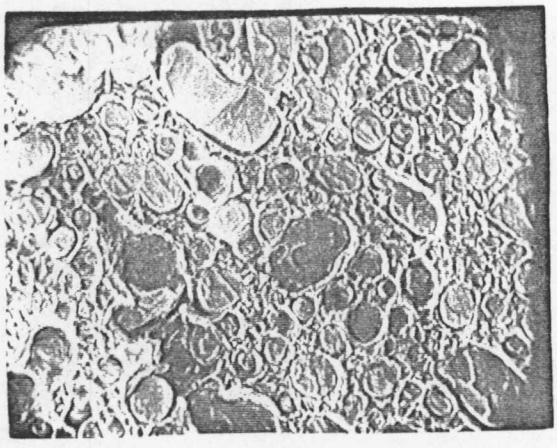
(d) PE30/ PS70 —10μ—



(b) PE 70/ PS30 —4μ—



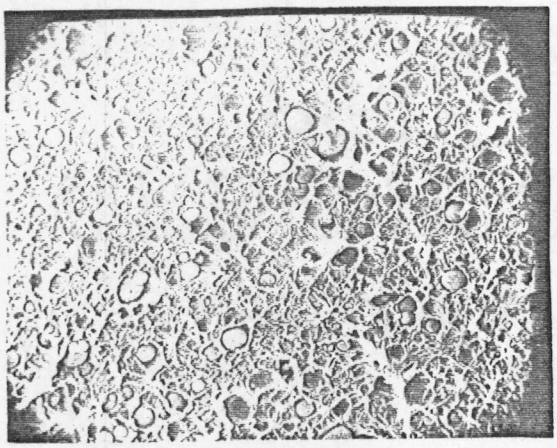
(e) PE10/ PS90 —4μ—



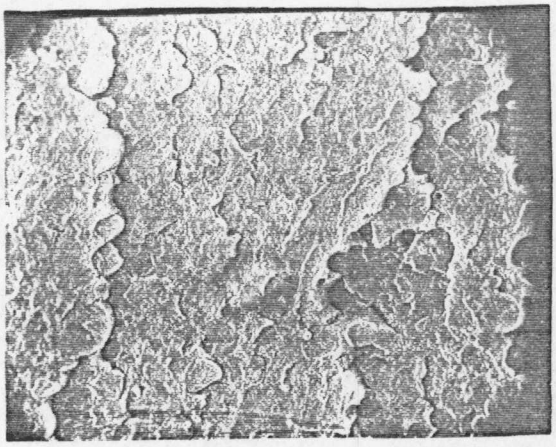
(c) PE50/ PS 50 —4μ—

* MIXER at 180°C

Figure IV-3. SEM microphotographs of fracture surfaces of PE-1/PS blends prepared in a screw extruder and Koch static mixer: (a) 90/10; (b) 70/30; (c) 50/50; (d) 30/70; (e) 10/90.



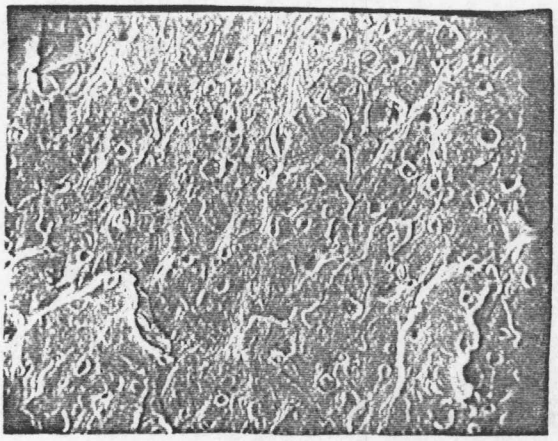
(a) PE 90/ PS10 ⊢20μ⊣



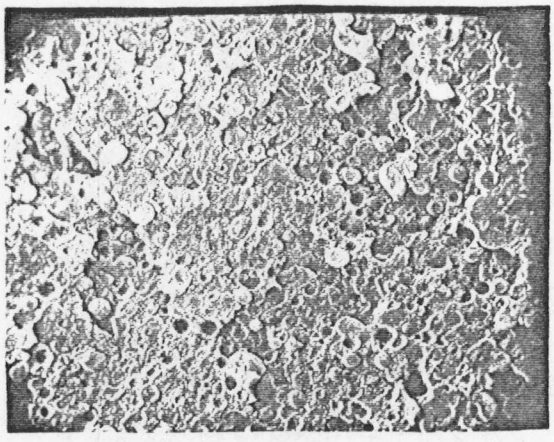
(d) PE 30/ PS 70 ⊢20μ⊣



(b) PE 70/ PS30 ⊢20μ⊣



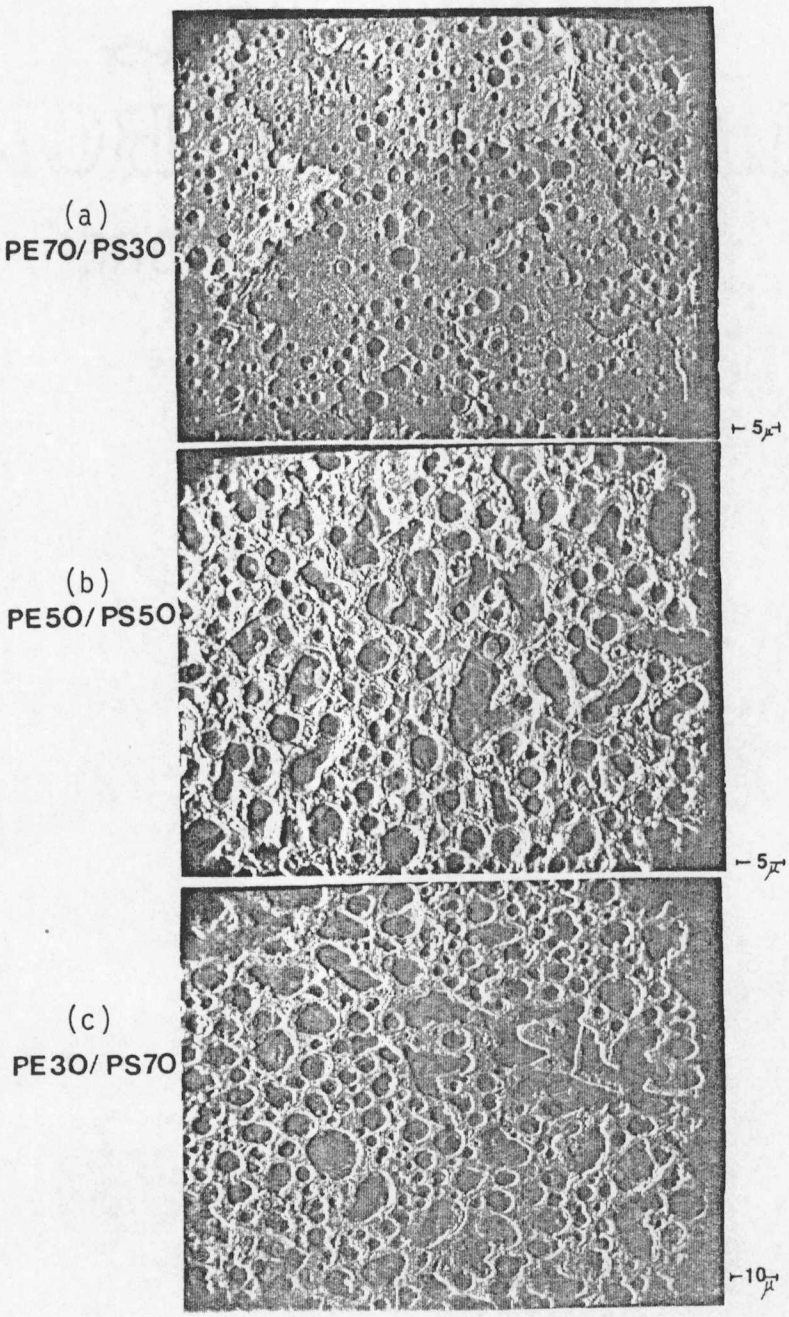
(e) PE 10/ PS90 ⊢4μ⊣



(c) PE50/ PS50 ⊢20μ⊣

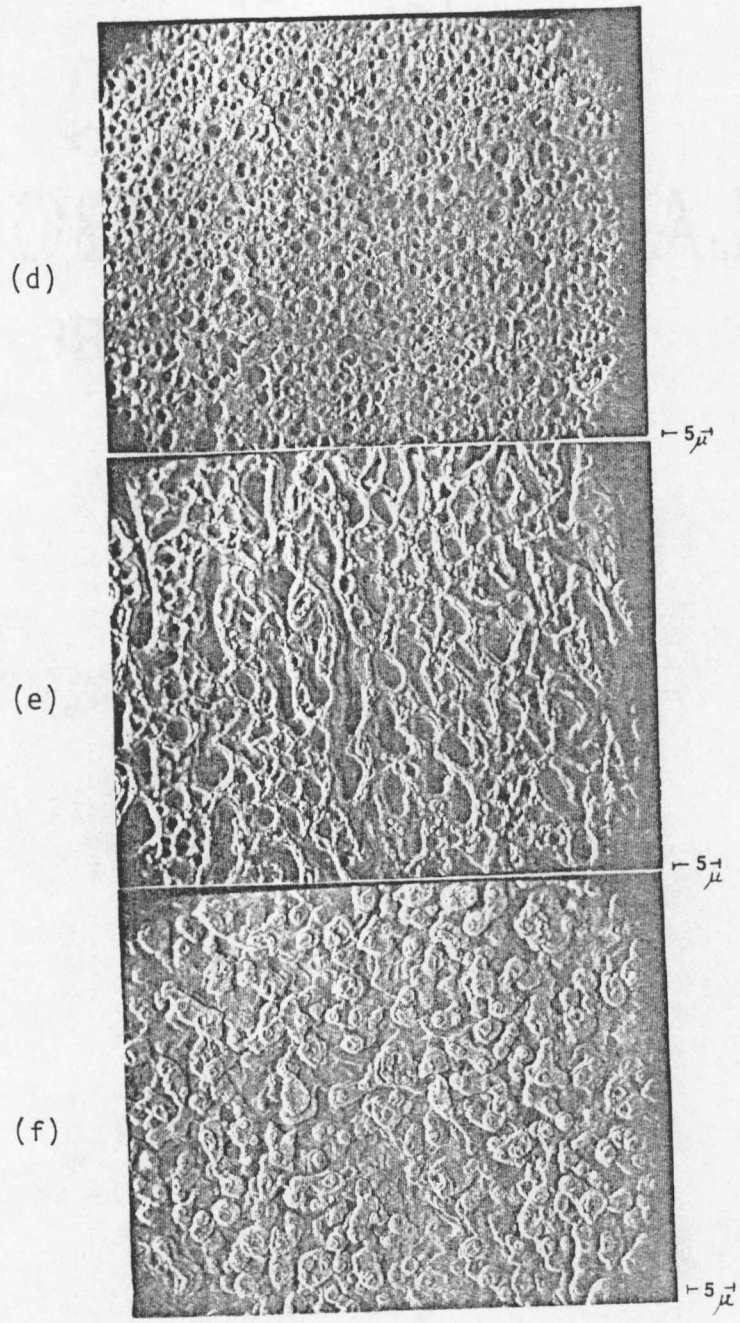
* MIXER at 180 °C

Figure IV-4. SEM microphotographs of fracture surfaces of PE-3/PS blends prepared in a screw extruder and Koch static mixer: (a) 90/10; (b) 70/30; (c) 50/50; (d) 30/70; (e) 10/90.



(A)

Figure IV-5. SEM microphotographs of extracted cross-sections of PE-3/PS (A) and PE-1/PS (B) blends: (a) 70/30; (b) 50/50; (c) 30/70; (d) 70/30; (e) 50/50; (f) 30/70.



(B)

Figure IV-5 (continued)

morphology is independent upon the temperature. Comparing the phase morphology at 180°C shown in Figure IV-1 to those at 240°C shown in Figure IV-2. The size of discrete phases at 180°C and 240°C is listed in Table IV-1. Extrusion at 240°C yielded finer droplets than extrusion at 180°C. The effect of temperature was explored to change composition of the phase inversion from 50/50 to 30/70.

The effect of viscosity and molecular weight on the mode of dispersion was explored by preparing equivalent blends with PE of varying molecular weight or melt index. The SEM microphotographs of fracture surfaces of PE-1/PS and PE-3/PS systems are shown in Figures IV-3 and IV-4. For both the higher viscosity polyethylene (PE-1)-polystyrene blends and lower viscosity polyethylene (PE-3)-polystyrene blends, the PE/PS-90/10, 70/30, and 50/50, show polystyrene islands in a polyethylene sea. SEM microphotographs of toluene extracted phase morphology of PE-1/PS and PE-3/PS blends shown in Figure IV-5 (A) and (B) indicate that PE/PS-30/70 shows the inverse morphology. The morphology does not change significantly even if the polyethylenes used have different viscosity, molecular weight, or molecular weight distribution are used. The dimension of the discrete islands is 0.5-10 microns. The dimensions and the weight average size of the discrete phase vs. composition of polyethylene are shown in Table IV-2. This is plotted in Figure IV-6.

The effect of introducing additives to the polyethylene-polystyrene system on the mode of dispersion was examined by adding styrene/ethylene-butene/styrene block copolymer (SES) (PS 25 percent, ethylene-butene 75 percent, Kraton G. Shell Chemical Co.).

Table IV-1. The dimensions of discrete phase of PE-2/PS blends prepared in a screw extruder and Koch static mixer

Composition PE-2/PS	Domain Size (μ)			
	dn (No. Average)		dw (Weight Average)	
	180°C	240°C	180°C	240°C
90/10	2.5	2.2	2.9	3.0
70/30	3.4	3.2	3.9	3.6
50/50	5.8	3.7	9.2	4.4
30/70	2.0	3.4	2.6	5.4
10/90	1.3	1.8	1.4	2.6

Table IV-2. The dimensions of the discrete phase of PE/PS blends prepared in a screw extruder and Koch static mixer

η_{OE}/η_{OS} PE/PS Composition	dn (μ) PE-1 3.8	dn (μ) PE-2 2.0	dn (μ) PE-3 0.2	dw (μ) PE-1 3.8	dw (μ) PE-2 2.0	dw (μ) PE-3 0.2
90/10	0.97	2.88	1.15	1.11	2.45	1.55
70/30	1.06	3.38	2.01	1.25	3.89	2.02
50/50	1.75	5.80	2.70	2.25	9.15	3.26
30/70	1.52	1.95	4.70	1.82	2.59	6.89
10/90	0.51	1.25	0.41	0.81	1.44	0.47

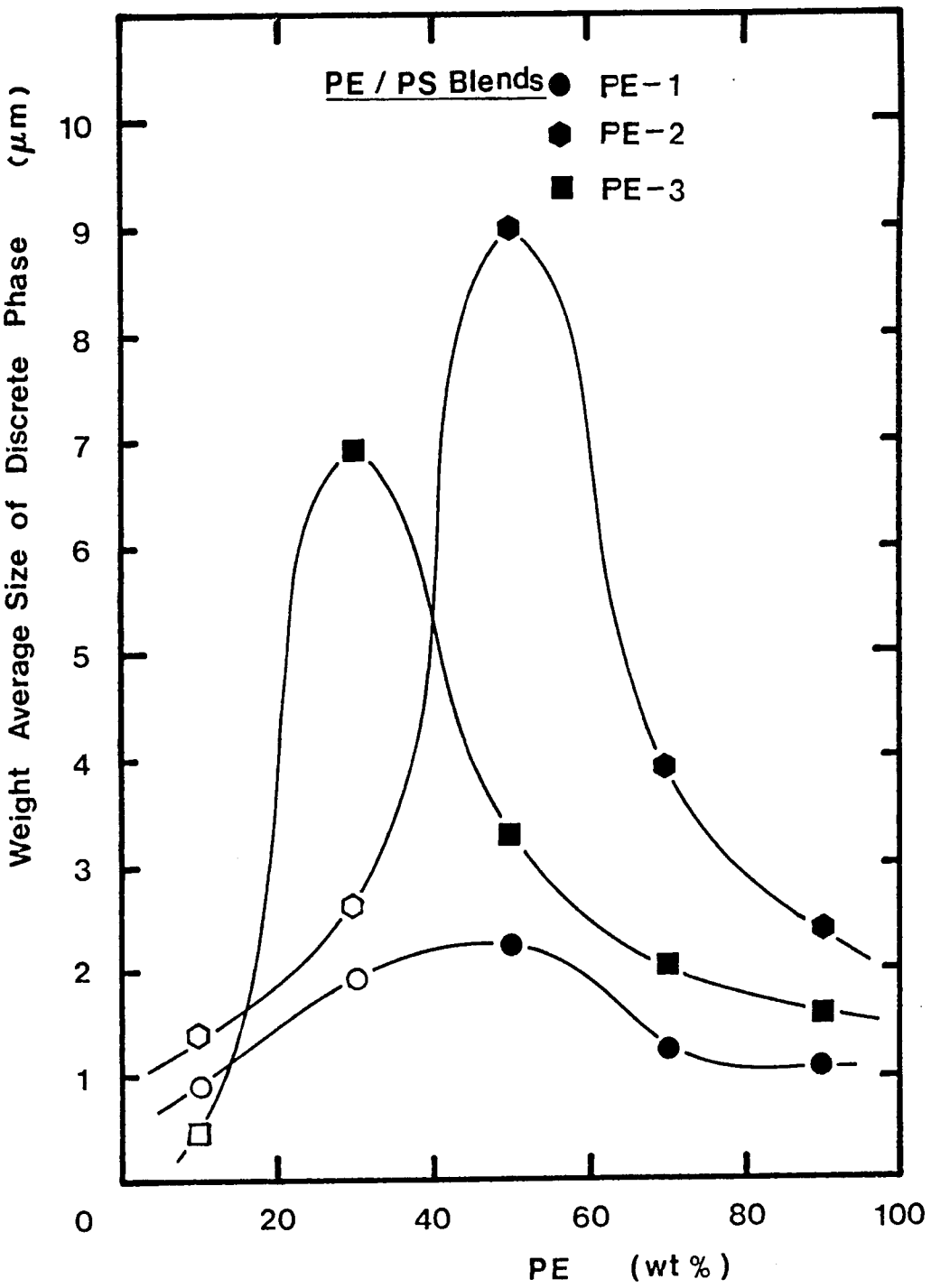


Figure IV-6. The comparison of discrete phases of different polyethylenes.

Figure IV-7 shows the SEM microphotographs of the SES block copolymer/PE/PS blends extrudated at 180°C and 240°C. A small amount addition of block copolymer to HDPE-2/PS-50/50 blend at 180°C produces no change in the size of islands of polystyrene and the type of morphology. The distribution of dispersed phase size becomes more uniform than that of PE/PS-50/50 systems. A large amount addition of block copolymer produces a three-phase structure (PS, crystalline PE, amorphous EB) shown in Figure IV-7(c). With increase in temperature from 180°C to 240°C, the phase morphology of SBS/PE/PS-5/50/50 blend became much finer.

By varying the second component of the mixture polyethylene (PE-2), the effect of interfacial tension difference was explored. Nylon-6 and polycarbonate were chosen to blend with PE-2. SEM microphotographs of fracture surface of PE-2/nylon-6 blends at 240°C and PE-2/polycarbonate blends at 240°C are shown in Figures IV-8 and IV-9.

The PE-2/N6, 90/10, and 70/30 blends show nylon 6 islands in a polyethylene sea. The PE-2/N6, 50/50, 30/70, and 10/90 show polyethylene islands in a nylon-6 sea. Coarser morphologies with larger discrete phase are found in PE-2/N6-50/50, 30/70, 10/90 and much a finer morphology in the PE-2/N6-90/10 and 70/30. This is summarized in Figure IV-10.

In the polyethylene-polycarbonate (PC) blends, the finely dispersed PC discrete phases are found in the PE-2/PC-90/10 and 70/30. The larger dimension of polyethylene islands in a PC sea is observed in the PE-2/PC-30/70. The PE-2/PC-50/50 blend has an intermixed

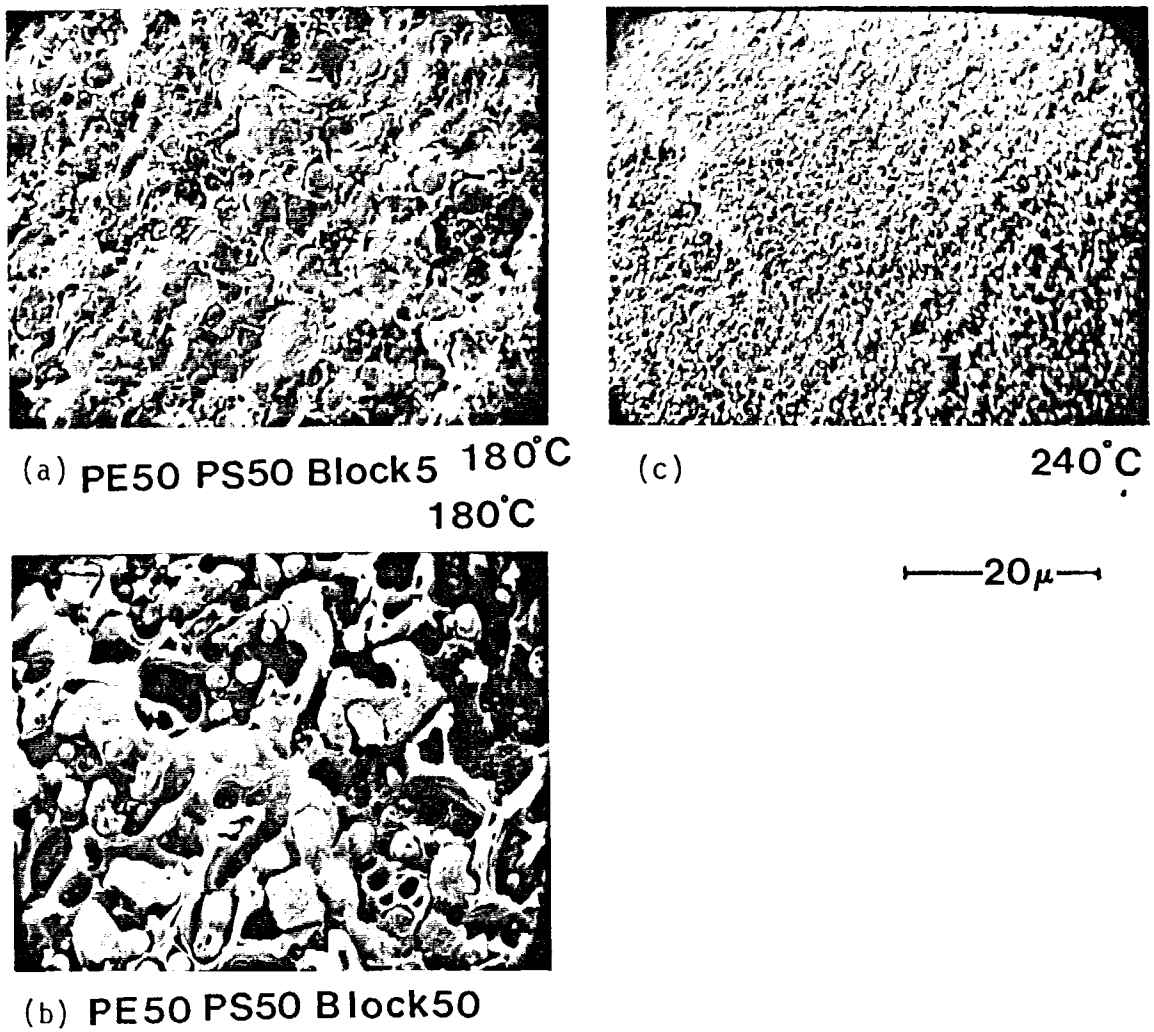
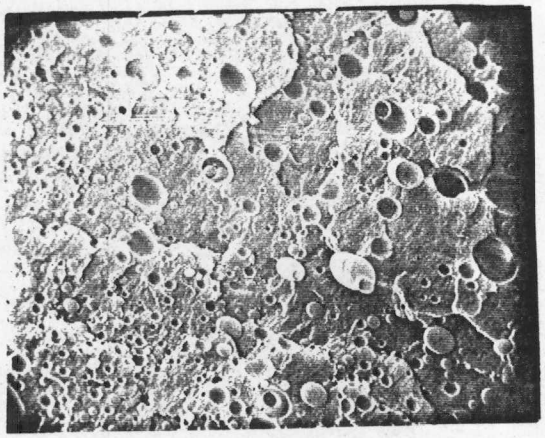
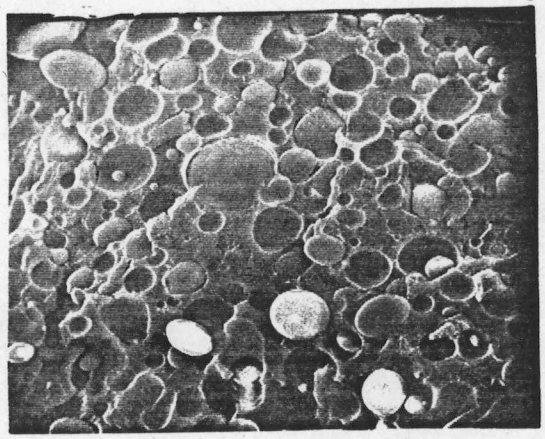


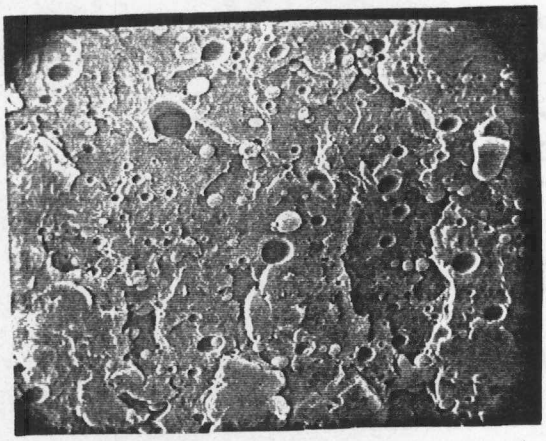
Figure IV-7. SEM microphotographs of PE-2/PS/SES blends prepared in screw extruder and Koch static mixer: (a) 50/50/5 at 180°C; (b) 50/50/5 at 240°C; (c) 50/50/50 at 180°C.



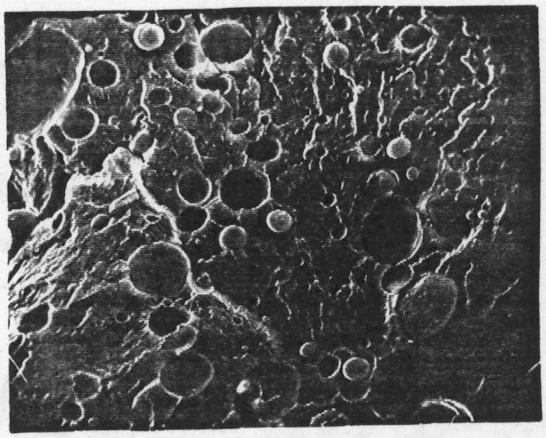
(a) PE90/ N610 ⊢ 20μ⊣



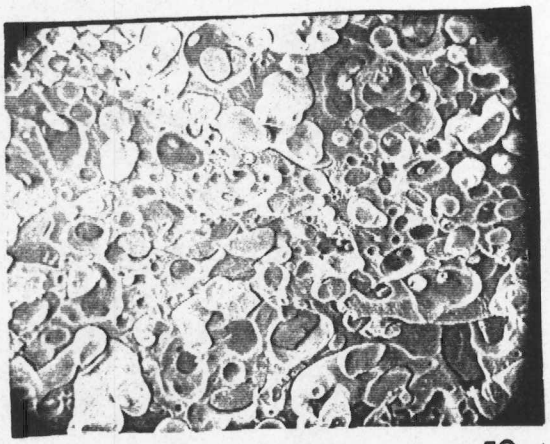
(d) PE30/ N670 ⊢ 20μ⊣



(b) PE70/ N630 ⊢ 20μ⊣



(e) PE10/ N690 ⊢ 20μ⊣



(c) PE50/ N650 ⊢ 50μ⊣

*MIXER at 240°C

Figure IV-8. SEM microphotographs of PE-2/N6 blends prepared in a screw extruder and Koch static mixer: (a) 90/10; (b) 70/30; (c) 50/50; (d) 30/70; (e) 10/90.

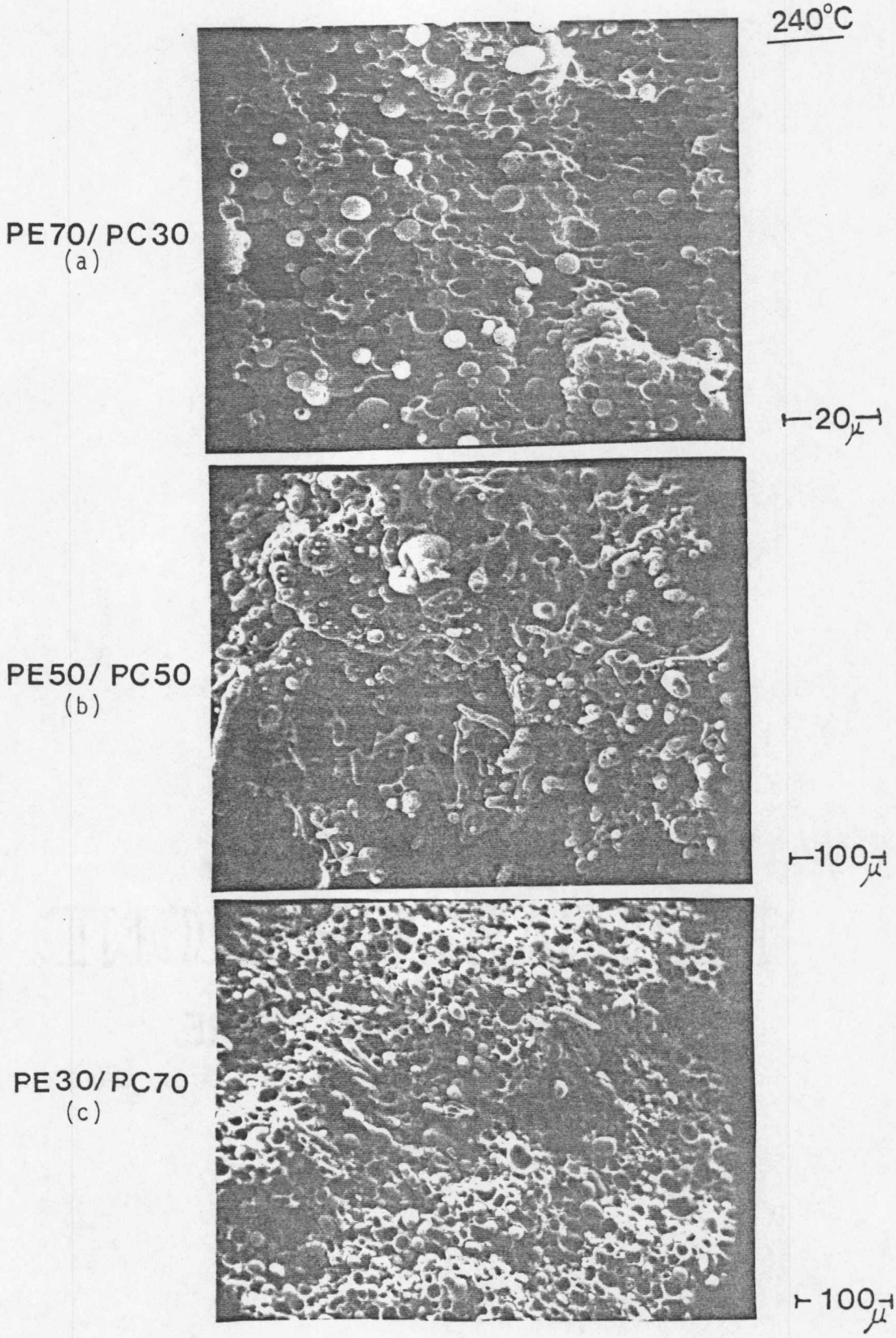


Figure IV-9. SEM microphotographs of PE-2/PC blends prepared in a screw extruder and Koch static mixer: (a) 70/30; (b) 50/50; (c) 30/70.

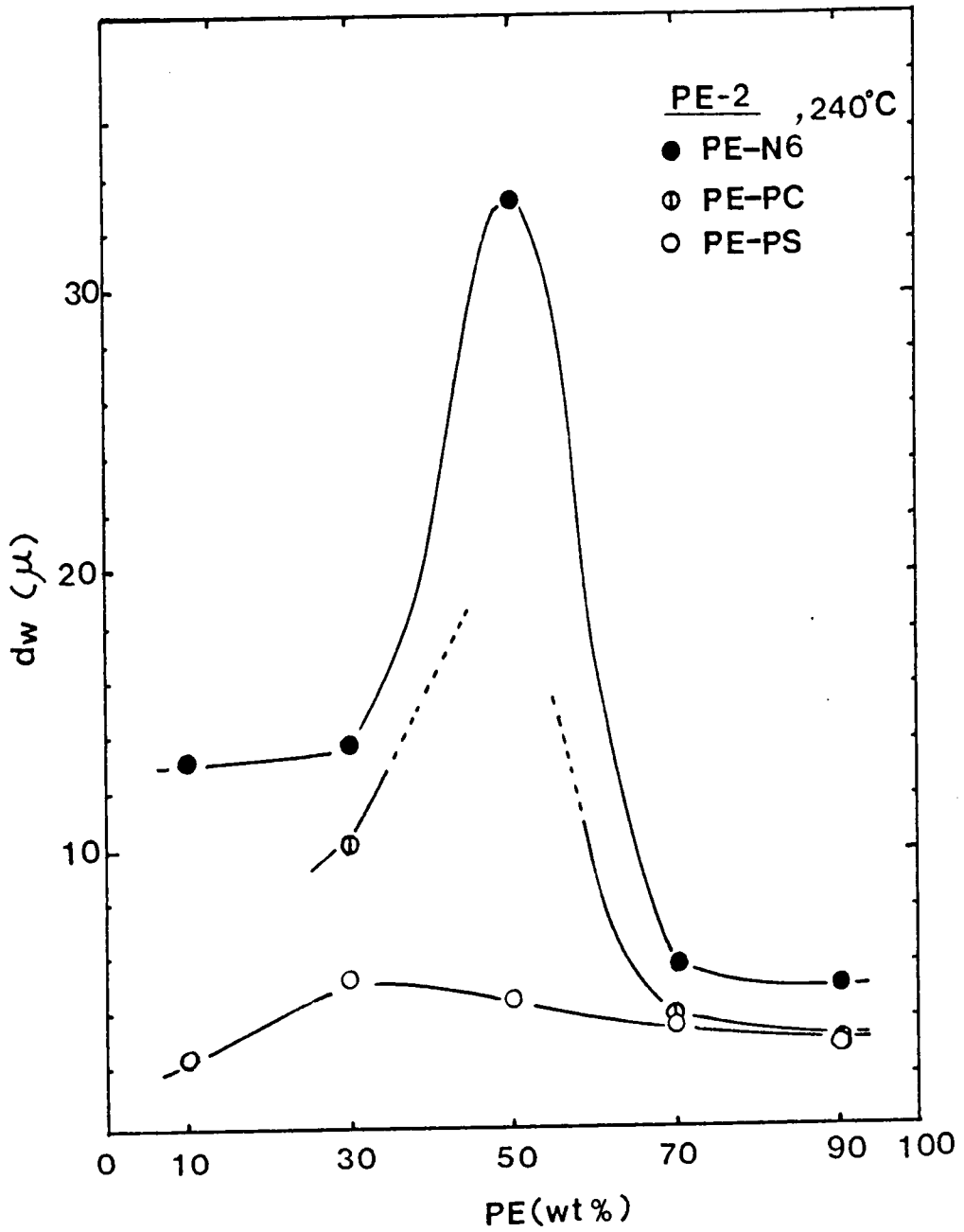


Figure IV-10. The comparison of discrete phase sizes of PE-2/PS, PE-2/N6 and PE-2/PC.

co-continuous morphology. The polyethylene islands in a nylon 6 sea and a polycarbonate sea are larger than that in the polystyrene sea. They are about two to three times as large as those in the PE islands in PS.

A.2. Discussion

Heikens et al. (62)(63) and Han et al. (53)(54)(55) used different mixing devices to blend polyethylene and polystyrene at the various temperatures. The comparisons of morphologies are listed in Table IV-3. The dimensions of the discrete phase are almost the same as ours. The dimensions are 1-10 microns. The phase morphology and the size of the discrete phase seem largely independent on the mixing device and the processing temperature.

The viscosities of each of the pure polymers were measured using the cone-plate rheometer and the Instron Capillary Rheometer and were shown in Figures IV-11, IV-12, and IV-13. The viscosities of the three different polyethylenes used were compared to that of polystyrene at 180°C in Figure IV-12. The viscosity of PE-1 shows much higher than that of polystyrene. The viscosity of PE-2 is similar to that of PS, but it shows the cross-over above $3 \times 10^{-1} sec^{-1}$. The viscosity of PE-3 is much lower than that of PS. Although the ratio of viscosities increased by raising temperature or changing molecular weight, the morphology of the dispersion and the size of the discrete phase exhibit little change. Generally, the morphology at the higher temperature system has a finer morphology.

Table IV-3. Comparisons of morphologies from different investigators (HDPE-PS)

Investigators	Mixing Device	Domain Size[1] (μ) Composition PE/PS 90/10	70/30	50/50	30/70	10/90
Heikens et al. Heikens et al.	Brabender Blender (Single Screw Extruder) 150°C	2.5	8.0	*	35	1.5
Han et al.[2]	Single Screw Extruder plus Kenics Static Mixer 200°C and 240°C	-	*	6.2	7.0	-
		-	*	5.1	5.6	-
This Dissertation	Single Screw Extruder plus Koch Static Mixer 180°C and 240°C	2.5	3.9	9.2	2.6	1.4
		3.0	3.6	4.4	5.4	2.6

*Co-continuous phase.

[1]Weight average.

[2]75/25 and 25/75.

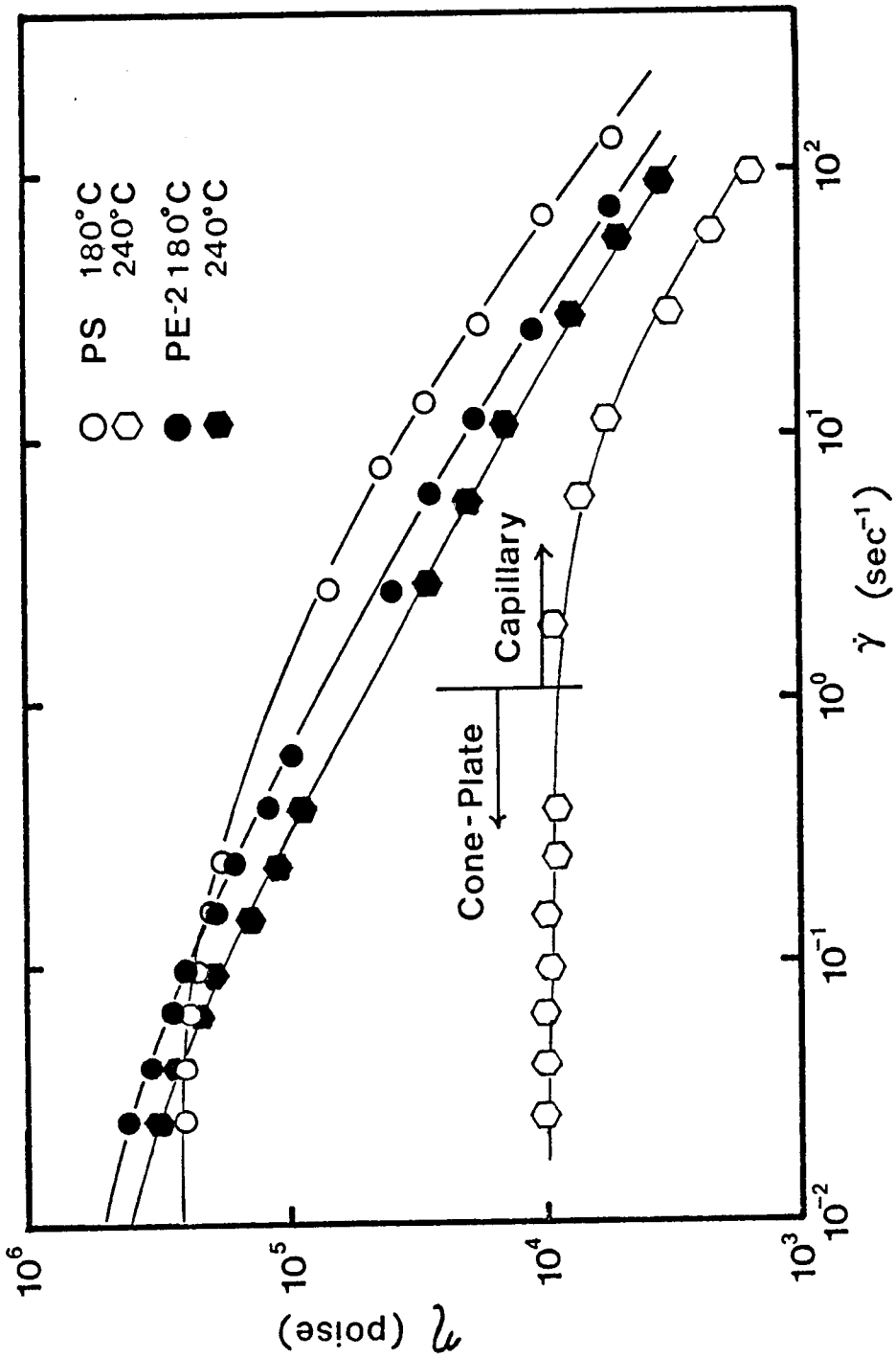


Figure IV-11. Viscosity, η, as a function of shear rate for polyethylene and polystyrene at two different temperatures.

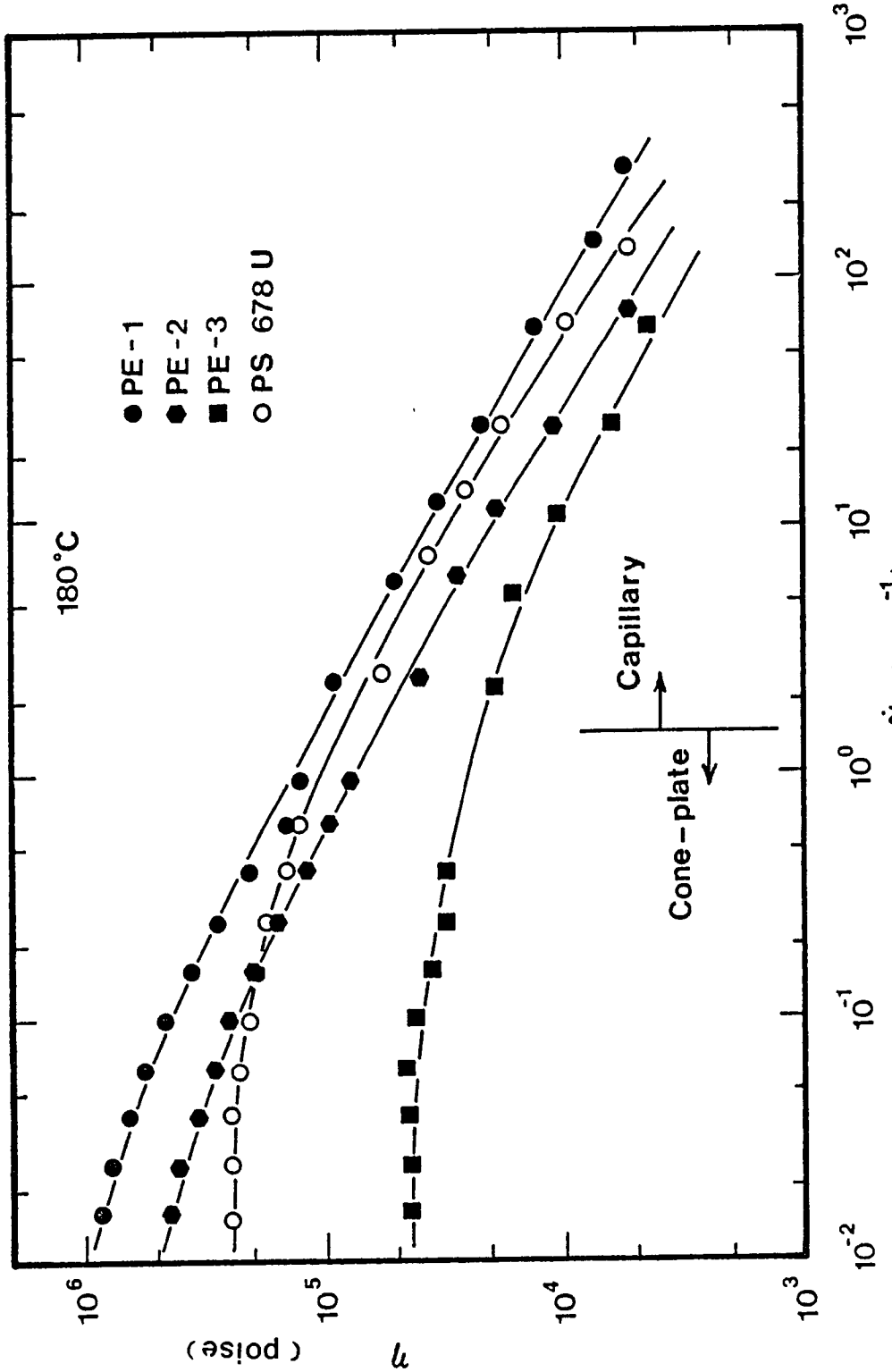


Figure IV-12. Viscosity, η, as a function of shear rate for different polyethylenes at 180°C.

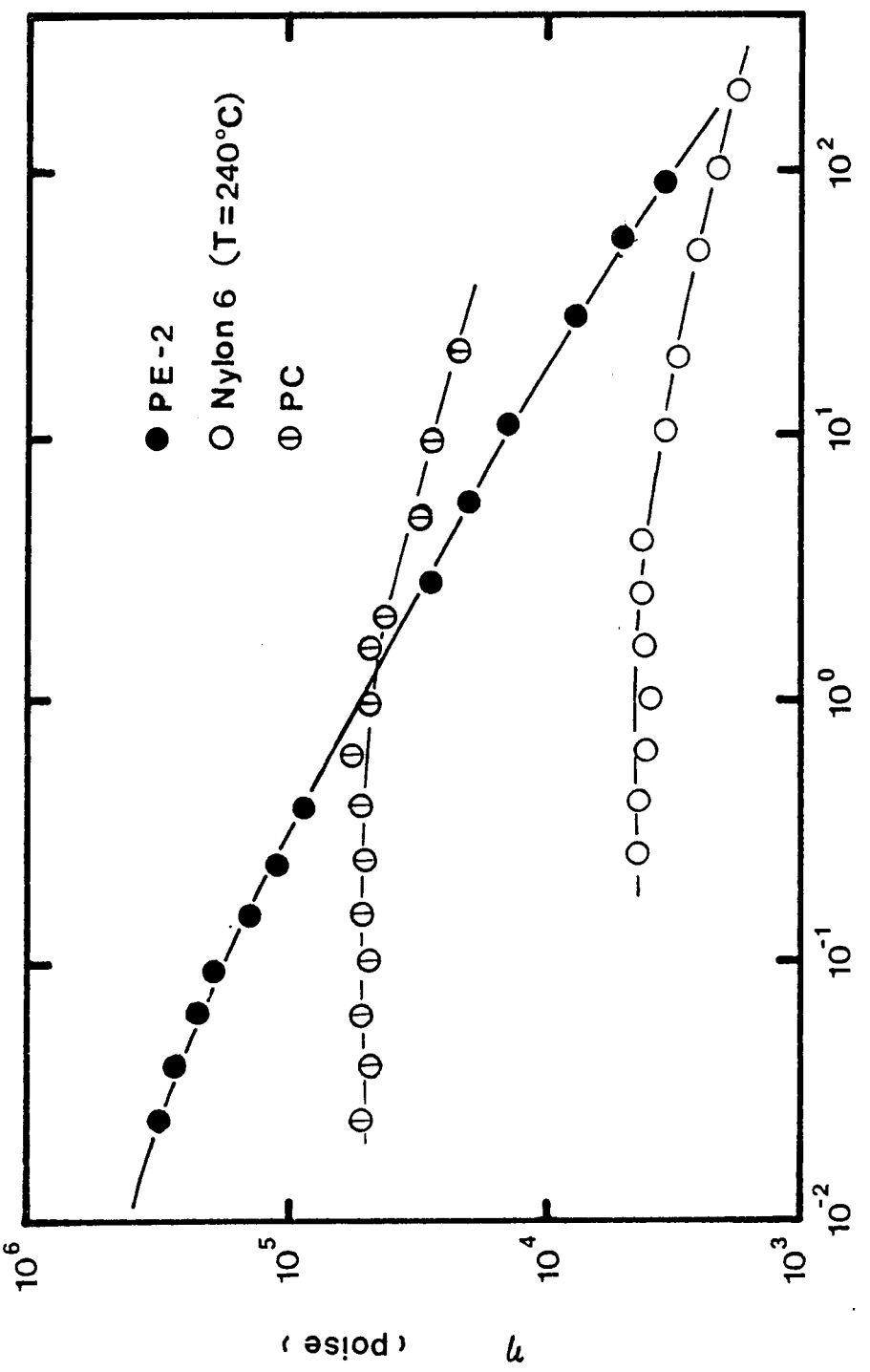


Figure IV-13. Viscosity, η, as a function of shear rate for polystyrene-2 (PE-2), nylon 6 (N_6) and polycarbonate (PC).

A comparison of viscosities of PE-2, N6 and PC is plotted against shear rate in Figure IV-13. Those of N6 and PC have a wider Newtonian region than that of PS. The viscosity ratios correspond to those of PE-PS systems. Therefore, the morphology from mixer is independent on the temperature, viscosity. The difference in scale of morphology (Figure IV-10 and Table IV-4) of PE/PS, PE/N6 and PE/PC would seem to reflect differences in interfacial tension and matrix viscosity of these systems. This view was developed by Liang et al. (90), who expressed it in terms of the dimensionless group representing the interaction of interfacial tension and viscous forces.

B. MORPHOLOGY OF SAMPLES SHEARED IN A CONE-PLATE RHEOMETER

B.1. Results

The extrudates from the static mixer were placed in a cone-plate rheometer, the surface of which was covered by a commercial epoxy resin in order to allow removal of samples without breakage or severe plastic deformation. The samples were then observed using SEM. SEM micrographs of the cross-sections of polyethylene (PE-2)-polystyrene sheared in a cone-plate rheometer at 180°C are shown in Figure IV-14. The cross-sections were observed in the different directions: parallel to flow direction and perpendicular to the flow direction. The phase morphology is not different from those of the extrudates from the static mixer. The PE/PS-90/10, 70/30, and 50/50 have polystyrene islands in a polystyrene sea. The

Table IV-4. Comparison of the discrete phase size of PE-2/PS, PE-2/N6, PE-2/PC blends at 240°C

Composition	PE-2/PS		PE-2/N6		PE-2/PC	
	dn (μ)	dw (μ)	dn (μ)	dw (μ)	dn (μ)	dw (μ)
90/10	2.2	3.0	3.8	5.2	2.4	2.7
70/30	3.2	3.6	5.0	5.7	2.6	3.1
50/50	3.7	4.4	24.9	33.4	co-continuous	
30/70	3.4	5.4	11.6	14.0	8.8	10.3
10/90	1.8	2.6	10.3	13.3	-	

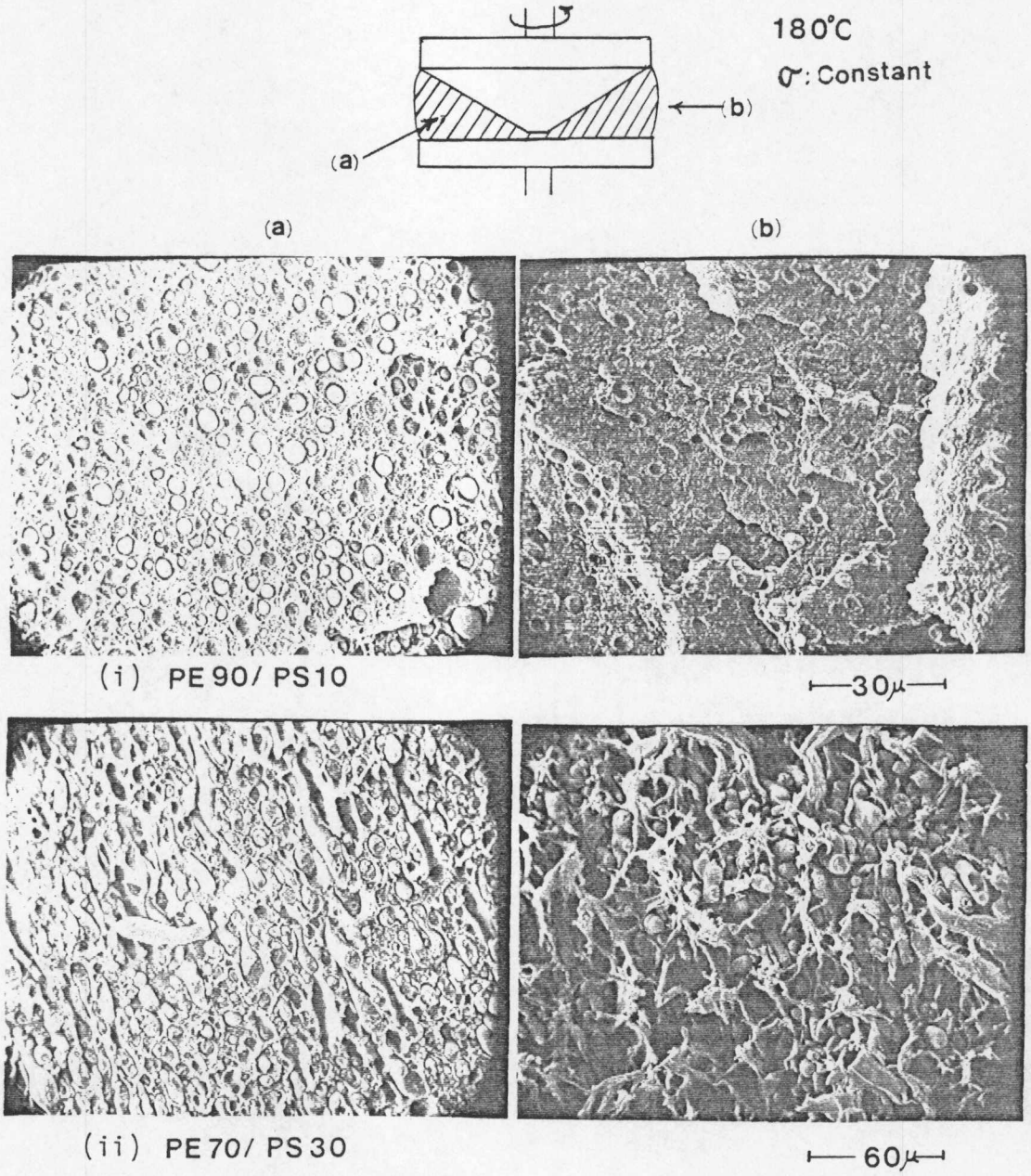


Figure IV-14. SEM microphotographs of PE-2/PS blends stressed in a cone-plate: (i) 90/10; (ii) 70/30; (iii) 50/50; (iv) 30/70; (v) 10/90.

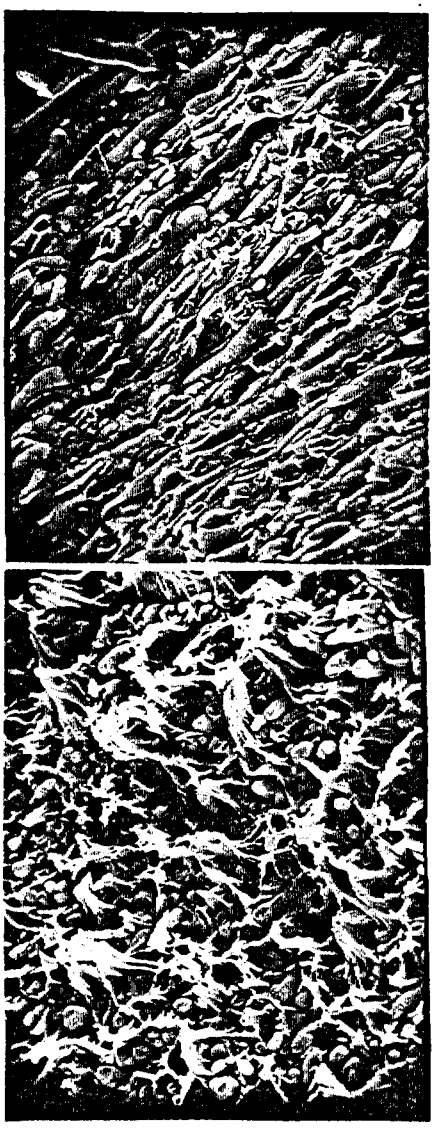


Figure IV-14 (continued)

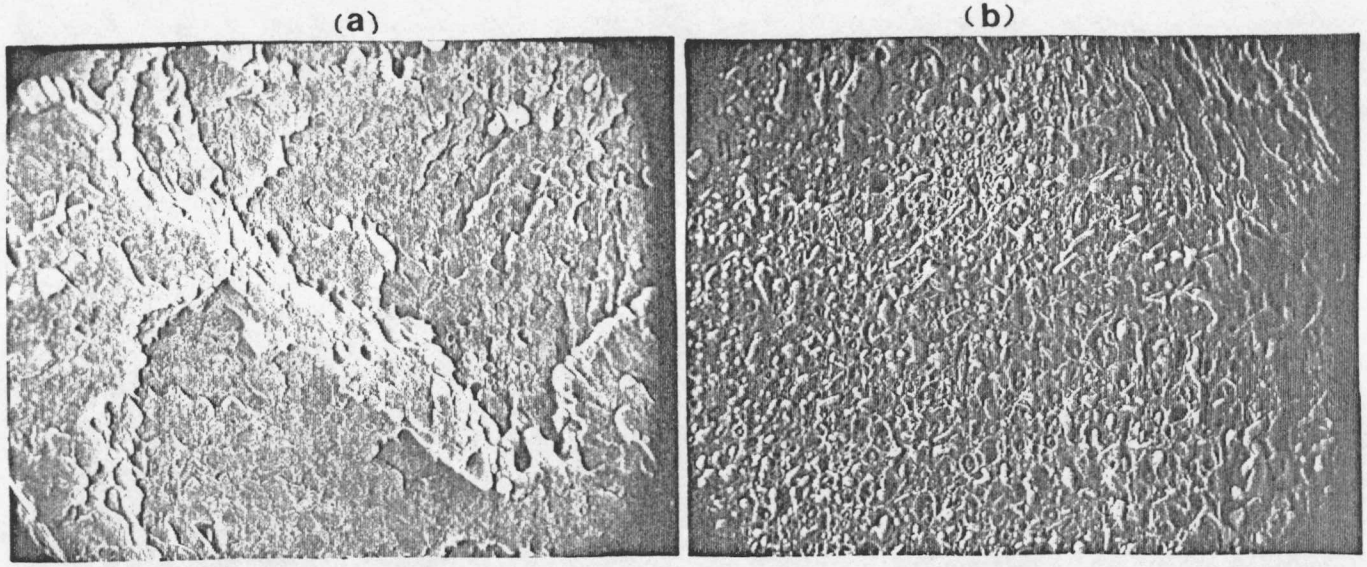
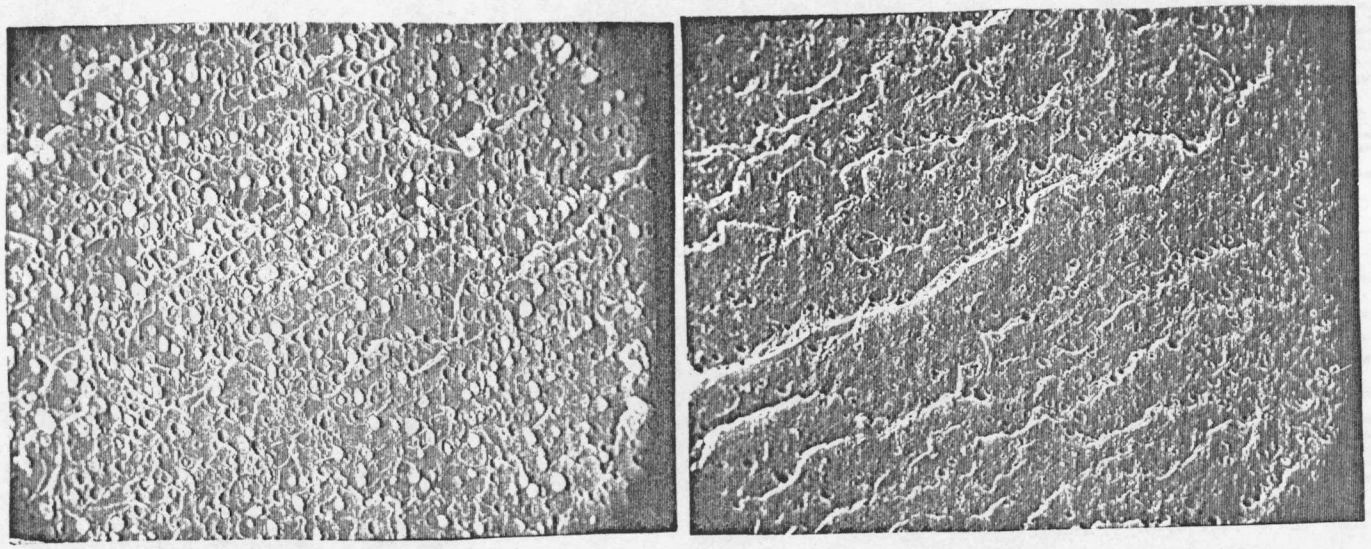


Figure IV-14 (continued)



(v) PE10/PS90

Figure IV-14 (continued)

PE/PS-70/30, 50/50 and 30/70 show the rodlike structure of the discrete phase. It was observed that the rods are arranged parallel to the flow direction.

B.2. Discussion

The size of discrete phase at low shear rate and shear stress is almost equal to those of the extrudates from the static mixer. Table IV-5 shows the size of the discrete phase at different shear stresses. The mode of dispersion was found to be very similar to the extrudates from the static mixer.

C. CAPILLARY EXTRUDATE

C.1. Results

The extrudates from the static mixer were placed in the barrel of the Instron Capillary Rheometer and heated at 180°C for PE/PS and 240°C for PE-2/N6 and PE-2/PC.

For the series of polyethylene-polystyrene blends, the phase morphology shows little change with increasing shear rate and shear stress as shown in Figures IV-15 through IV-27. PE90/PS10, 70/30, and 50/50 show the polystyrene dispersed phases in polyethylene matrix and PE/PS-30/70 and 10/90 show polyethylene rods in polystyrene matrix. For most of the PE/PS systems, the discrete phase size decreased with increasing the shear stress except the PE-3/PS-90/10 as listed in Tables IV-6, IV-7, and IV-8 and plotted in Figures IV-28, IV-29, and IV-30. The phase size seems to reach a critical value, and the reduction is stable with increasing stress.

Table IV-5. The dimensions of discrete phase of PE-2/PS blends stressed in a cone-plate

PE-2/PS Composition	$\dot{\gamma}$ (sec^{-1})	σ_{12} ($dyne/cm^2$)	Size of Dispersed Phase dn (μ)	dw
90/10	0.1	2.46×10^4	2.3	2.5
70/30	0.1	2.68	5.6	6.0
50/50	0.1	2.71	4.9	5.4
30/70	0.1	2.64	4.3	5.0
10/90	0.063	2.52	1.4	1.6

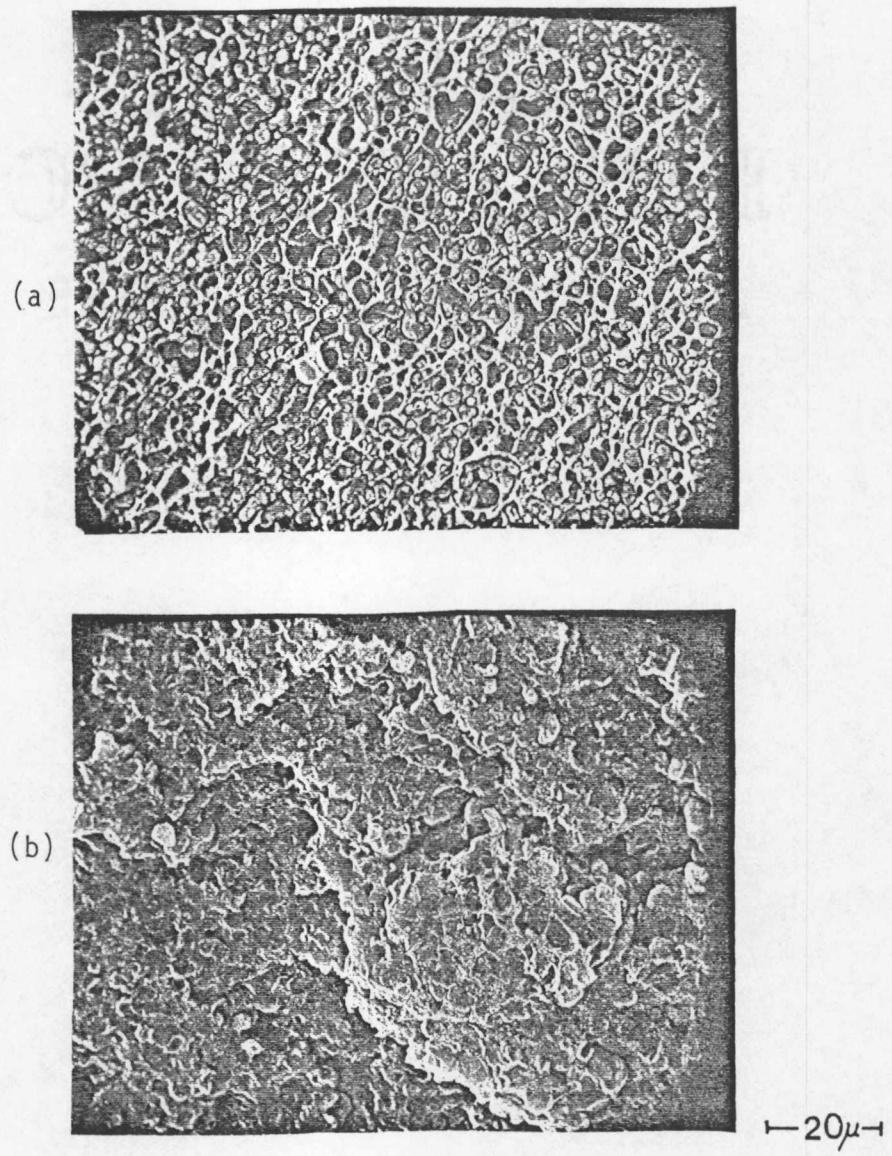


Figure IV-15. SEM microphotographs of PE-2/PS-70/30 blend extrudates as a function of die wall shear rate $32Q/\pi D^3$: (a) 12.2 sec^{-1}; (b) 69.6 sec^{-1}.

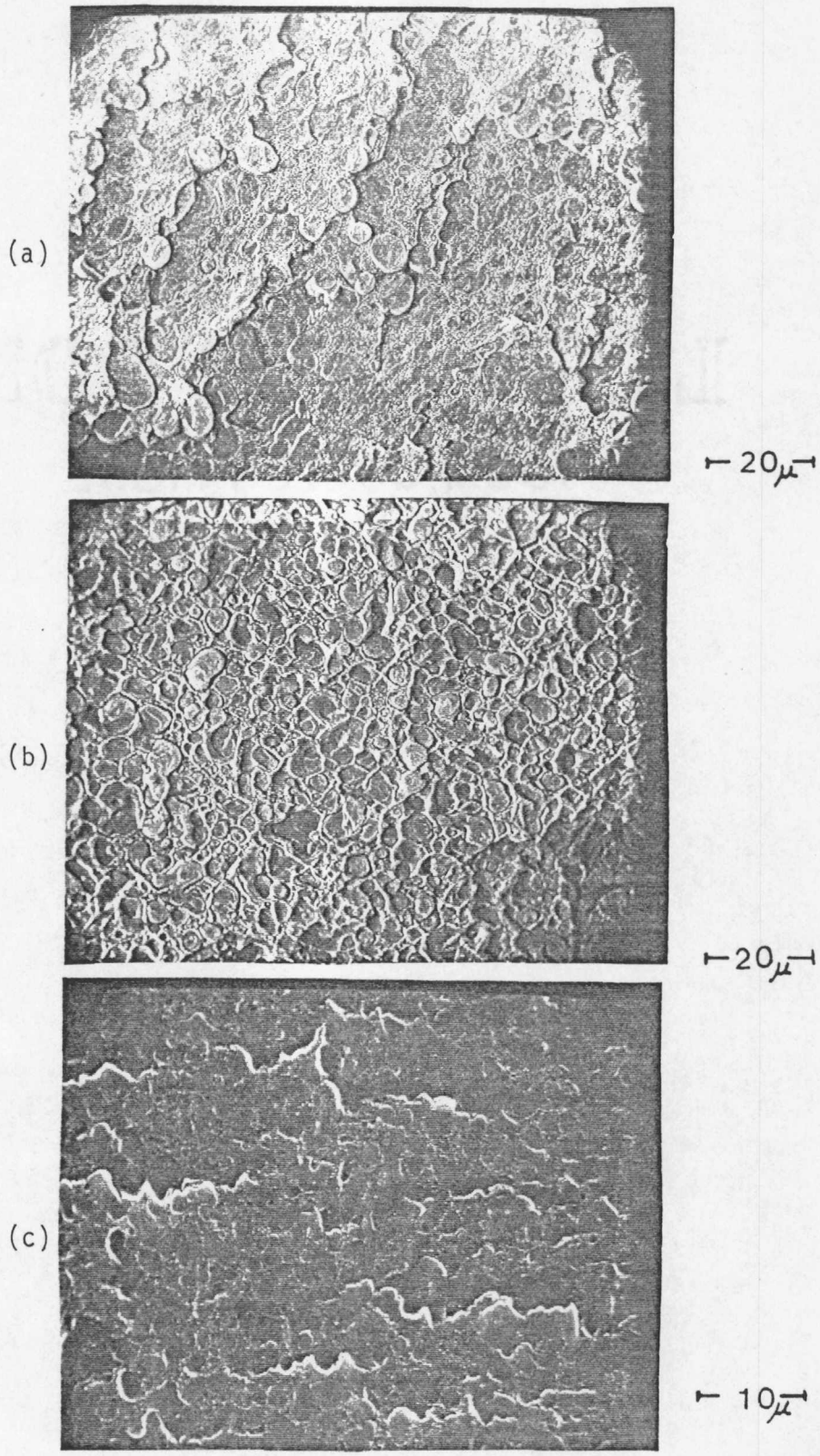


Figure IV-16. SEM microphotographs of PE-2/PS-50/50 blend extrudates as a function of die wall shear rate $32Q/\pi D^3$: (a) 2.0 sec^{-1}; (b) 11.0 sec^{-1}; (c) 70.8 sec^{-1}.

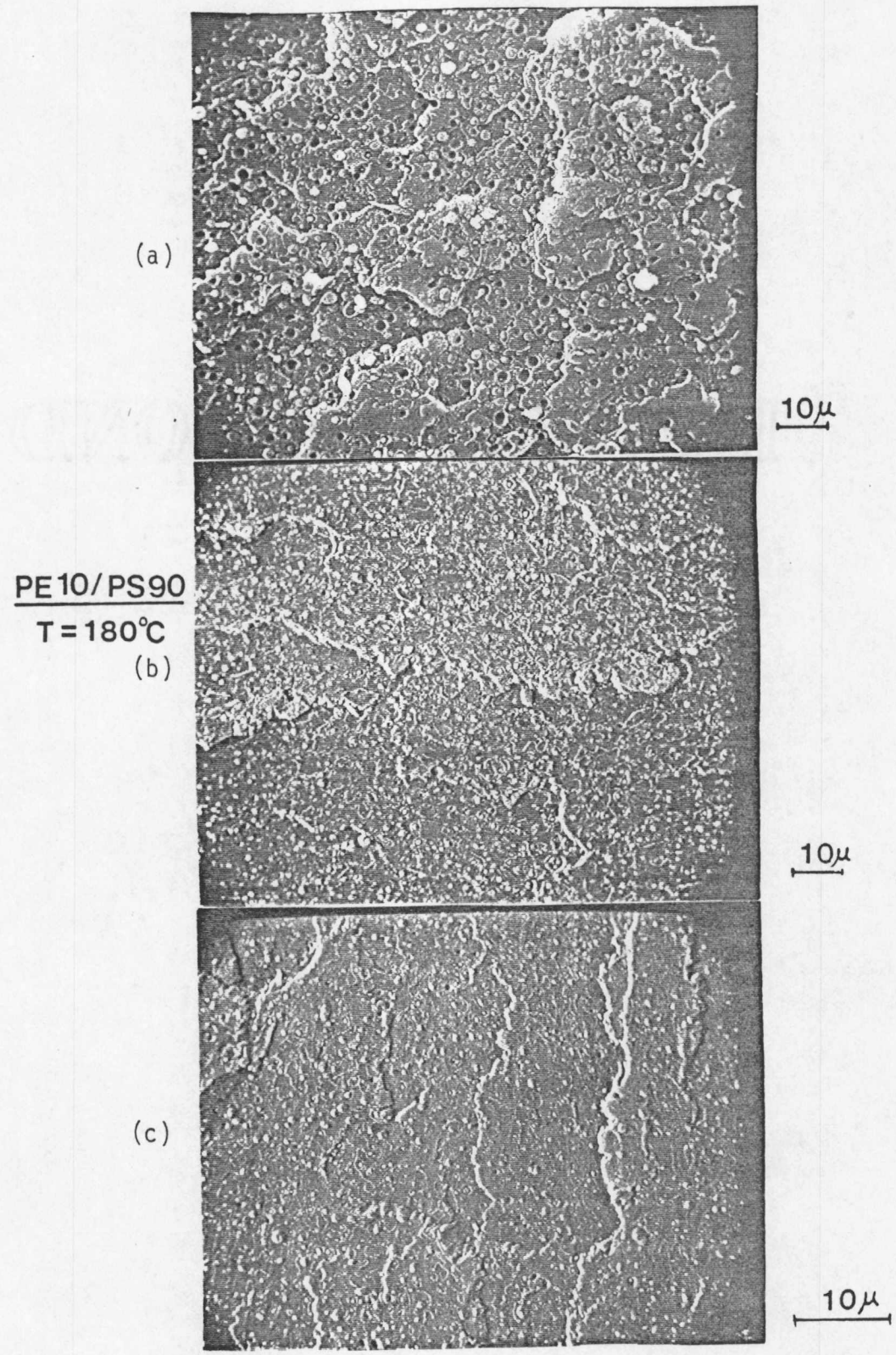


Figure IV-17. SEM microphotographs of PE-2/PS-10/90 blend extrudates as a function of die wall shear rate $32Q/\pi D^3$: (a) 2.6 sec^{-1}; (b) 13.0 sec^{-1}; (c) 60.0 sec^{-1}.

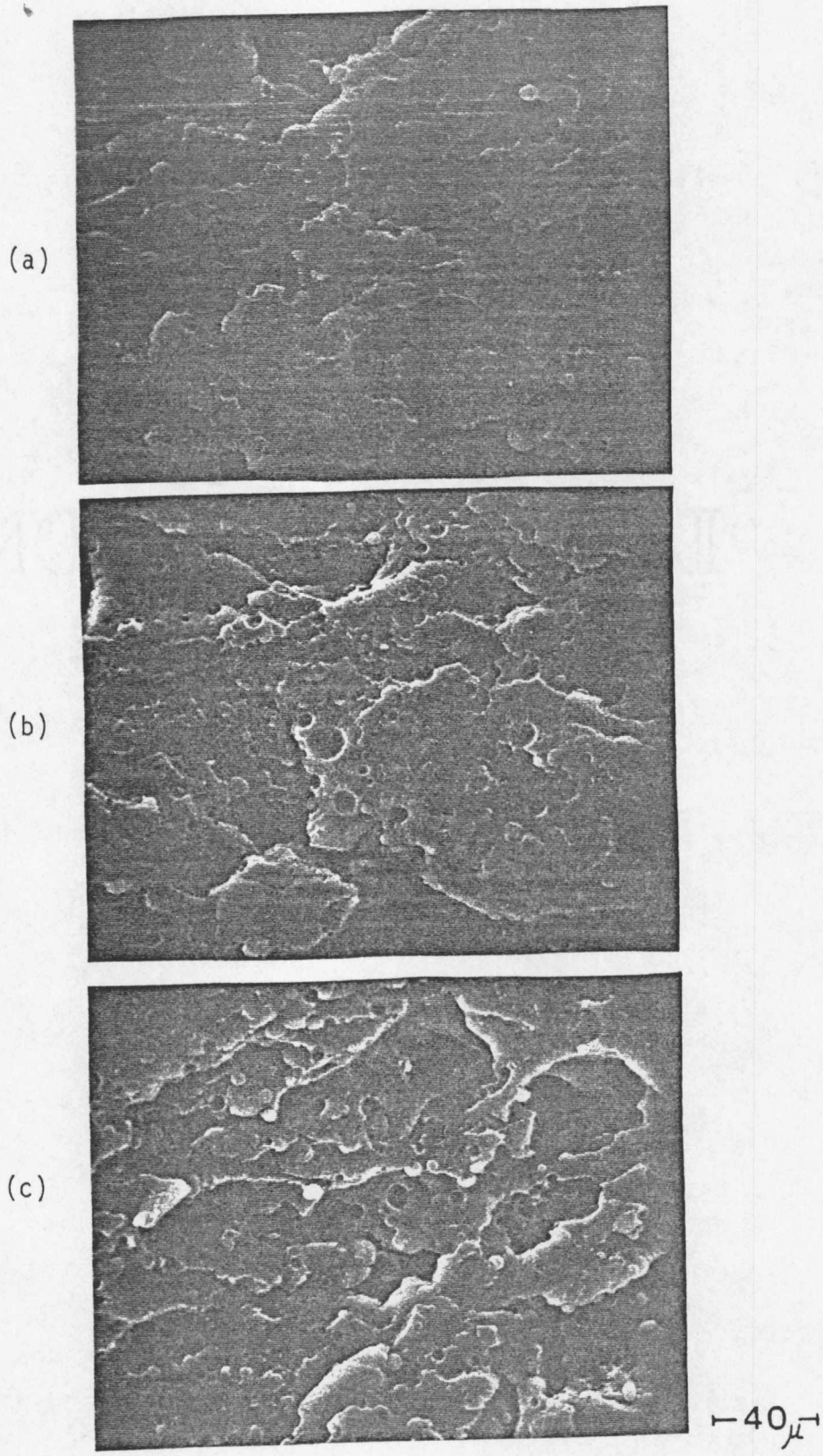


Figure IV-18. SEM microphotographs of PE-3/PS-90/10 blend extrudates as a function of die wall shear rate $32Q/\pi D^3$: (a) 2.2 sec^{-1}; (b) 11.2 sec^{-1}; (c) 55.2 sec^{-1}.

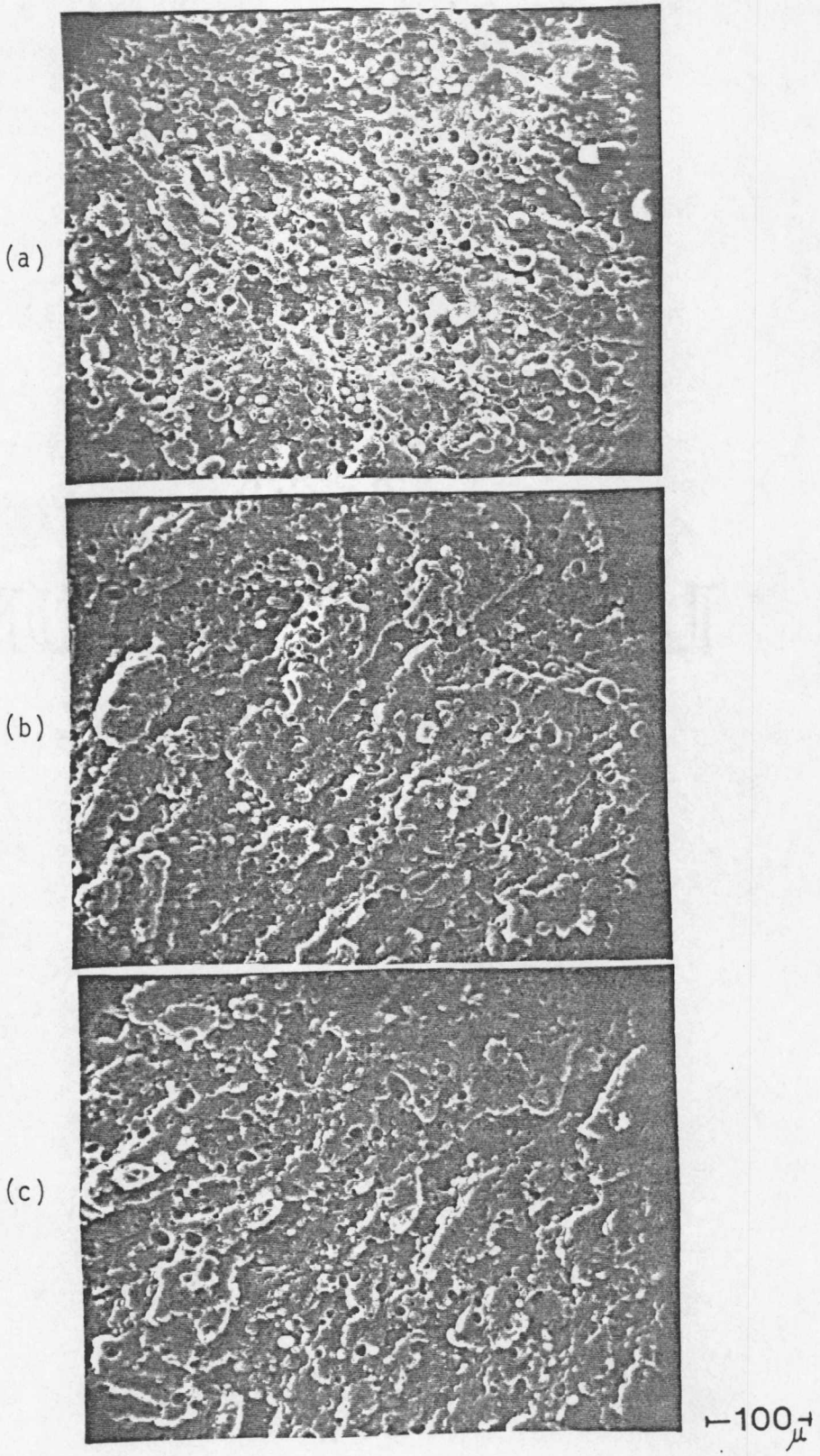


Figure IV-19. SEM microphotographs of PE-3/PS-70/30 blend extrudates as a function of die wall shear rate $32Q/\pi D^3$: (a) 2.4 sec^{-1}; (b) 11.7 sec^{-1}; (c) 56.8 sec^{-1}.

PE50/PS50

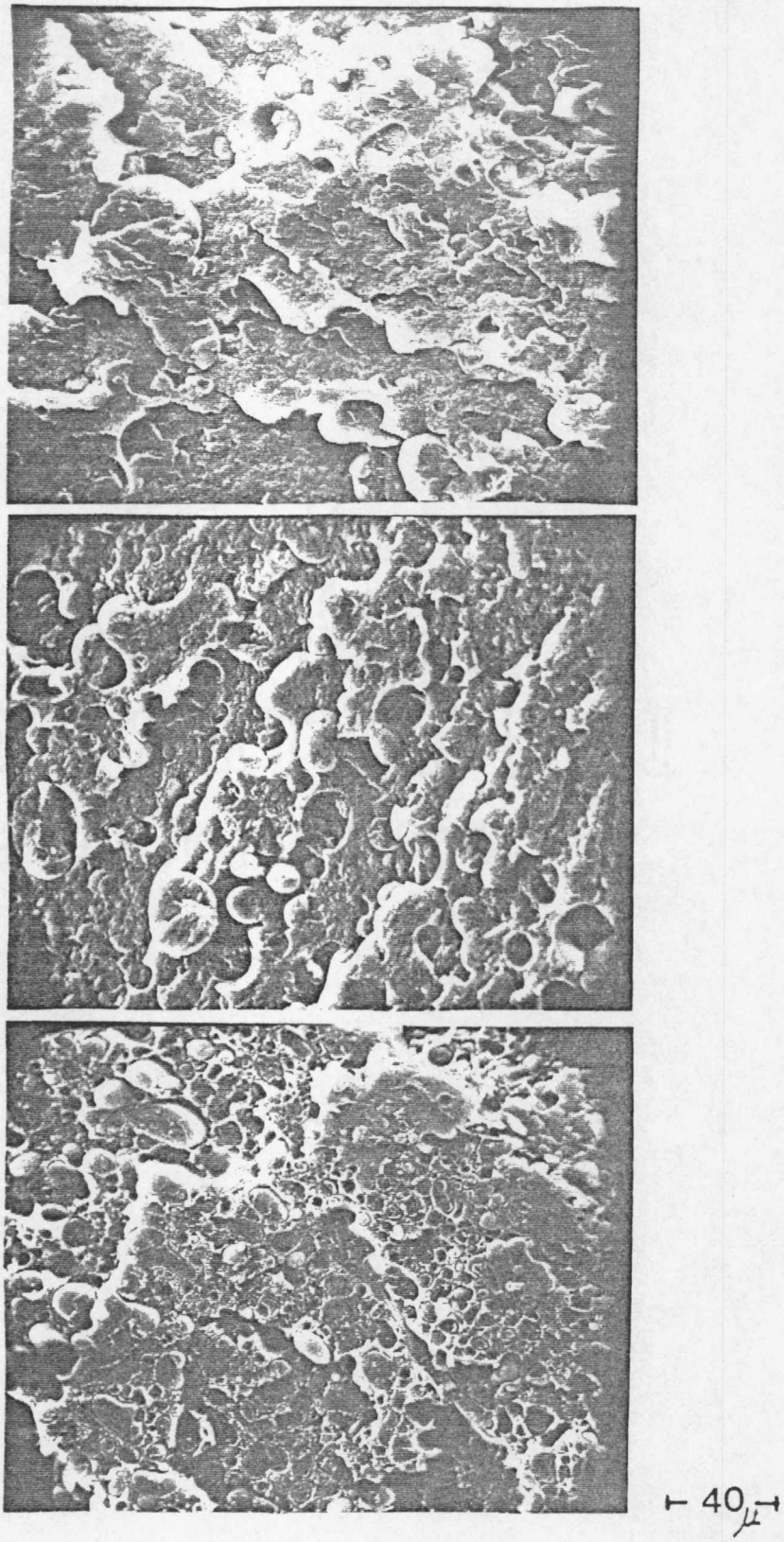


Figure IV-20. SEM microphotographs of PE-3/PS-50/50 blend extrudates as a function of die wall shear rate $32Q/\pi D^3$: (a) 2.0 sec^{-1}; (b) 11.6 sec^{-1}; (c) 54.5 sec^{-1}.

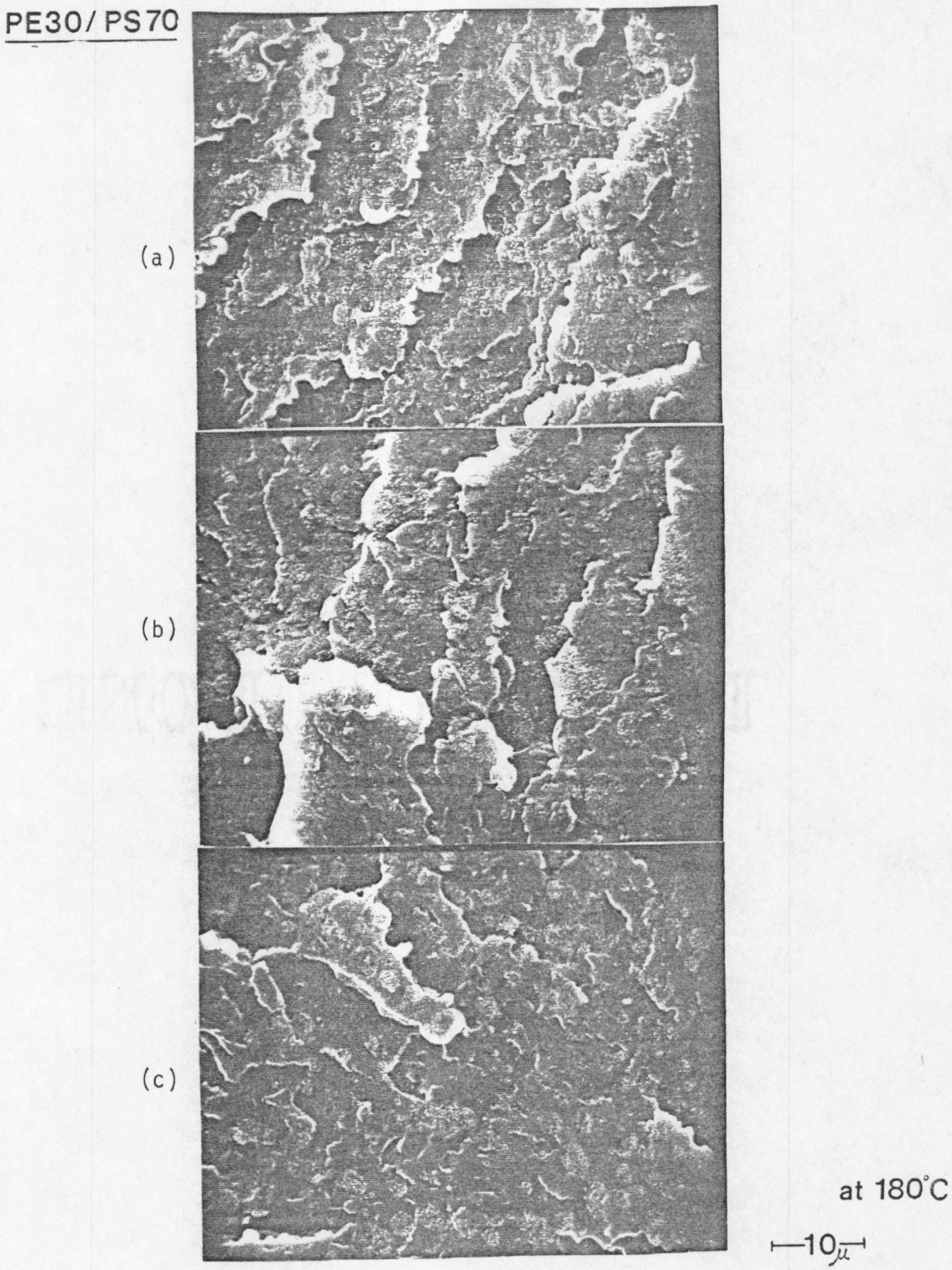


Figure IV-21. SEM microphotographs of PE-3/PS-30/70 blend extrudates as a function of die wall shear rate $32Q/\pi D^3$: (a) 2.0 sec^{-1}; (b) 10.6 sec^{-1}; (c) 61.8 sec^{-1}.

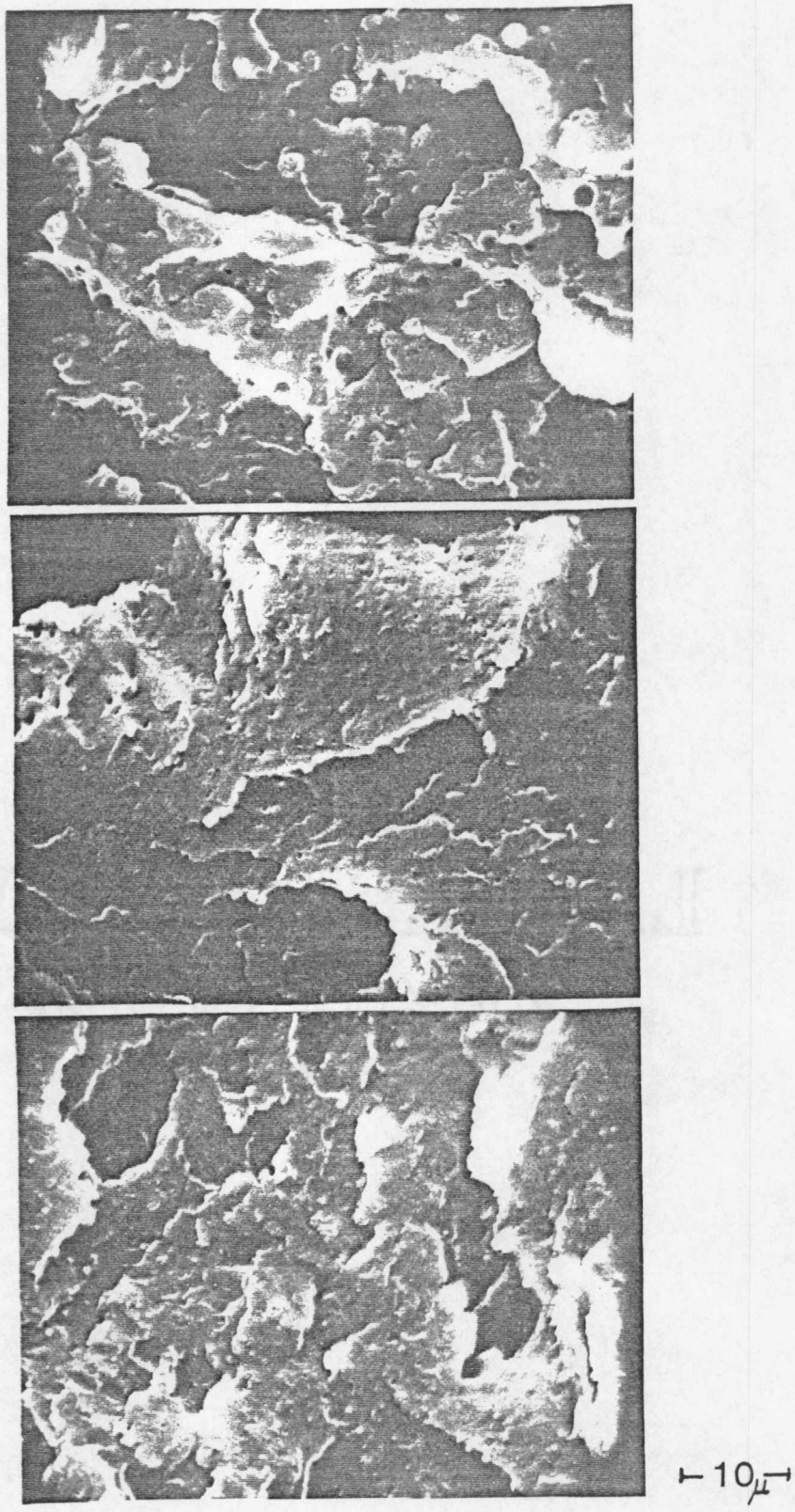


Figure IV-22. SEM microphotographs of PE-3/PS-10/90 blend extrudates as a function of die wall shear rate $32Q/\pi D^3$: (a) 2.5 sec^{-1}; (b) 12.1 sec^{-1}; (c) 69.0 sec^{-1}.

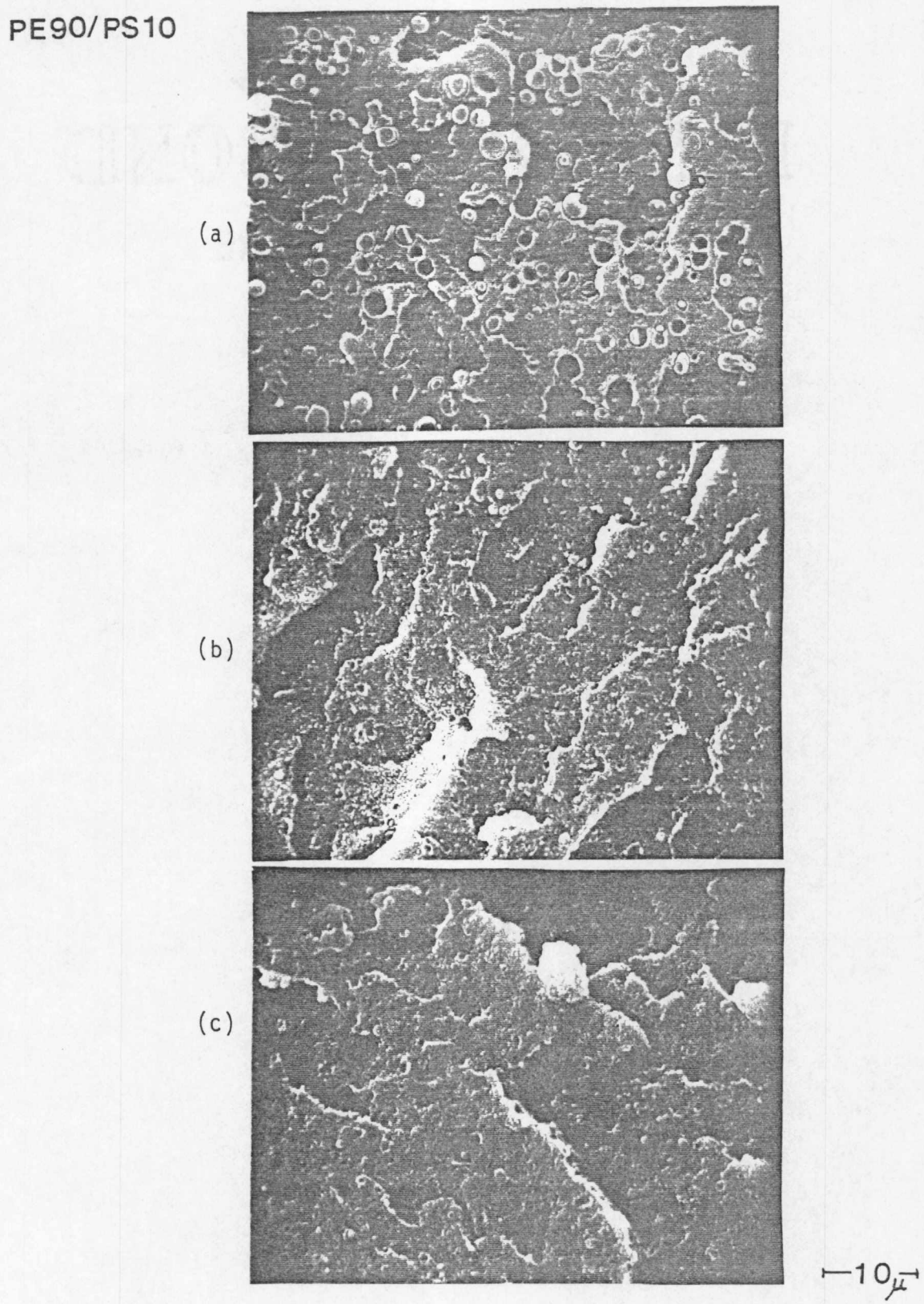


Figure IV-23. SEM microphotographs of PE-1/PS-90/10 blend extrudates as a function of die wall shear rate $32Q/\pi D^3$: (a) 2.2 sec^{-1}; (b) 11.7 sec^{-1}; (c) 58.6 sec^{-1}.

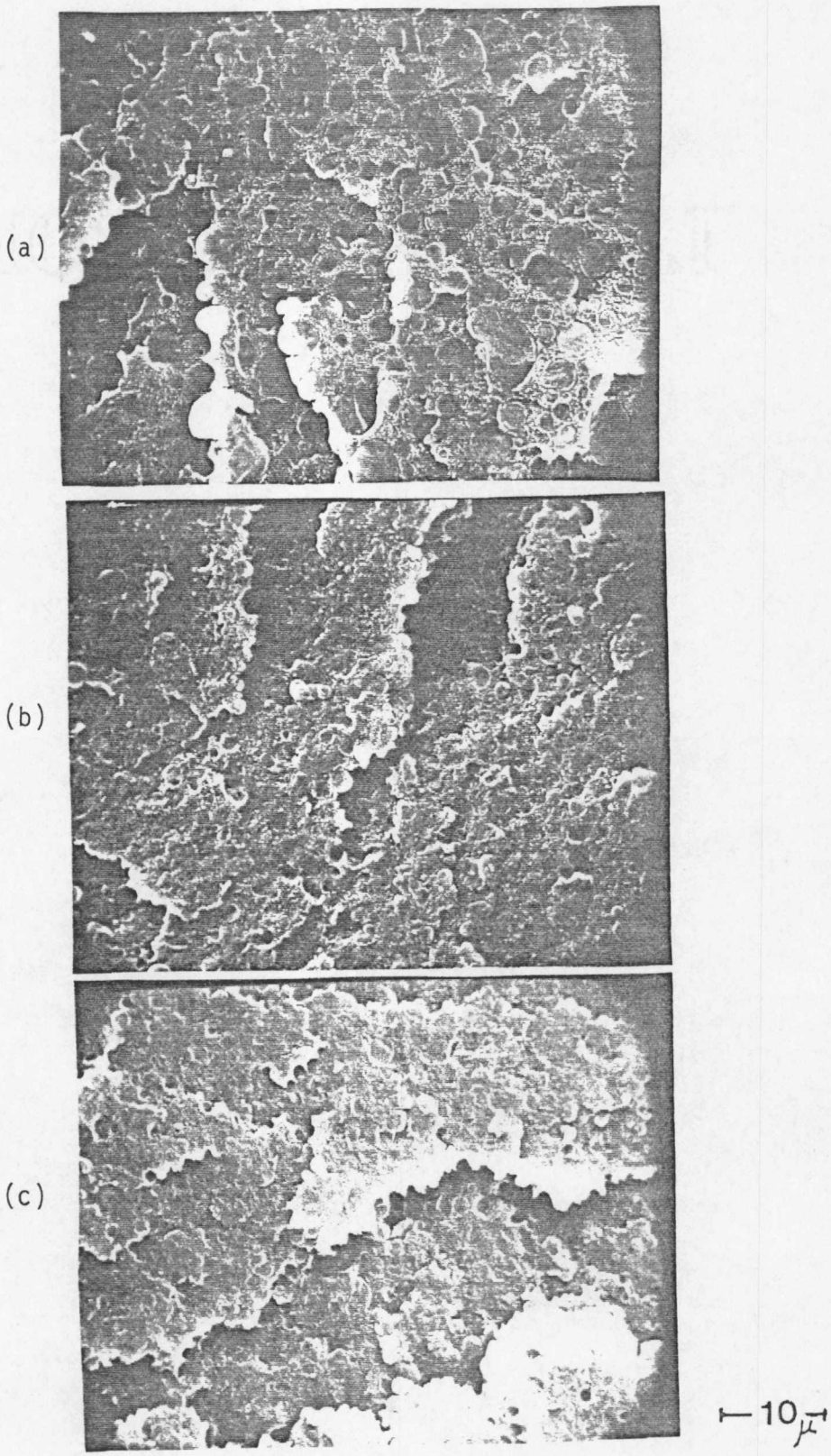


Figure IV-24. SEM microphotographs of PE-1/PS-70/30 blend extrudates as a function of die wall shear rate $32Q/\pi D^3$: (a) 2.3 sec^{-1}; (b) 11.4 sec^{-1}; (c) 61.8 sec^{-1}.

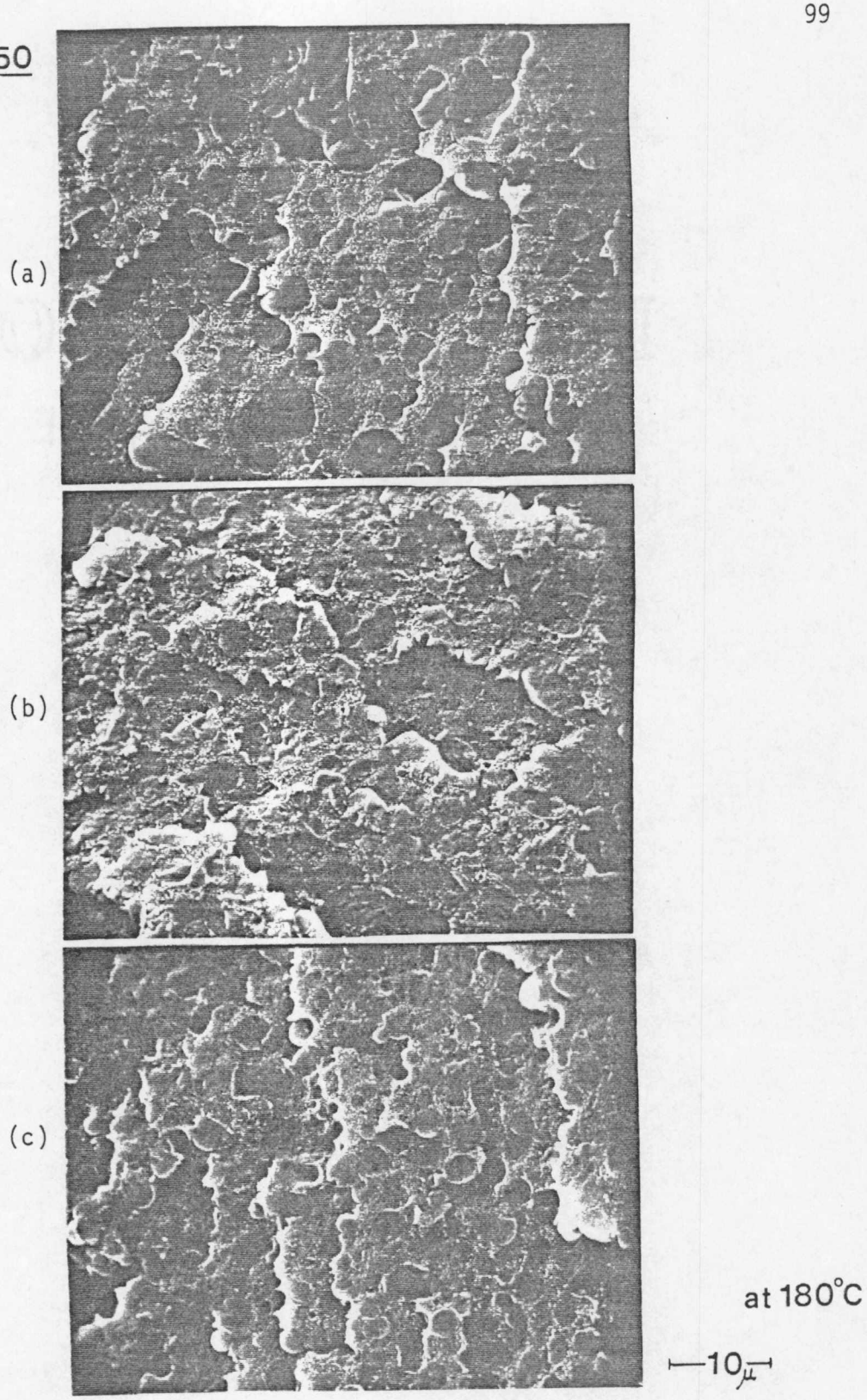


Figure IV-25. SEM microphotographs of PE-1/PS-50/50 blend extrudates as a function of die shear wall rate $32Q/\pi D^3$: (a) 2.5 sec^{-1}; (b) 12.4 sec^{-1}; (c) 67.2 sec^{-1}.

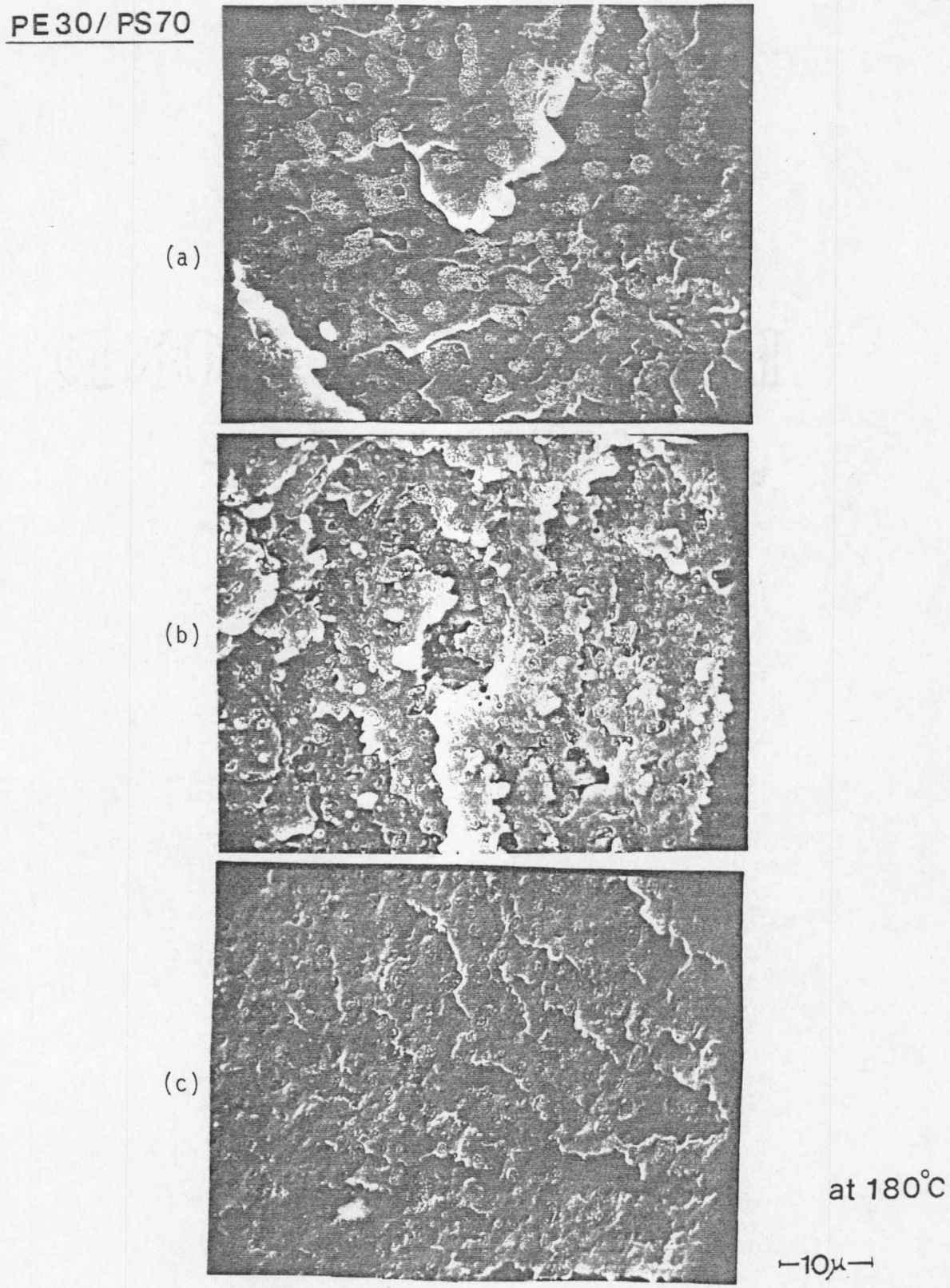


Figure IV-26. SEM microphotographs of PE-1/PS-30/70 blend extrudates as a function of die wall shear rate $32Q/\pi D^3$: (a) 2.6 sec^{-1}; (b) 12.9 sec^{-1}; (c) 83.9 sec^{-1}.

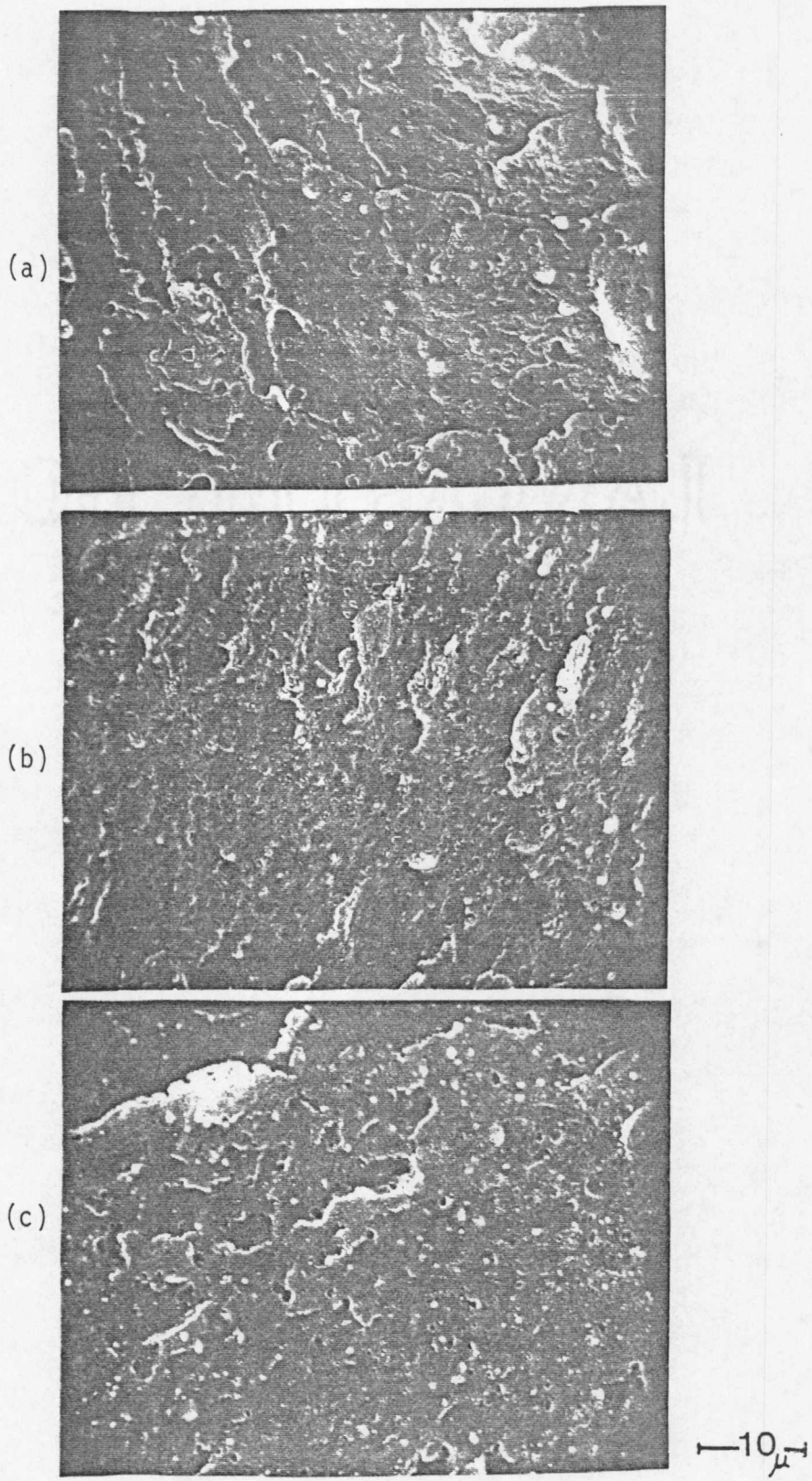


Figure IV-27. SEM microphotographs of PE-1/PS-10/90 blend extrudates as a function of die wall shear rate $32Q/\pi D^3$: (a) 2.6 sec^{-1}; (b) 12.9 sec^{-1}; (c) 72.9 sec^{-1}.

Table IV-6. The influence of extrusion conditions on discrete phase size extrudated from capillary (PE-2/PS)

Blends	Shear Rate (sec^{-1})	Shear Stress ($dyne/cm^2$)	d_n (μ)	d_w (μ)
PE90/PS10	2.1	1.02×10^5	1.94	2.13
	11.5	2.60×10^5	1.29	1.38
	64.8	4.80×10^5	1.17	1.33
PE70/PS30	2.3	0.94×10^5	3.33	4.27
	12.2	2.75×10^5	2.46	2.96
	69.6	5.70×10^5	2.19	2.45
PE50/PS50	2.0	0.94×10^5	3.72	4.25
	11.0	2.20×10^5	2.65	3.02
	70.8	4.68×10^5	2.30	2.71
PE30/PS70	2.2	1.56×10^5	1.70	1.85
	12.2	3.12×10^5	1.44	1.52
	52.8	5.00×10^5	0.87	1.18
PE10/PE90	2.6	2.50×10^5	1.59	1.72
	13.9	3.90×10^5	0.70	0.91
	60.0	7.03×10^5	0.44	0.53

Table IV-7. The influence of extrusion conditions on discrete size extrudates from capillary (PE-3/PS)

PE-3/PS Composition	$\dot{\gamma}_{NW_1}$ (sec^{-1})	σ_{12} ($dyne/cm^2$)	Size (d_n (μ))	Size (d_w (μ))
90/10	2	4.36×10^4	5.83	6.91
	11.8	1.32×10^5	5.16	6.72
	55.2	3.58×10^5	5.02	6.56
70/30	2.4	8.73×10^4	9.21	10.71
	11.7	1.91×10^5	9.20	9.70
	56.8	3.82×10^5	8.90	9.40
50/50	2.0	6.54×10^4	13.93	23.30
	11.4	1.76×10^5	9.46	11.90
	54.5	4.06×10^5	6.60	9.56
30/70	2.0	5.45×10^4	2.27	3.03
	10.6	1.98×10^5	1.96	2.86
	61.8	4.71×10^5	1.72	2.32
10/90	2.50	1.53×10^5	1.09	1.28
	12.1	3.11×10^5	0.46	0.54
	69.0	5.69×10^5	0.25	0.30

Table IV-8. The influence of extrusion conditions on discrete size extrudates from capillary (PE-1/PS)

PE-1/PS Composition	$\dot{\gamma}_{NW_1}$ (sec^{-1})	σ_{12} ($dyne/cm^2$)	Size (d_n (μ)	d_w)
90/10	2.2	1.42×10^5	1.69	1.84
	11.7	3.11×10^5	0.74	0.75
	58.6	7.50×10^5	0.70	0.72
70/30	2.3	1.53×10^5	1.80	2.22
	11.4	4.06×10^5	1.35	1.38
	61.8	8.11×10^5	1.27	1.37
50/50	2.5	2.20×10^5	2.95	3.61
	12.4	4.55×10^5	1.76	2.17
	67.2	9.24×10^5	1.76	1.99
30/70	2.6	1.76×10^5	2.32	2.47
	12.9	3.35×10^5	0.99	1.29
	83.9	7.21×10^5	0.98	1.27
10/90	2.6	2.20×10^5	0.71	0.81
	12.9	4.54×10^5	0.47	0.56
	72.9	7.50×10^5	0.37	0.42

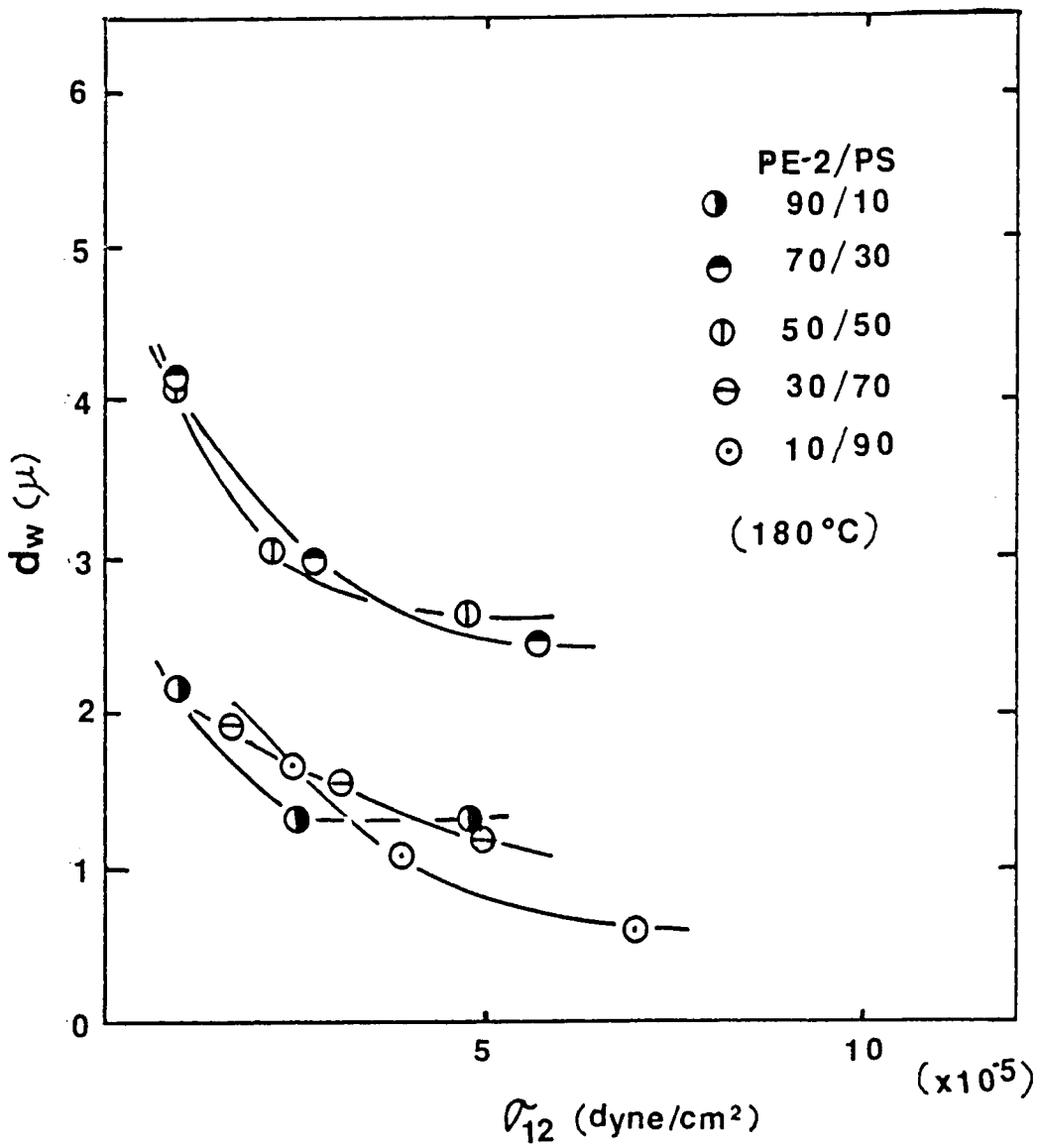


Figure IV-28. Mean dimension of discrete phase in PE-1/PS blends as a function of die wall shear stress (σ_{12}).

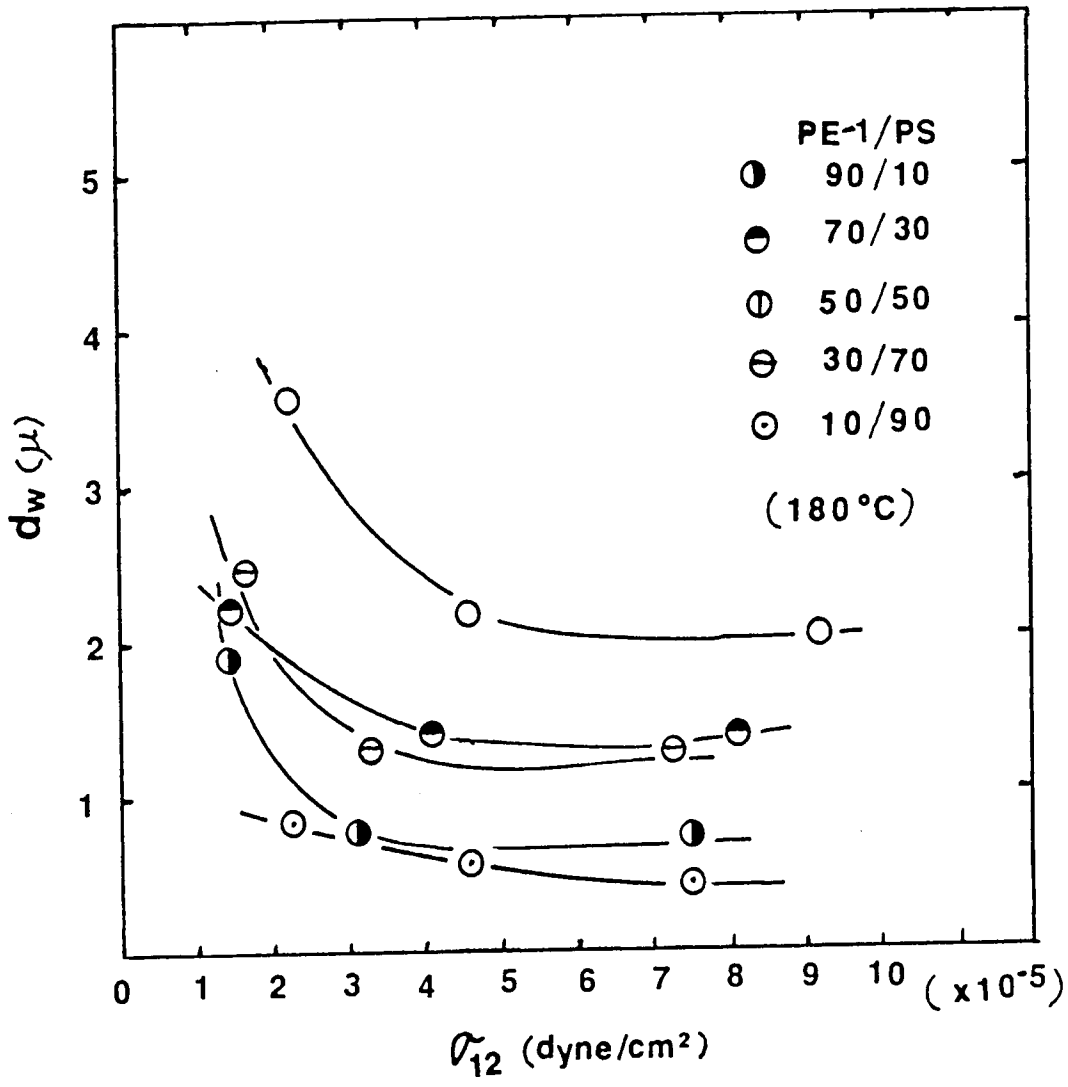


Figure IV-29. Mean dimension of discrete phase in PE-1/PS blends as a function of die wall shear stress (σ_{12}).

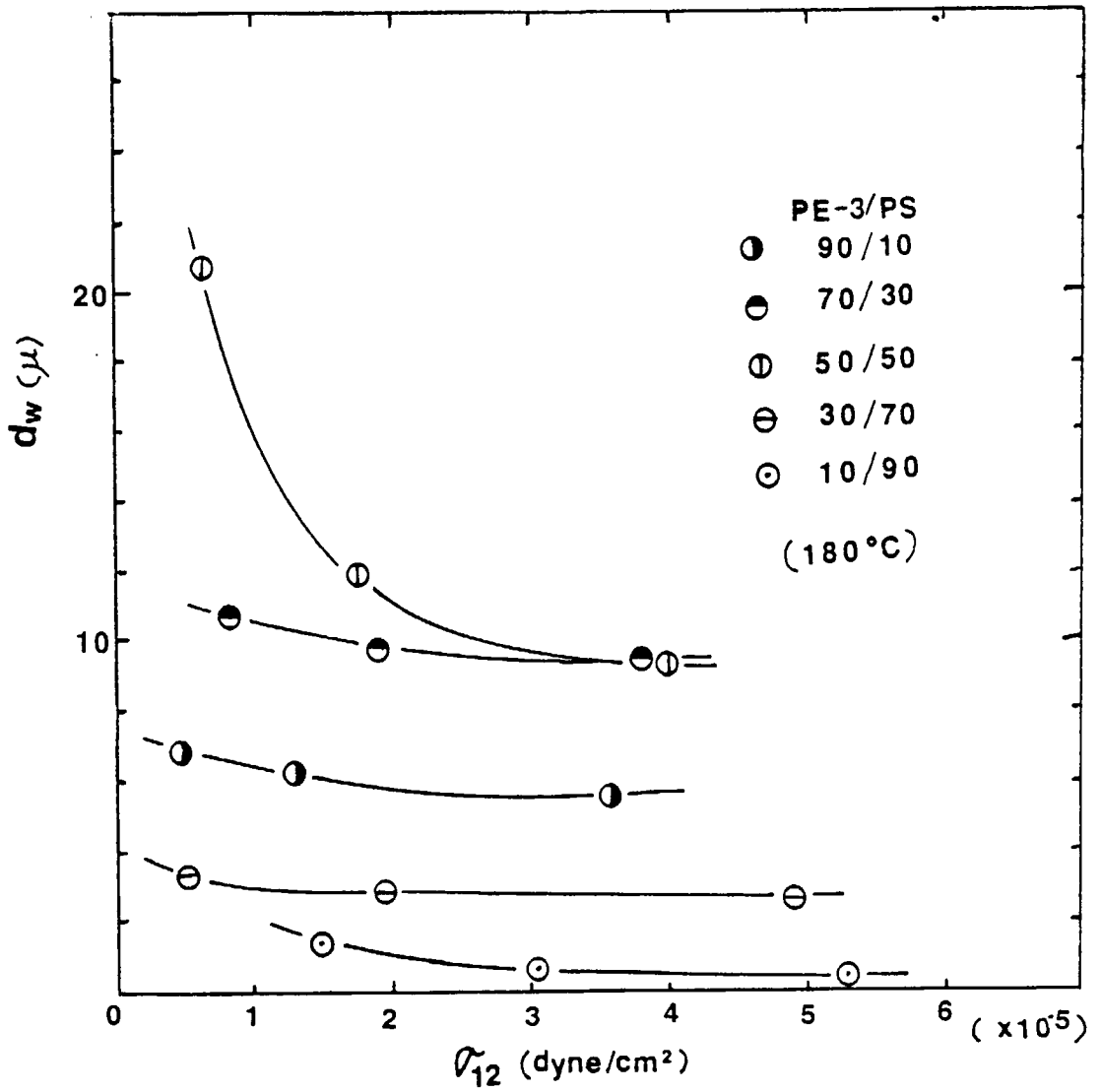


Figure IV-30. Mean dimension of discrete phase in PE-3/PS as a function of die shear stress (σ_{12}).

PE-2/N6-30/70 and 70/30 and PE/PC-30/70 and 70/30 exhibit islands which reduced in size with increasing stress (Figures IV-31, IV-32, IV-33, and IV-34). These reductions also reach an asymptotic critical value plotted on Figure IV-35(a) and (b). The phase morphology does not change with increasing shear stress. This is quantified in Table IV-9. The initial rods seem to become long thin threads.

The PE-2/N6-50/50 and PE/PC-50/50 at 240°C have a coarse co-continuous morphology in the region near the center of the capillary as shown in Figures IV-36 and IV-37. The discrete phases in the higher shear stress region near the wall exhibit a finer morphology.

C.2. Discussion

In Figures IV-28 to IV-30 and IV-35, comparisons are mode of the phase dimensions of PE in PE-2/PS, PE-2/N6, and PE-2/PC extrudates as a function of shear stress. The variation of the morphology of the PE-2/N6 and PE-2/PC extrudates across the cross-section is a most interesting result. Attention is called to the material in the center of the cross-section. In Figures IV-36 and IV-37, the evolution in phase morphologies for the PE-2/N6-50/50 blends and PE-2/PC-50/50 blends are observed. The increase in phase dimensions compared with the extrudates from the static mixer is clear. This recalls Liang et al.'s experiments of phase growth of PP islands in PP/N6 blends. Observation for similarly prepared polyethylene-polystyrene blends show much more fine-grained morphologies (1-10μ) even if the

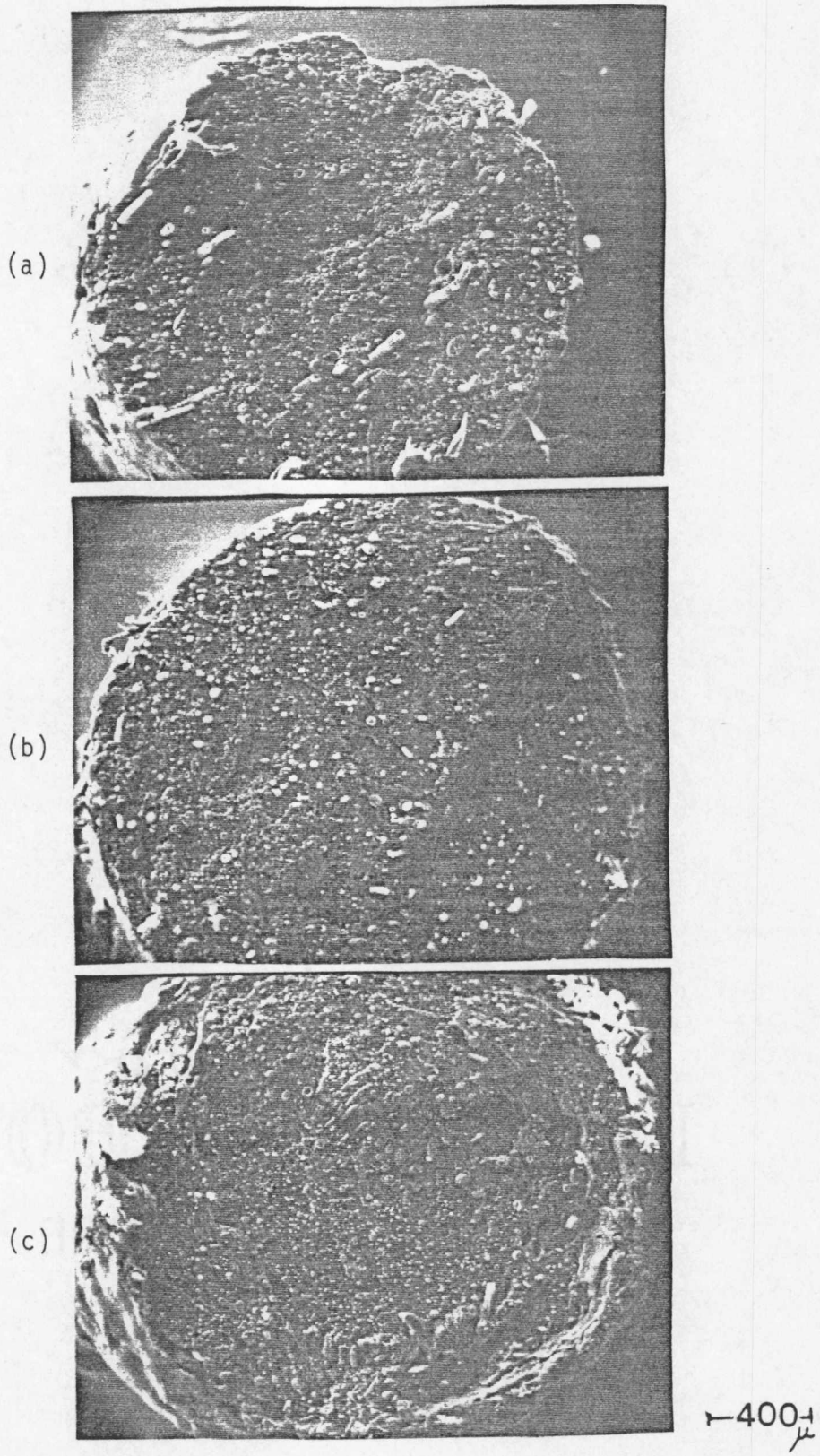


Figure IV-31. SEM microphotographs of PE-2/N6-70/30 blend extrudate as a function of die wall shear rate: (a) 2.4 sec^{-1}; (b) 11.7 sec^{-1}; (c) 62.7 sec^{-1}.

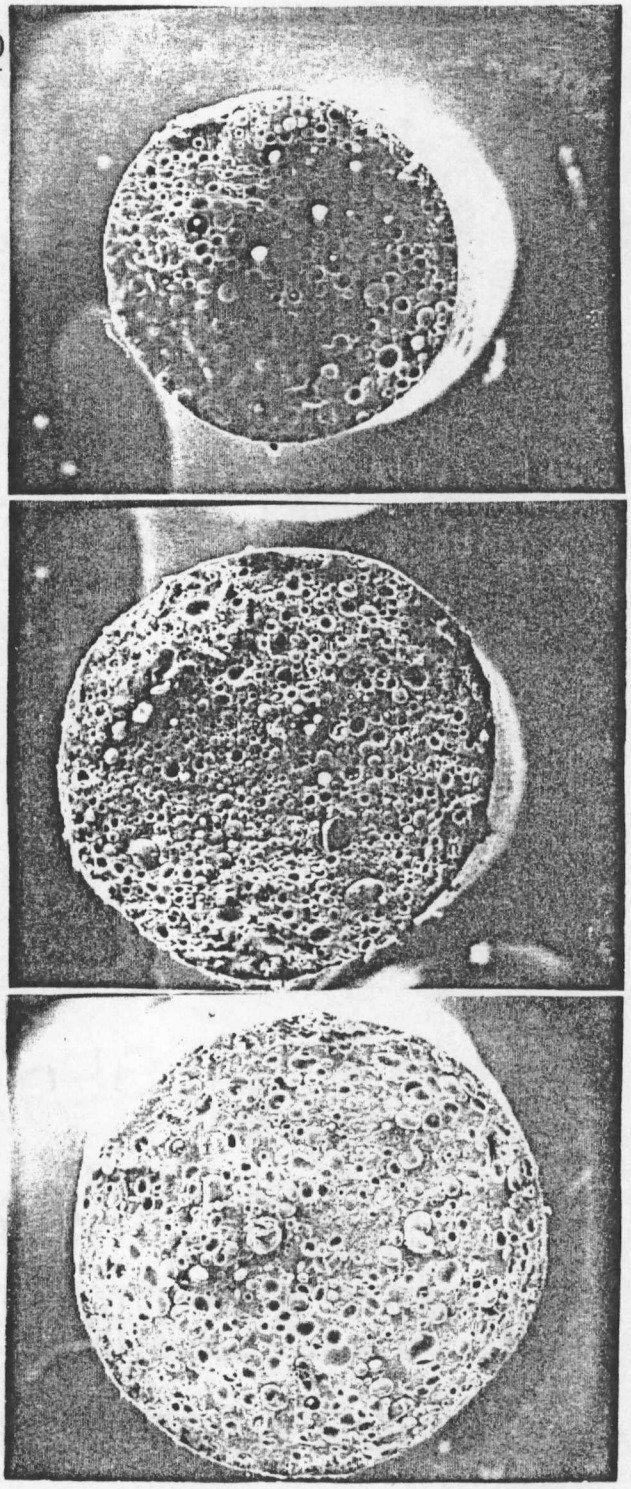


Figure IV-32. SEM microphotographs of PE-2/N6-30/70 blend extrudate as a function of wall shear rate: (a) 2.2 sec^{-1}; (b) 10.6 sec^{-1}; (c) 56.0 sec^{-1}.

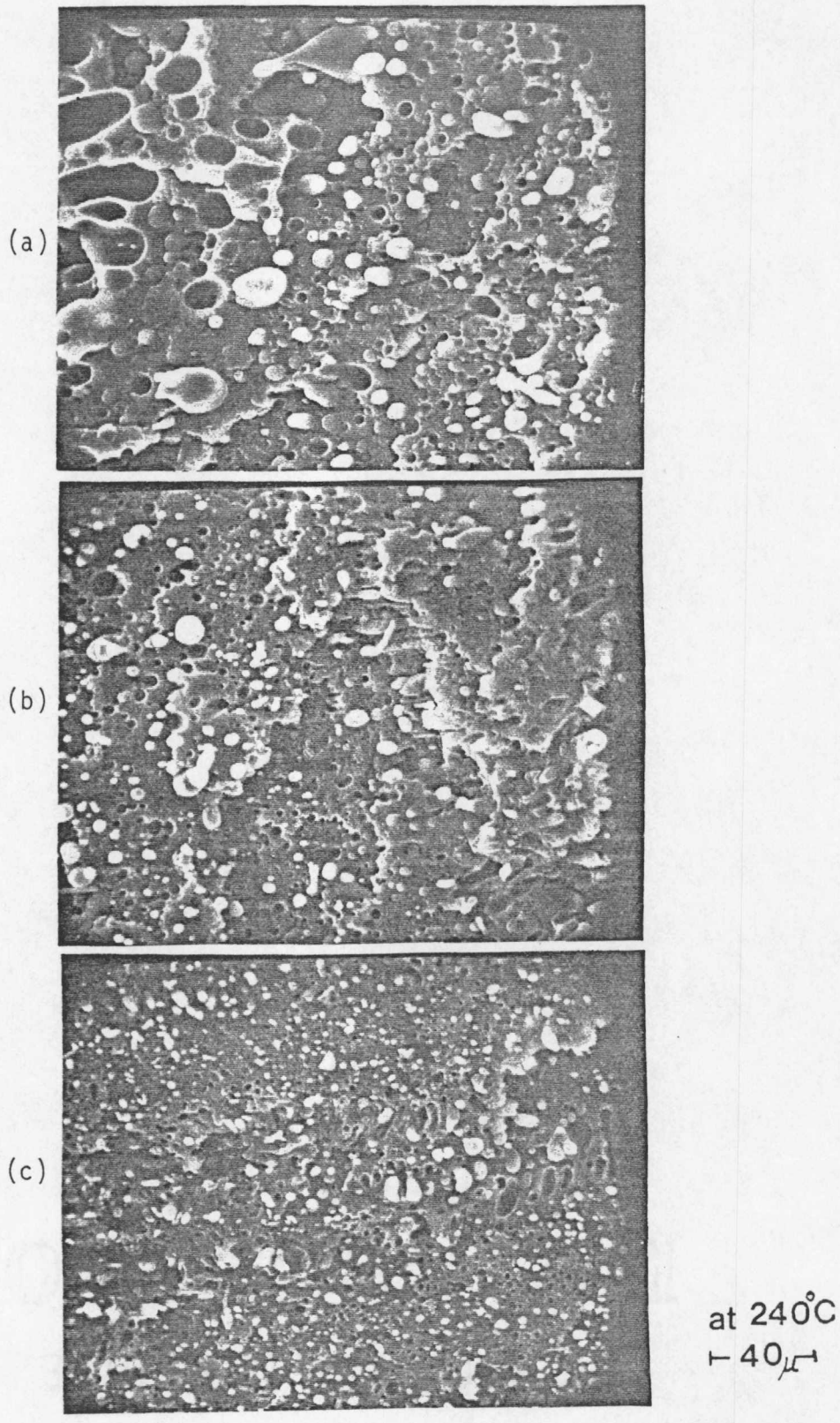


Figure IV-33. SEM microphotographs of PE-2/PC-70/30 blend extrudate as a function of die wall shear rate: (a) 2.2 sec^{-1}; (b) 11.3 sec^{-1}; (c) 56.0 sec^{-1}.

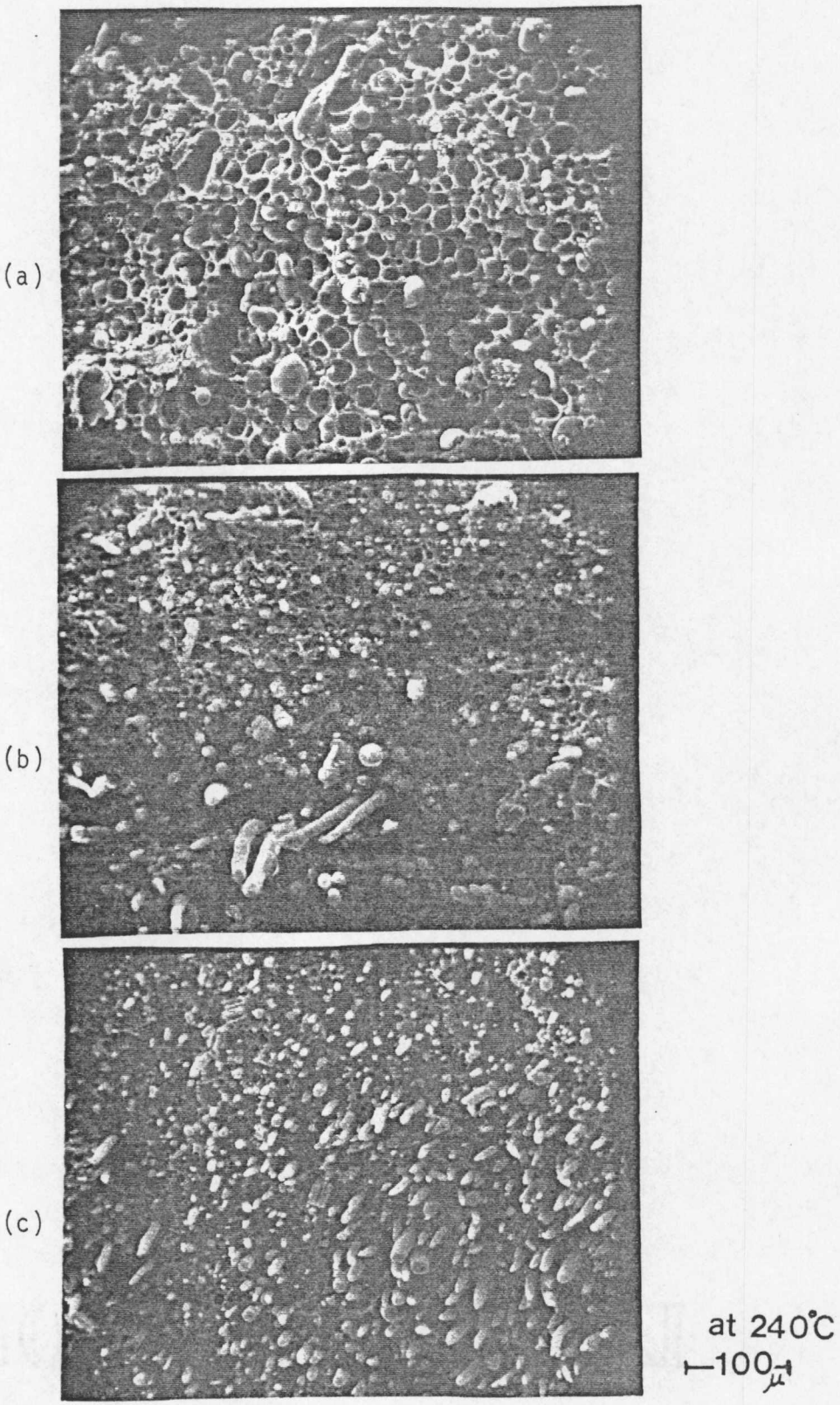
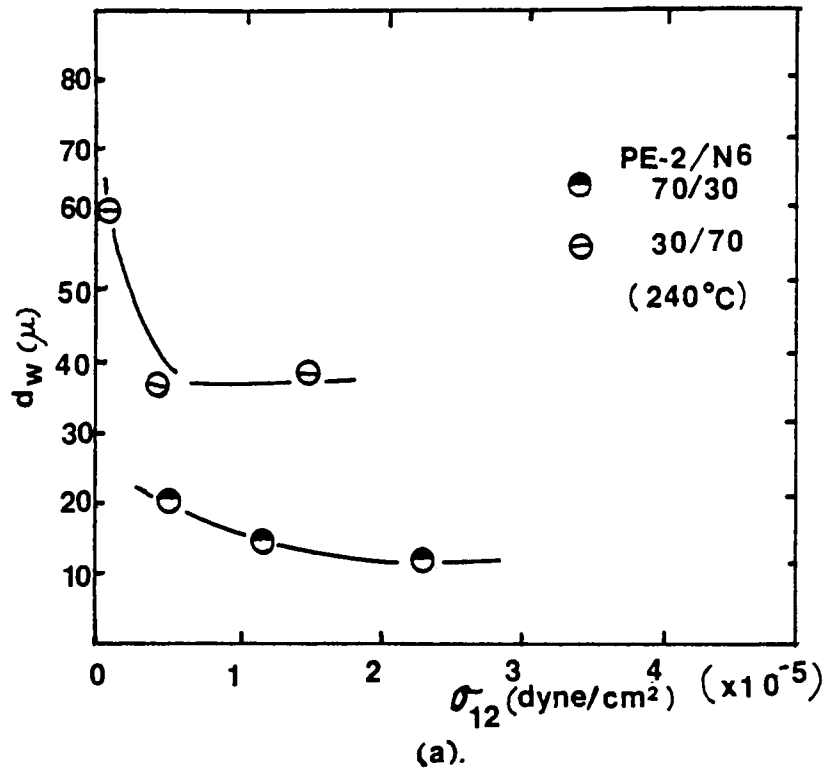


Figure IV-34. SEM microphotographs of PE-2/PC-30/70 blend extrudate as a function of die wall shear rate: (a) 2.2 sec^{-1}; (b) 10.9 sec^{-1}; (c) 56.0 sec^{-1}.



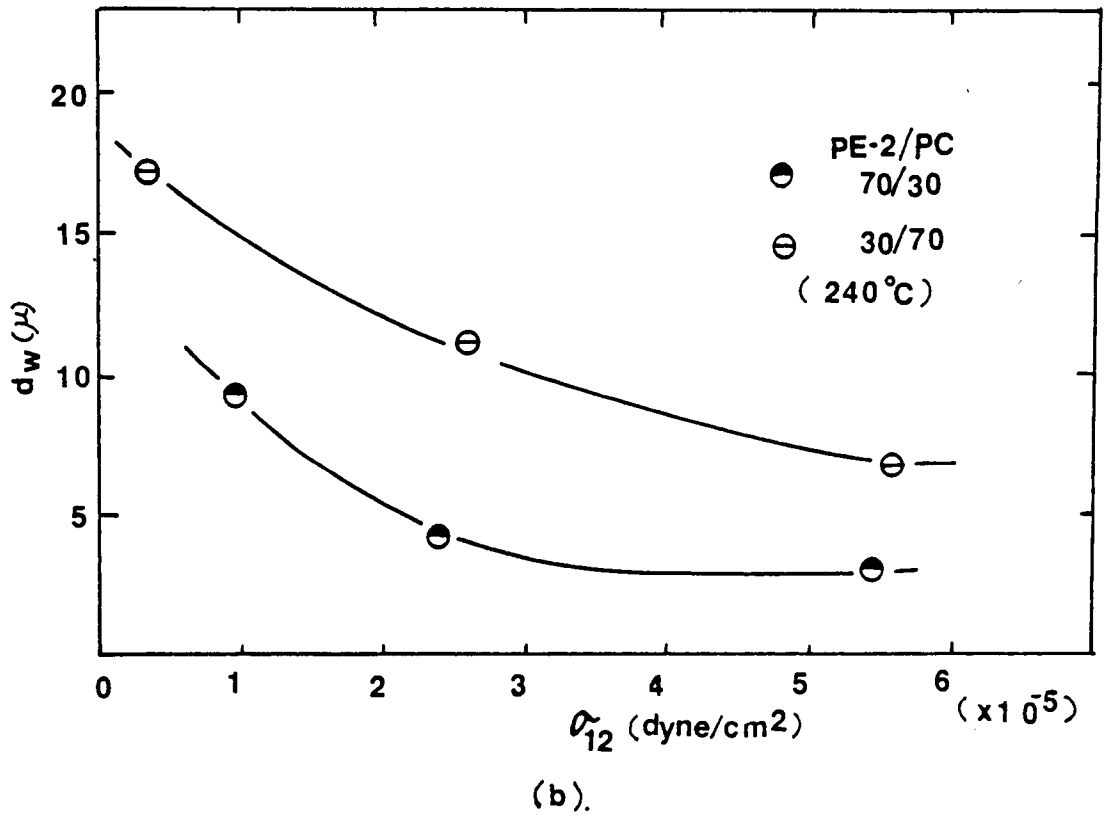


Figure IV-35. Mean dimension of discrete phase in (a) PE-2/N6 and (b) PE-2/PC blends as a function of die shear stress (σ_{12}).

Table IV-9. The influence of extrusion conditions on discrete size extruded from capillary

Composition	$\dot{\gamma}_{NW}$ (sec^{-1})	σ_{12} ($dyne/cm^2$)	Size (d_n (μ))	Size (d_w (μ))
[A] PE-2/N6				
70/30	2.4	5.07×10^4	15.0	20.5
	11.7	1.14×10^5	10.98	14.82
	62.7	2.26×10^5	8.52	11.92
30/70	2.2	9.75×10^3	44.0	61.6
	10.6	4.44×10^4	34.16	36.6
	56.0	1.52×10^5	33.32	34.92
[B] PE-2/PC				
70/30	2.24	9.58×10^4	6.56	8.48
	11.3	2.34×10^5	3.82	4.79
	56.0	5.46×10^5	2.33	3.20
30/70	2.21	8.77×10^4	16.27	17.76
	10.9	2.85×10^5	8.56	11.36
	56.0	7.41×10^5	6.04	6.65

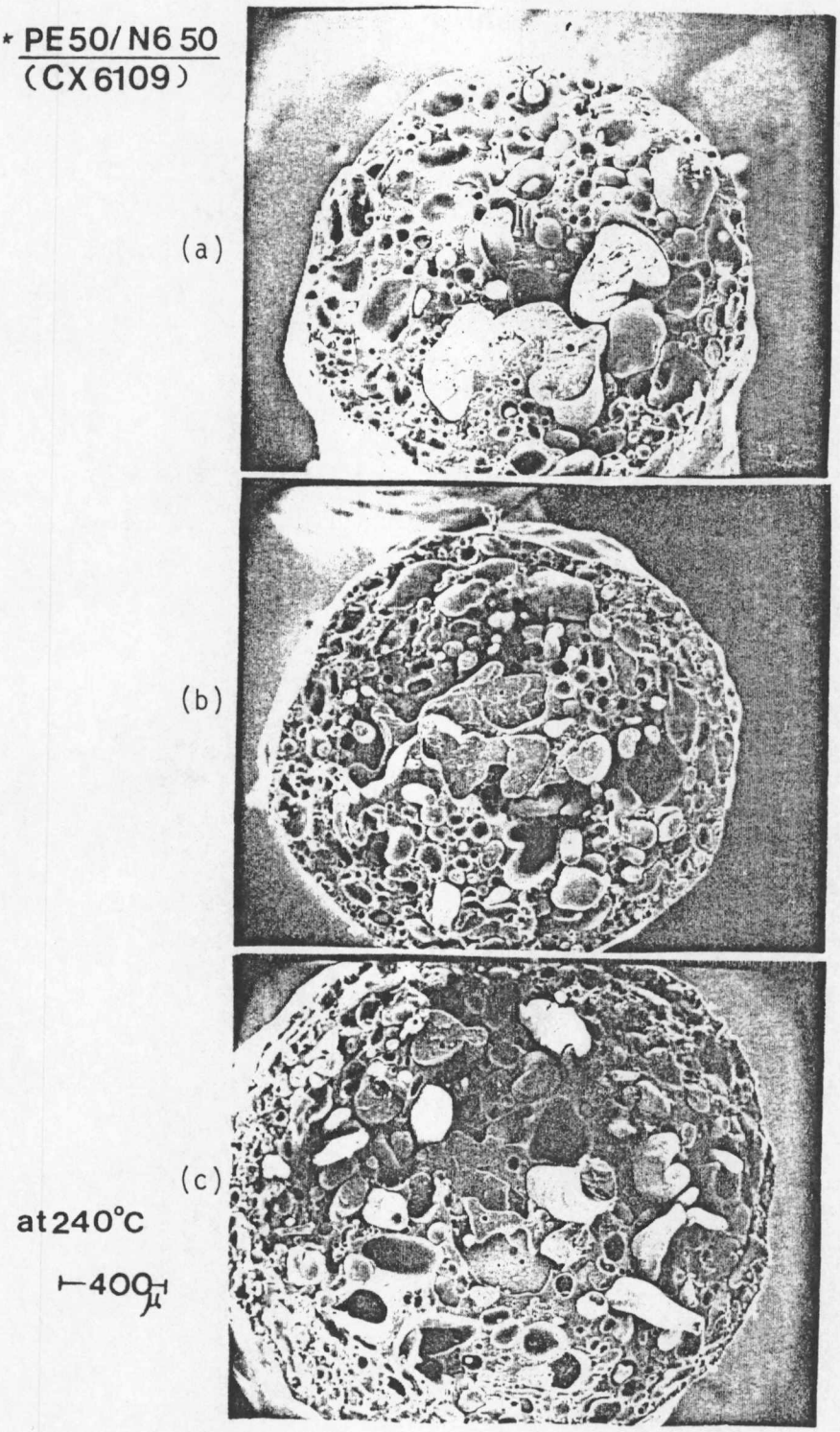


Figure IV-36. SEM microphotographs of PE-1/N6-50/50 blend extrudate as a function of die wall shear rate: (a) 2.1 sec^{-1}; (b) 10.9 sec^{-1}; (c) 57.1 sec^{-1}.

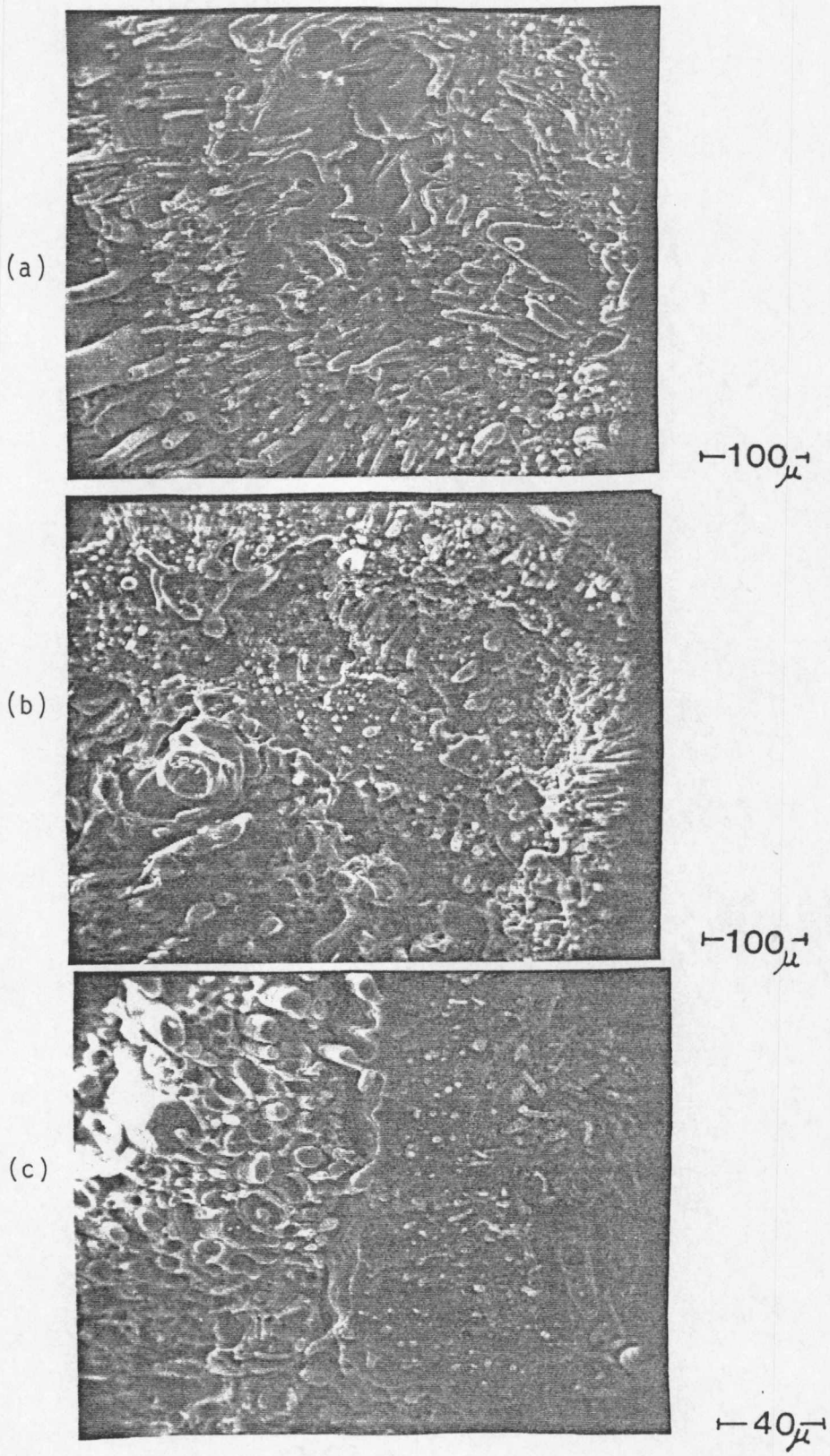


Figure IV-37. SEM microphotographs of PE-2/PC-50/50 blend extrudate as a function of die wall shear rate: (a) 2.3 sec^{-1}; (b) 12.0 sec^{-1}; (c) 57.4 sec^{-1}.

viscosity ratio was varied. In Figure IV-38, the various types of dispersion were explored. For the series of polyethylene-polystyrene blends, the transition from type I to type II, shown in Figure IV-33, was dependent on the composition, viscosity, and temperature, but independent of the time, shear rate, or shear stress. For the PE-2/N6 and PE-2/PC, it was dependent on the composition, the time, the shear rate, or shear stress.

The phases in 50/50 blends showed a transition from type II to type III with increasing shear rate or shear stress. Comparison of the various blends suggests through the coarseness of the morphology that the phase growth is greatest for the PE-2/N6-50/50 blend followed by the PE-2/PC-50/50 blend.

The phase growth can be considered from the view of thermodynamics. As described in Chapter II, Section A, the Gibbs free energy per unit volume of mixture can be represented by

$$\Delta\bar{G}_m = \Delta\bar{H}_m - \bar{T}\Delta S_m$$

For incompatible blends, $\Delta\bar{G}_m > 0$ and $\Delta\bar{S}_m$ is negligible. Thus

$$\Delta\bar{G}_m \simeq \Delta\bar{H}_m \qquad \text{and} \qquad \Delta\bar{H}_m = A\Delta W \tag{IV-1}$$

where ΔW is the interfacial contact energy between the two components and A is the area of dispersed component. With increasing shear rate or shear stress, the free energy may be represented by

$$G - G_o = \Delta G = (A - A_o)\Delta W \tag{IV-2}$$

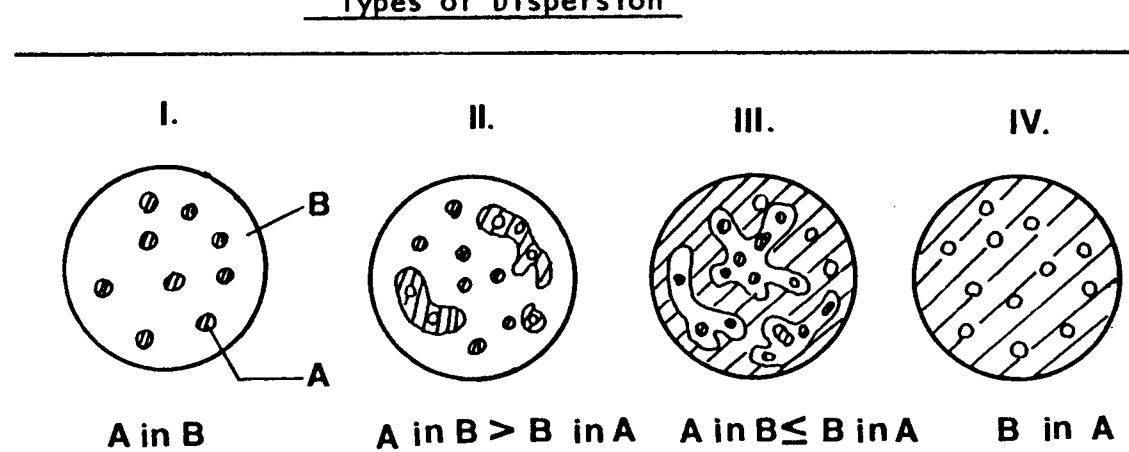


Figure IV-38. The scheme of types of dispersion.

where A_o is the initial surface area and A is the stressed surface area. For PE-2/N6 and PE-2/PC-50/50 blends, the surface area A increased with increasing shear stress. It is clear that with increasing surface area, the free energy is increasing and the incompatibility increases.

We can discuss this phenomenon using Vinogradov (173) and Liang et al.'s (90) interpretation of the mechanism of transient phase growth as associated with the interfacial tension, κ, between the phases. This should lead to stresses of form κ/d where d represents a radius of curvature which will be of the same order as the dimensions of the island. The resistance to interfacial movement will be due to the viscosity η of the continuous phase. This is of form $\eta V/d$ where V is a velocity. The tendency of different blend systems towards phase growth is determined by the ratio of these stresses

$$\frac{\text{Interfacial Stresses}}{\text{Viscous Stresses}} = \frac{\kappa/d}{\eta V/d} = \frac{\kappa}{\eta V} \qquad \text{(IV-3a)}$$

This dimensionless group is well known in the theory of Newtonian fluid. It arises in investigations of formation of droplets by the breakup or the thin thread (160)(161)(167)(168). It is useful to write equation (IV-1) in the form:

$$\frac{\kappa}{\eta \bar{V}} \simeq \frac{\kappa}{\eta \dot{\gamma} d} \simeq \frac{\kappa}{\sigma_{12} d} \qquad \text{(IV-3b)}$$

Phase growth may be promoted by large interfacial tensions, small shear stresses, and small phase dimensions. Phase size reduction may

be promoted by large shear stresses and phase dimensions and be opposed by the interfacial tension.

Various investigators (127)(128)(136)(199) reported the interfacial tensions and surface tensions. The interfacial tensions for PE-PS and PE-N6 have been described in the literature. They give PE/PS of 5 dynes/cm (198) and for PE-N6 of 15 dynes/cm (127)(128). We are able to correlate our data for dispersed phase dimensions as a function of κ/σ_{12}. We assume that the interfacial tension of PE/PS systems is 0.8 dyne/cm, 15 dyne/cm for PE/PC and 30 dyne/cm for PE/N6. This is shown in Figure IV-39.

D. FIBRILLATION IN FLOW THROUGH THE CAPILLARY

D.1. Results

Droplets in the melt blend become threads with extrusion rate increases. The longitudinal sections of polyethylene-polystyrene blends extrudate from the capillary rheometer at 180°C were observed by SEM. The SEM microphotographs are shown in Figures IV-40 through IV-48. Figures IV-40 to IV-42 show the rods whose diameter decreased with increasing shear stress for PE-2/PS-70/30 to 30/70. The mode of droplet-fiber for motion is independent of the composition. The dispersed polyethylene droplets in a polystyrene matrix can be made into thinner thread with increasing shear rate or shear stress. These thin threads are arranged along the flow direction and continuous.

Three types of droplet-fiber transition are found with increasing shear stress. These are undulant diameter thin thread

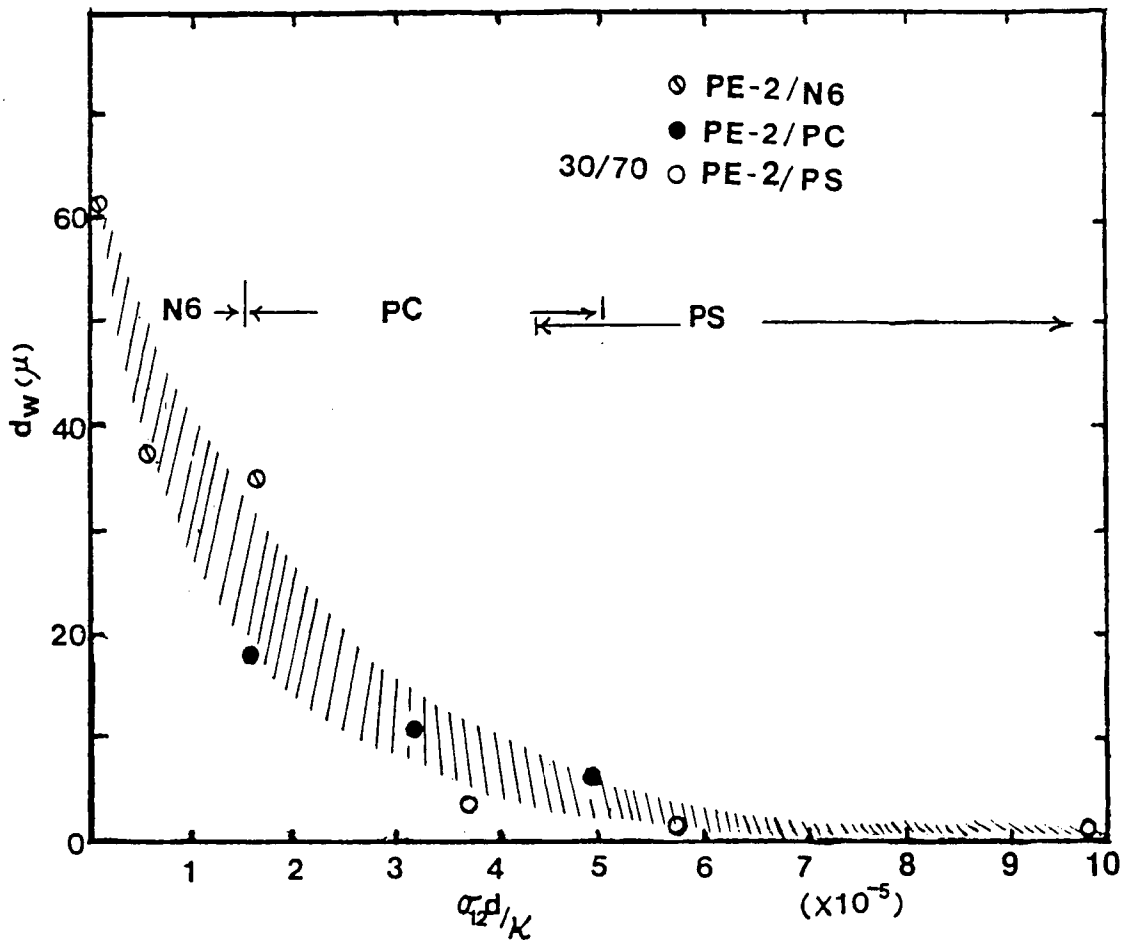


Figure IV-39. The comparisons of the discrete phase size as a function of the dimensionless parameter ($\sigma_{12}d/\kappa$).

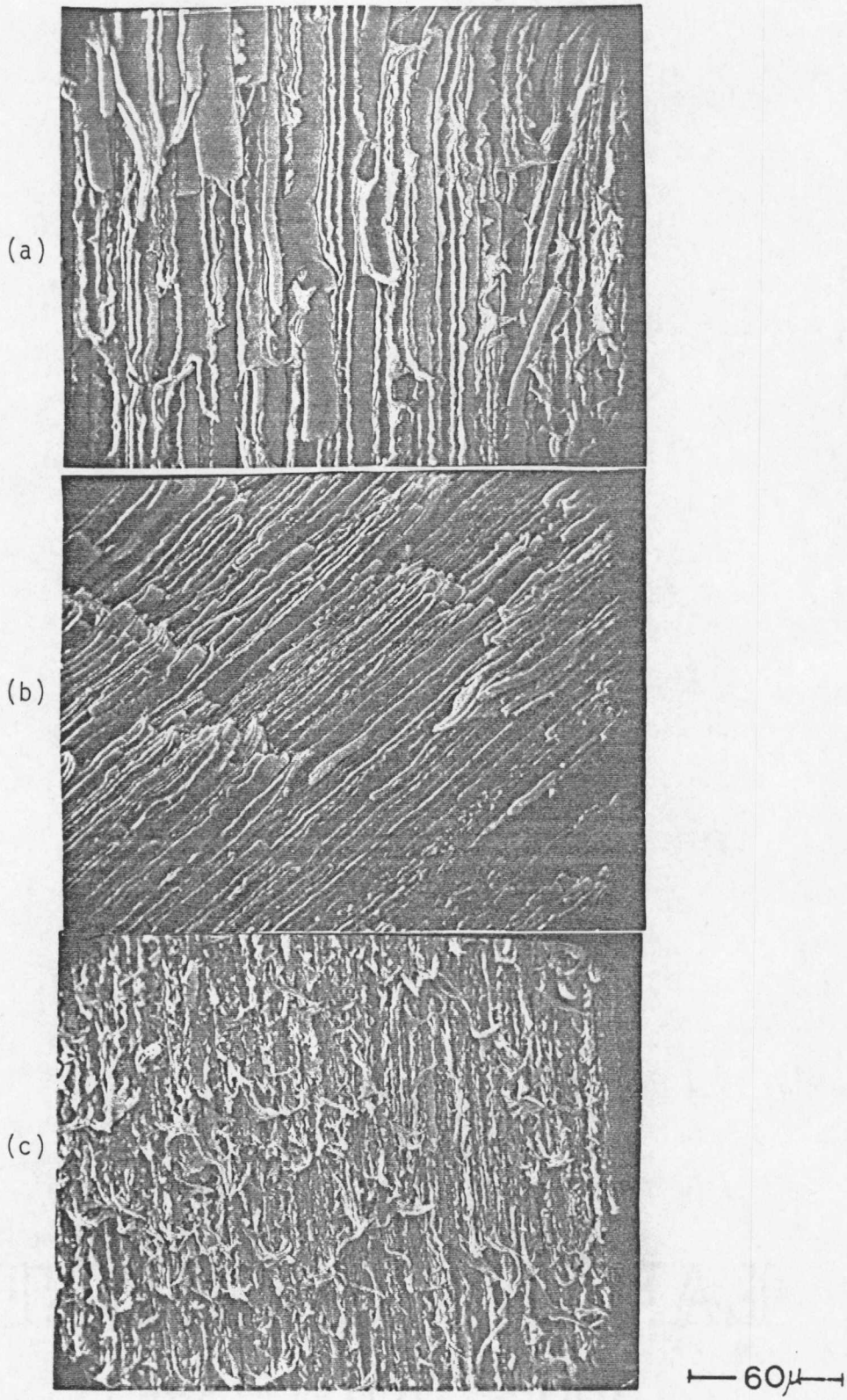


Figure IV-40. SEM microphotographs of longitudinal sections of PE-2/PS-70/30 blend extrudates as a function of die wall shear rate: (a) 2.3 sec^{-1}; (b) 12.2 sec^{-1}; (c) 69.6 sec^{-1}.

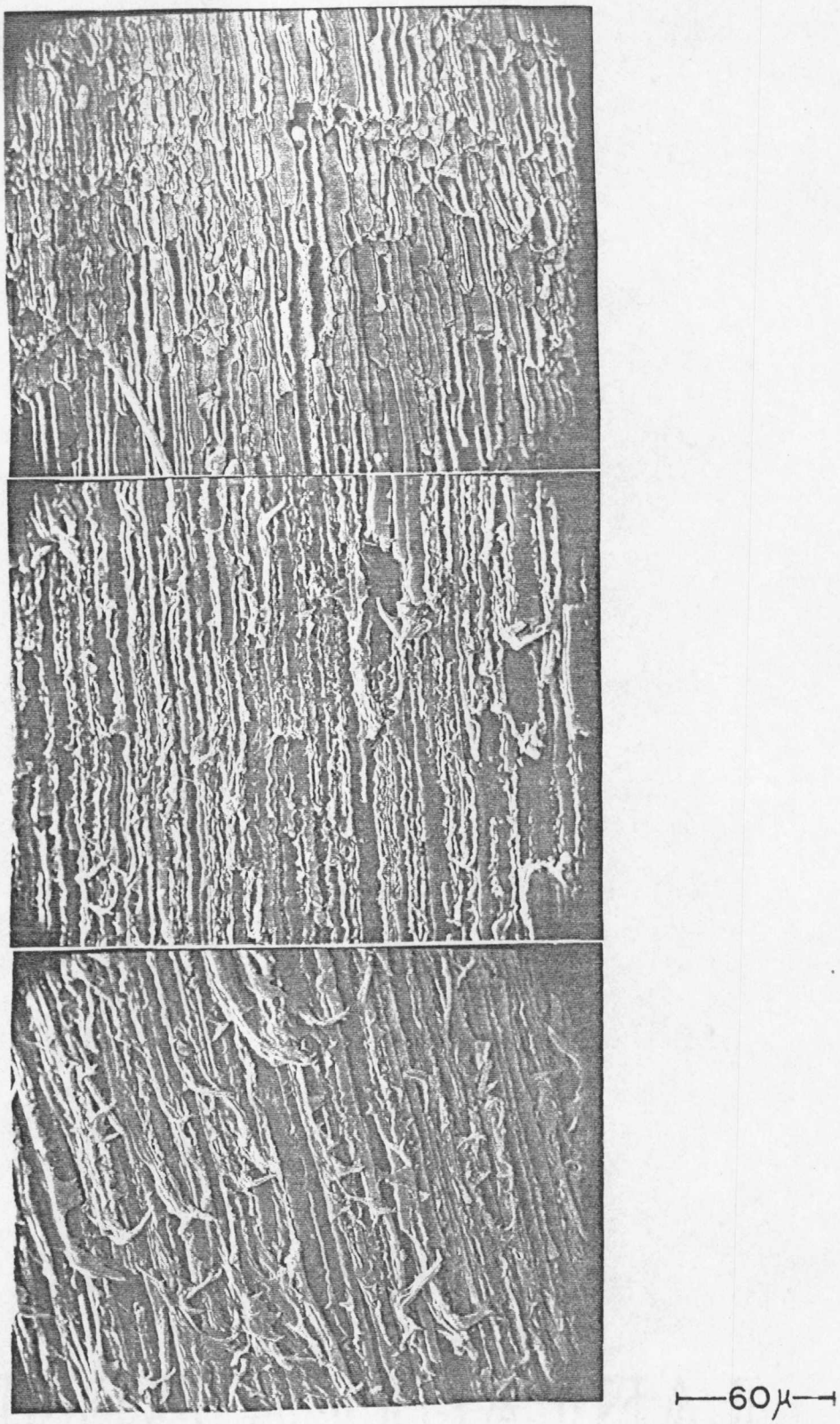


Figure IV-41. SEM microphotographs of longitudinal sections of PE-2/PS-50/50 blend extrudates as a function of die wall shear rate: (a) 2.0 sec^{-1}; (b) 11.0 sec^{-1}; (c) 70.8 sec^{-1}.



Figure IV-42. SEM microphotographs of longitudinal sections of PE-2/PS-10/90 blend extrudates as a function of die wall shear rate: (a) 2.2 sec^{-1}; (b) 12.2 sec^{-1}; (c) 52.8 sec^{-1}.

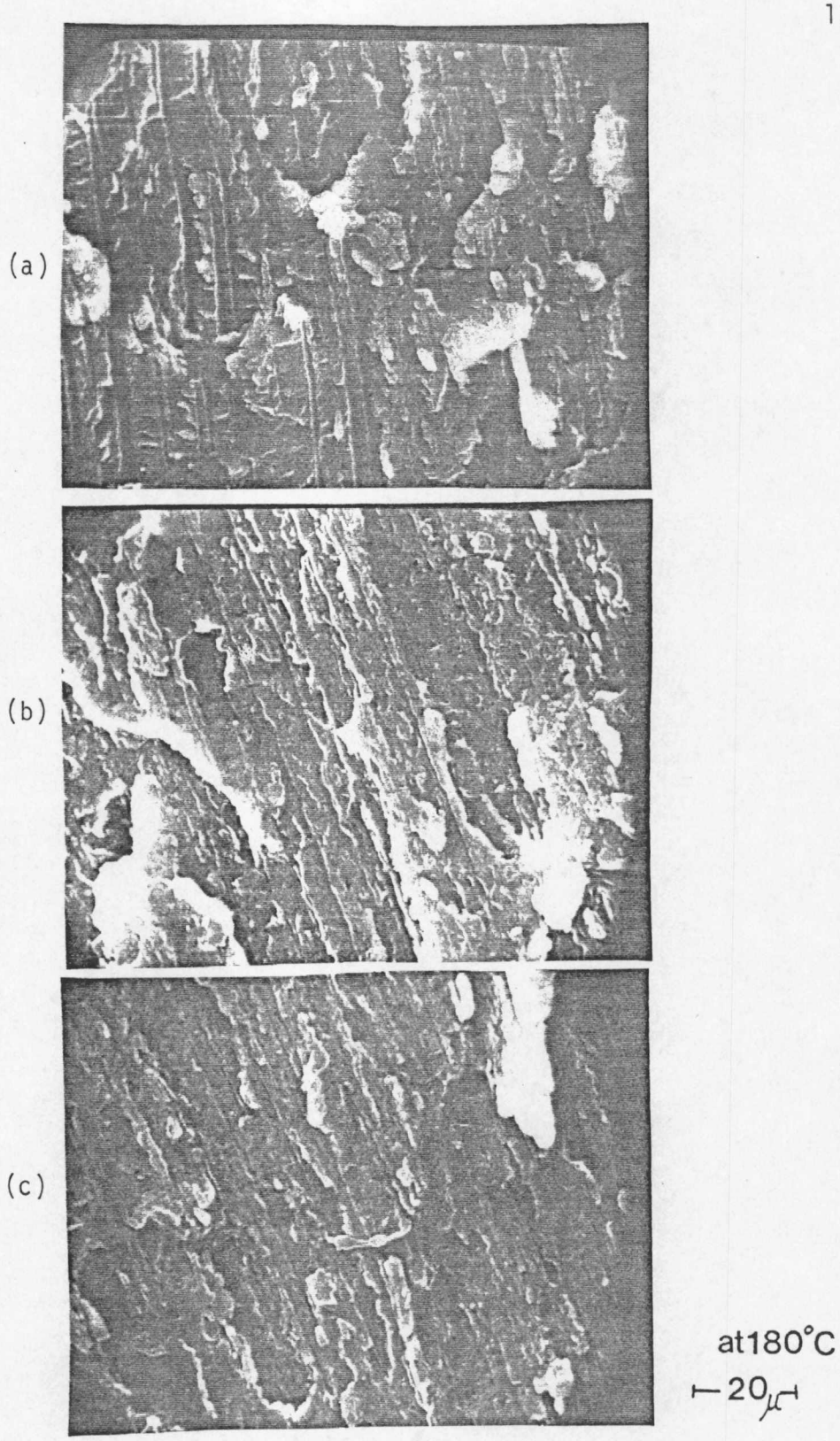


Figure IV-43. SEM microphotographs of longitudinal sections of PE-1/PS-10/90 blend extrudates as a function of viscosity ratio: η_d/η_m: (a) 0.81; (b) 0.56; (c) 0.42.

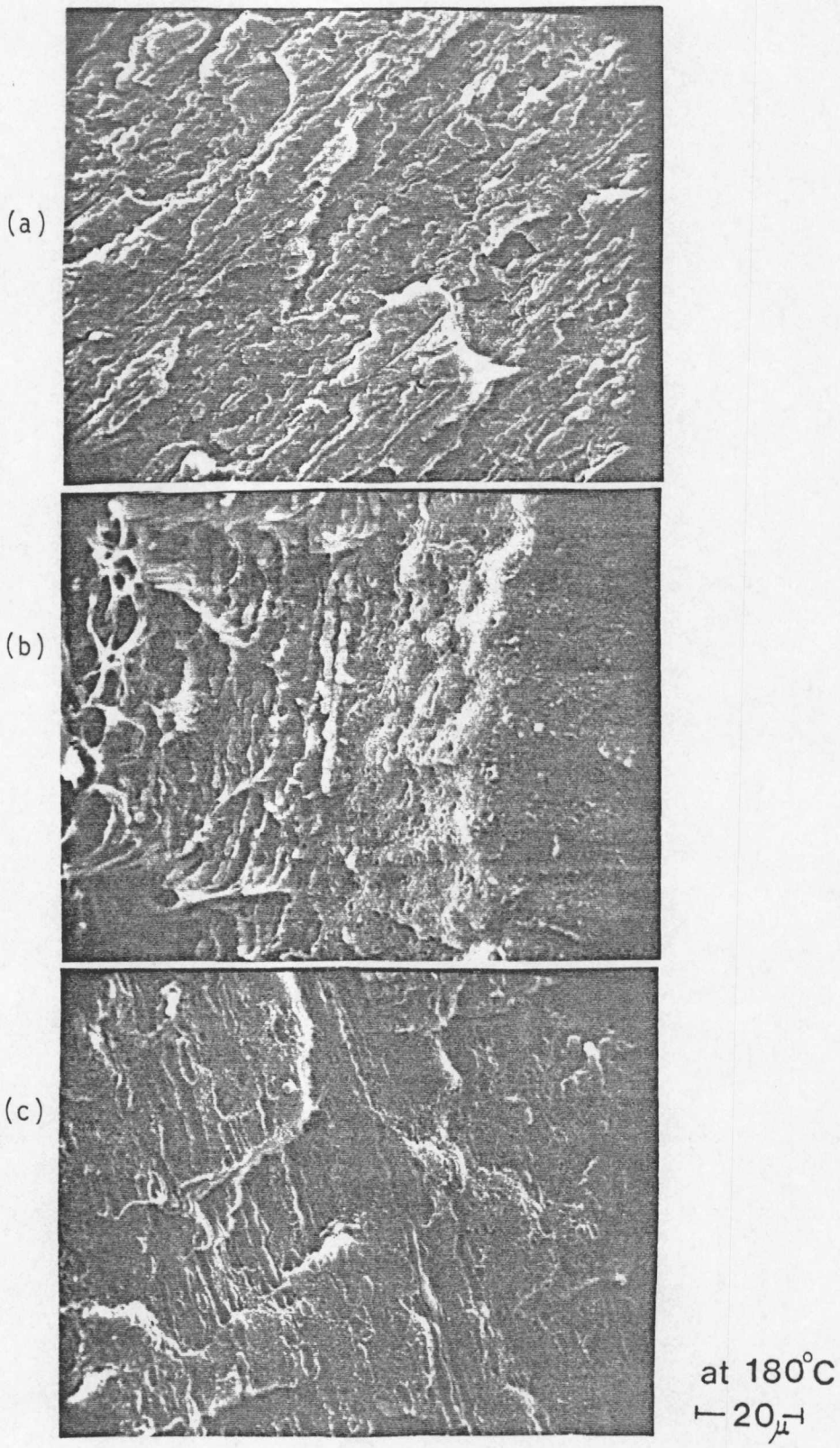


Figure IV-44. SEM microphotographs of longitudinal sections of PE-1/PS-90/10 blend extrudates as a function of viscosity ratio η_d/η_m: (a) 1.93; (b) 1.51; (c) 1.38.

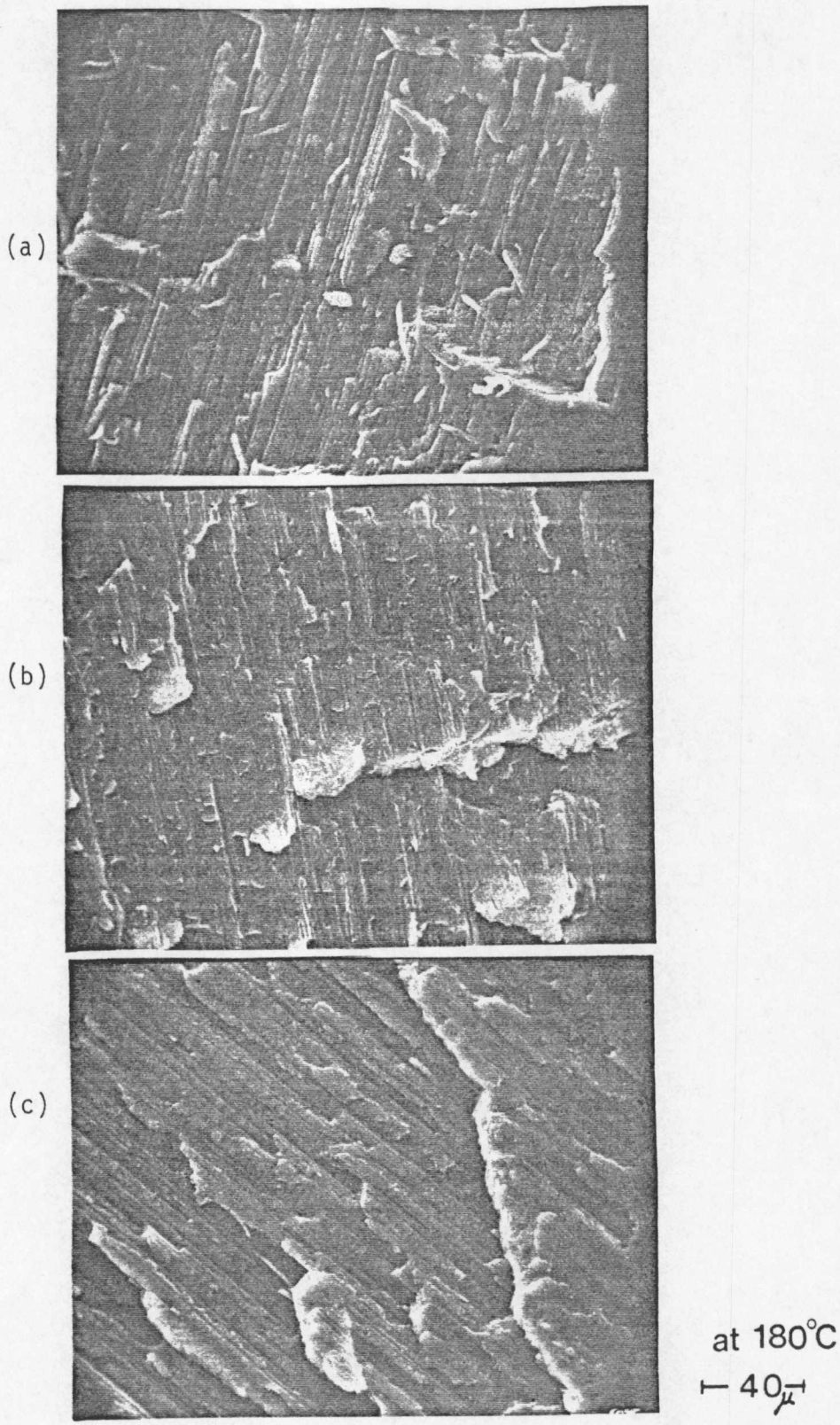


Figure IV-45. SEM microphotographs of longitudinal cross section of PE-3/PS-10/90 blend extrudates as a function of viscosity ratio: η_d/η_m: (a) 0.45; (b) 0.37; (c) 0.27.

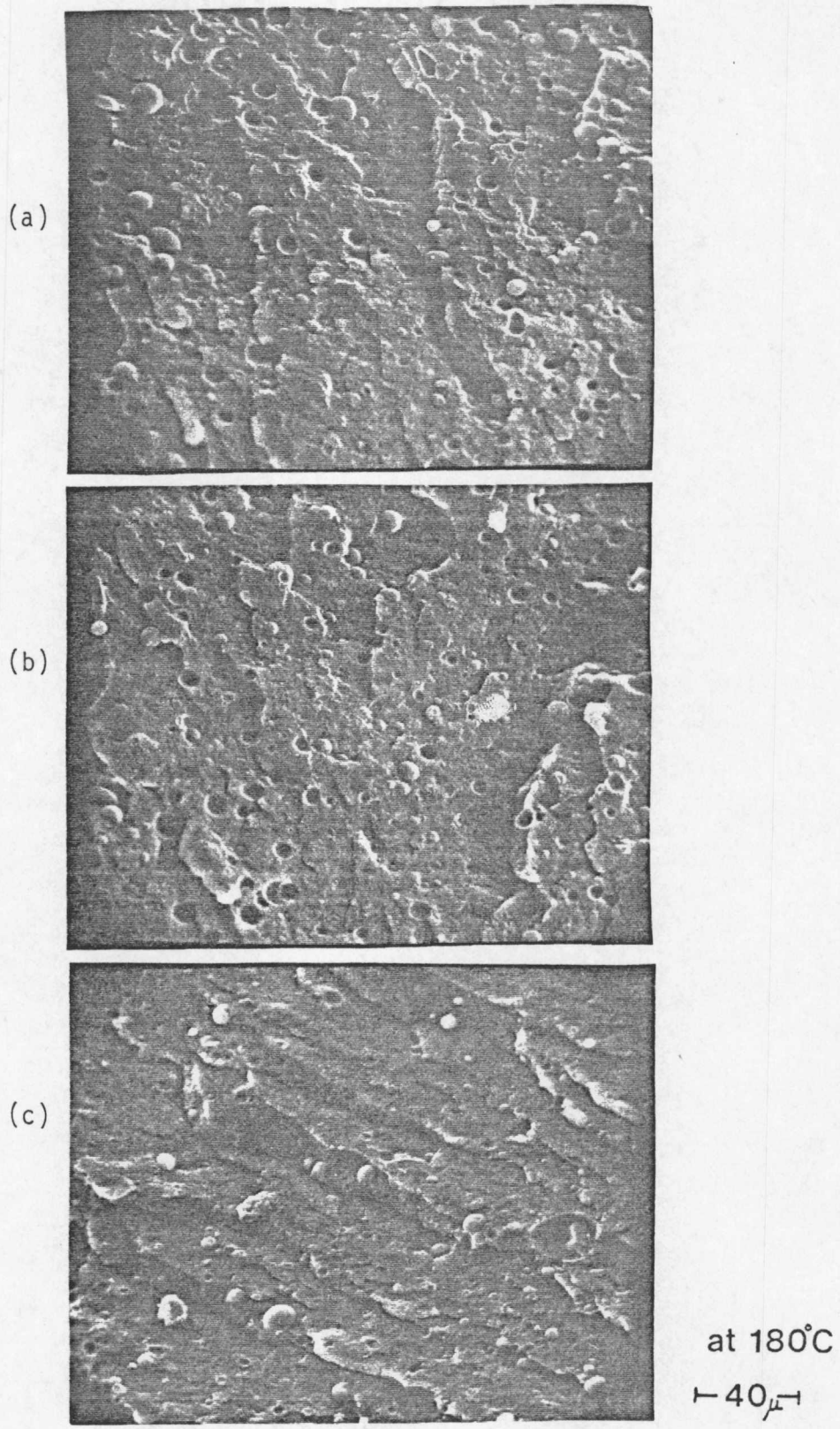


Figure IV-46. SEM microphotographs of longitudinal sections of PE-3/PS-90/10 blend extrudates as a function of viscosity ratio: η_d/η_m: (a) 2.22; (b) 2.71; (c) 3.66.

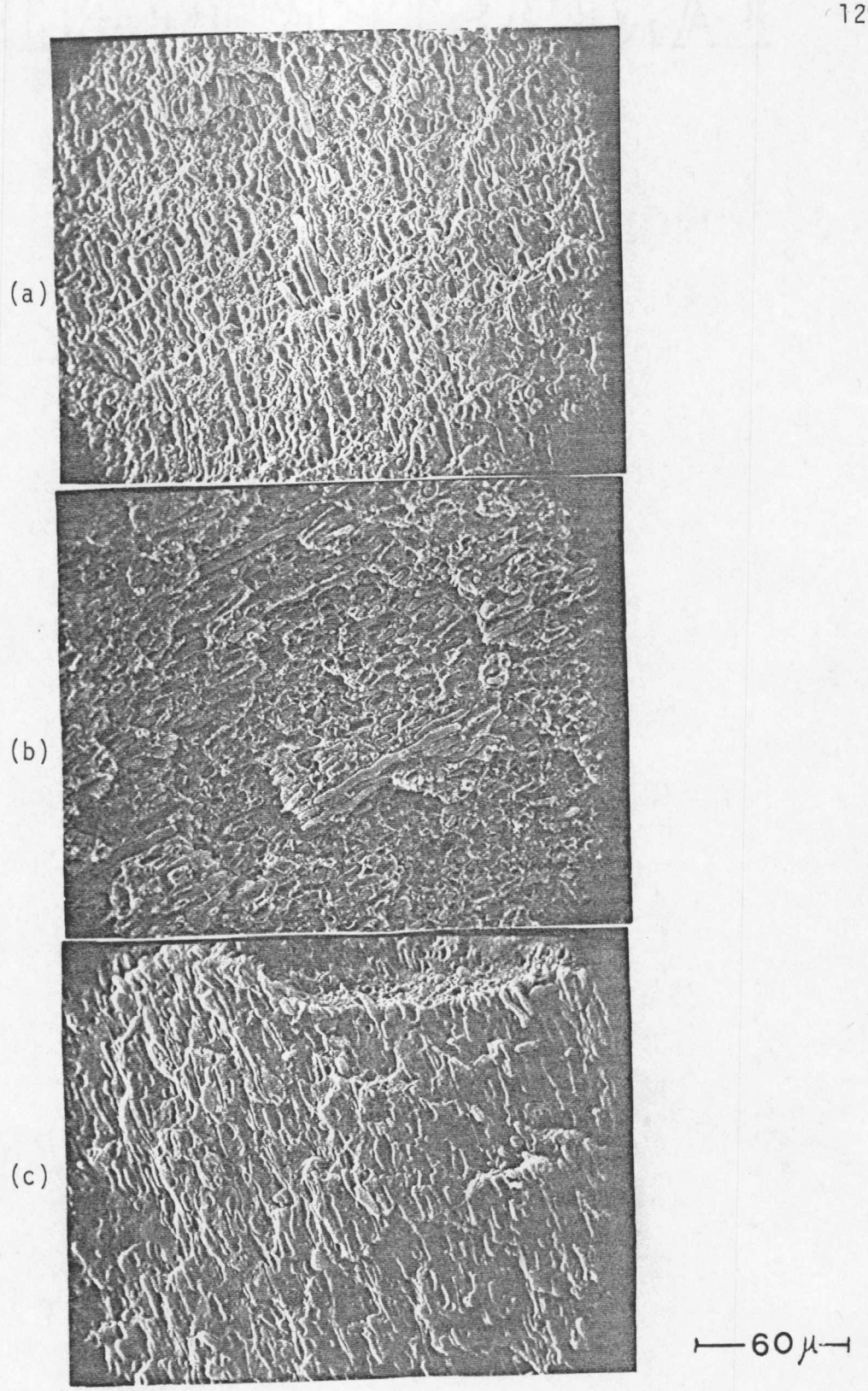


Figure IV-47. SEM microphotographs of longitudinal sections of PE-2/PS-90/10 blend extrudates as a function of viscosity ratio: η_d/η_m: (a) 1.93; (b) 1.51; (c) 1.38.

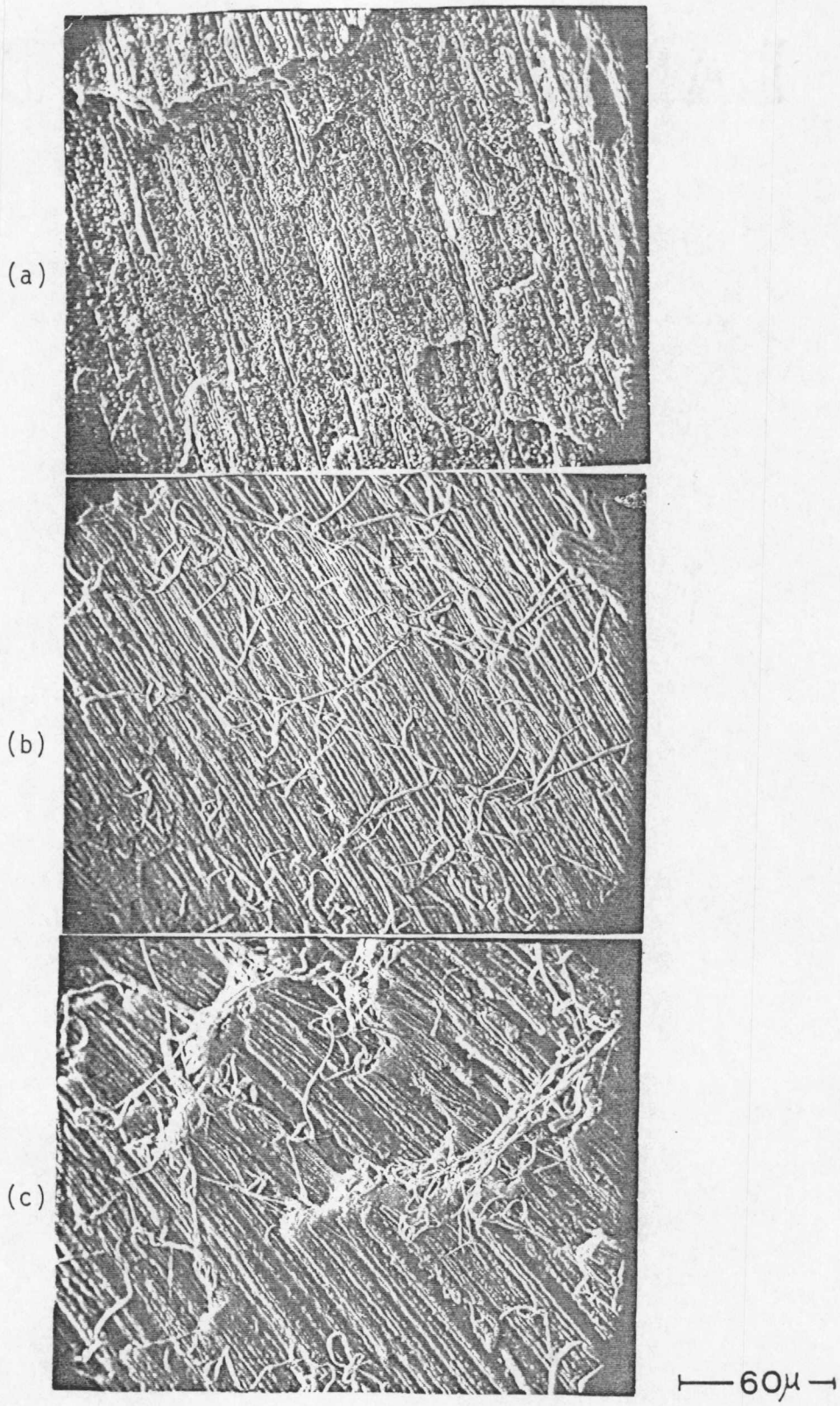


Figure IV-48. SEM microphotographs of longitudinal cross section of PE-2/PS-10/90 blend extrudates as a function of viscosity ratio: η_d/η_m: (a) 0.52; (b) 0.66; (c) 0.72.

or rods, smooth thin thread (infinite), spheres (non-deformation). (See Table IV-10.)

The PE-1/PS-10/90 and 90/10 formed thin threads, but they are undulant in diameter and unstable (Figures IV-43 and IV-44). The PE-3/PS-10/90 formed very smooth thin fibrils in Figure IV-45. However, PE-3/PS-90/10 did not form fibrils in Figure IV-46. The PE-2/PS-90/10 and 10/90 have similar droplet-fiber formation behavior to the PE-3/PS systems (Figures IV-47 and IV-48).

D.2. Discussion

The droplet-to-fiber transition in Newtonian fluids was studied by various investigators (27)(160)(161)(167)(168)(170). They note that the major parameter for fiber formation was the viscosity ratio of the dispersed fluid to the medium. Tsebrenko and Vinogradov et al. (171)(172)(173) investigated fibrillation for POM/copolyamide systems. They reported that if the viscosity ratio was close to unity, a uniform thin thread fibril was formed.

Two dimensionless parameters, $\kappa/d\sigma_{12}$ and $\eta(\dot{\gamma}_w)_{dispersed}/\eta(\dot{\gamma}_w)_{matrix}$, are listed in Table IV-10 for polyethylene-polystyrene blends. The series of PE/PS systems could be assumed to have the same initial diameters and the same interfacial tension. Therefore, the viscosity ratio will play the most important role in deformation of droplets. Judging from Table IV-10, it can be seen that the droplets become thin smooth infinite fibers if $\lambda\ (\eta_d/\eta_m) < 0.7$ and

Table IV-10. The viscosity ratio $\eta_{dispersed}/\eta_{matrix}$ and $\kappa/\eta_m\dot{\gamma}d_w$ on the fibrillation

PE/PS Composition	Fibrillation	$\eta_{dispersed}/\eta_{matrix}$	$\kappa/\eta_m\dot{\gamma}d_w$	d_w (μ)
PE-1/PS				
10/90	thin thread (undulant)	1.2 ~ 1.3	0.37 ~ 0.76	0.4 ~ 0.8
90/10	thin rods (undulant)	0.8 ~ 1.3	0.64 ~ 1.12	0.7 ~ 1.8
PE-2/PS				
10/90	thin thread (smooth)	0.5 ~ 0.7	0.31 ~ 0.92	0.5 ~ 1.7
90/10	deformed rods or ellipsoids	1.4 ~ 1.9	0.47 ~ 0.54	1.3 ~ 2.1
PE-3/PS				
10/90	thin thread (smooth)	0.3 ~ 0.5	0.09 ~ 0.66	0.3 ~ 1.3
90/10	spheres (non-deformation)	2.2 ~ 3.7	1.0 ~ 2.0	6.5 ~ 6.9

form undulant and unstable fibers. If $0.7 < \lambda < 1.7$; further, the droplets do not deform if $\lambda > 2.2$.

It can be concluded that when the dispersed phase has less viscosity than the continuous phase, the droplets are elongated by the shear stress and form the fibrils parallel to the flow direction as shown in Figure IV-49(a). On the contrary, when the dispersed phase is more viscous than the matrix phase, the droplets are elongated to the rods with undulating or not deformed as shown in Figure IV-49(b) or IV-49(c).

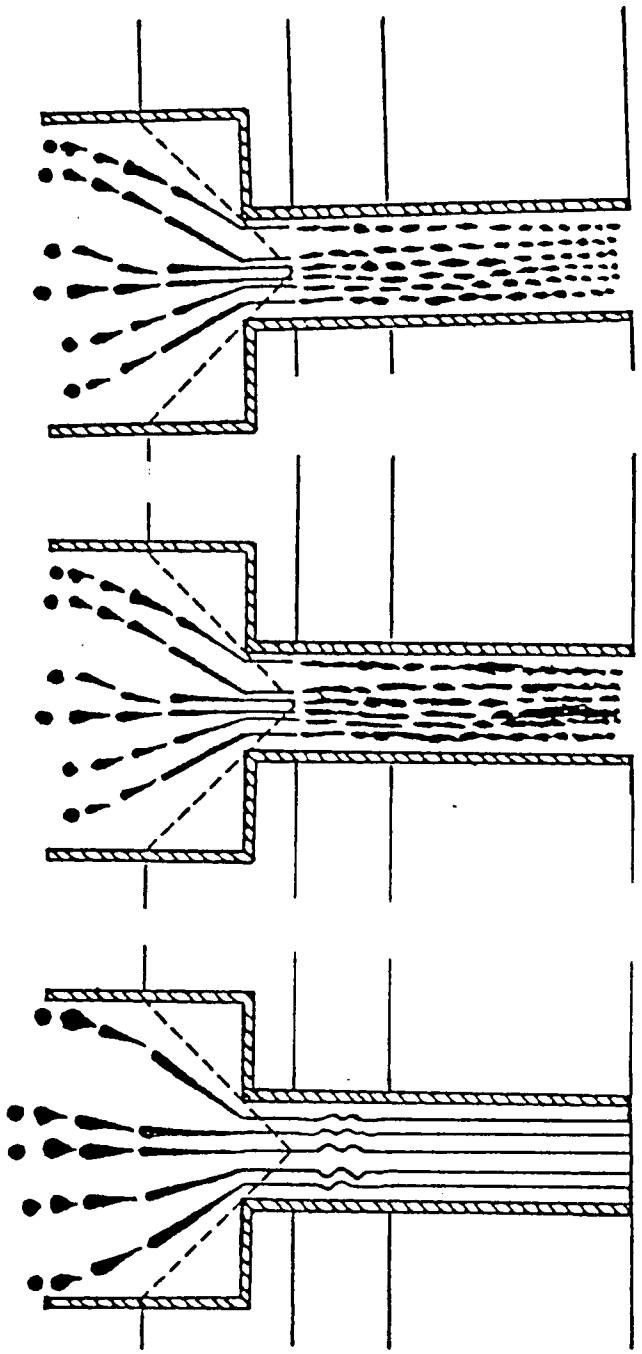


Figure IV-49. Schematic representation of droplet-fiber transformation.

CHAPTER V

RHEOLOGICAL PROPERTIES OF BLENDS

A. SHEAR VISCOSITY

A.1. Results

A.1.1. PE-PS blends. In the previous chapter, viscosity was reported as a function of shear rate for three polyethylenes and a polystyrene at 180°C in Figure IV-12 (p. 79). One of them, PE-2, is similar in viscosity level to that of polystyrene. The others are higher or lower than polystyrene.

Figure V-1 shows the shear viscosity as a function of the shear rate for the PE-2/PS blends. This system tends not to show a Newtonian region. The viscosity at any shear rate does not change monotonically with loading level of PE. The PE-1/PS-10/90 viscosity curve is higher than that of polystyrene at a shear rate of 10 sec^{-1} where PS has a higher viscosity than PE. Figure V-2 shows the shear viscosity as a function of the shear rate for PE-1/PS blends. The zero shear viscosity of PE-1 is about four times larger than that of PS. This blend system does not show a clear low shear rate Newtonian region. The viscosity increases monotinically with loading level of PE in the range of lower shear rates. The behavior becomes more complex at higher shear rates. Figure V-3 is a plot of the viscosity of PE-3/PS vs. shear rate. The viscosity of PE is much lower than that of polystyrene. The viscosity of the blends is found to increase

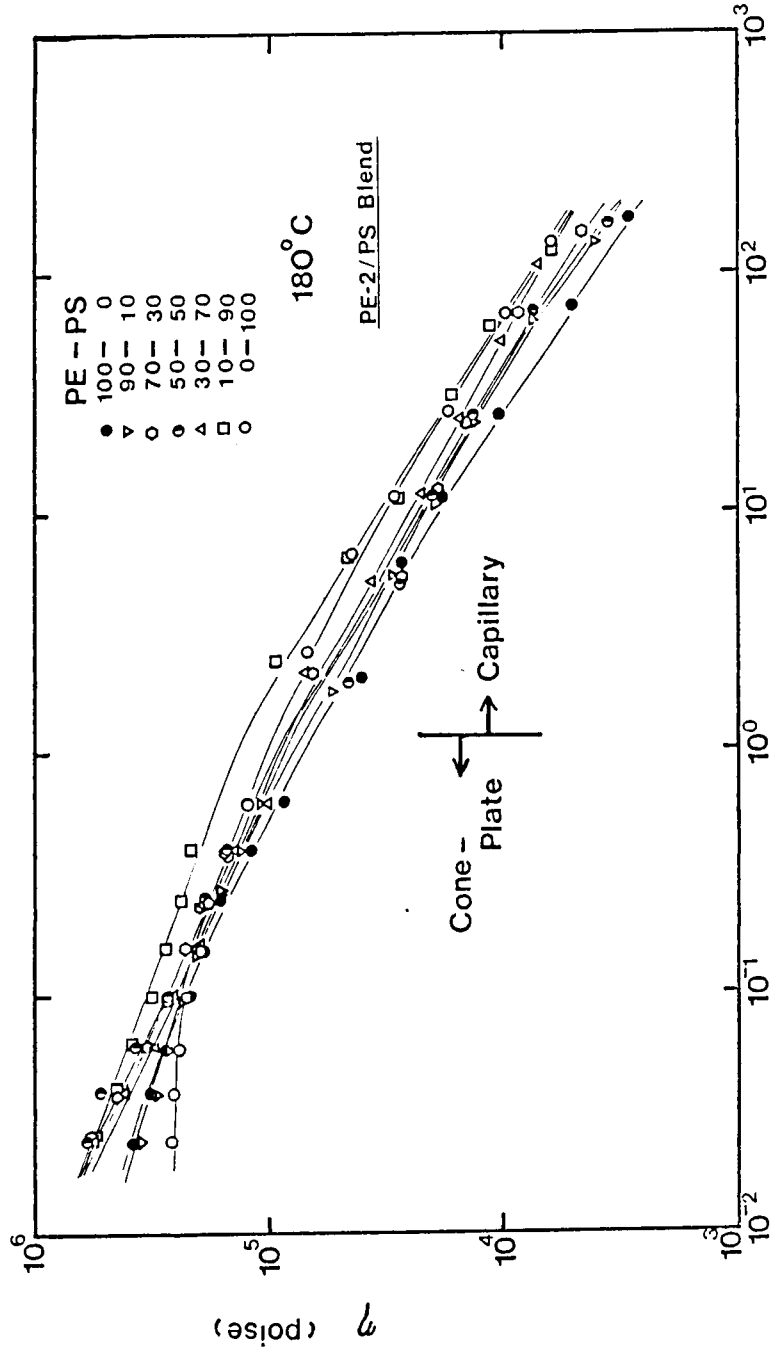


Figure V-1. Shear viscosity versus shear rate for PE-2/PS blends.

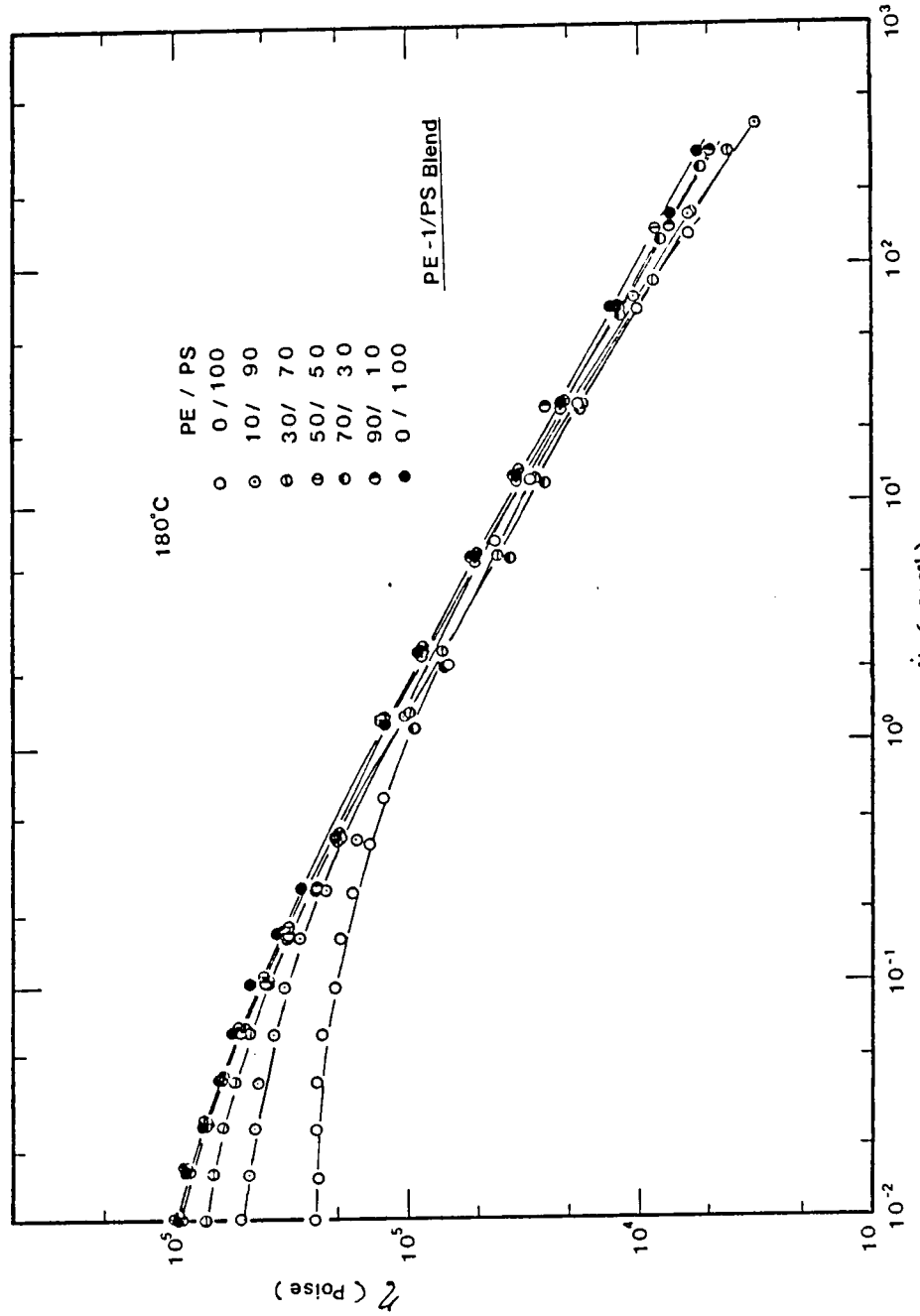


Figure V-2. Shear viscosity versus shear rate for PE-1/PS blends.

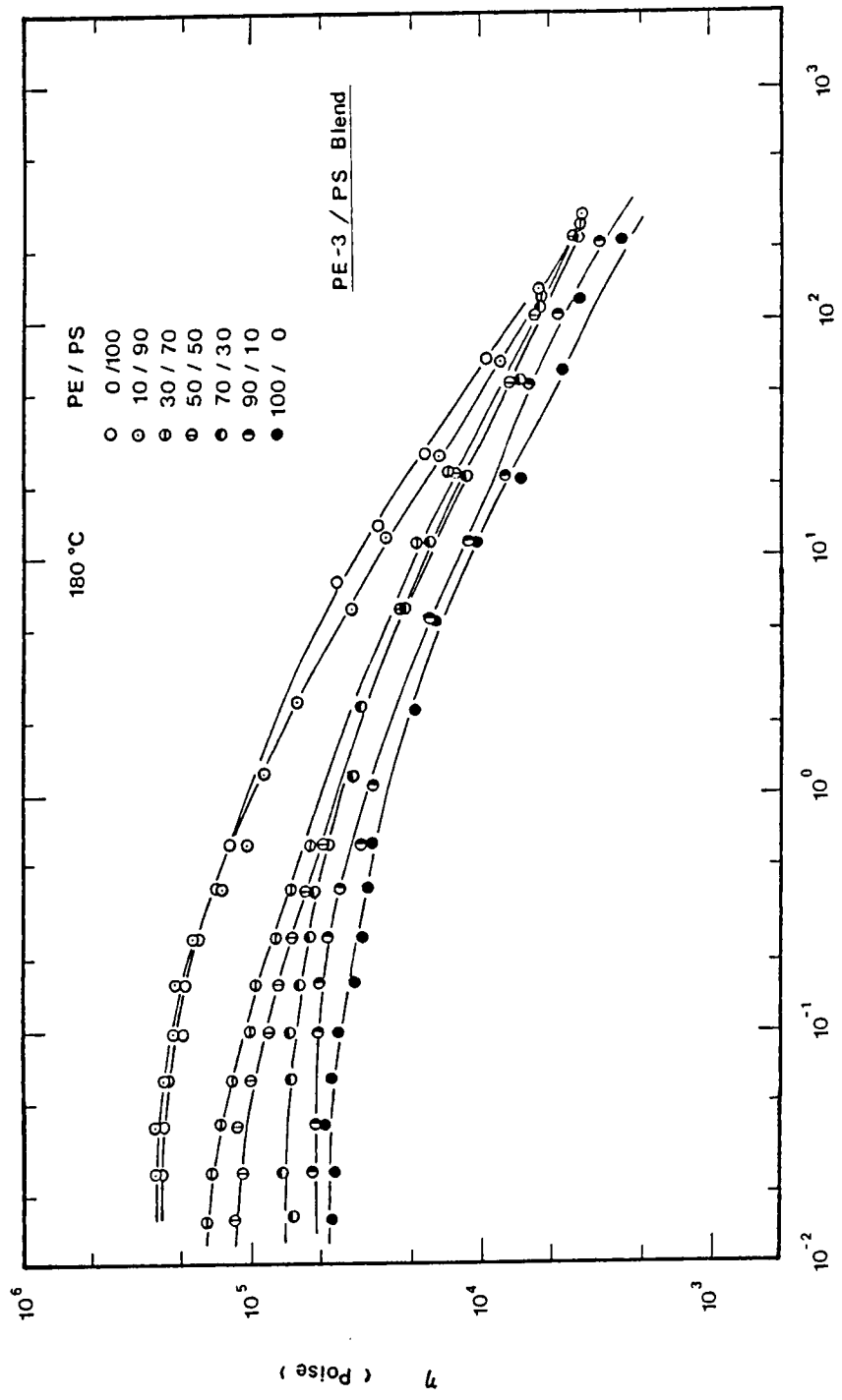


Figure V-3. Shear viscosity versus shear rate for PE-3/PS blends.

monotonically with loading level of polystyrene in all range of shear rate.

A.1.3. PE-2/N6 and PE-2/PC blends. The corresponding experimental data for polyethylene (PE-2)-nylon 6 (N6) and polyethylene (PE-2)-polycarbonate (PC) blends are shown in Figures V-4 and V-5. The polyethylene (PE-2) has a much higher viscosity than either PC or N6. The viscosity at higher shear rates was measured. The viscosity of PE-2/PC blends increases with increasing the loading level of polycarbonate. The viscosity of PE-2/N6 decreases with increasing loading level of nylon 6.

A.2. Discussion

A.2.1. PE-PS blends. Figure V-6 shows the shear viscosity as a function of the composition of polyethylene at various shear rates for PE-2/PS blends. The curves exhibit a minimum and a sharp maximum, especially at PE/PS-10/90 blend. The maximum decreases with increasing shear rate. Figure V-7 shows the composition dependence of the viscosity of PE-2/PS as a function of shear stress. Figures V-8 and V-9 show the composition dependence of the viscosity of PE-3/PS blends and PE-1/PC blends at various shear stresses. To compare the composition dependence of the viscosities of PE-PS blends, Figure V-10 was plotted at a certain shear stress $\sigma_{12} \simeq 2.0 \times 10^4$ dyne/cm^2. It is seen that the upper bound, minimum and maximum, and lower bound are influenced by the viscosity ratio.

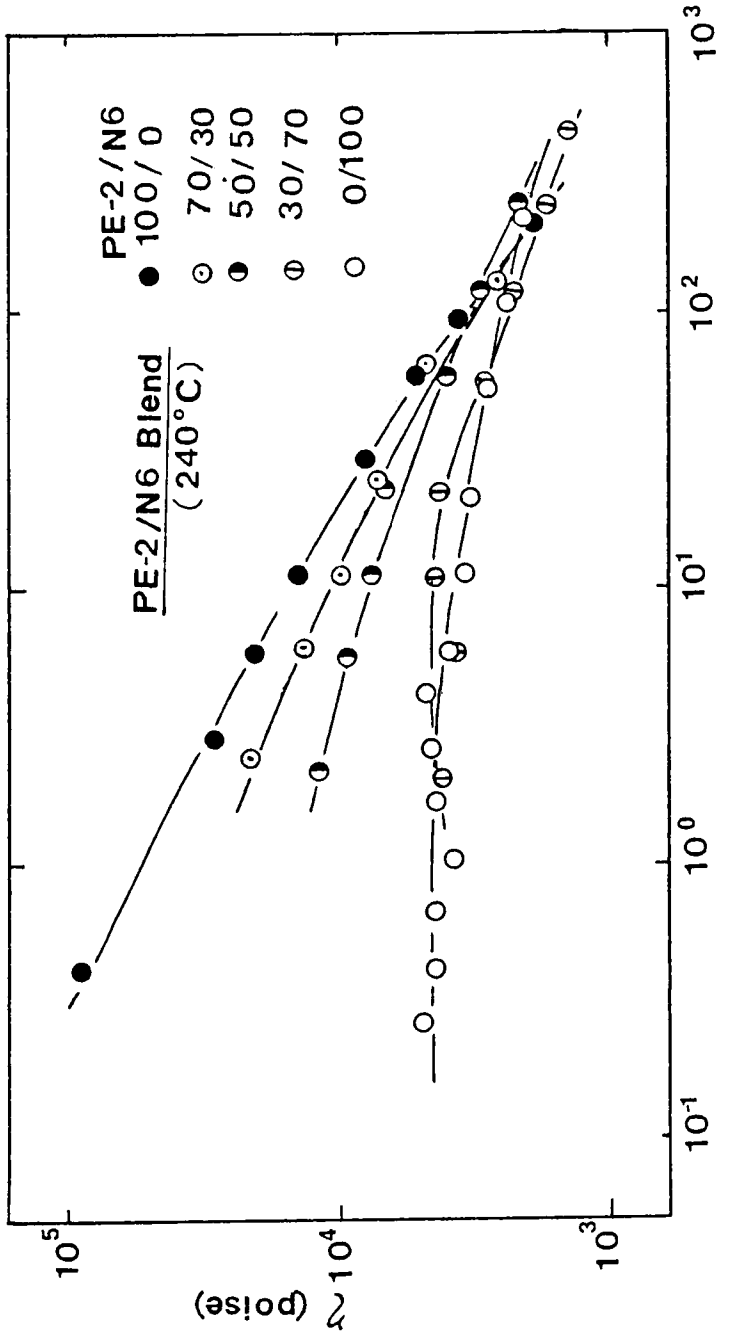


Figure V-4. Shear viscosity versus shear rate for PE-2/N6 blends.

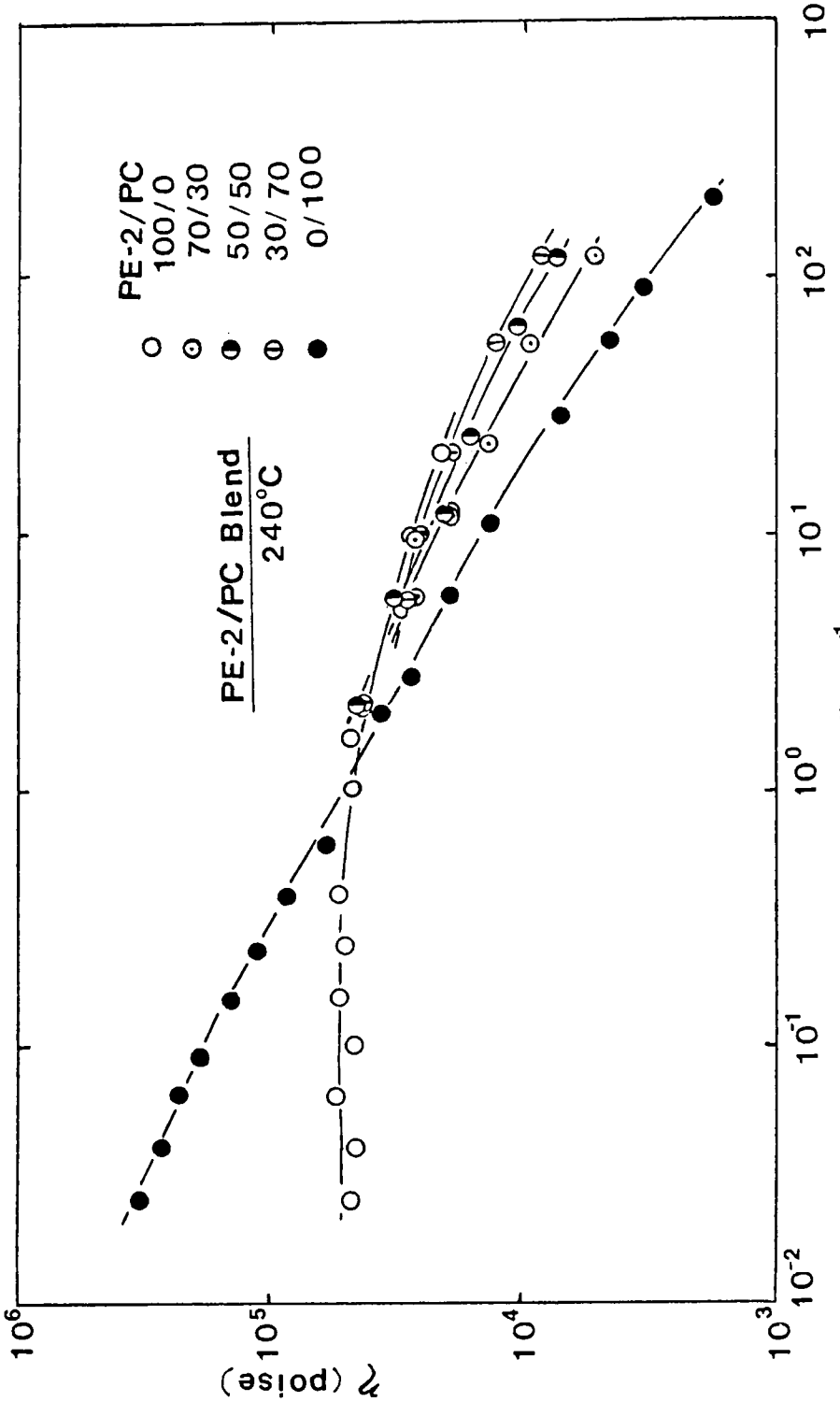


Figure V-5. Shear viscosity versus shear rate for PE-2/PC blends.

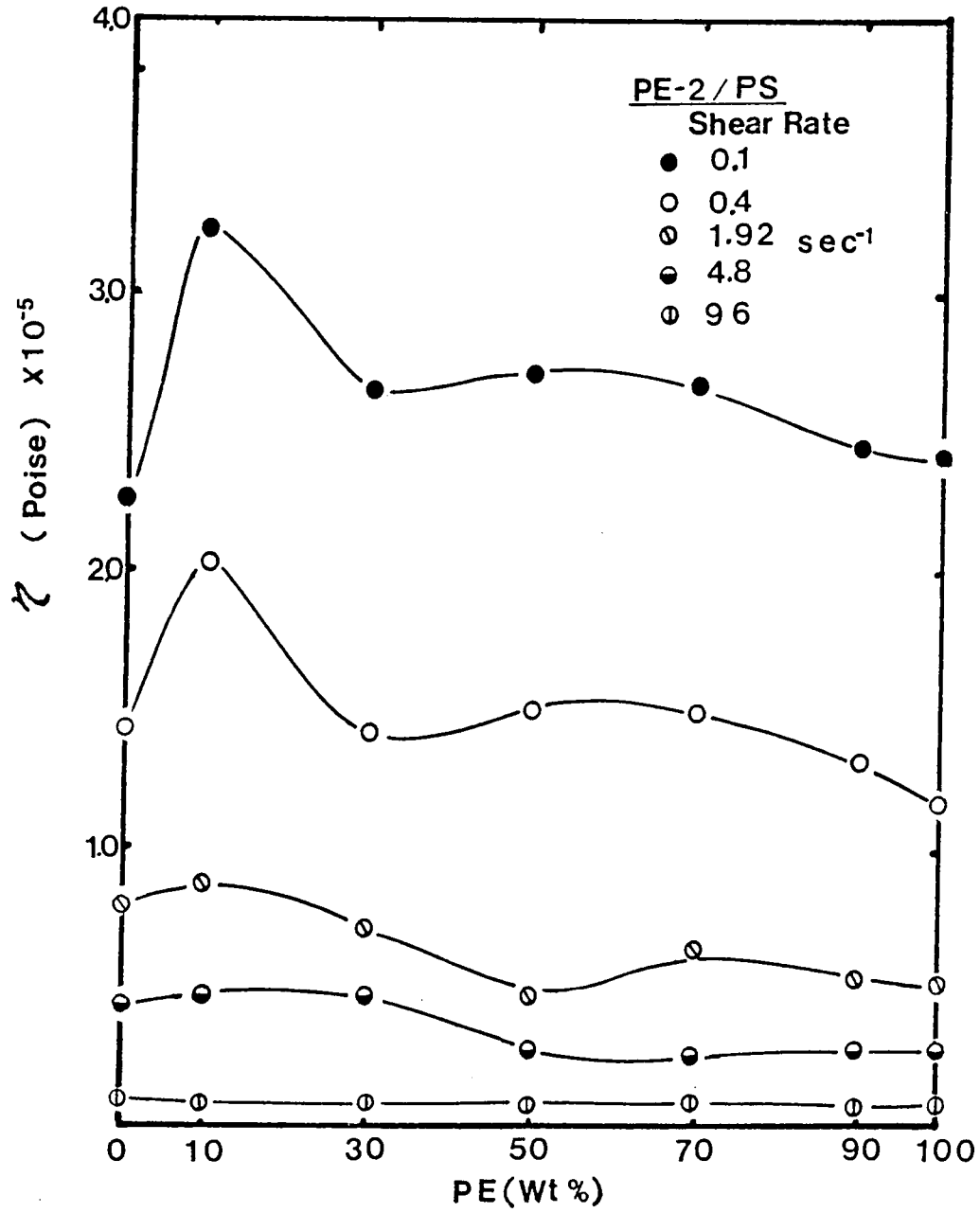


Figure V-6. Composition dependence of viscosity of blends of PE-2/PS as a function of shear rate.

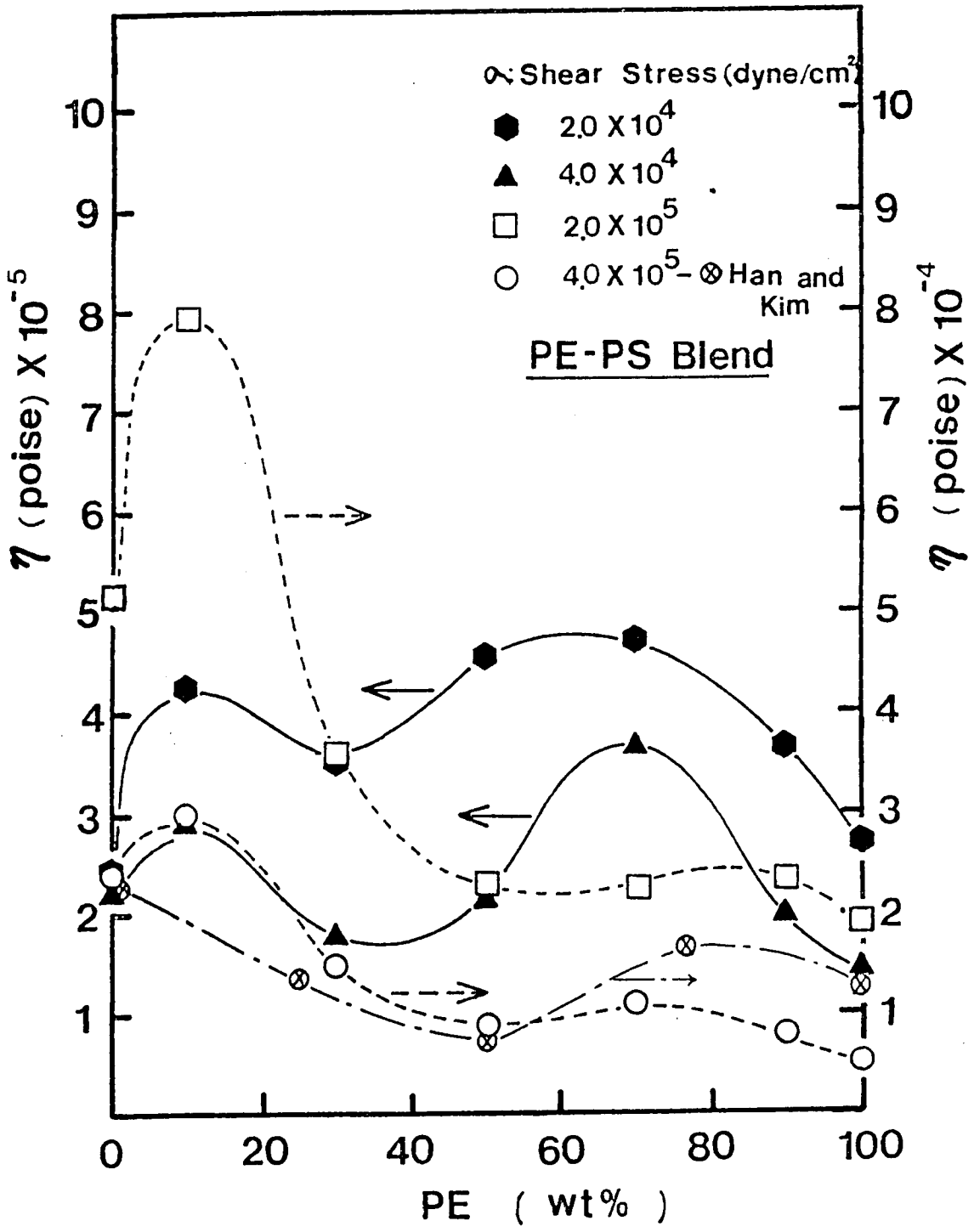


Figure V-7. Composition dependence of viscosity of PE-2/PS blends as a function of shear stress.

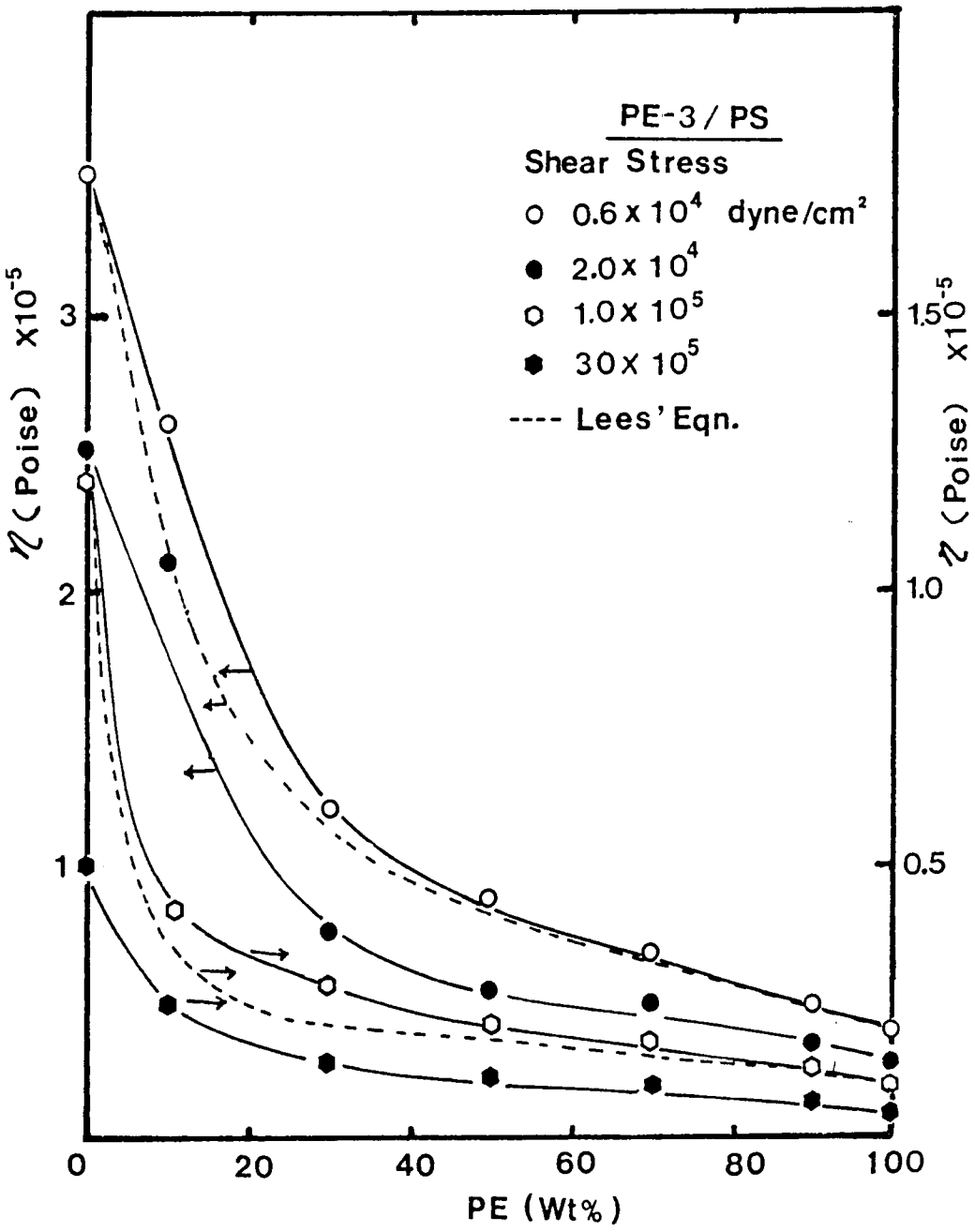


Figure V-8. Composition dependence of viscosity of PE-3/PS blends as a function of shear stress.

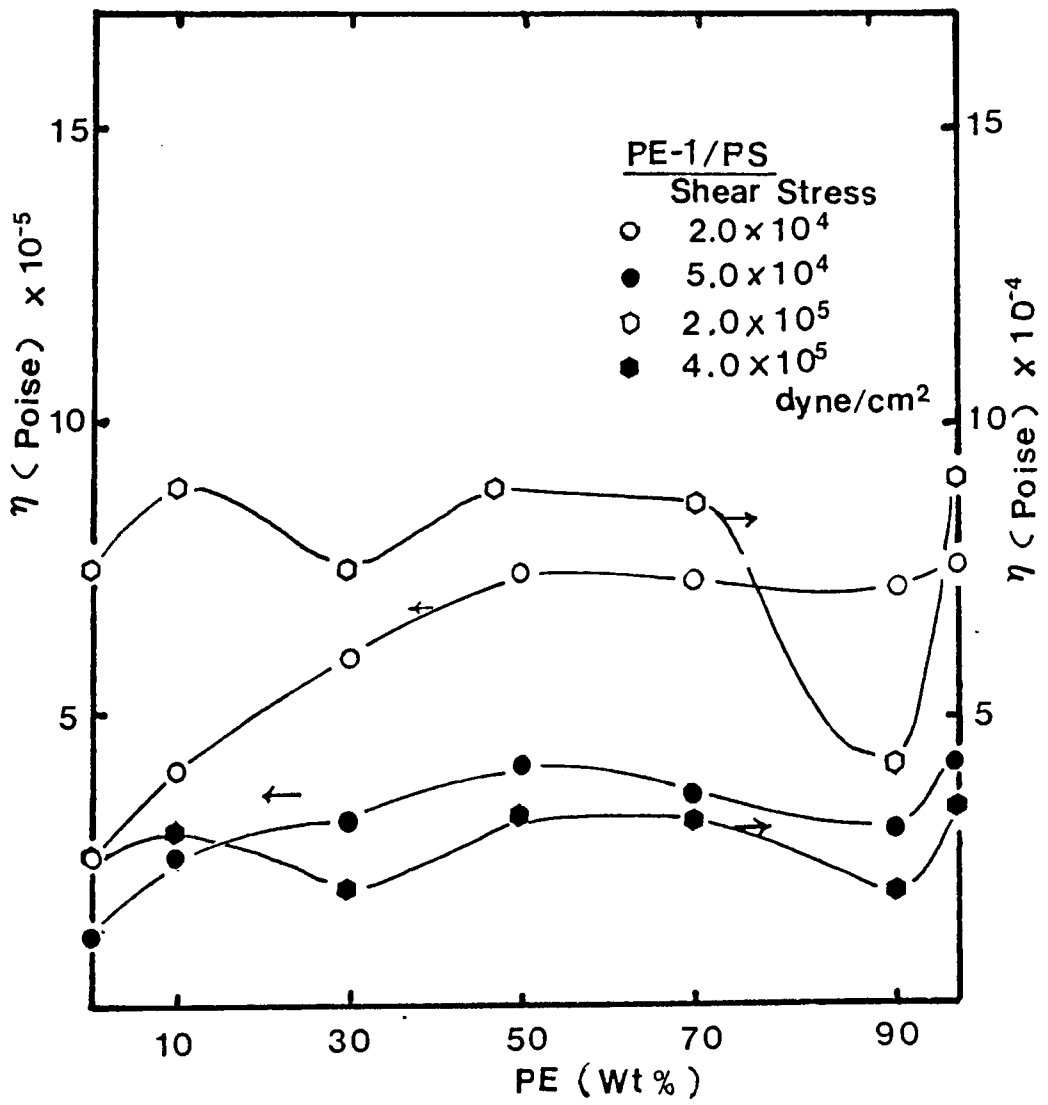


Figure V-9. Composition dependence of viscosity of PE-1/PS blends as a function of shear stress.

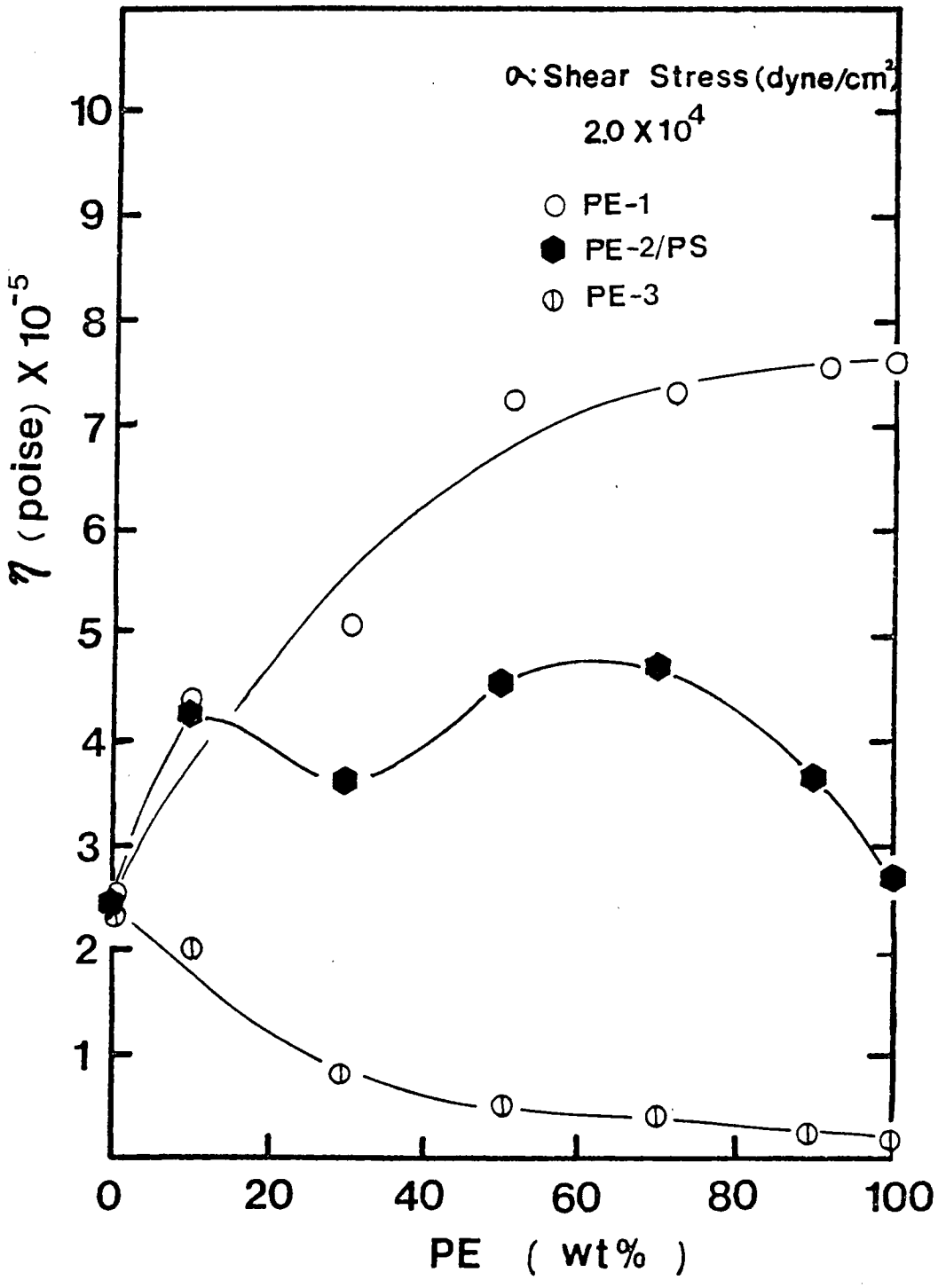


Figure V-10. Composition dependence of viscosity of PE-1/PS, PE-2/PS and PE-3/PS blends at a fixed shear stress.

Figure V-10 shows the effect of varying the viscosity of polyethylene at the same stress. The PE-2/PS blends which have viscosity values close to each other exhibit a minimum and a maximum. The other blends which have large difference of viscosity seem to change monotonically with composition. The present data on PE-PS blends have been compared with those of Han and Kim's (53)(54)(55) work shown in Figure V-7. They measured the viscosity of PE-PS blends at various temperatures from 200°C to 240°C. At shear stresses of 4×10^5 and 6×10^5 dyne/cm^2, the viscosity shows a sharp minimum and maximum, respectively. The viscosity-composition curve of PE-PS at 4.0×10^5 dyne/cm^2 at 200°C due to Han and Kim (53) is replotted in Figure V-7. The curve is quite similar to one of the present works except for the maximum of PE/PS-10/90. The comparisons enable us to consider the effect of the two-phase morphology at high shear stress. Han and Kim acted that the morphology of PE-PS blends in ratios 25/75 and 50/50 were similar, both blends have polystyrene droplets dispersed in a continuous phase of PE and in the 75/25 blends no clear continuous phase was apparent, the two components being interlocked. The blend with an interlocked morphology has a larger viscosity but a lower normal stress difference. In this work, interlocked morphologies were not observed. It was found that the morphology of PE-2/PS blends with 10/90 composition changed from droplets at low shear stress to thin threads at higher shear stresses. As the drops evolved into fibers, the viscosity maximum disappeared. On the contrary, the morphology of PE-2/PS-90/10 changed from deformed droplets at low shear stress to a deformed ellipsoid or

short rods at high shear stress. The morphology of PE-2/PS-70/30 which shows a maximum has a rod structure at low shear stress which became thin threads at high shear stress. The blends with spheres or short rods have a higher viscosity than other compositions. When threads are formed, the maxima disappear. Figures V-8 and V-9 show viscosity-composition curves for PE-1/PS blends and PE-3/PS blends. For PE-1/PS-90/10 and 10/90 blends, fibrils with undulations at high shear stresses were observed in the previous chapter. PE-1/PS-90/10 shows a minimum when the morphology changed from the droplets to the unstable fibers. For PE-3/PS, the viscosity-composition curves varied monotonically with composition.

In the previous chapter, the morphology of PE-3/PS-90/10 and 10/90 blends was described. For PE-3/PS-10/90, the droplet-fiber formation transformation seems to result in the rapid reduction of viscosity with increasing shear stress. For PE-3/PS-90/10, the droplets of polystyrene maintained their drop shape with increasing shear stresses. The viscosity of PE-3/PS-90/10 does not change with increasing shear stress.

A.2.3. PE-2/N6 blends. Figure V-11 has plotted the viscosity of PE-2/N6 blends as a function of composition at various high shear stress.

Hayashida et al. (61) have investigated the viscosity and the morphology of PE/N6 blends. The behavior of the viscosity-composition curve is quite similar to Hayashida et al.'s (61). The behavior

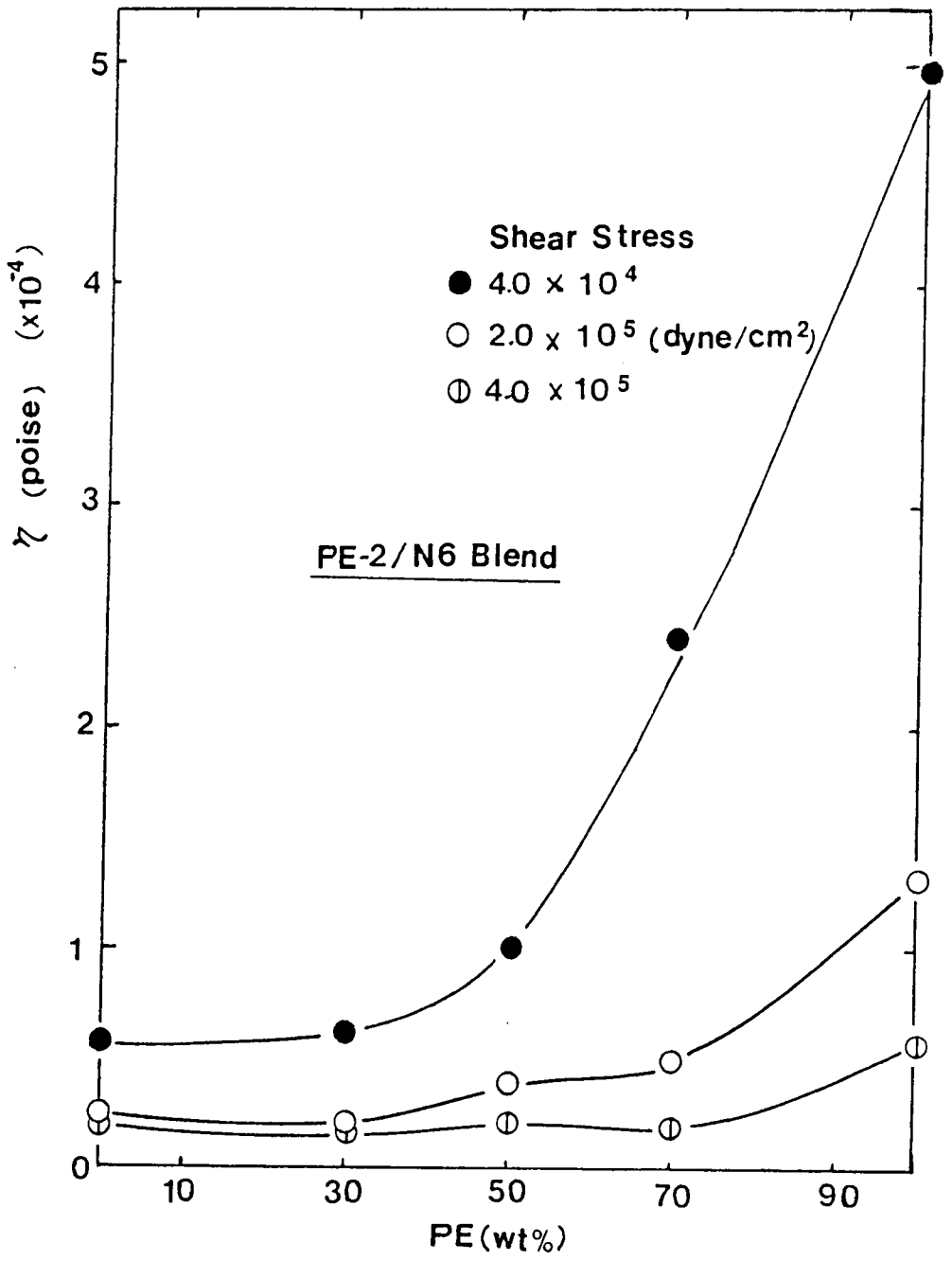


Figure V-11. Composition dependence of viscosity of PE-2/N6 blends as a function of shear stress.

is also quite similar to those of blends of high viscosity PE-1 with PS.

A.2.4. PE-2/PC blends. Figure V-12 was plotted the viscosity of PE-2/PC blends as a function of composition at fixed shear stresses. When the shear stress is 1.0×10^5 dyne/cm^2, the viscosity-composition curve shows a maximum at PE-2/PC-50/50. At 4.0×10^5, the maximum disappeared and the viscosity-composition curve became monotonic.

A.2.5. The morphological prediction of the composition dependence of viscosity. Since the turn of the century, viscosity-composition relations for blends have been investigated by various scientists. For polymer blends, minima and maxima have been observed in many systems. Theoretical mixing laws for emulsions or suspensions indicate viscosities higher than those of pure liquid due to enhanced viscous dispersion energy, etc. The theory developed by Choi and Schowalter, which includes the consideration of circulation inside of droplets, concentrated effects and the deformation of droplets indicates always a higher viscosity (Figure V-13(a)). On the contrary, the viscosity calculated from Lee's lamellar phases mutually perpendicular to each other theory described in Chapter II can indicate viscosity lower than that of the pure polymers (Figure V-13(a)--2,3). These mixing laws cannot explain a minima or a maxima.

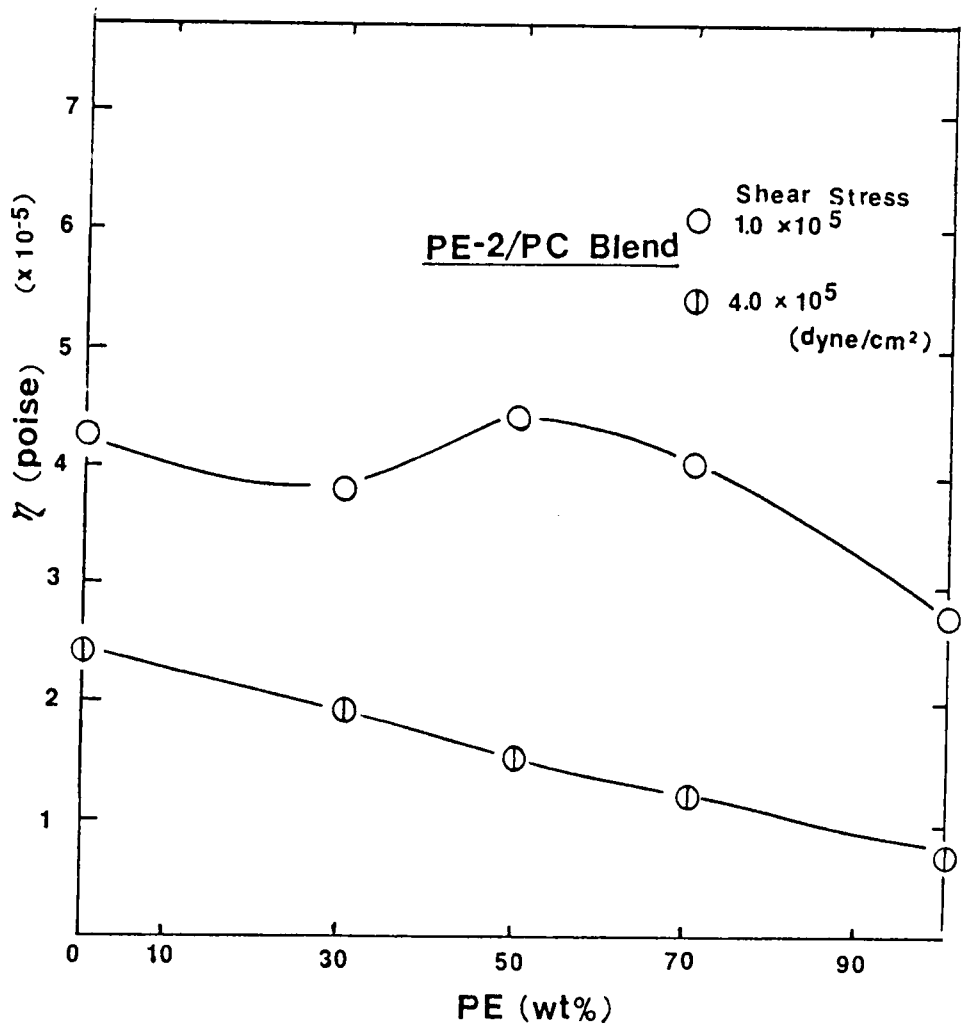
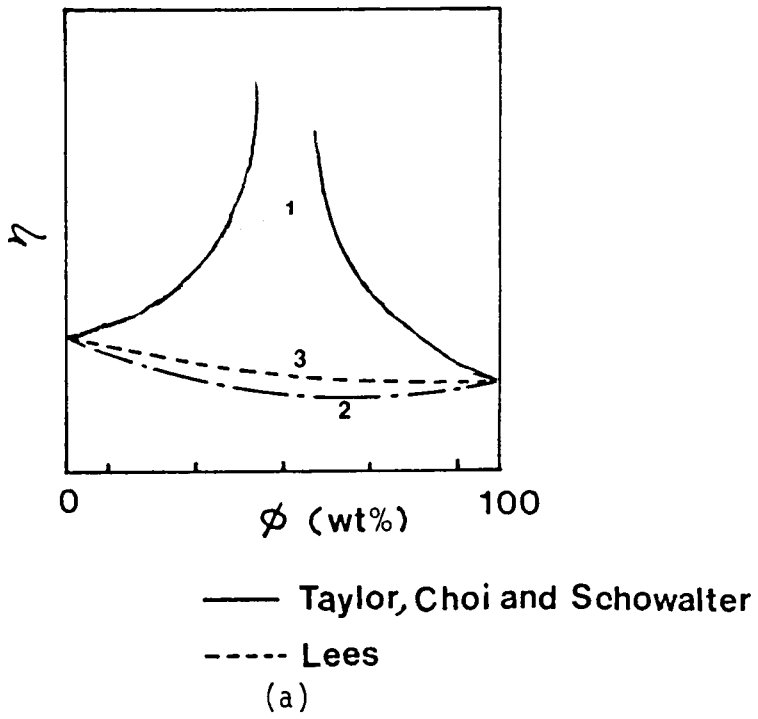
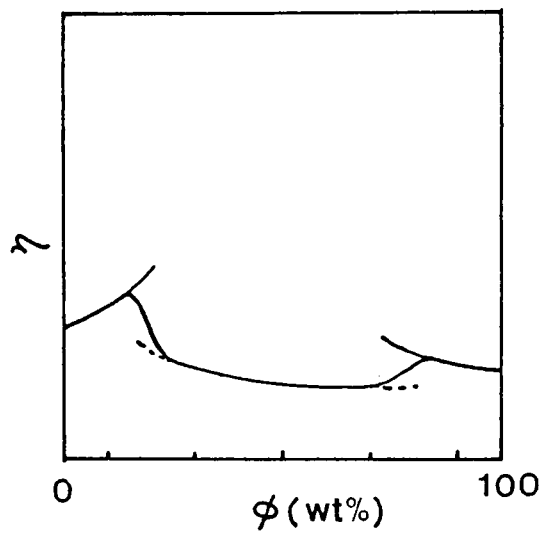


Figure V-12. Composition dependence of viscosity of PE-2/PC blends as a function of shear stress.



(a)



(b)

Figure V-13. Comparison of viscosity-composition dependence with theoretical prediction.

From the previous chapters, the two-phase morphology of polyethylene-polystyrene blends is classified into three types: a) dispersed droplets, b) thin fibers parallel arranged to the flow direction, and c) thin lamellae parallel to the flow directions as shown in Figures V-14 and V-15. It has been noted that the morphology is strongly dependent on the composition. To represent the effect of the morphology change from the droplets to thread, it could be argued that the analysis of Taylor-Choi-Schowalter should be replaced with that of Lees (86). This is tested in Figures V-14 to V-16.

For blends of PE-PS, some points shown in Figures V-14 and V-15 agree with the predictions from Lees or Choi-Schowalter at fixed shear stress. A combined morphology of fine fibers, lamellar structure, and droplets for polymer blends in shearing flow may be considered (Figure V-15). Taylor-Choi-Schowalter's equations (II-22) and (II-32), and the two Lees equations (II-17) and (II-19) from Chapter II are assumed.

The viscosity-composition curves can be predicted by the combination of Choi-Schowalter's and Lees' theory as shown in Figure V-16 where the relative contributions have been predicted from the SEM microphotographs. The predicted curves of viscosity-composition seem to be similar to the experimental curves.

B. FIRST NORMAL STRESS DIFFERENCE

In this section, the first normal stress difference N_1 and its composition dependence and phase morphology are discussed.

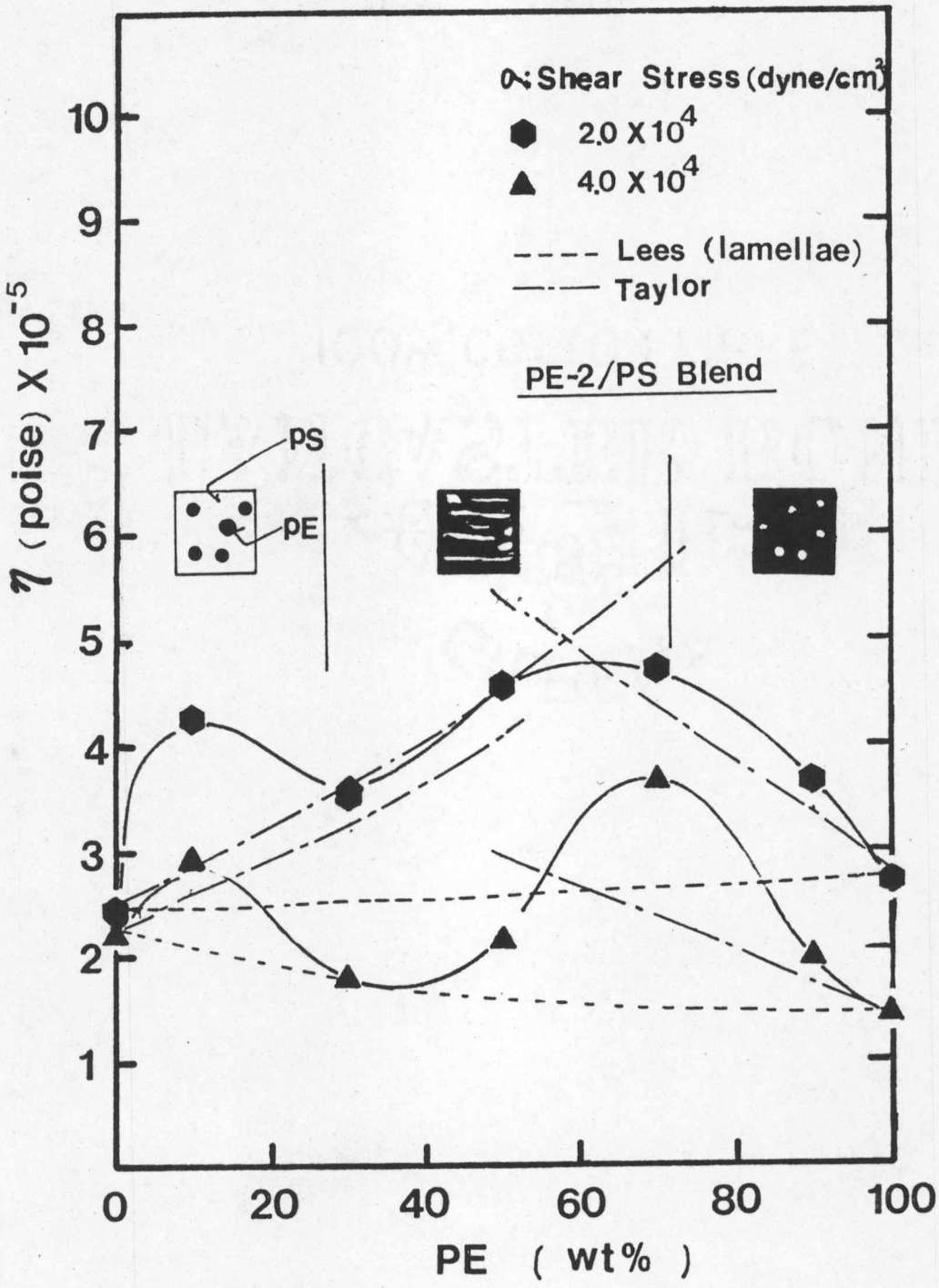


Figure V-14. Comparison of observed composition dependence with theoretical predictions and morphologies at low shear stresses.

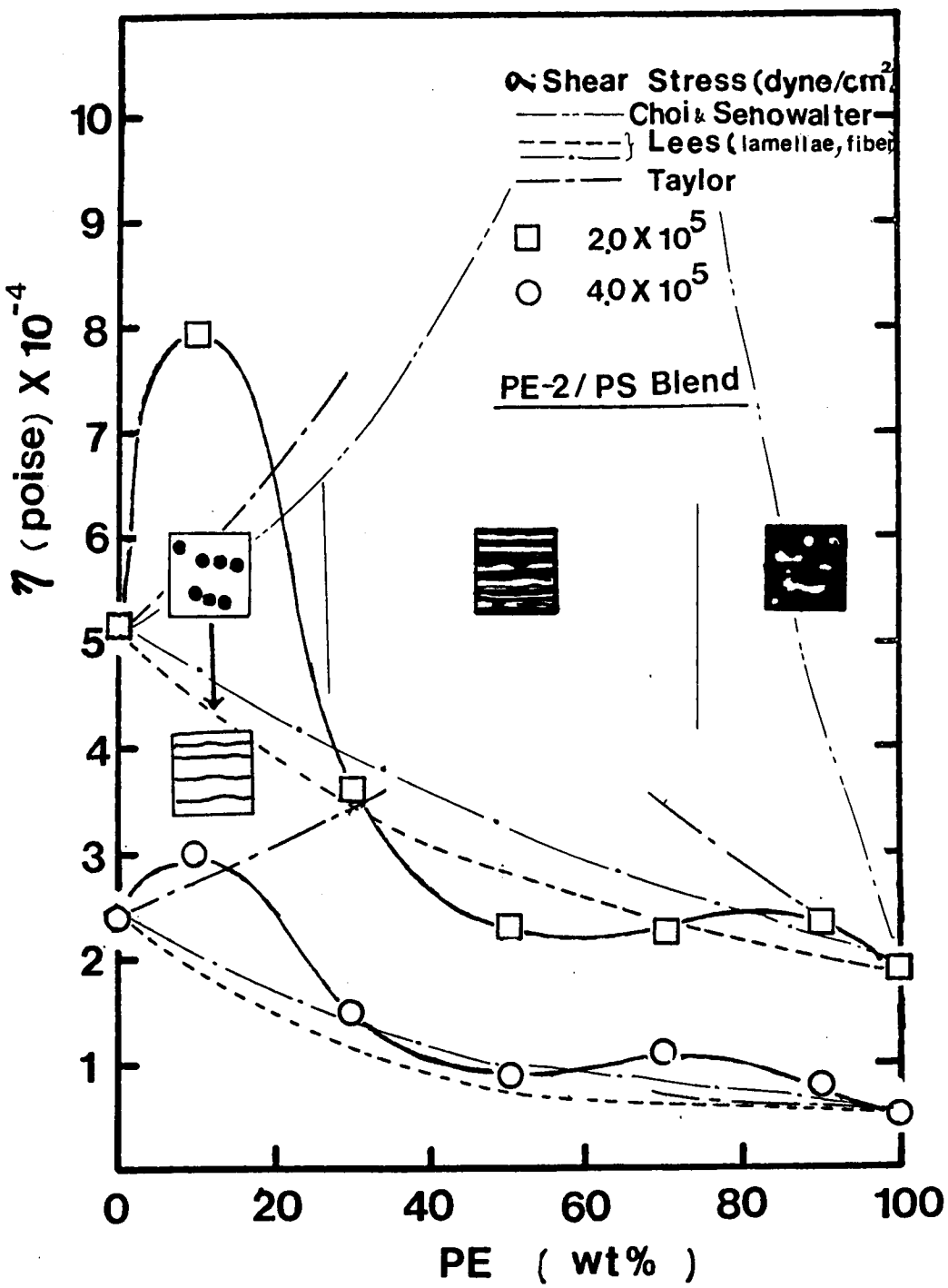


Figure V-15. Comparison of observed composition dependence with theoretical predictions and morphologies at high shear stresses.

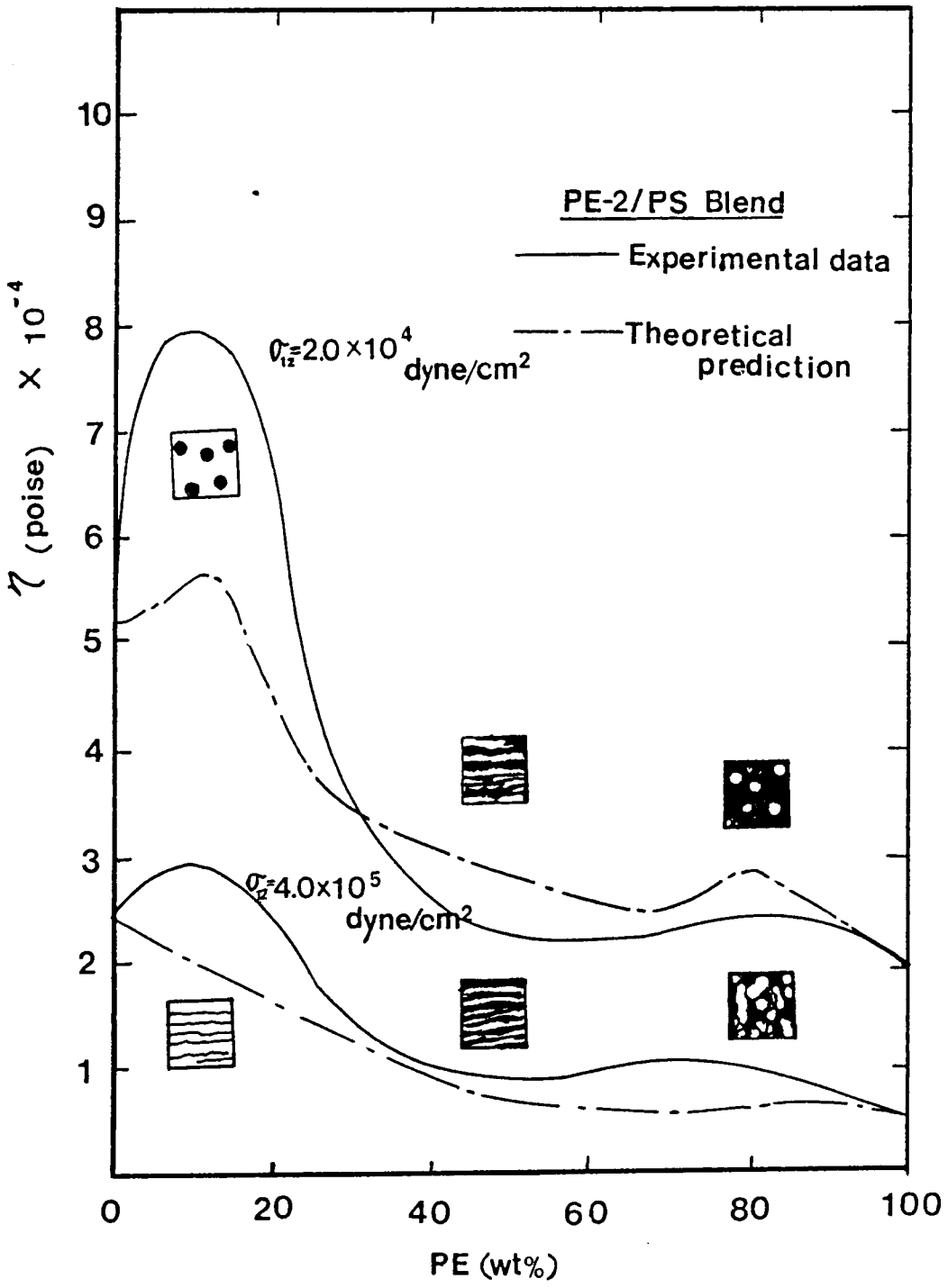


Figure V-16. Comparison of observed composition dependence with theoretical predictions.

B.1. Results

As pointed out by Han (49) and Oda, White, and Clark (111), a plot of the normal stress against the shear stress is more useful than that against the shear rate. It is independent of temperature and molecular weight, but is dependent upon molecular weight distribution. Figure V-17 represents the plot of the principal normal stress difference N_1 of pure polymers against the shear stress. It is seen that in each case polyethylene has a higher value of N_1 at fixed shear stress σ_{12} than polystyrene. PE-1, -2, and -3 have different molecular weight and different molecular distribution, as shown in Chapter III, Table III-1, p. 42. PE-3 has the narrowest molecular weight distribution of three polyethylenes.

Figures V-18 through V-20 show the first normal stress difference of polyethylene-polystyrene blends as a function of shear stress. The normal stress differences of PE-PS blends behave similarly to those of polyethylenes.

B.2. Discussion

The composition dependence of the normal stress difference N_1 at a certain stress is shown in Figures V-21 to V-24 for polyethylene-polystyrene blends. Increasing the loading of polyethylene increases N_1. The N_1-composition curves shows a minimum and a maximum.

Han and Kim (53) obtained the first normal stress difference from the extrapolated value of the exit pressure. They reported a minimum at the 75/25-PE/PS blend, which has an interlocked morphology. The concentration dependence of the viscosity is opposite to that of

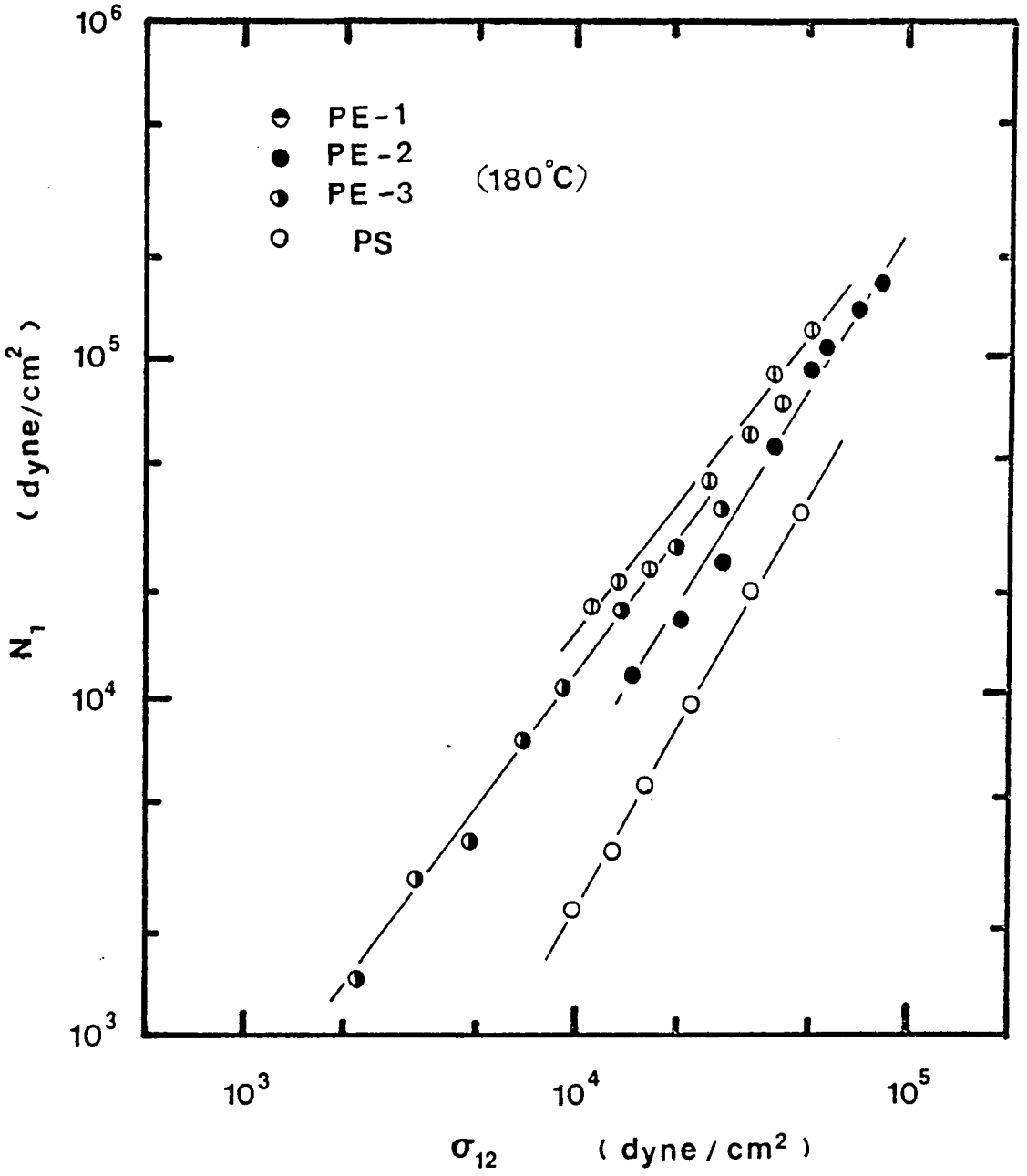


Figure V-17. First normal stress difference (N_1) as a function of shear stress (σ_{12}) for polyethylenes and polystyrene.

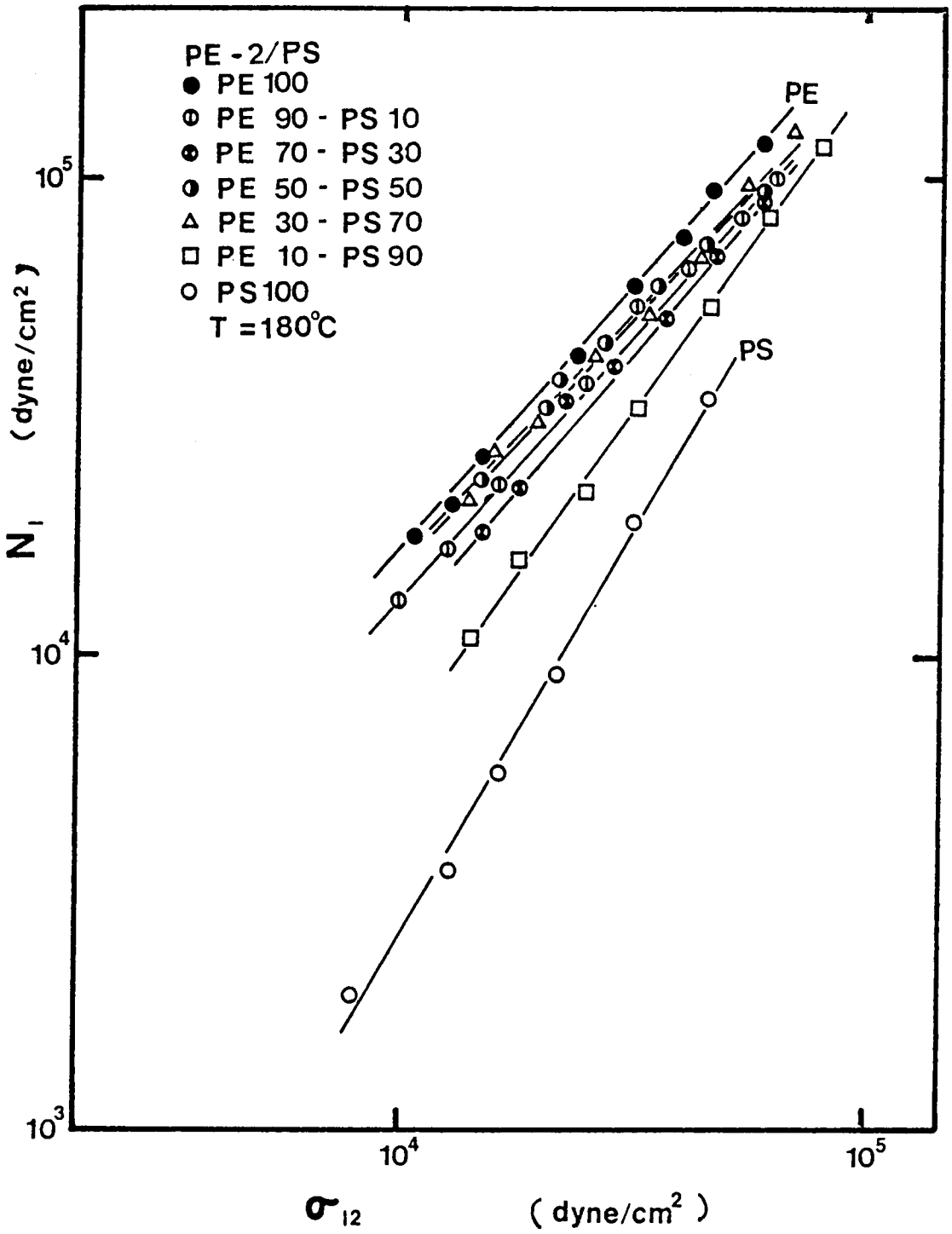


Figure V-18. First normal stress difference (N_1) as a function of shear stress (σ_{12}) for PE-2/PS blends.

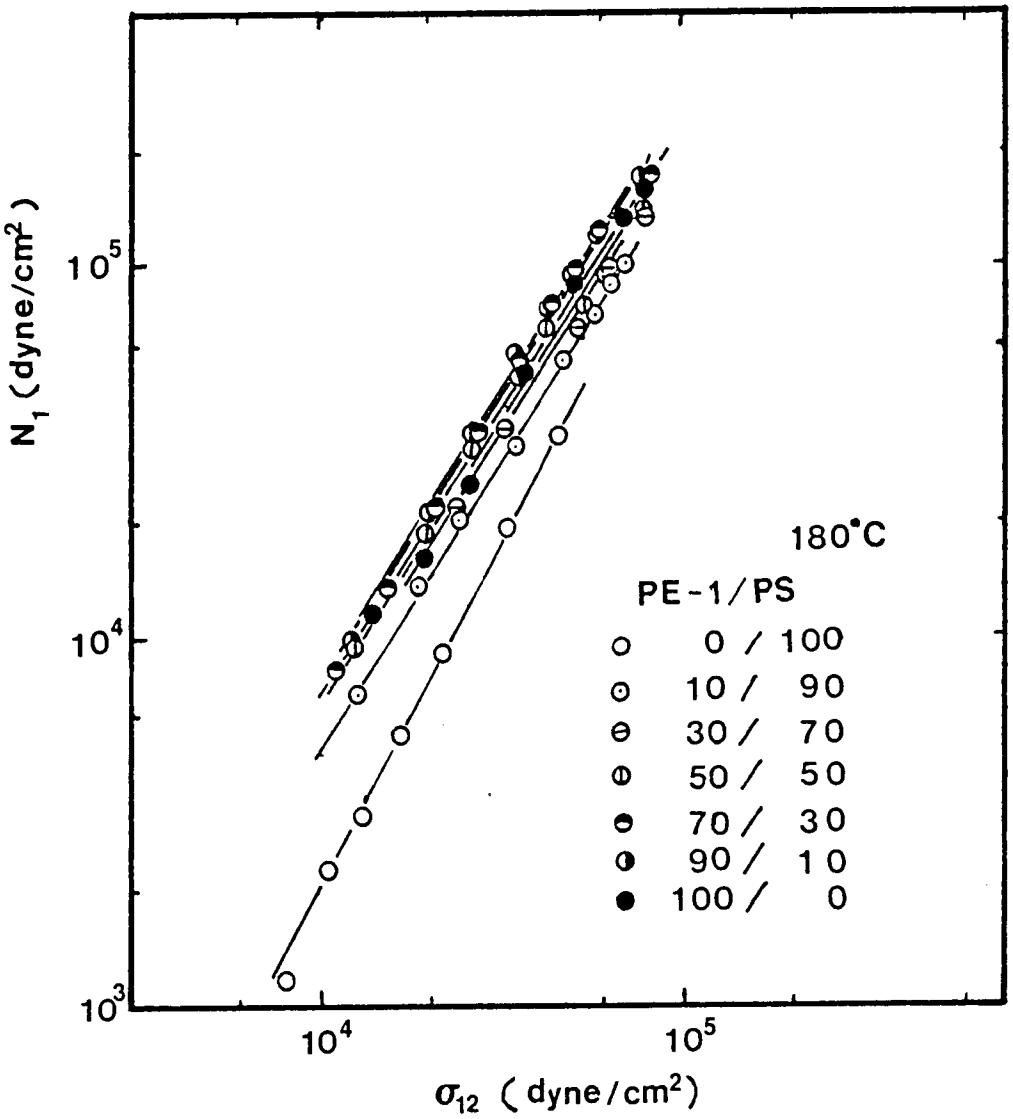


Figure V-19. First normal stress difference (N_1) as a function of shear stress (σ_{12}) for PE-1/PS.

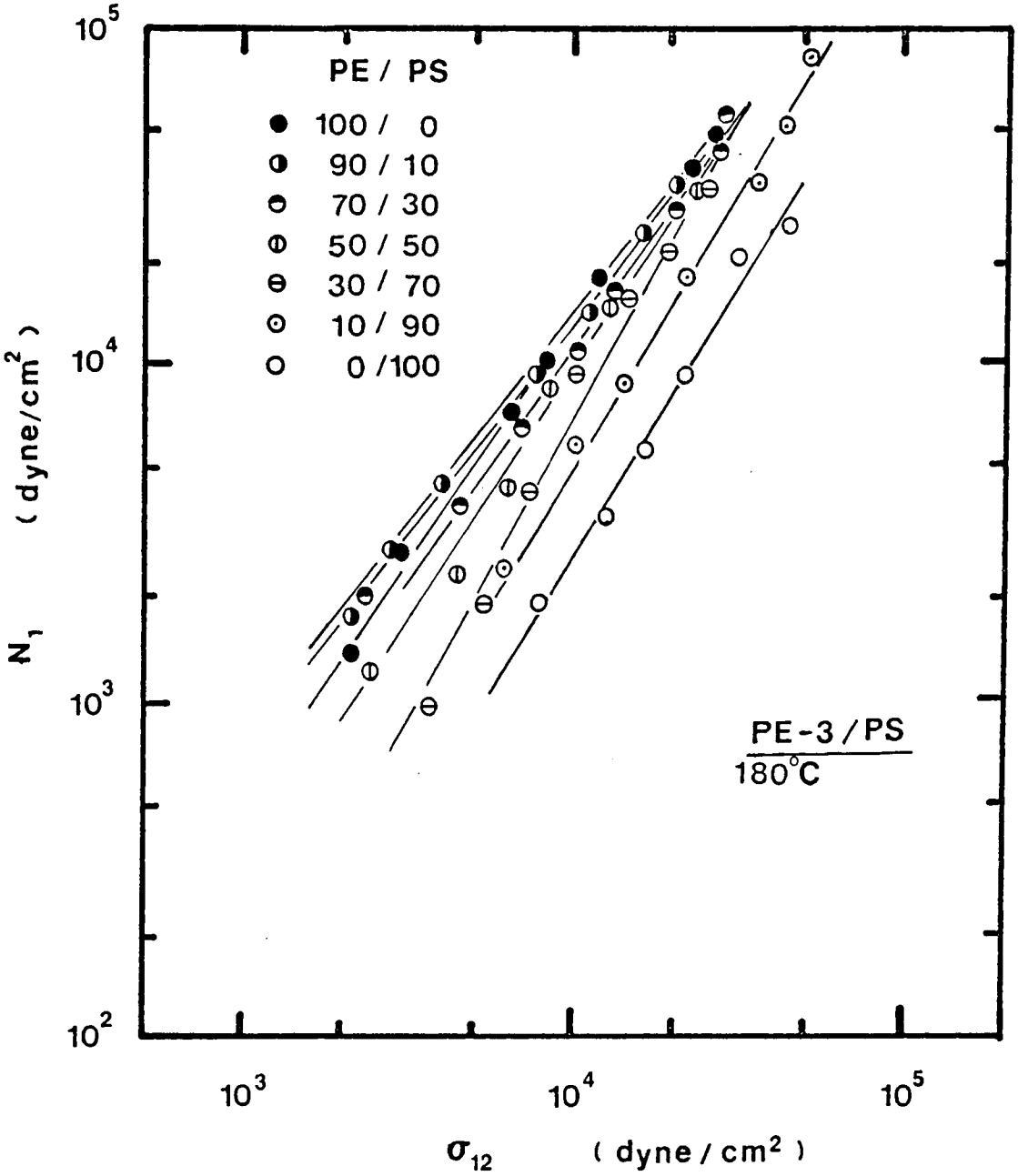


Figure V-20. First normal stress difference (N_1) as a function of shear stress (σ_{12}) for PE-3/PS.

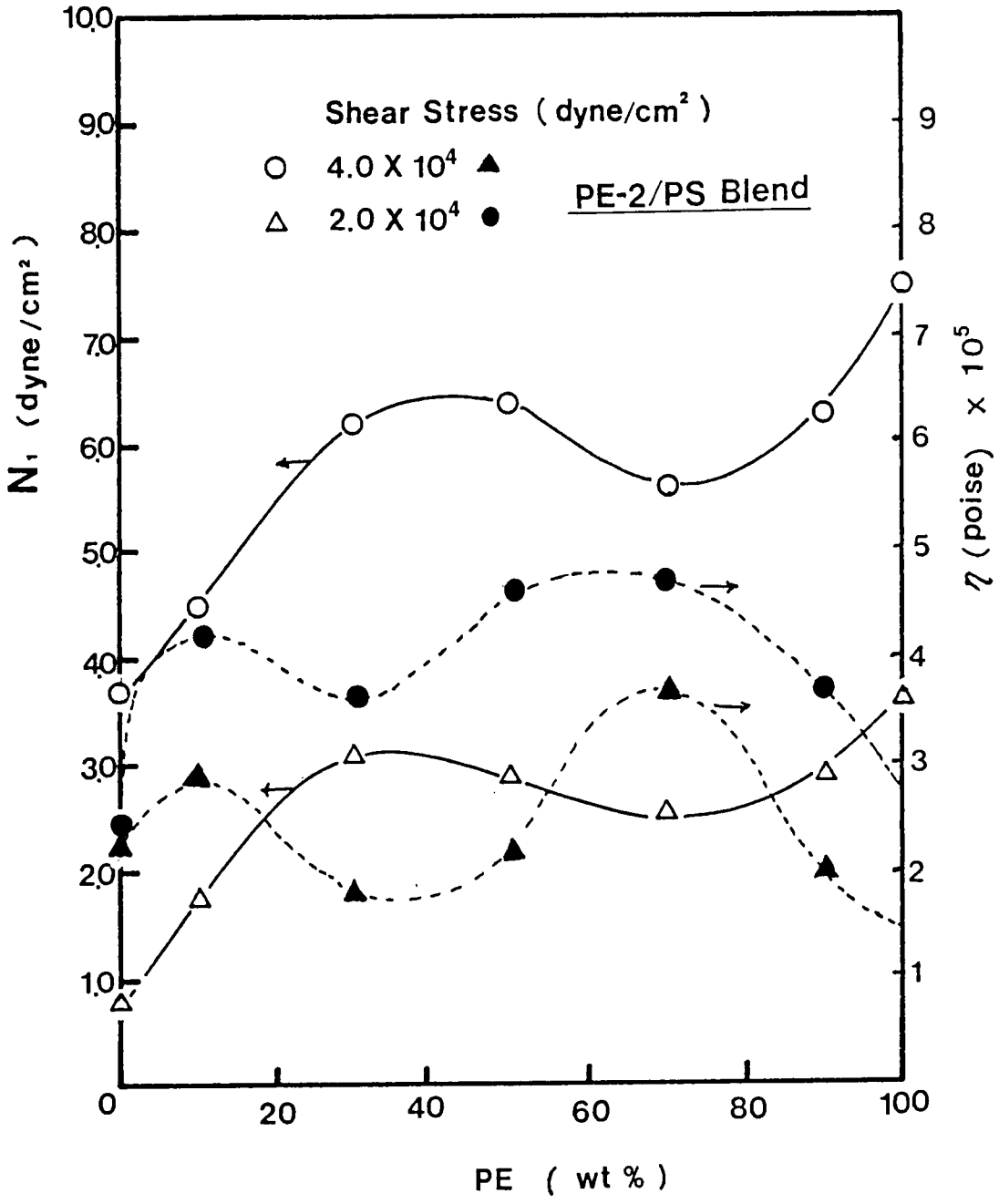


Figure V-21. Comparison of the composition dependence of viscosity and first normal stress for PE-2/PS at various shear stress blends.

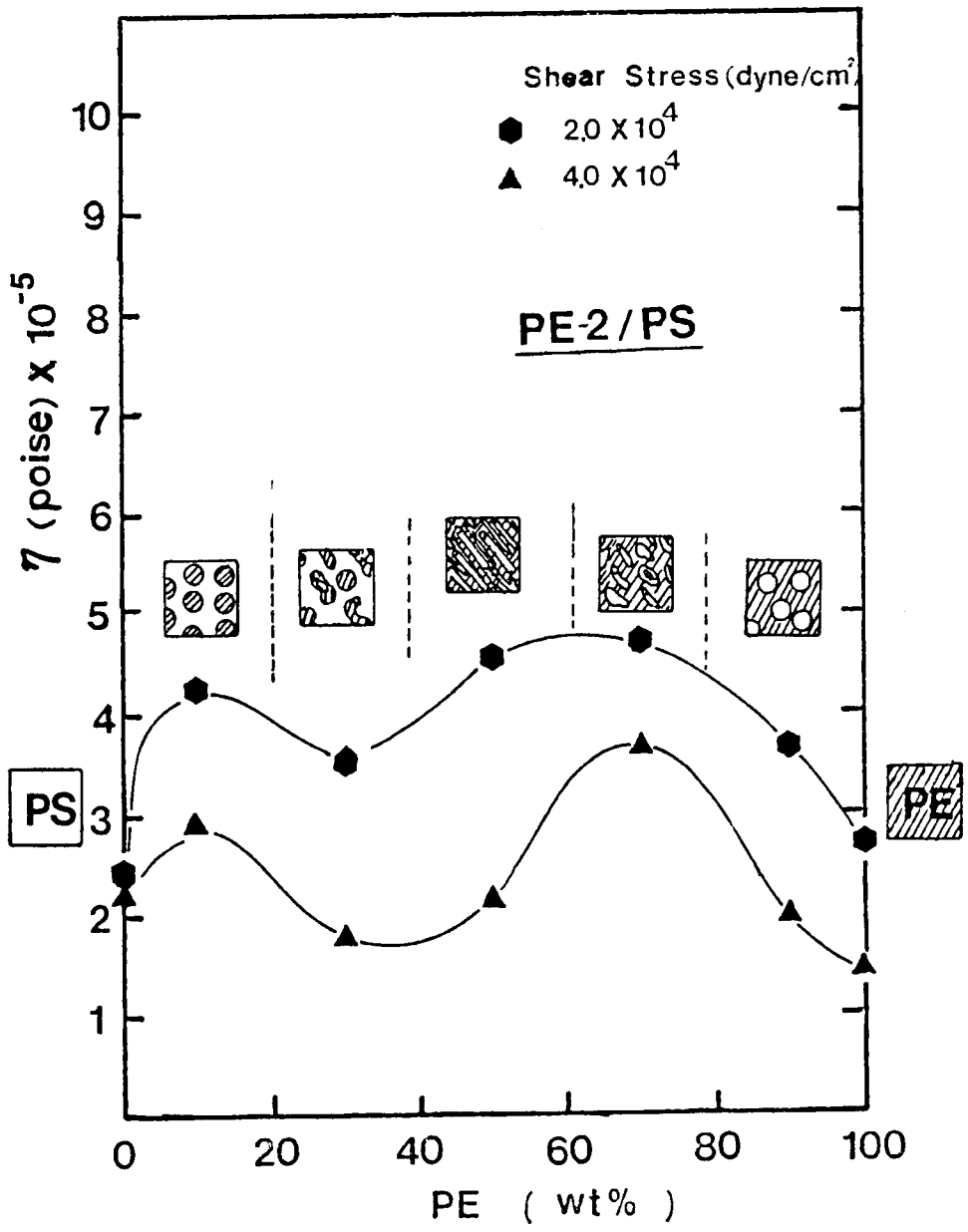


Figure V-22. Comparison of the composition dependence of first normal stress difference and morphology for PE-2/PS blends at various shear stresses.

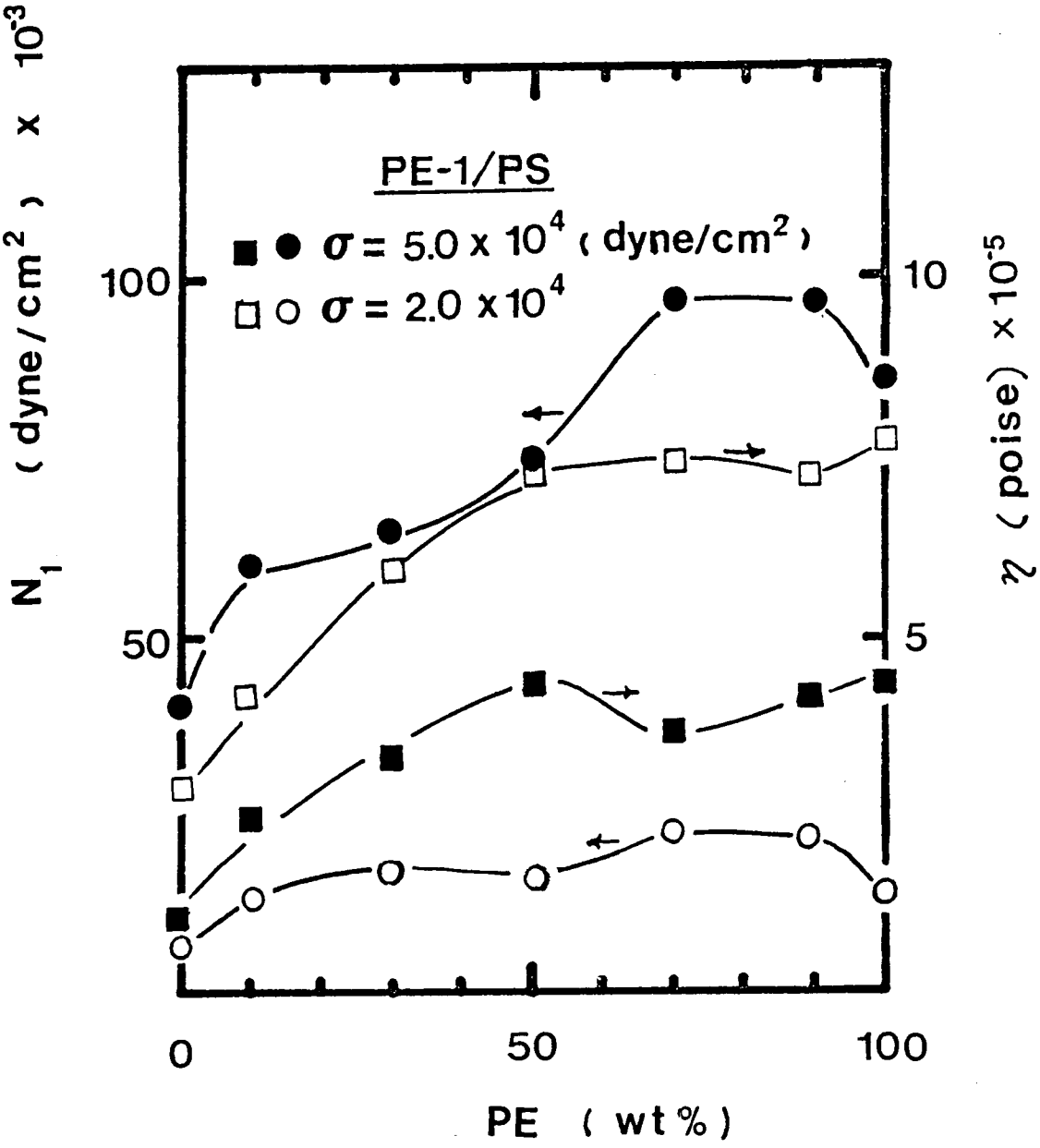


Figure V-23. Comparison of the composition dependence of viscosity and first normal stress difference for PE-1/PS blends at various shear stresses.

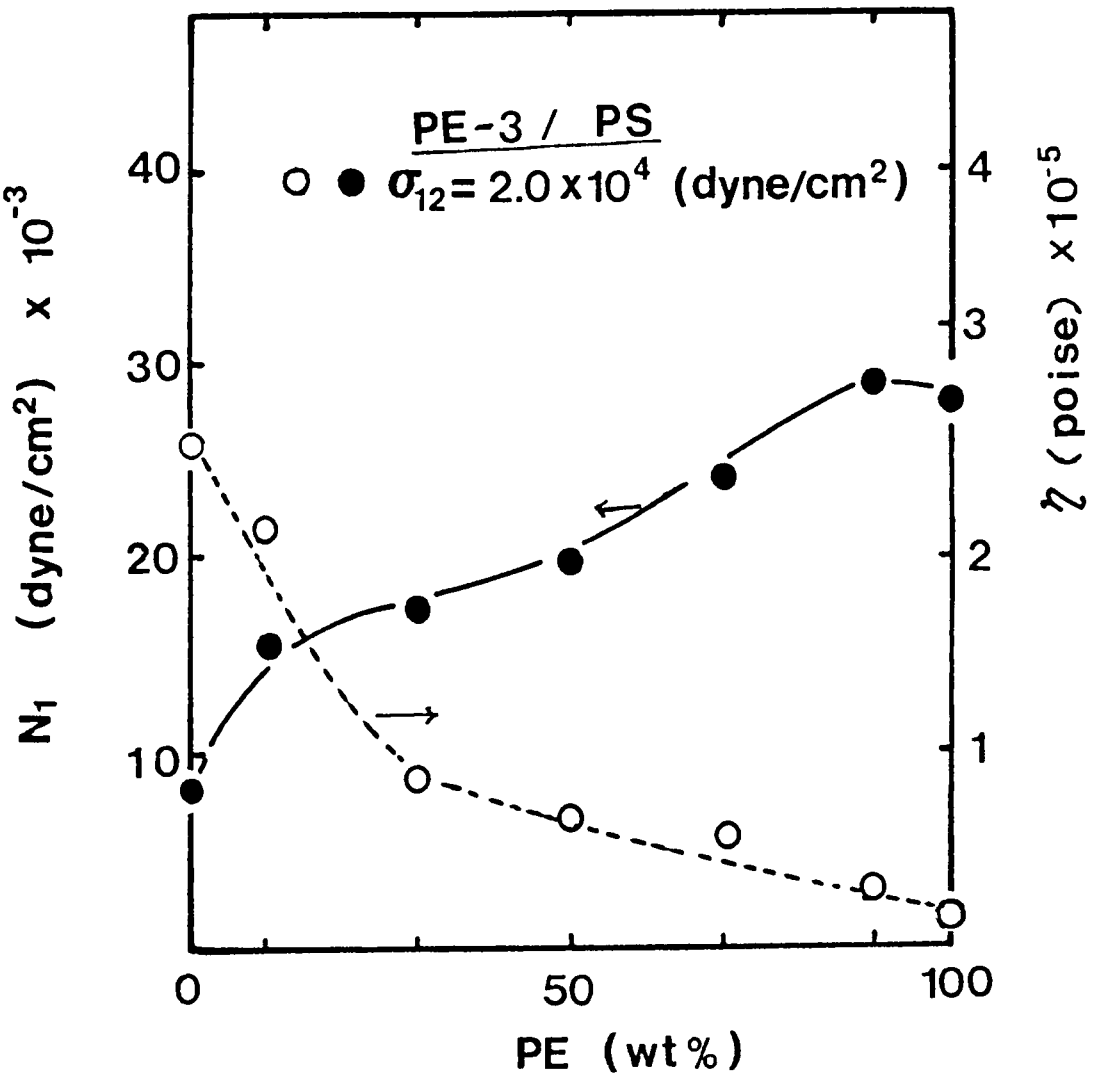


Figure V-24. Comparison of the composition dependence of viscosity and first normal stress differences for PE-3/PS blends at a fixed shear stress.

the normal stress function. Comparing the present data of the dependence of composition of the normal stress difference at fixed stress with those of composition dependence of viscosity, it is clearly observed that the normal stress difference is opposite to that of the viscosity especially for PE-2/PS systems. Figure V-22 shows the morphology scheme judged from SEM microphotographs of the samples in the cone-plate. The feature of morphology which shows a maximum has the long rodlike structure as shown in Figure V-22. It is apparent that the normal stress difference-composition relationship may be sensitive to two-phase morphology at a certain stress. For HDPE-1/PS and HDPE-2/PS blends, Figures V-23 and V-24 show the first normal stress vs. the composition. The N_1 vs. composition of HDPE-1/PS represents the opposite shape to the viscosity-composition curve. The HDPE-3/PS data have a maximum and a shallow minimum corresponding to the minimum and the maximum of viscosity-composition curves.

C. ELONGATIONAL FLOW

The rheological responses of uniaxial elongational flow of PE/PS blends polymer melts are presented in this section. It was not possible to make measurements for the PE-2/N6 and PE-2/PC systems because the temperature of measurements was over 200°C at which the silicone oil began to degrade and vaporize. The elongational viscosity χ, shrinkage $\frac{\Delta L}{L}$ and elongation to break $\ln \frac{L_B}{L_o}$ of polyethylene-polystyrene blends are discussed.

C.1. Shrinkage

C.1.1. Results. We found that the blend samples extruded from the single extruder exhibited considerable shrinkage when immersed in the silicon oil bath (180°C). The degree of shrinkage was expressed in terms of $\frac{\Delta L}{L_o}$ where $\Delta L = L - L_o$, L is the shrinkaged length and L_o is the initial length. Figure V-25 shows the shrinkage of polyethylene-polystyrene blends against composition. The shrinkage increased suddenly with loading of high density polyethylene. A 10 percent addition of PE into PS led to a 6-9 fold increasing shrinkage. At 50/50, those curves show a slight maximum.

C.1.2. Discussion. The shrinkage of polyethylene is larger than that of polystyrene. The tendency of shrinkage of PE/PS blends is similar to polyethylene. In general, the shrinkage shows the ability of viscoelastic liquid to recover from shear strain. In the case of blends, the filaments possess continuous ligaments of PE extended by shear strain in the extruder. The recovery and shrinkage of these ligaments generates the shrinkage of the bulk filament.

C.2. Elongational Viscosity

C.2.1. Results. Figures V-26 to V-44 show the transient elongational viscosity, $\chi(\dot{E},t)$ for PS, PE, and PE-PS blends at 180°C. In pure PS, $\chi(\dot{E},t)$ increases to steady-state values, almost equal to the Trouton prediction of viscosity which is three times the zero shear viscosity, indicated in these figures. In pure PE, $\chi(\dot{E},t)$

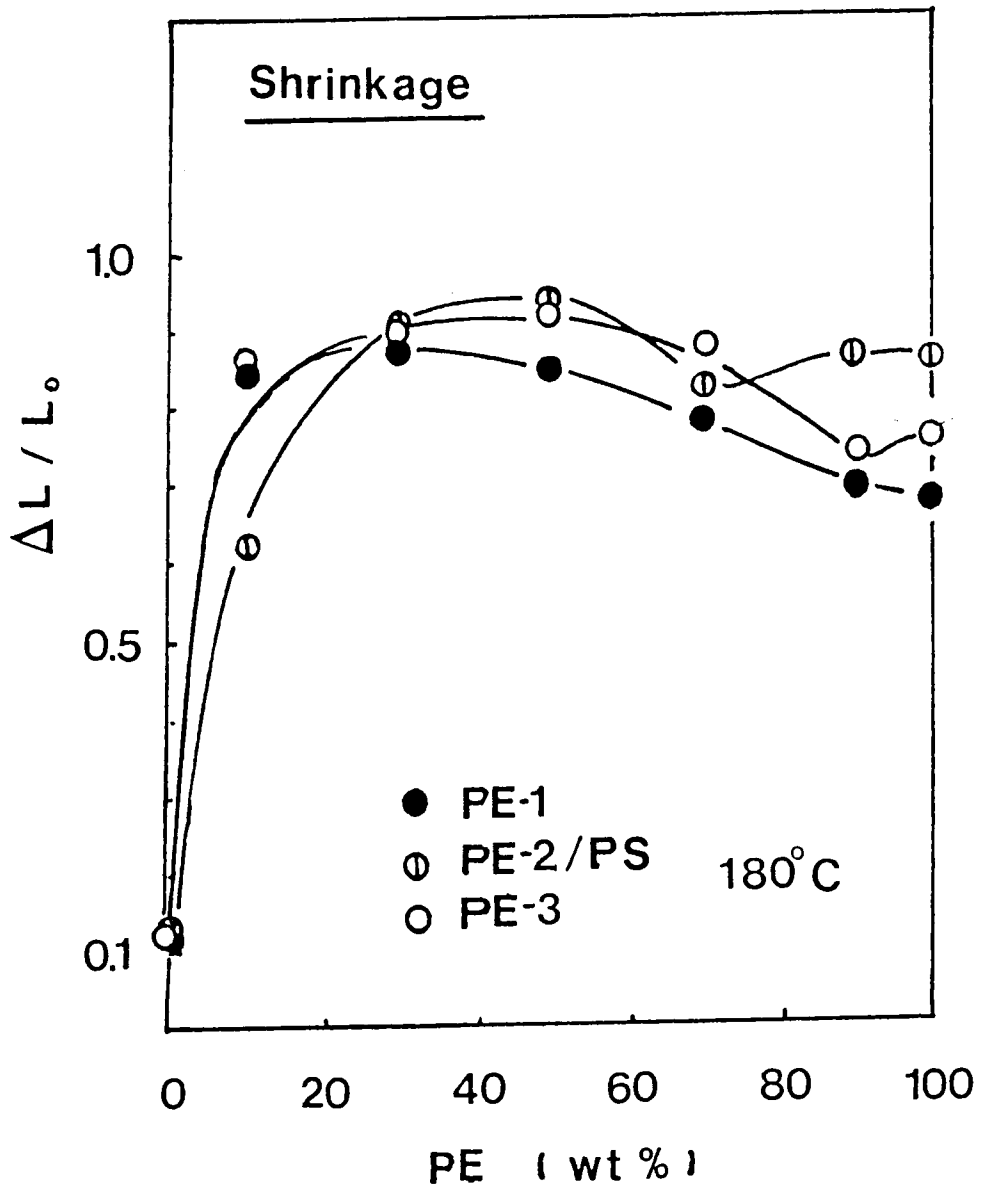


Figure V-25. Composition dependence of shrinkage for PE-1, 2, 3/PS blends.

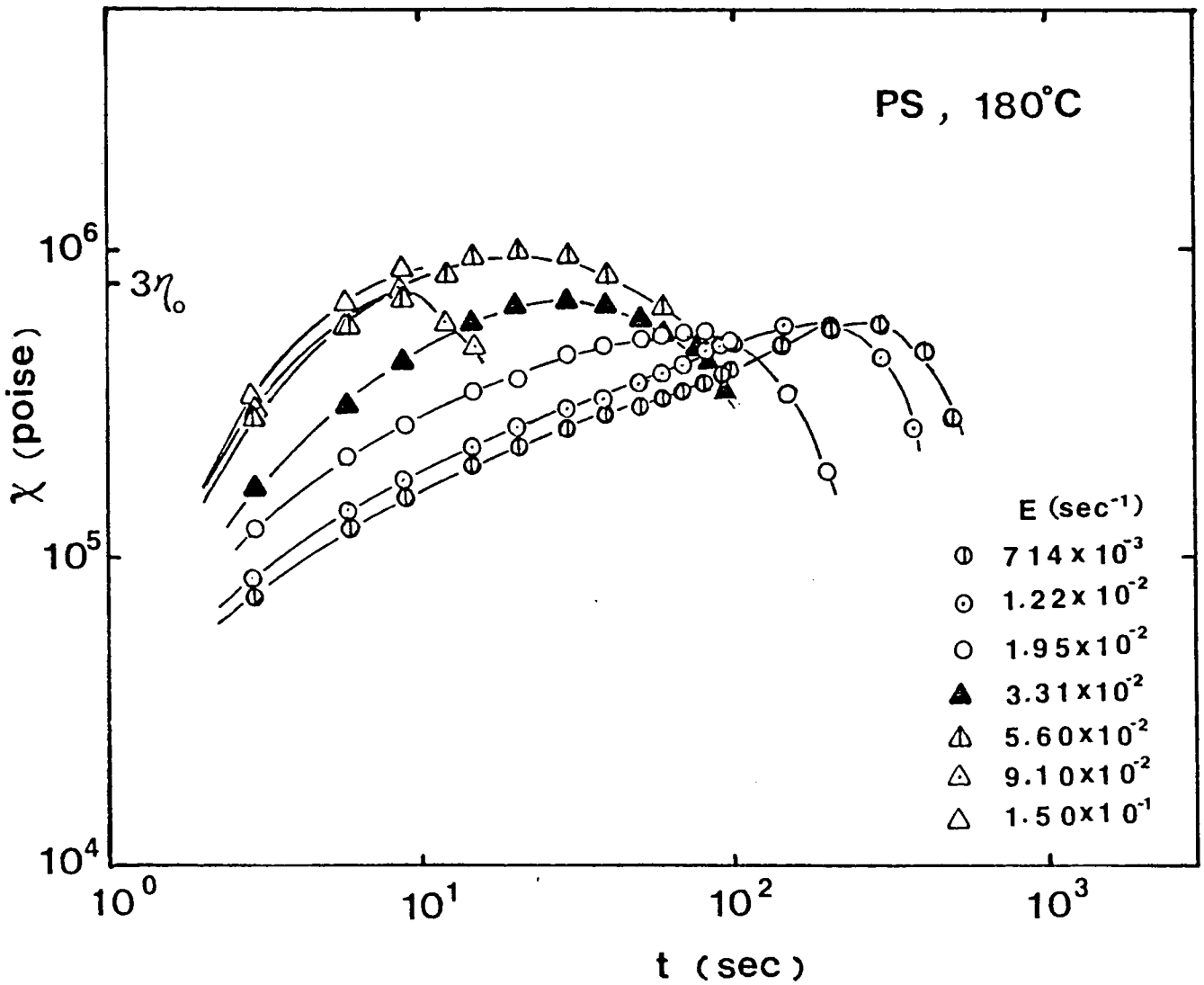


Figure V-26. Transient elongational viscosity ($\chi(t)$) as a function of elongation rate and time (t) for polystyrene.

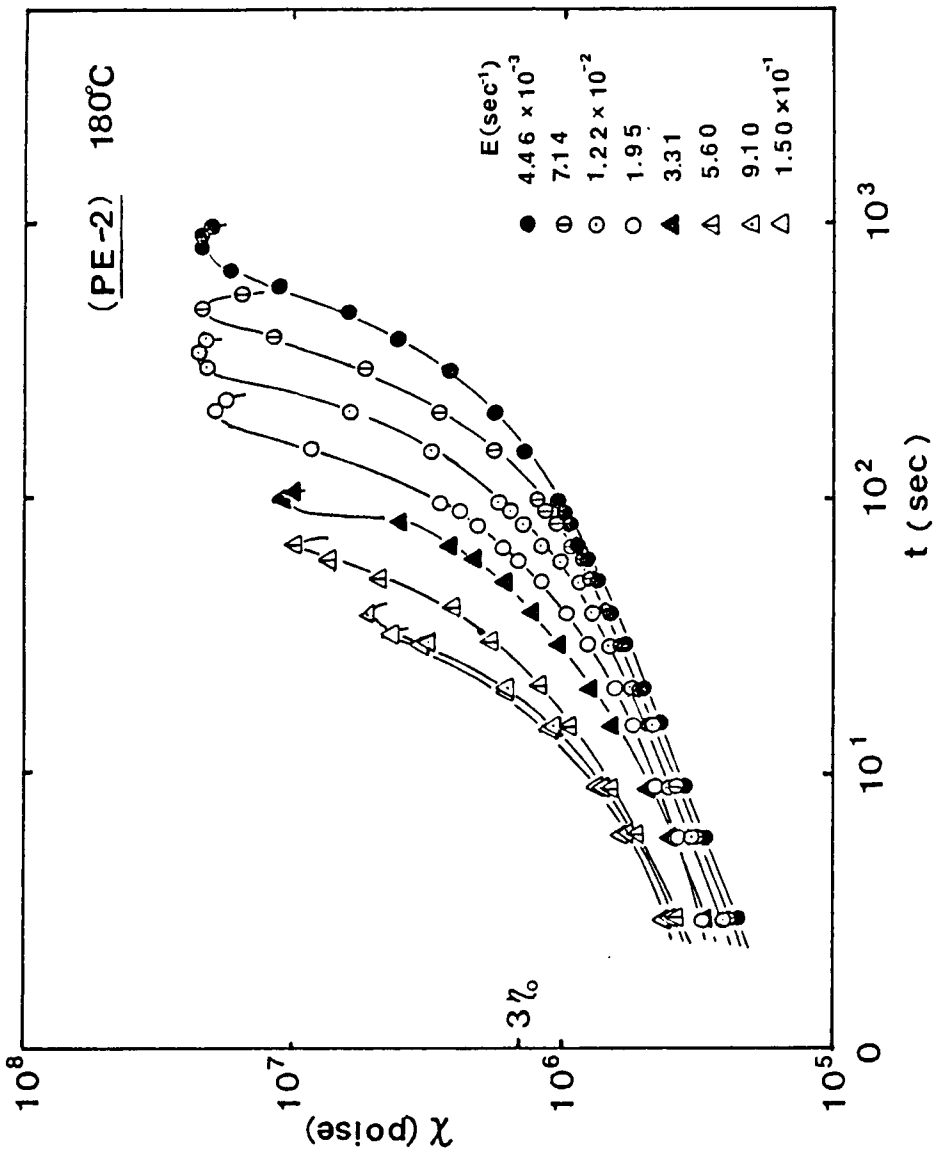


Figure V-27. Transient elongational viscosity ($\chi(t)$) as a function of elongation rate and time (t) for polyethylene (PE-2).

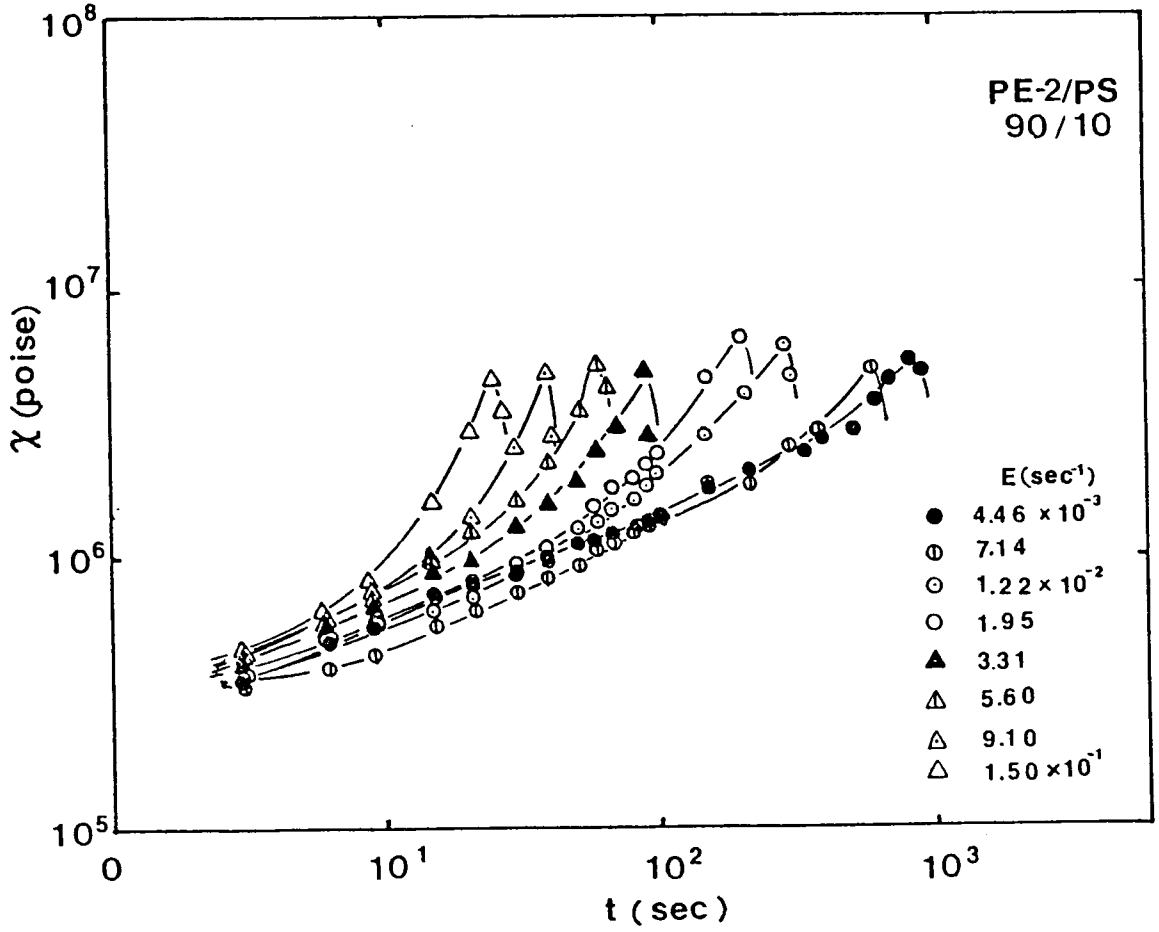


Figure V-28. Transient elongational viscosity ($\chi(t)$) as a function of elongation rate and time (t) for PE-2/PS-90/10 blend.

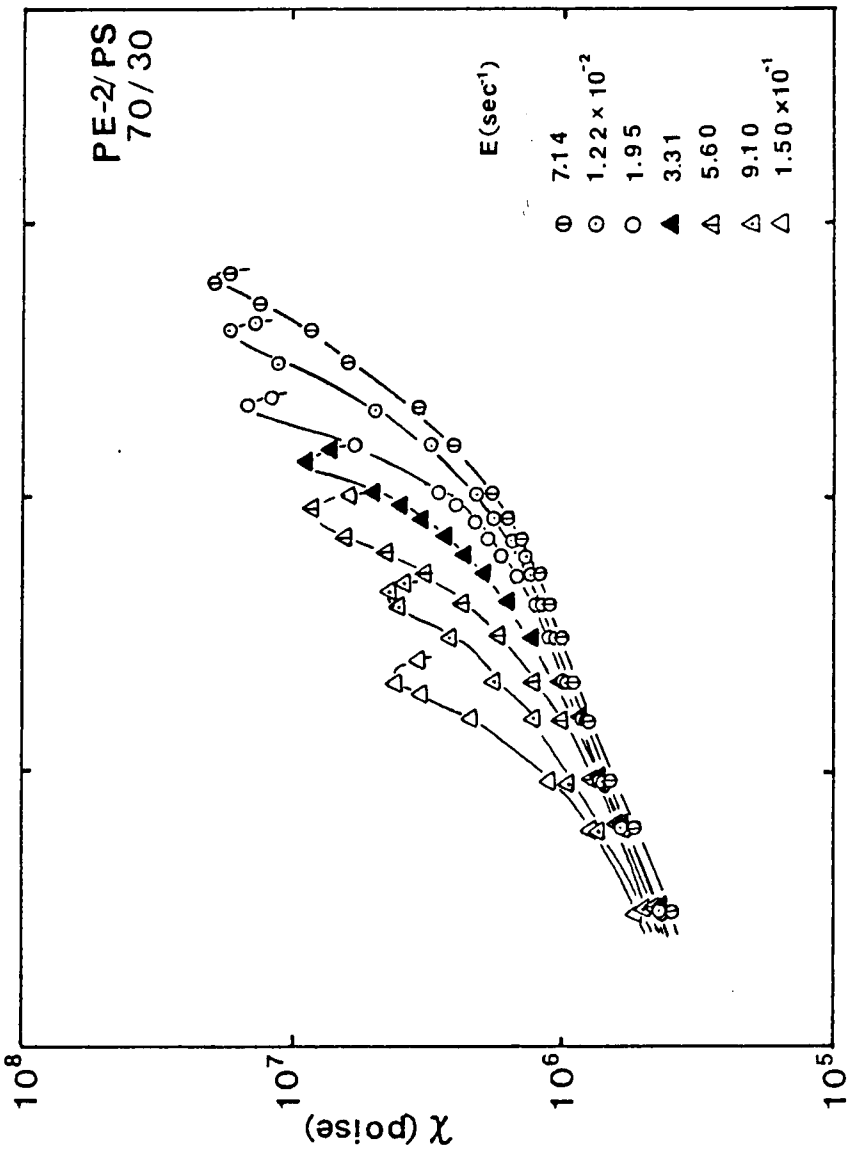


Figure V-29. Transient elongational viscosity ($\chi(t)$) as a function of elongation rate and time (t) for PE-2/PS-70/30 blend.

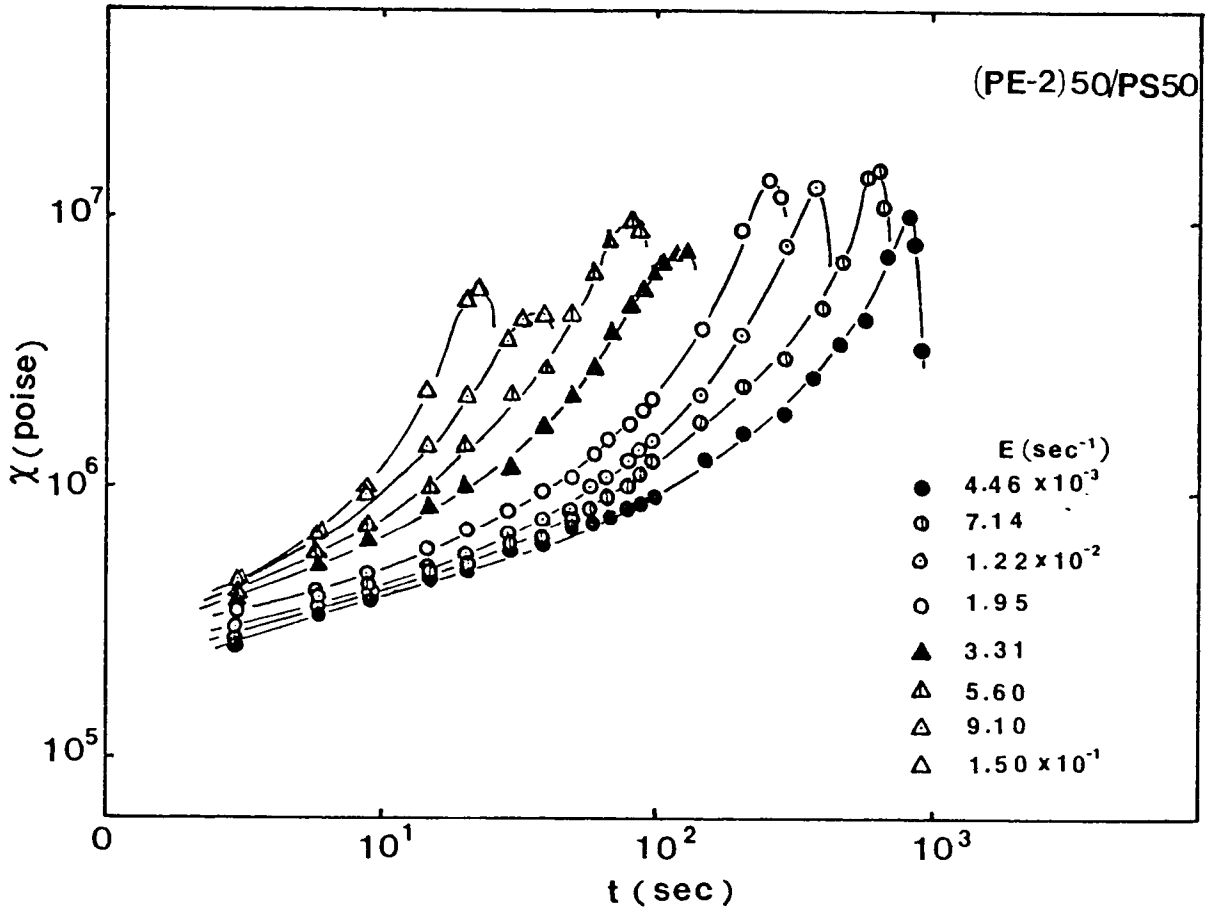


Figure V-30. Transient elongational viscosity ($\chi(t)$) as a function of elongation rate and time (t) for PE-2/PS-50/50 blend.

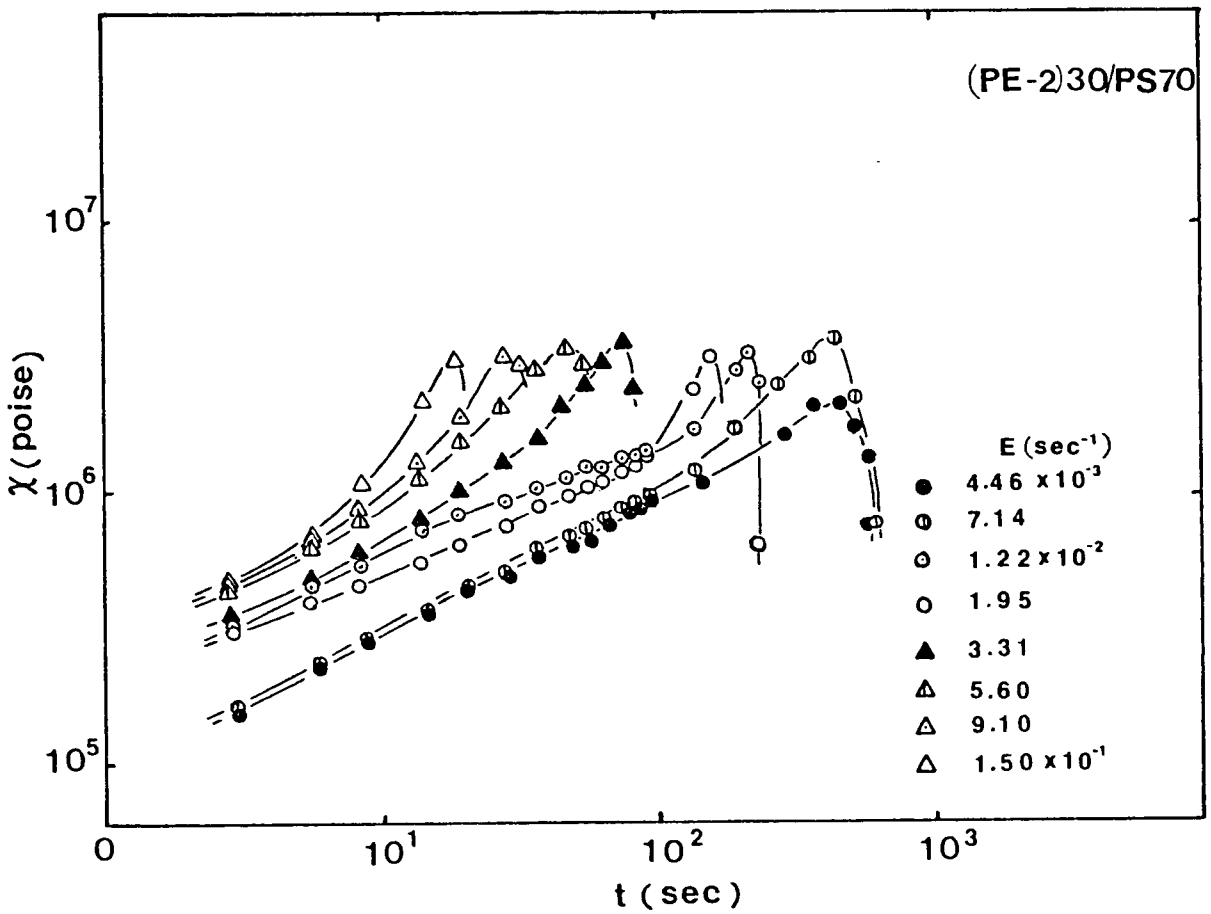


Figure V-31. Transient elongational viscosity ($\chi(t)$) as a function of elongation rate and time (t) for PE-2/PS-30/70 blend.

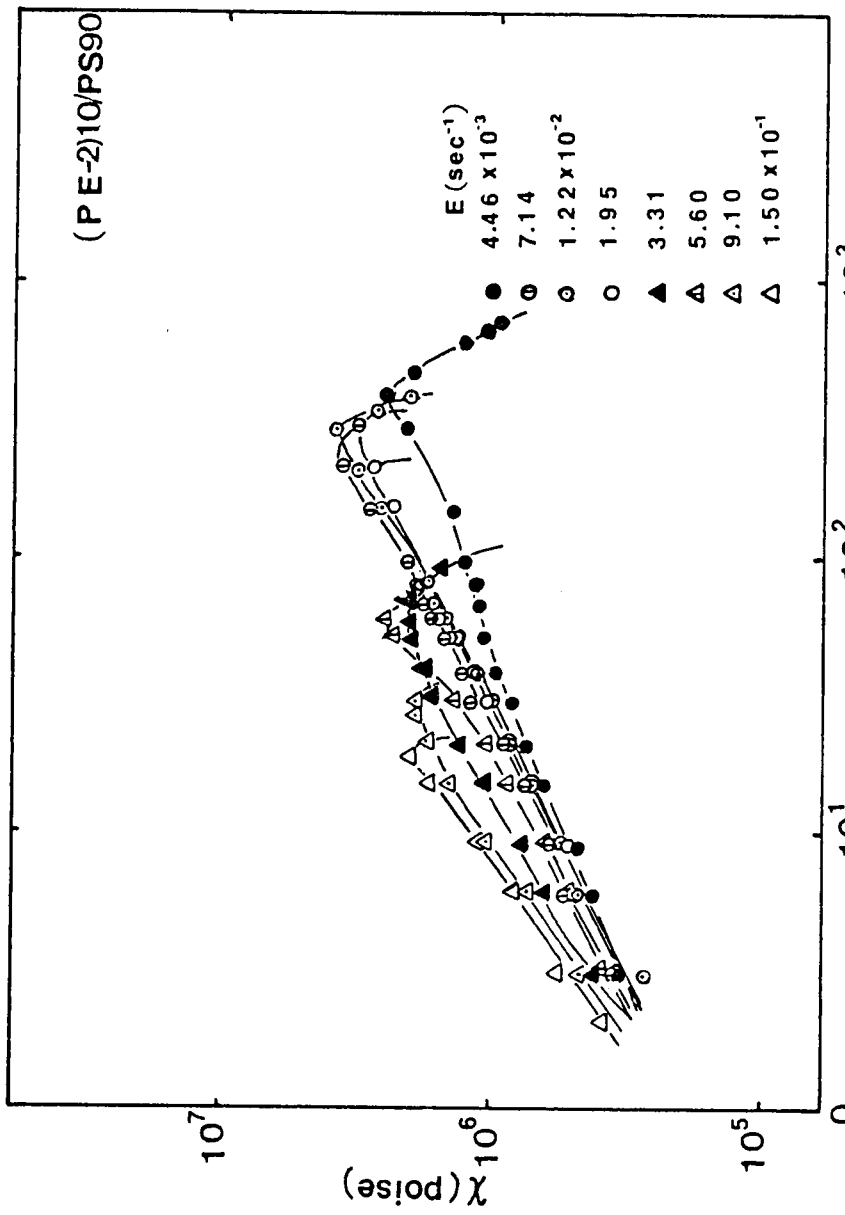


Figure V-32. Transient elongational viscosity ($\chi(t)$) as a function of elongation rate and time (t) for PE-2/PS-10/90 blend.

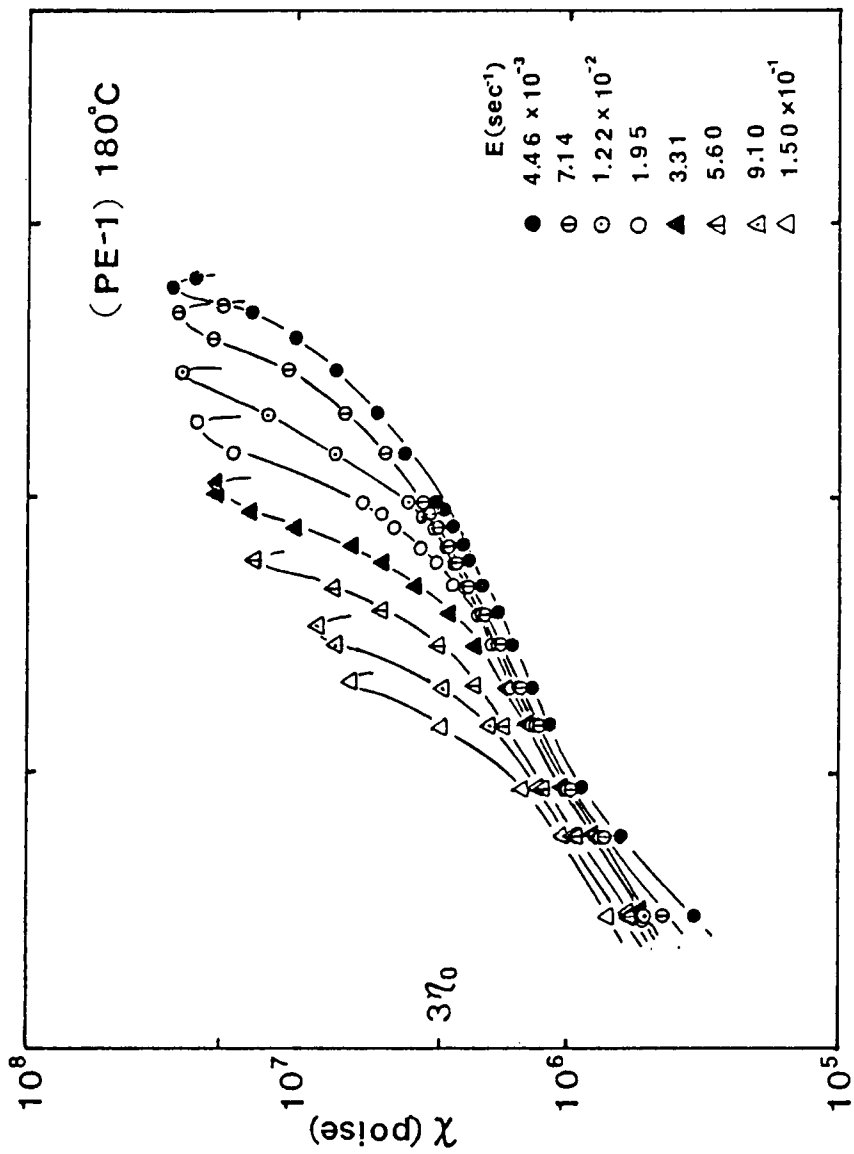


Figure V-33. Transient elongational viscosity ($\chi(t)$) as a function of elongation rate and time (t) for high density polyethylene (PE-1).

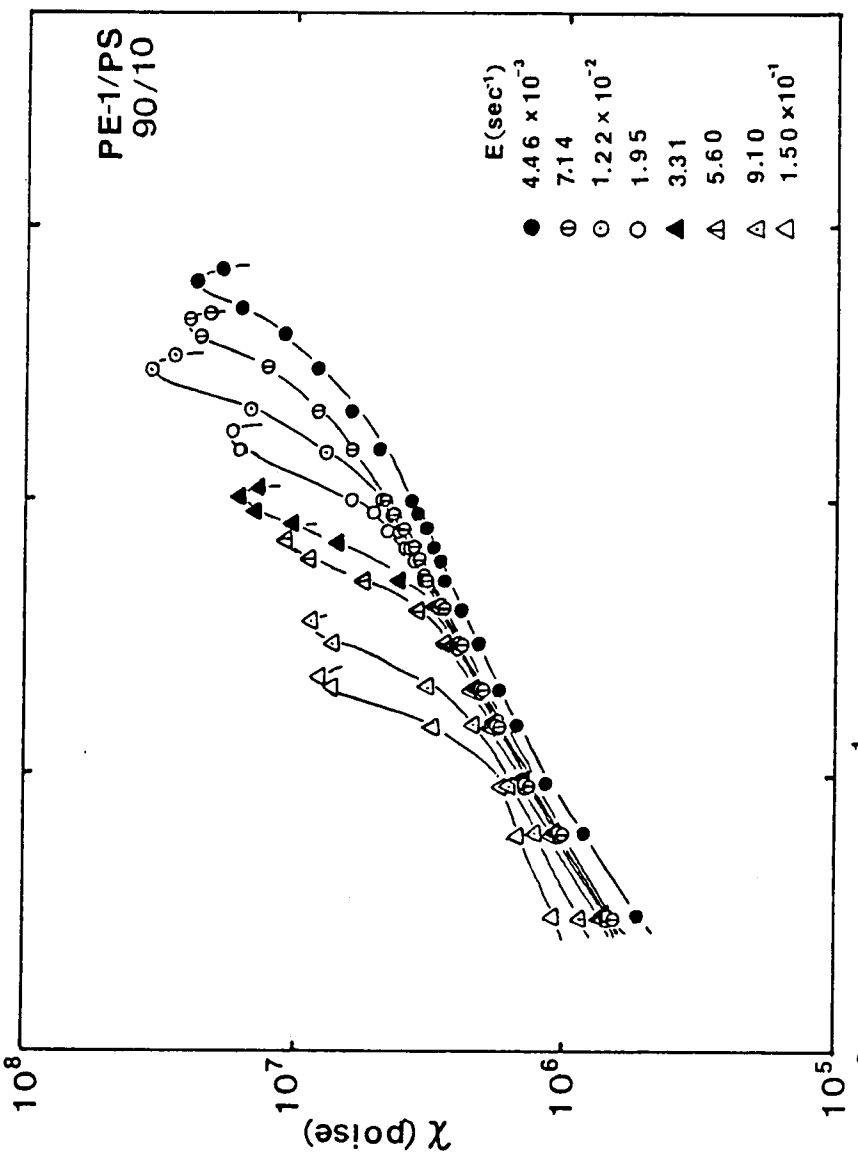


Figure V-34. Transient elongational viscosity ($\chi(t)$) as a function of elongation rate and time (t) for PE-1/PS-90/10 blend.

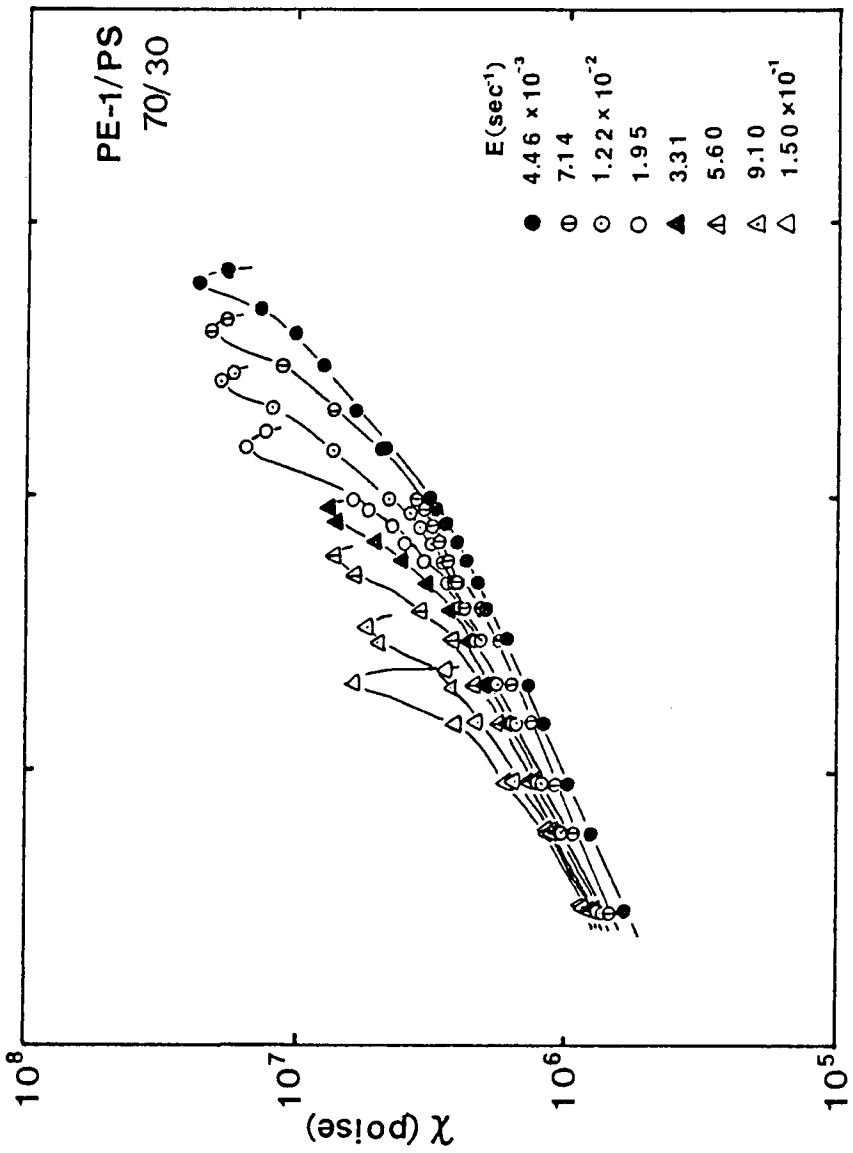


Figure V-35. Transient elongational viscosity ($\chi(t)$) as a function of elongation rate and time (t) for PE-1/PS-70/30 blend.

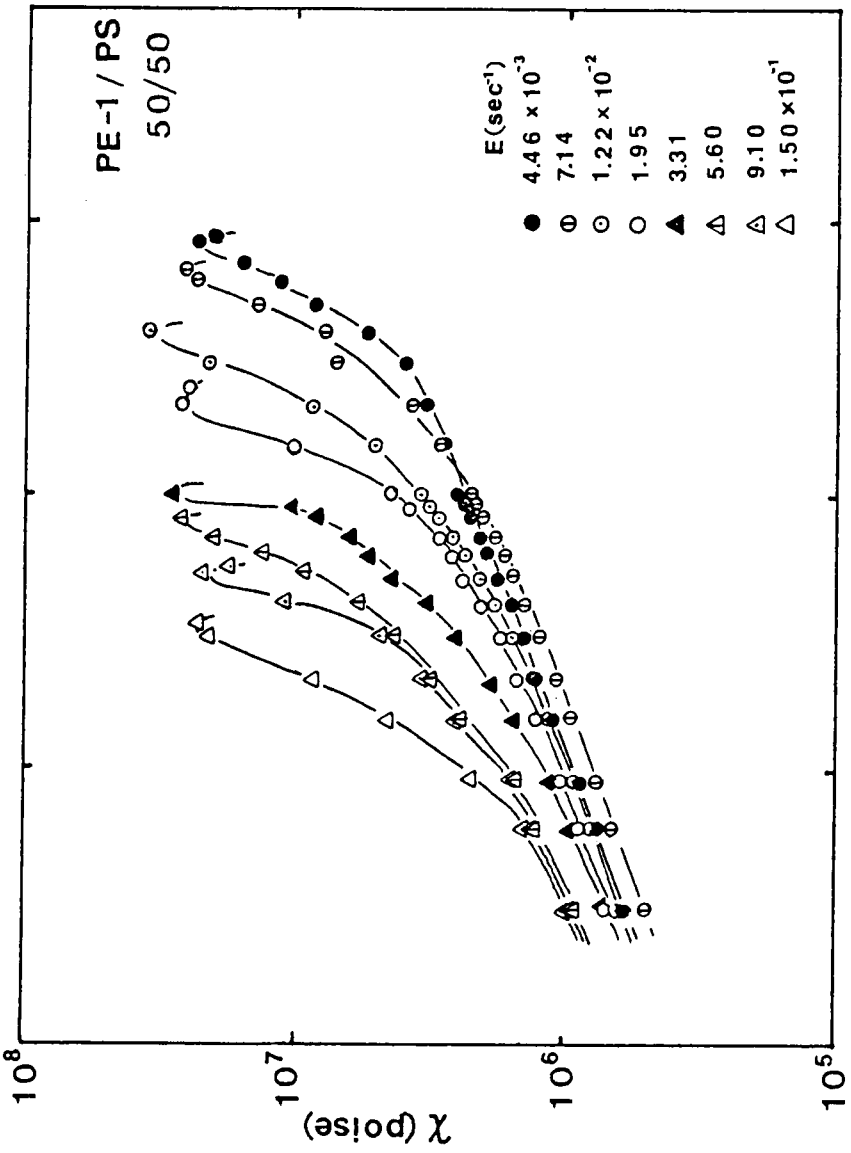


Figure V-36. Transient elongational viscosity ($\chi(t)$) as a function of elongation rate and time (t) for PE-1/PS-50/50 blend.

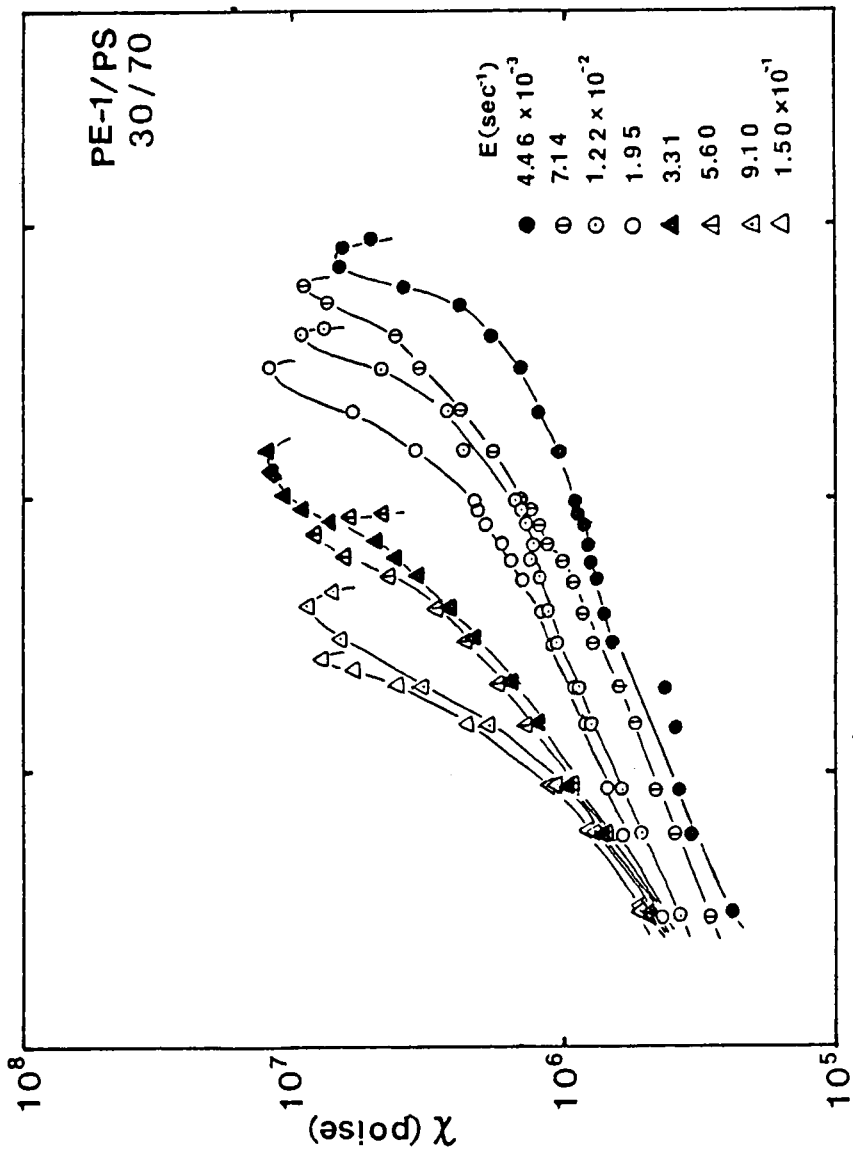


Figure V-37. Transient elongational viscosity ($\chi(t)$) as a function of elongation rate and time (t) for PE-1/PS-30/70 blend.

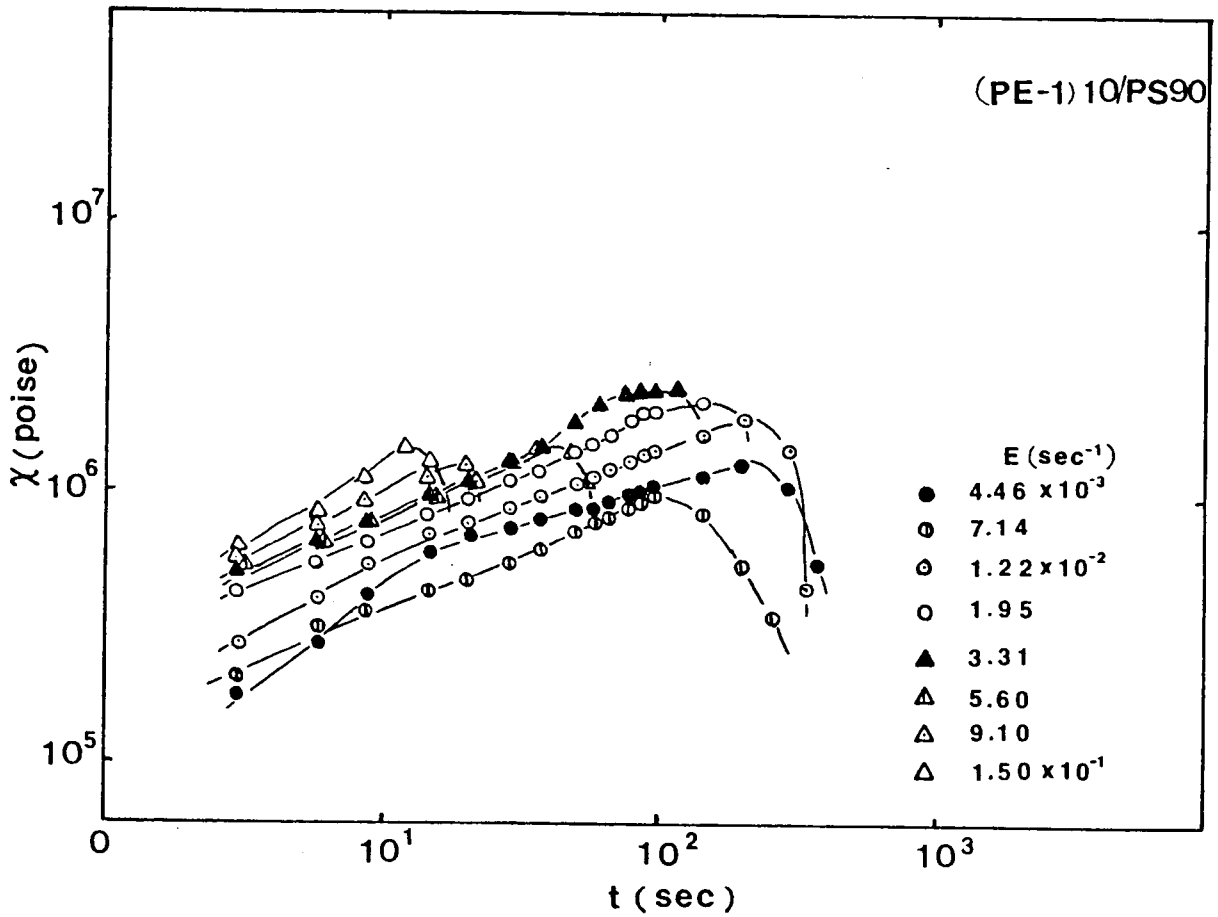


Figure V-38. Transient elongational viscosity ($\chi(t)$) as a function of elongation rate and time (t) for PE-1/PS-10/90 blend.

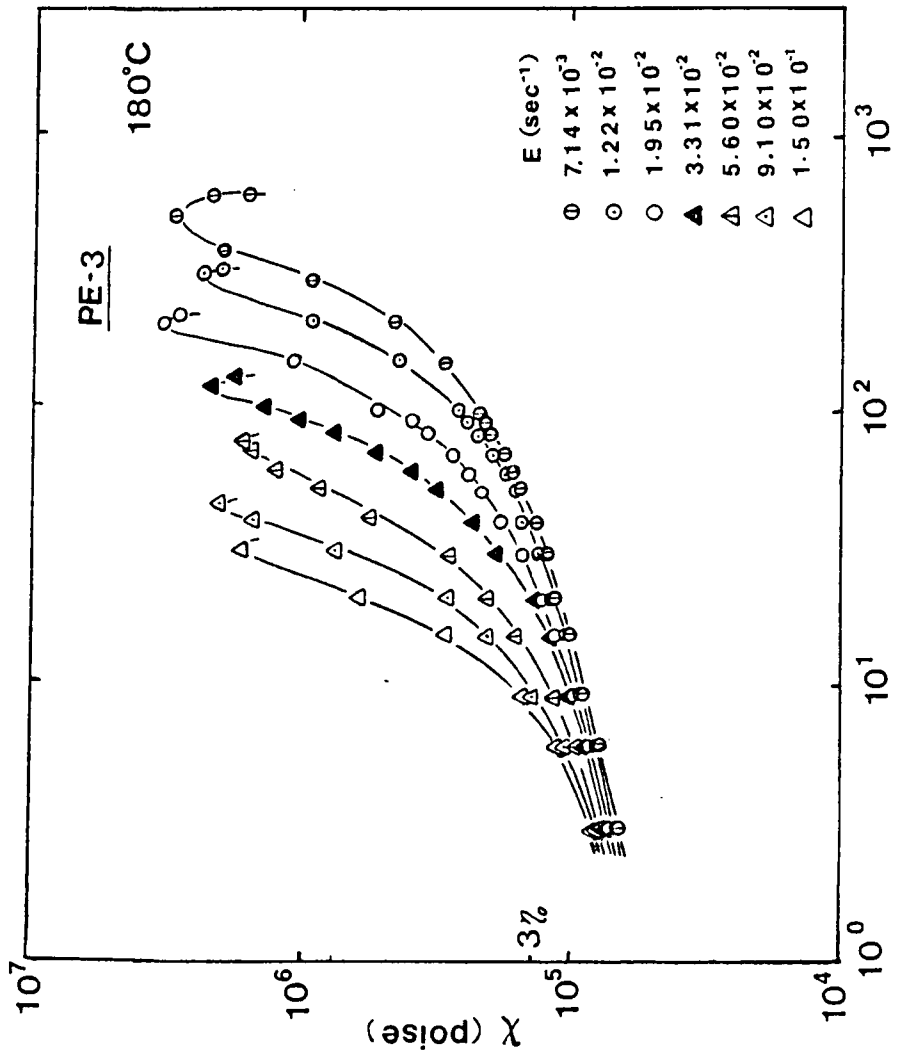


Figure V-39. Transient elongational viscosity ($\chi(t)$) as a function of elongation rate and time (t) for high density polyethylene (PE-3).

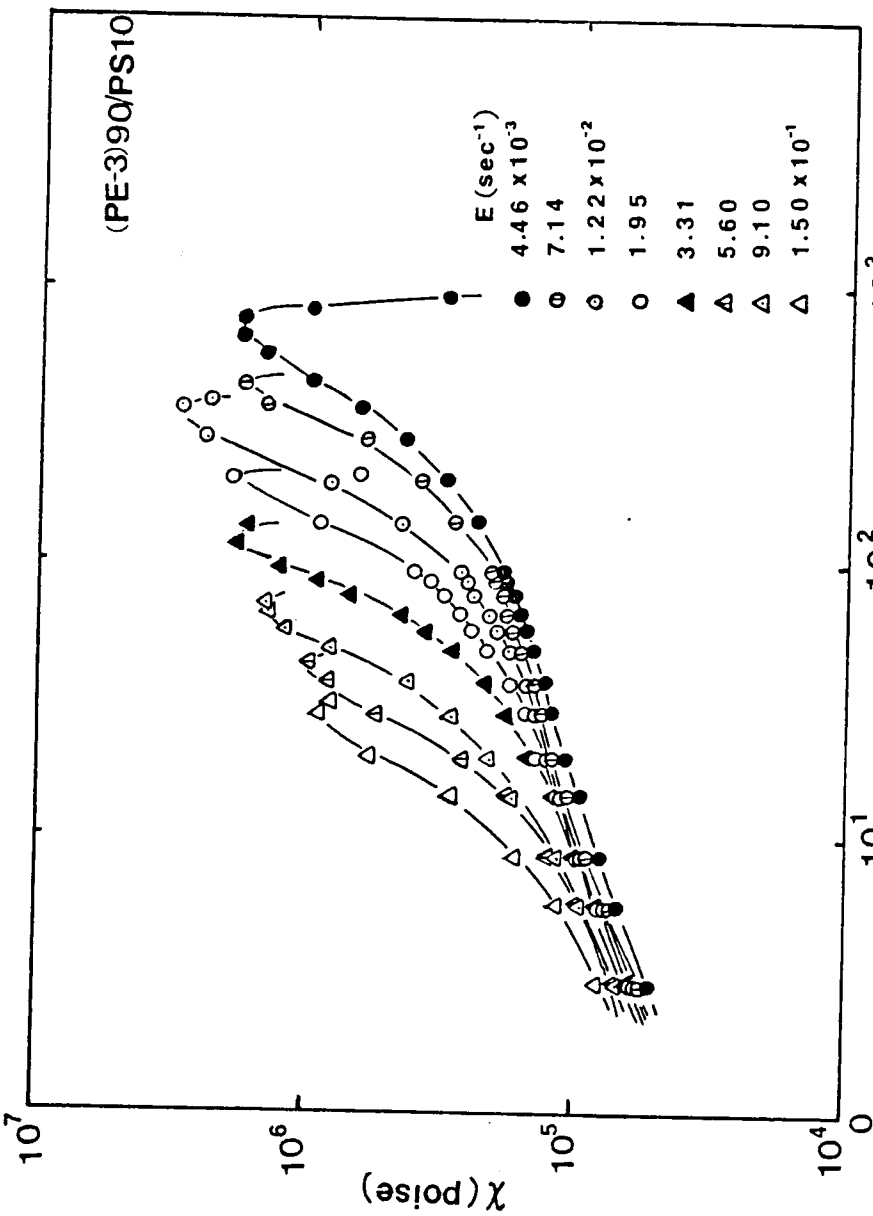


Figure V-40. Transient elongational viscosity ($\chi(t)$) as a function of elongation rate and time (t) for PE-3/PS-90/10 blend.

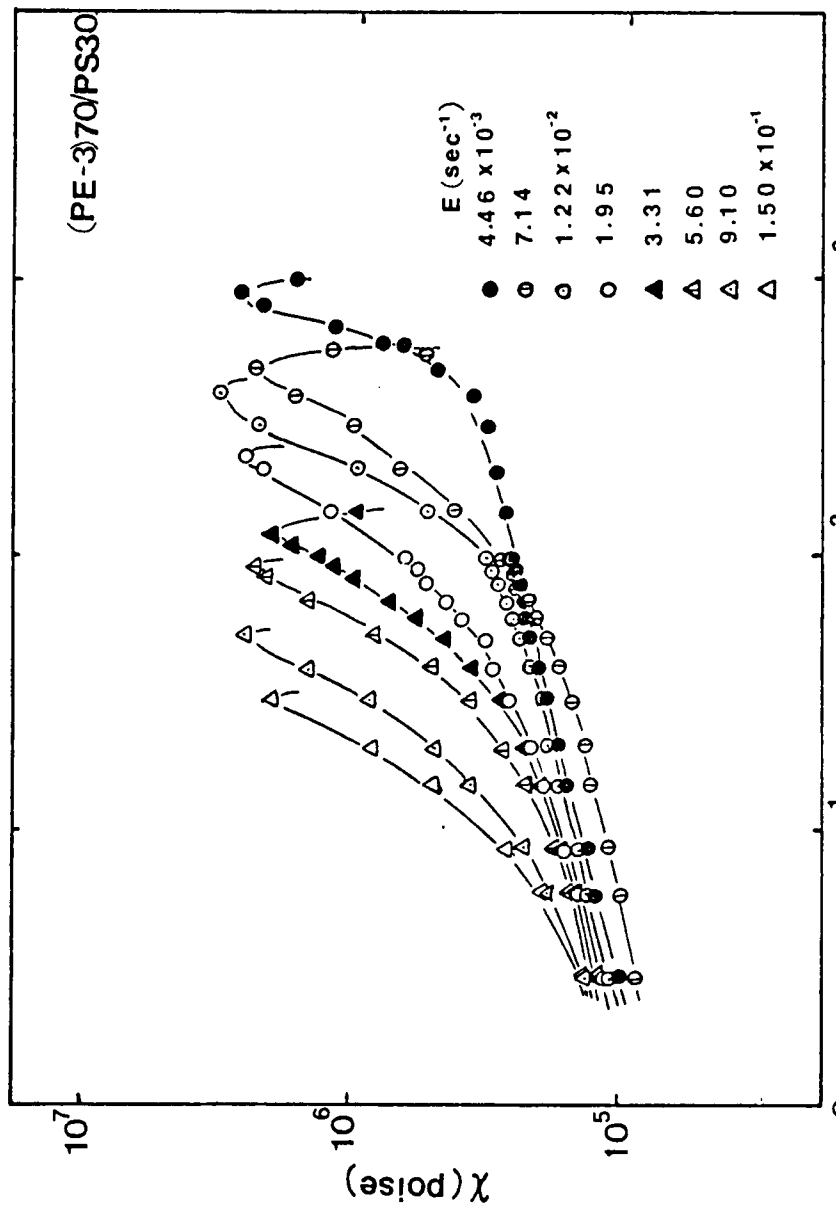


Figure V-41. Transient elongational viscosity ($\chi(t)$) as a function of elongation rate and time (t) for PE-3/PS-70/30 blend.

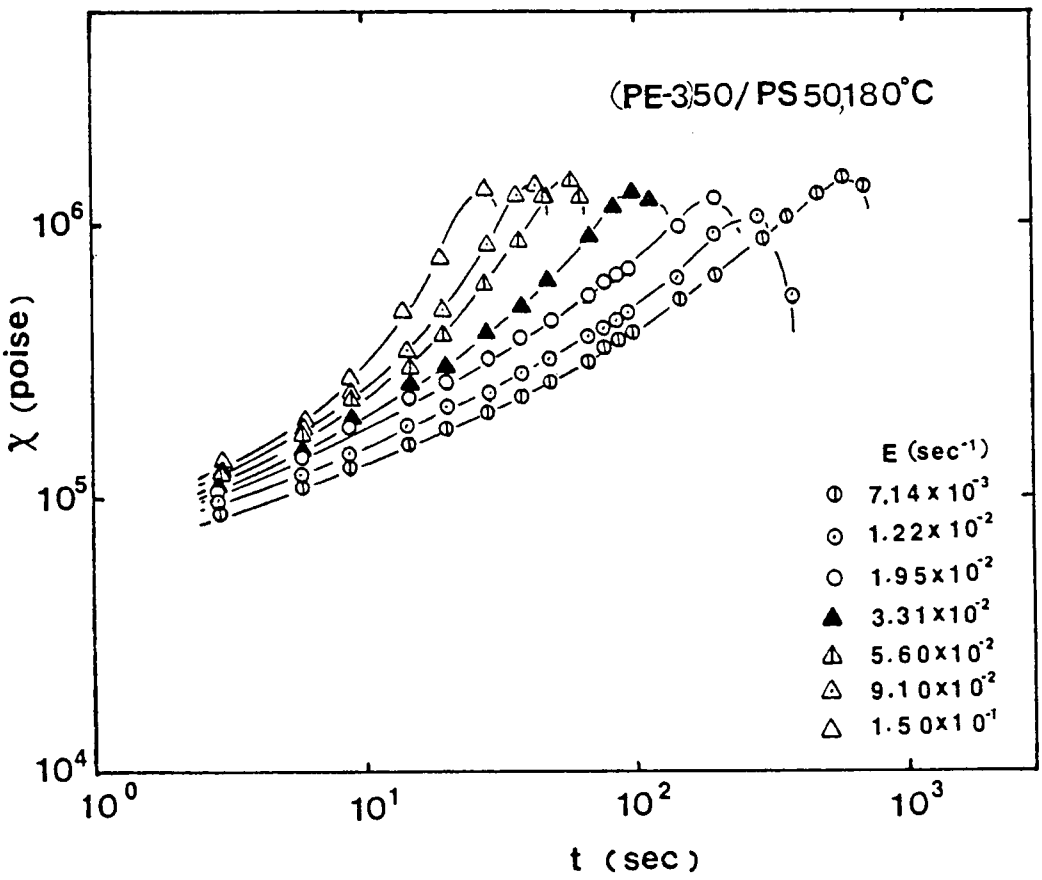


Figure V-42. Transient elongational viscosity ($\chi(t)$) as a function of elongation rate and time (t) for PE-3/PS-50/50 blend.

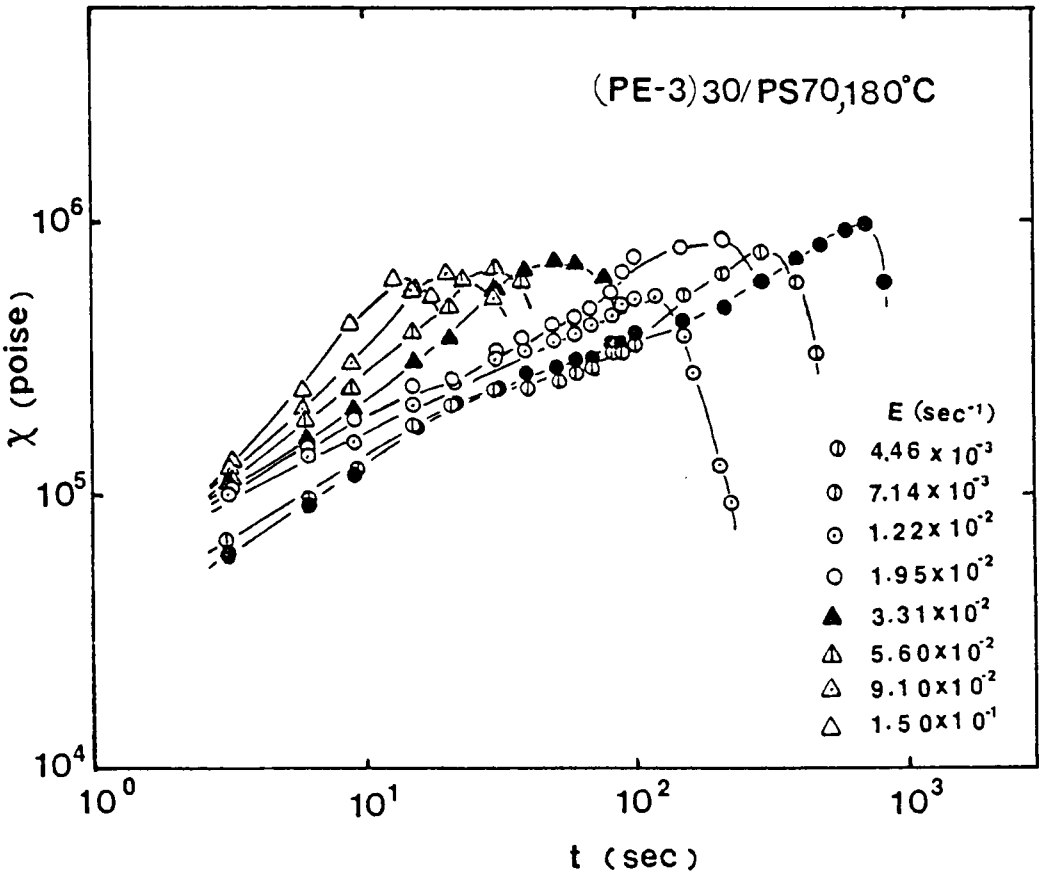


Figure V-43. Transient elongational viscosity ($\chi(t)$) as a function of elongation rate and time (t) for PE-3/PS-30/70 blend.

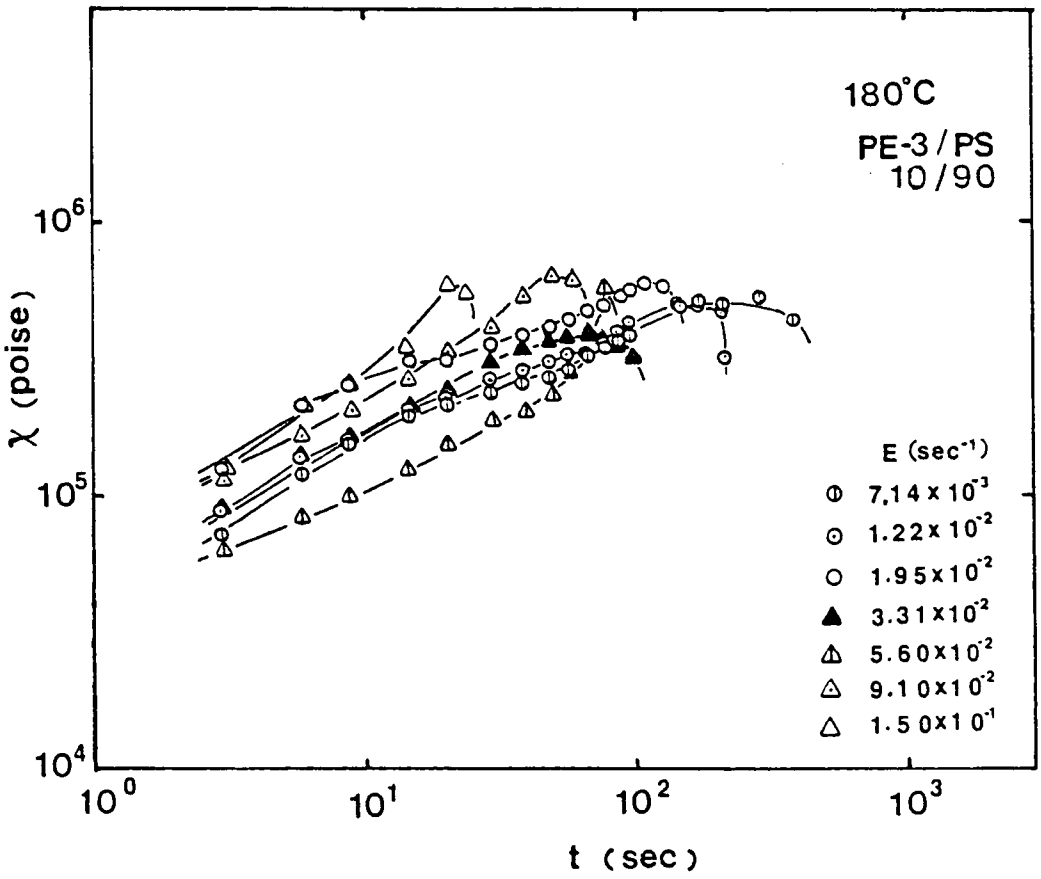


Figure V-44. Transient elongational viscosity ($\chi(t)$) as a function of elongation rate and time (t) for PE-3/PS-10/90 blend.

increases to a value much greater than $3\eta_0$ and reaches a maximum when failure proceeds. $\chi(\dot{E},t)$ for PE/PS blends which has a matrix of polyethylene with dispersed polystyrene behaves similarly to that of pure polyethylene. $\chi(\dot{E},t)$ for PE/PS blends which have a matrix of polystyrene with dispersed polyethylene do not show very large stresses, but their elongation to break are short. The effect of varying the polyethylenes which have different molecular weight and molecular weight distribution was observed. The PE-1/PS blends show higher maximum in Figures V-33 to V-38, pages 176-181, and shorter elongations to break. The PE-3/PS blends show lower maximum in Figures V-39 to V-44 and longer elongations to break. The transient behavior of all polyethylene-polystyrene blends systems are quite similar.

The steady-state elongational viscosity χ can be determined for each elongational rate from the transient elongational viscosity if a steady state is achieved. It was not possible to obtain a steady-state elongational viscosity χ of polyethylene and PE/PS-90/10 to 50/50 in the transient data. The maximum values are assumed to be the steady-state ones for PE and the PE/PS blends. Figures V-45 to V-47 are plots of χ versus $\dot{E}$ for PE, PS, and PE/PS blends. χ for three kinds of polyethylene shows the same behavior. Here, χ decreases with increasing elongational rate in comparison to polystyrene. The behavior of PE/PS blends resembles that of pure polyethylene.

C.2.2. Discussion. There is a complete lack in the literature of studies on the elongational viscosity on polymer melt blends.

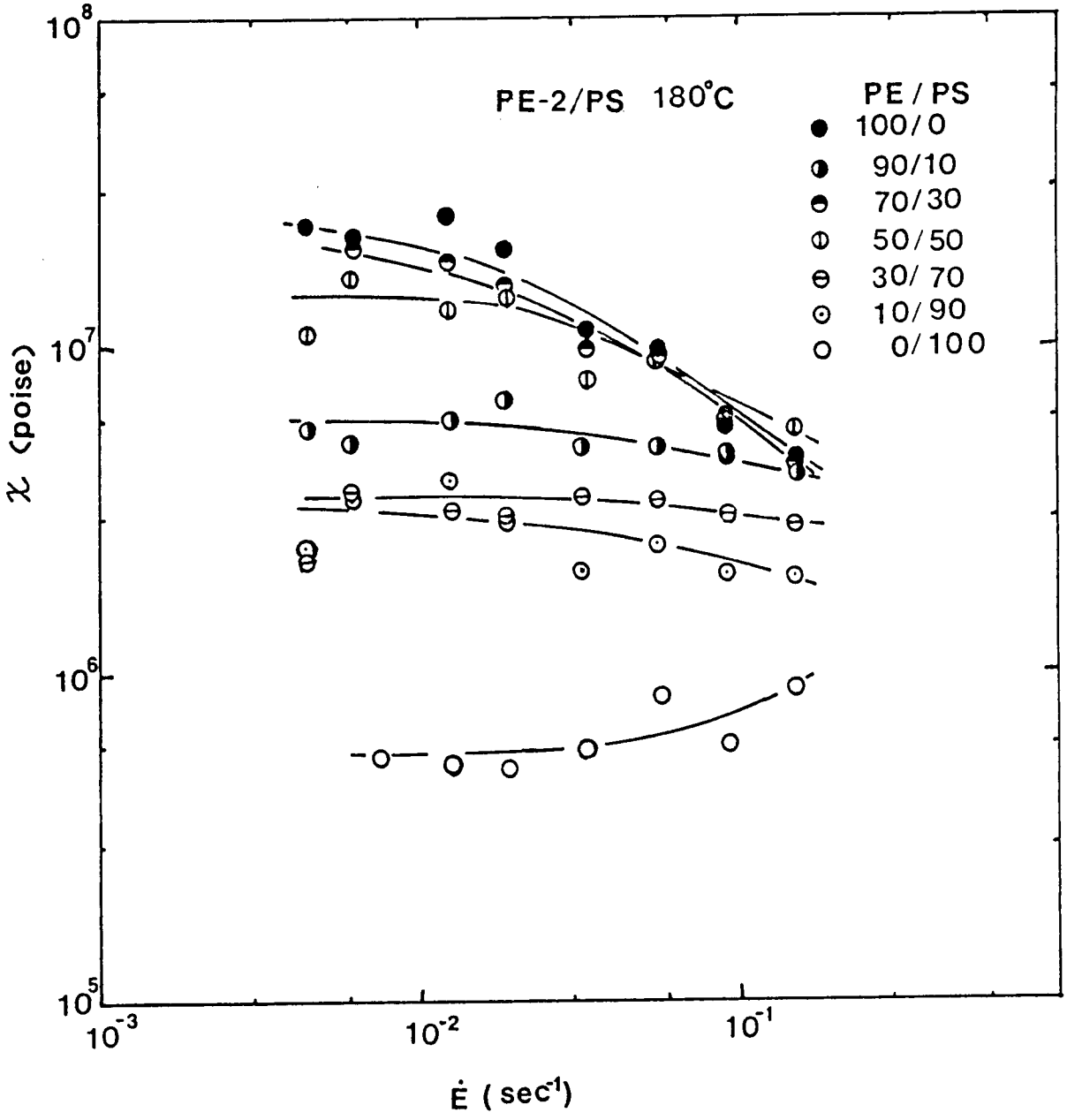


Figure V-45. Maximum elongational viscosity (χ) as a function of elongation rate ($\dot{E}$) for PE-2/PS blends.

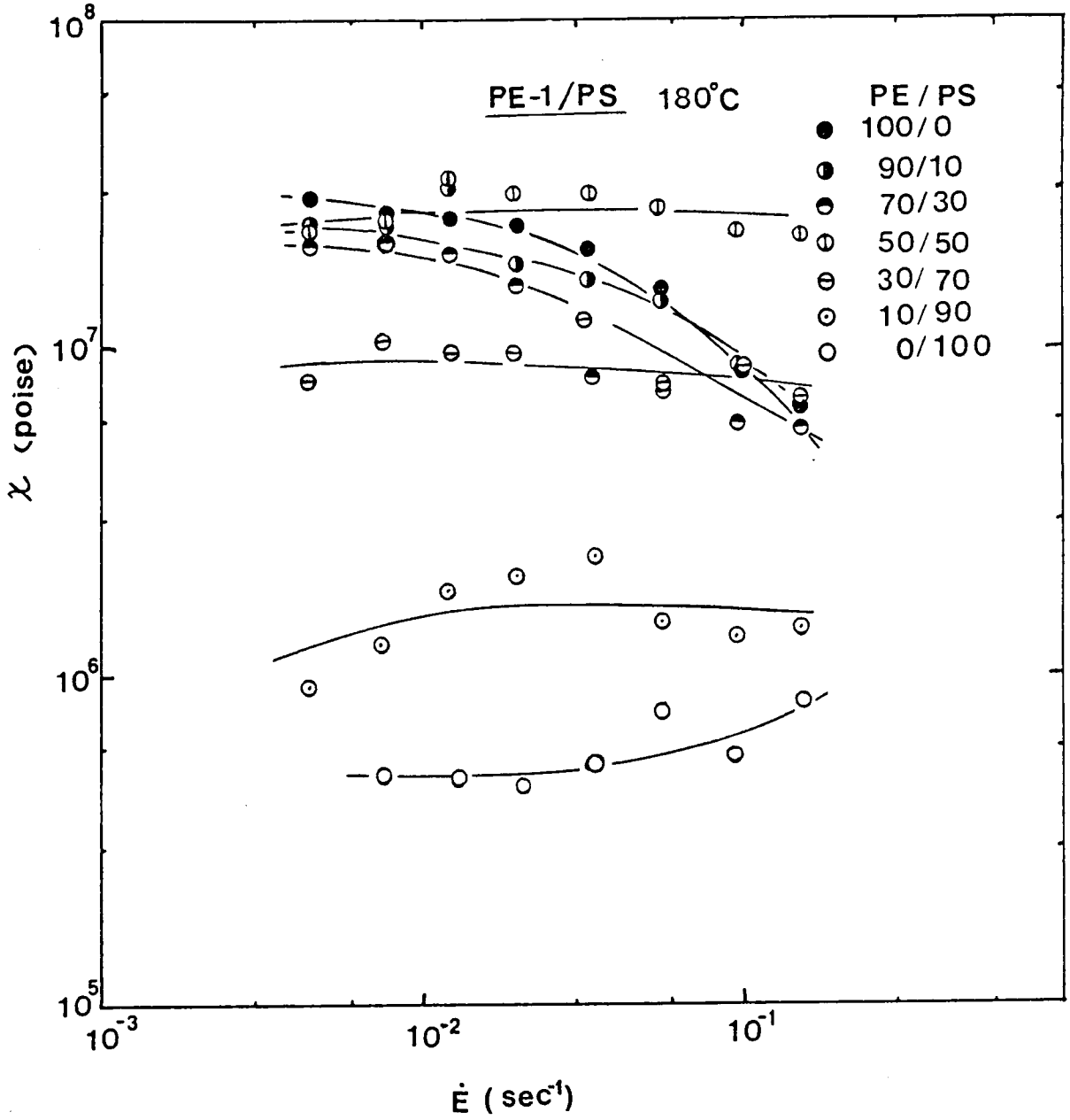


Figure V-46. Maximum elongational viscosity (χ) as a function of elongation rate ($\dot{E}$) for PE-3/PS blends.

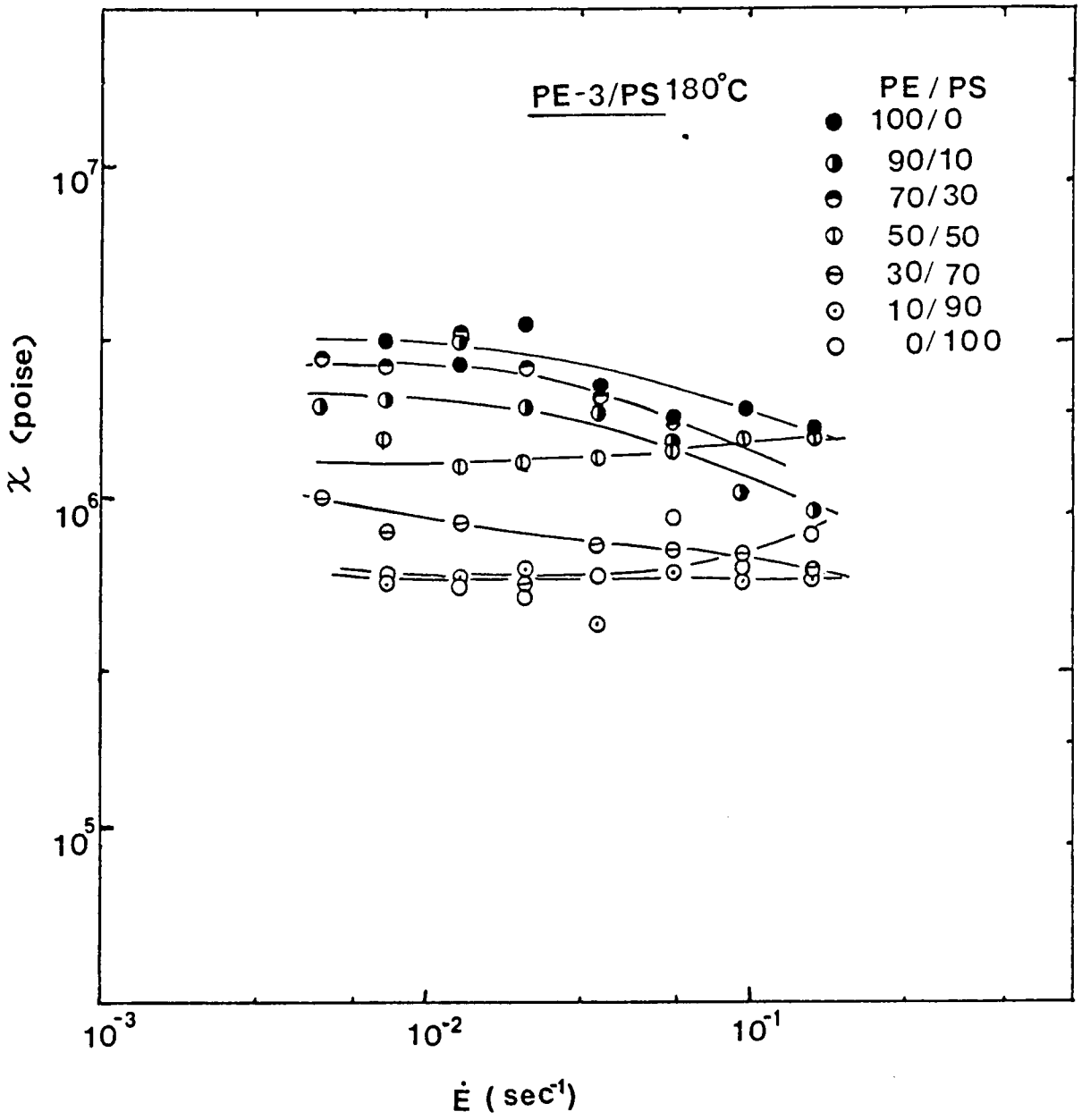


Figure V-47. Maximum elongational viscosity (χ) as a function of elongation rate ($\dot{E}$) for PE-3/PS blends.

Ide (71)(72) investigated high density polyethylene/polystyrene 50/50 blend and found that the 50/50 blend resembled PE which exhibited necking. In the present work, the PE/PS blends also resemble PE behavior.

For comparison purposes, the steady-state elongational viscosities reduced by their Trouton viscosities $3\eta_0$ are plotted in Figures V-48 to V-50. For the three PE/PS blends from these figures, one can observe the separation of materials into two groups according to the morphology, i.e., the dispersed polyethylene in the matrix of polystyrene or the dispersed polystyrene in a matrix of polyethylene.

Ide and White (71)(72) found that polystyrene and low density polyethylene have strongly increasing $\chi/3\eta_0$ with increasing elongational rate, while commercial high density polyethylene exhibited decreasing functional behavior. The $\chi/3\eta_0$ of PE/PS blends seems to be influenced by the morphology in the filaments. The PE/PS-90/10 to 50/50 which have the dispersed polystyrene in the polyethylene matrix shows strongly decreasing $\chi/3\eta_0$ with increasing elongational rate. The PE/PS-30/70 to 10/90 which have the dispersed polyethylene in the polystyrene matrix show constant or slightly decreasing behavior at high elongational rate. Pure PS shows constant and later increasing χ. One can see that the behavior of PE/PS blends primarily resembles that of polyethylene. The manner of elongational viscosity for PE, PS, and PE/PS blends is summarized in Table V-1.

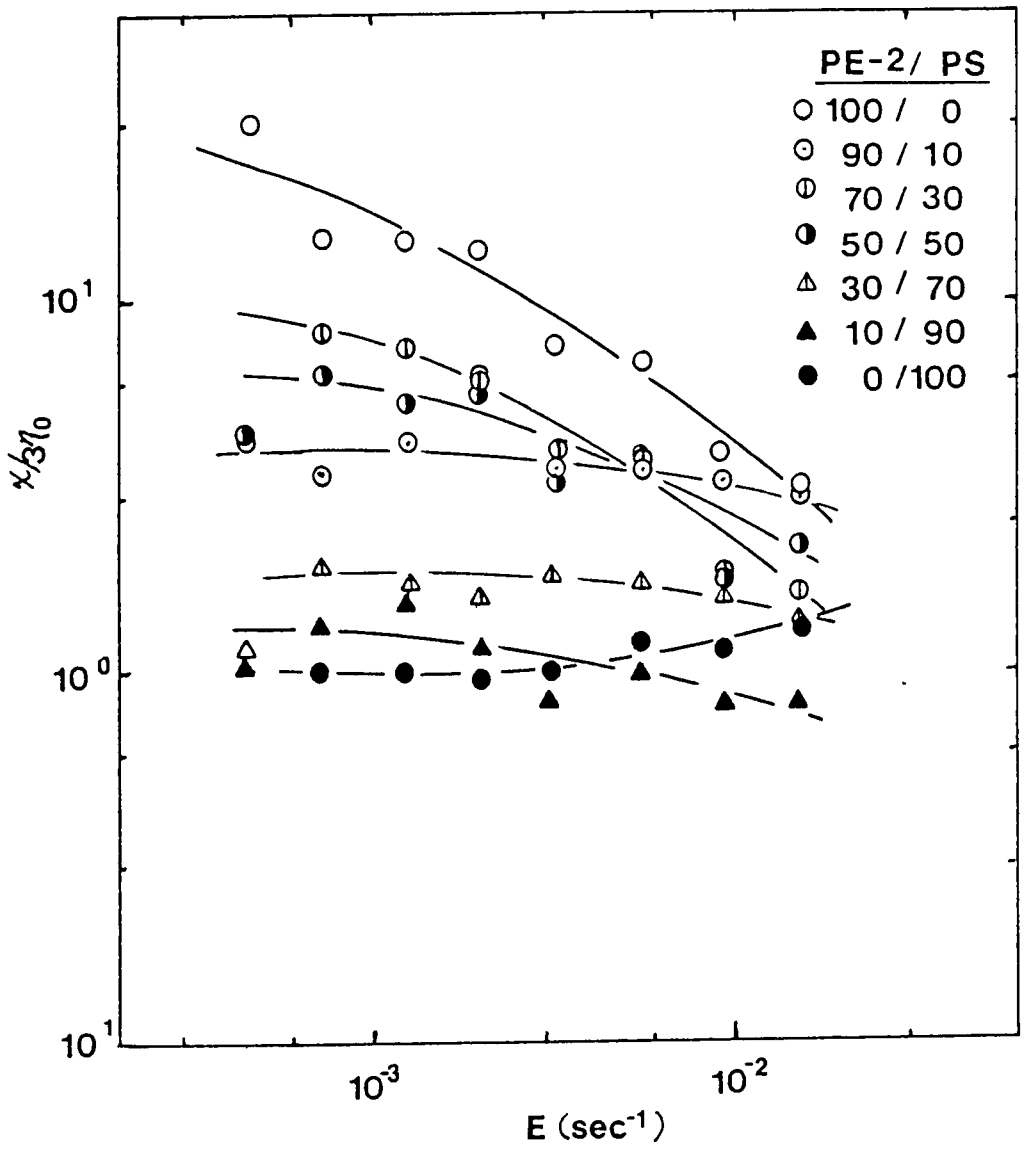


Figure V-48. Reduced elongational viscosity ($\chi/3\eta_0$) as a function of elongation rate ($\dot{E}$) for PE-2/PS blends.

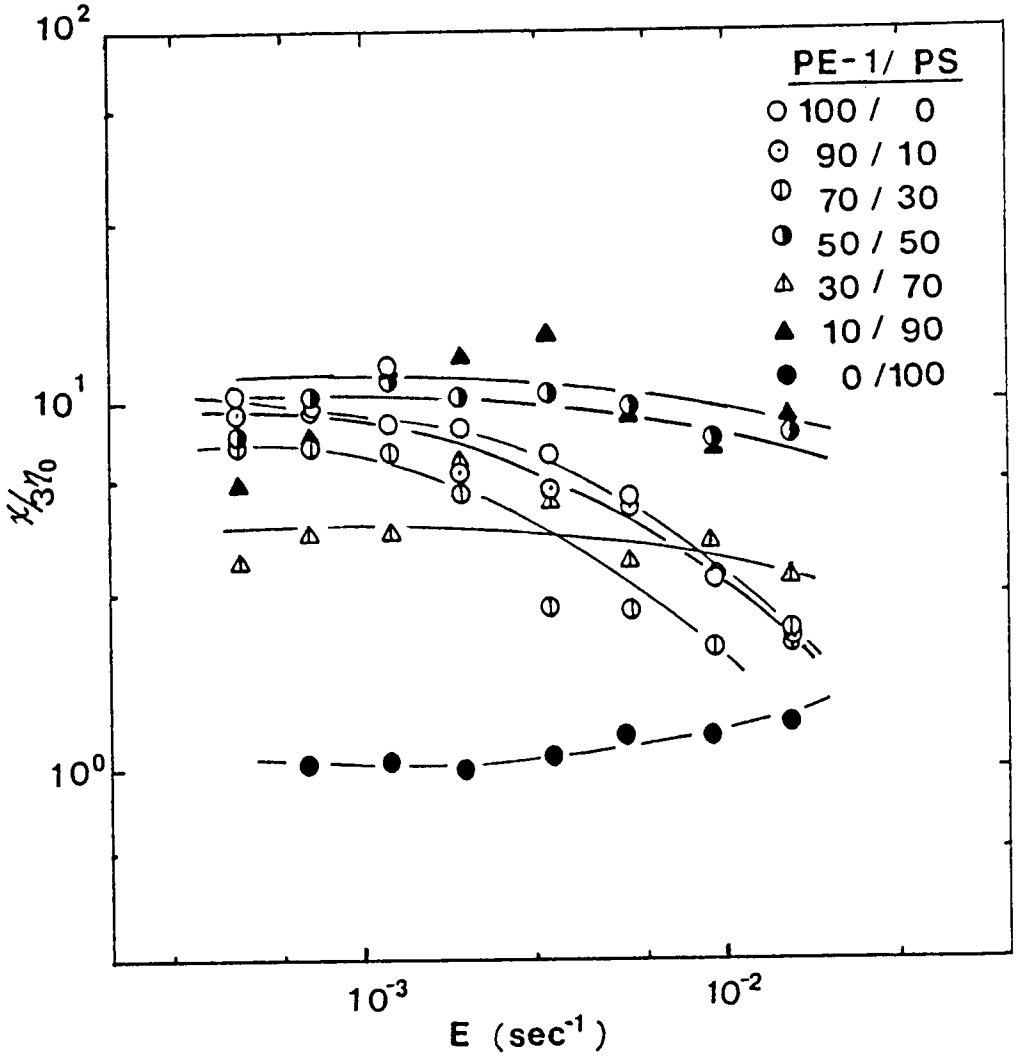


Figure V-49. Reduced elongational viscosity ($\chi/3\eta_0$) as a function of elongation rate ($\dot{E}$) for PE-1/PS blends.

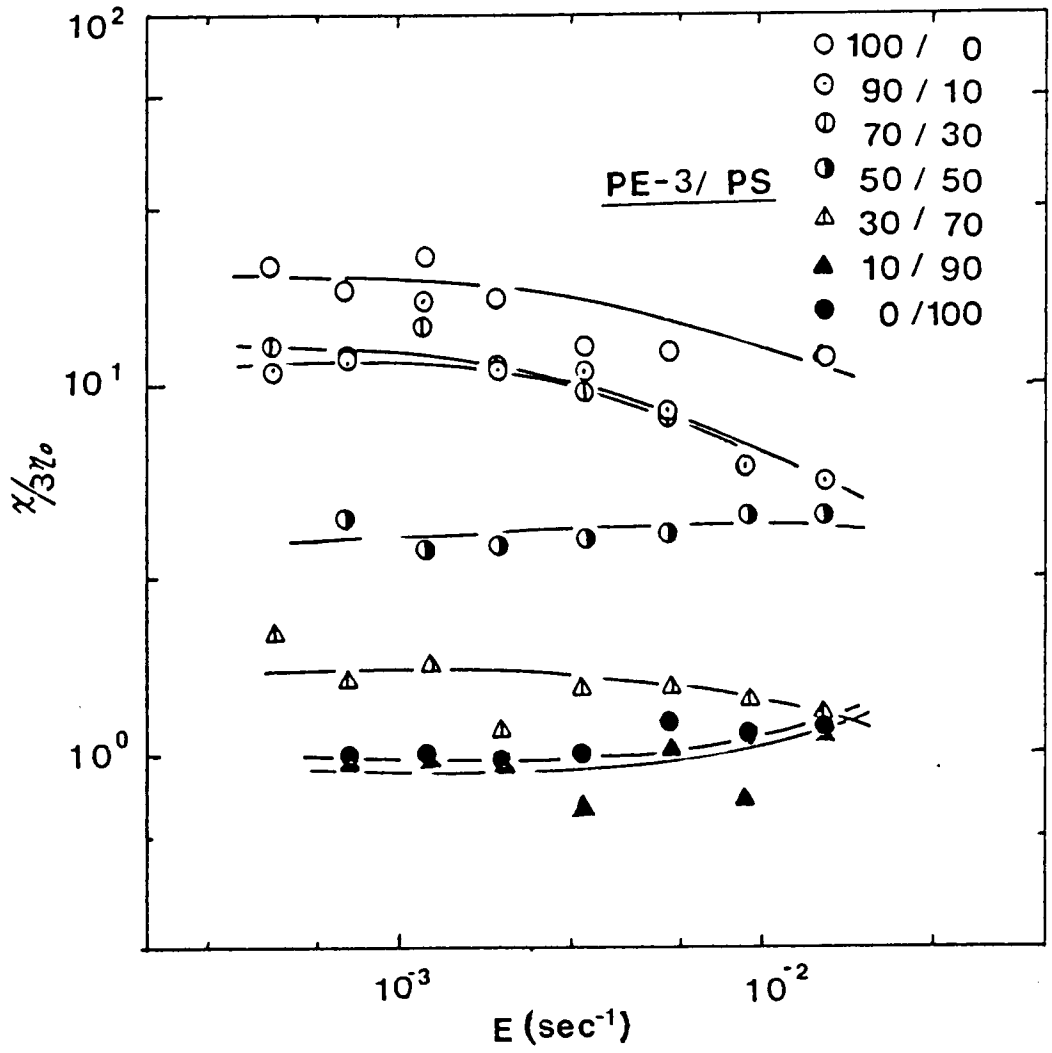


Figure V-50. Reduced elongational viscosity ($\chi/3\eta_0$) as a function of elongation rate ($\dot{E}$) for PE-3/PS blends.

Table V-1. Summary of maximum elongational viscosity for PE, PS and PE/PS blends

PE/PS Polymer Composition	$\chi/3\eta_0$ (PE-1)		$\chi/3\eta_0$ (PE-2)		$\chi/3\eta_0$ (PE-3)	
	Value at $10^{-3}sec^{-1}$	Slope	Value at $10^{-3}sec^{-1}$	Slope	Value at $10^{-3}sec^{-1}$	Slope
100/0	9.0	strongly decreasing	17.0	strongly decreasing	19.5	decreasing
90/10	8.5	strongly decreasing	3.9	constant or slightly decreasing	11.8	decreasing
70/30	7.0	strongly decreasing	7.8	decreasing	12.0	decreasing
50/50	10.5	constant or slightly decreasing	5.9	decreasing	3.0	constant
30/70	4.3	constant	1.8	constant	1.7	constant or slightly decreasing
10/90	11.8	constant	1.3	constant or slightly decreasing	1.0	increasing
0/100	1.0	increasing	1.0	increasing	1.0	increasing

C.3. Elongation to Break

C.3.1. Results. Figures V-51 to V-53 show elongation to break against the elongational rate for polyethylene-polystyrene blends. The PS has a greater elongation to break than the PE. These present plots show that the elongation to break decreases with the addition of PE.

C.3.2. Discussion. The blended systems show constant elongations to break at low deformation rates, similar to the behavior of pure PE. The three series of PE have the different molecular weight, the molecular distribution, and the much different shear viscosity. Ide and White (71)(72) and Minoshima and White (104) argued that the failure mechanism of PE was ductile necking and that of PS was brittle. They found that the narrower the molecular weight distribution, the higher elongation to break, the less softening of the elongational viscosity with stretch rate and more stable filaments. This explains the difference in PE and PS. The comparisons of elongation to break for PE/PS blends are listed in Table V-2. The behaviors of elongation to break for PE/PS blends are quite similar to that of pure PE. The addition of PE to PS decreases the elongation to break. The present work for PE, PS and PE/PS-50/50 is compared to Tanaka's. His data for blends are much lower than ours due to the instrumental difference and probably dispersion. The tendency of PE/PS blend is the same as ours. However, the blend behavior similarity to PS must be associated with a weakest link perspective.

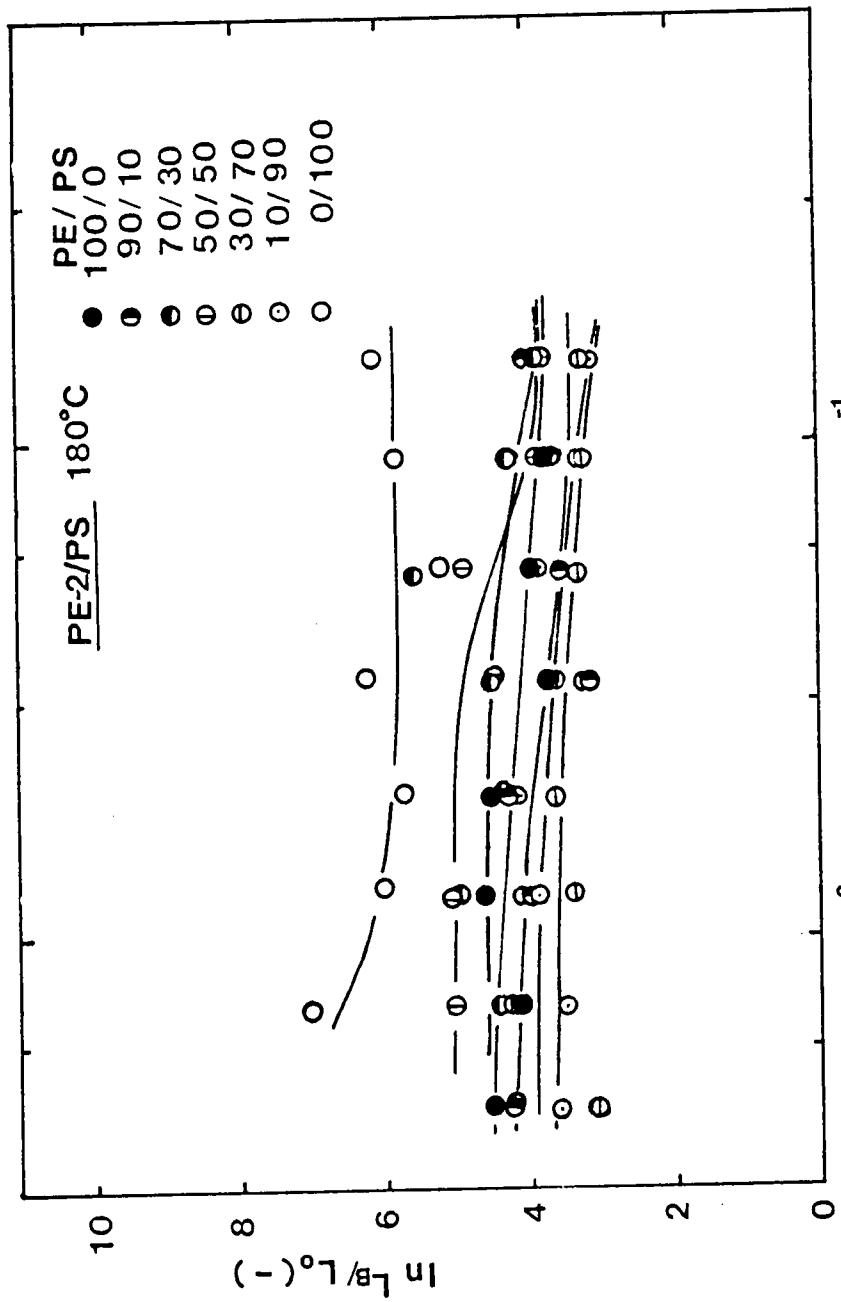


Figure V-51. Elongation to break (ln L_B/ln L_o) as a function of elongation rate ($\dot{E}$) for PE-2/PS blends.

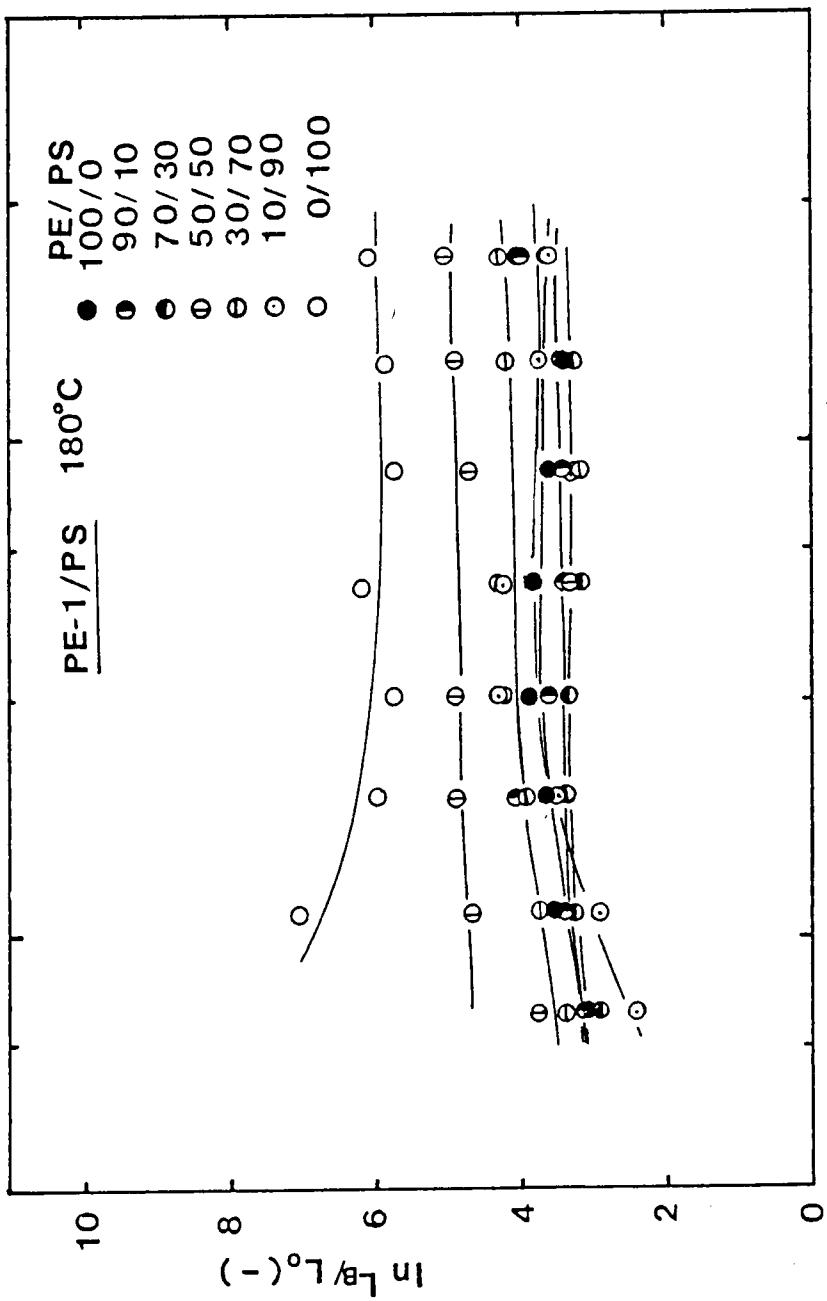


Figure V-52. Elongation to break (ln L_B/ln L_o) as a function of elongation rate ($\dot{E}$) for PE-1/PS blends.

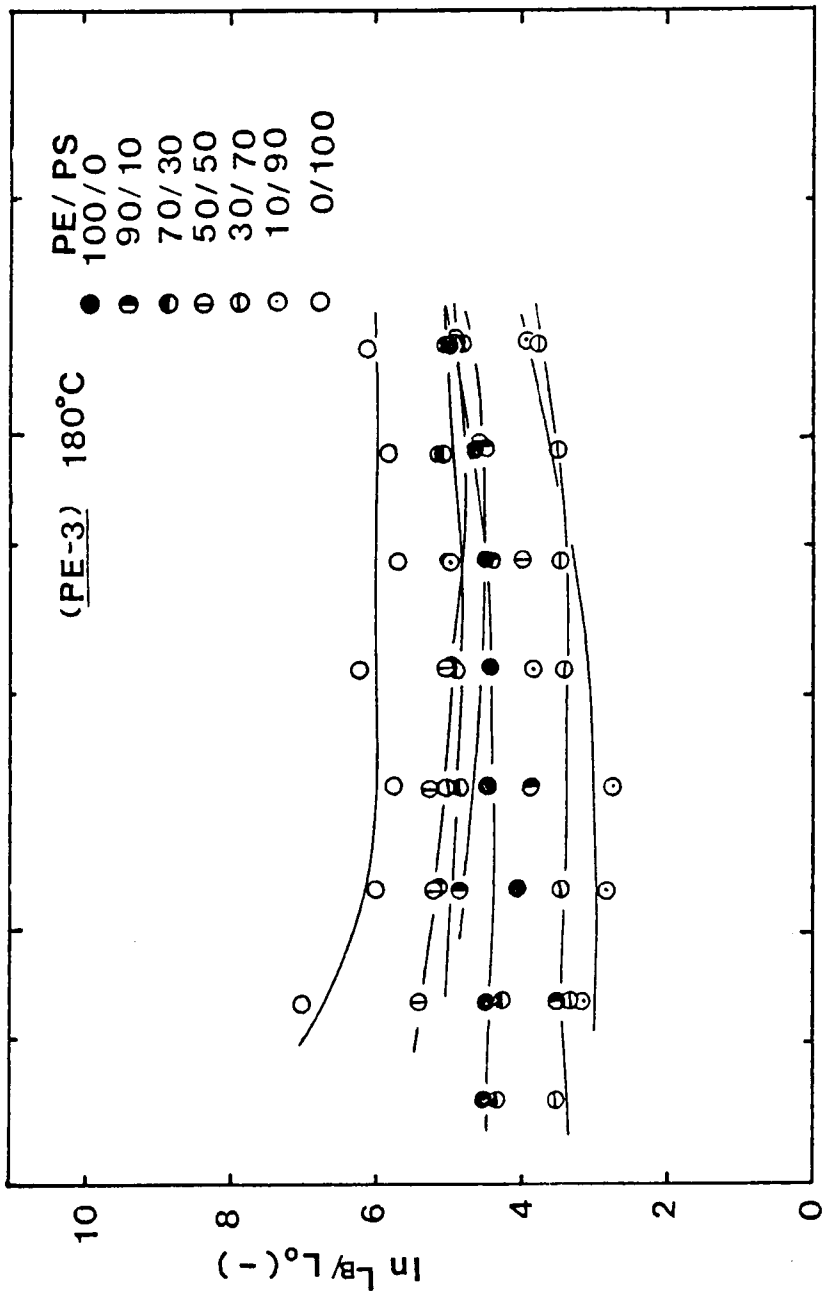


Figure V-53. Elongation to break ($\ln L_B/\ln L_o$) as a function of elongation rate ($\dot{E}$) for PE-3/PS blends.

Table V-2. Comparison of elongation to break ($\ln L_B / \ln L_o$) for PE/PS blends

Samples	PE-1	PE-2	PE-3
PE100	3.7	4.0	4.4
PE90-PS10	3.3	4.1	4.5 ~ 5.0
PE70-PS30	3.2	4.3	4.2 ~ 4.8
PE50-PS50	4.8 ~ 5.0	5.1	4.8 ~ 5.2
PE30-PS70	3.5 ~ 4.3	3.9	3.5
PE10-PS90	2.5 ~ 4.2	3.9	3.0 ~ 4.0
PS100		6.0	

Table V-3. Comparison of elongation to break ($\ln L_B/\ln L_o$) with Tanaka's data

Samples	Wt. % PE/PS	$\ln(L_B/L_o)$ By Tanaka's Data	$\ln(L_B/L_o)$ By Present Work
PE	100/0	2.0	PE-1. 3.7 -2. 4.0 -3. 4.4
PE-PS	50/50	3.0 ~ 1.0	PE-1. 5.0 ~ 3.9 -2. 5.1 -3. 4.9
PS	0/100	5.8	6.0

If the filament is viewed as a totality of PE/PS systems, failure will occur on manner determined by the weakest segment.

CHAPTER VI

PROCESSING STUDIES OF POLYMER MELT BLENDS

Studies of the influence of processing on the phase morphology and internal phase structure of two-phase polymer systems are very limited. In this chapter, the processing characteristics of PE/PS blends are studied. In particular, we consider: a) extrudate swell, and b) stable and unstable melt spinning behavior. In addition, the melt spun filaments are extracted, and small diameter mini-fibers are formed. Sheets have been compression-molded from blended samples and subsequently biaxially stretched to form films.

A. EXTRUDATE SWELL

A.1. Results

In Figure VI-1, the extrudate swell B ($=\frac{d}{D_o}$) of three PE's and polystyrene are plotted as a function of shear stress, where "d" is the diameter of the extrudate, and "D_o" is the inner diameter of the capillary die. Figures VI-2 to VI-4 plot the swell of polyethylene-polystyrene blends against the shear stress σ_{12}. For PE, PS, and PE/PS blends, the magnitude of the extrudate swell, B, increases with increasing shear stress. Generally, the swell of the PE's is higher than the PS. The composition dependence of the swell is complex.

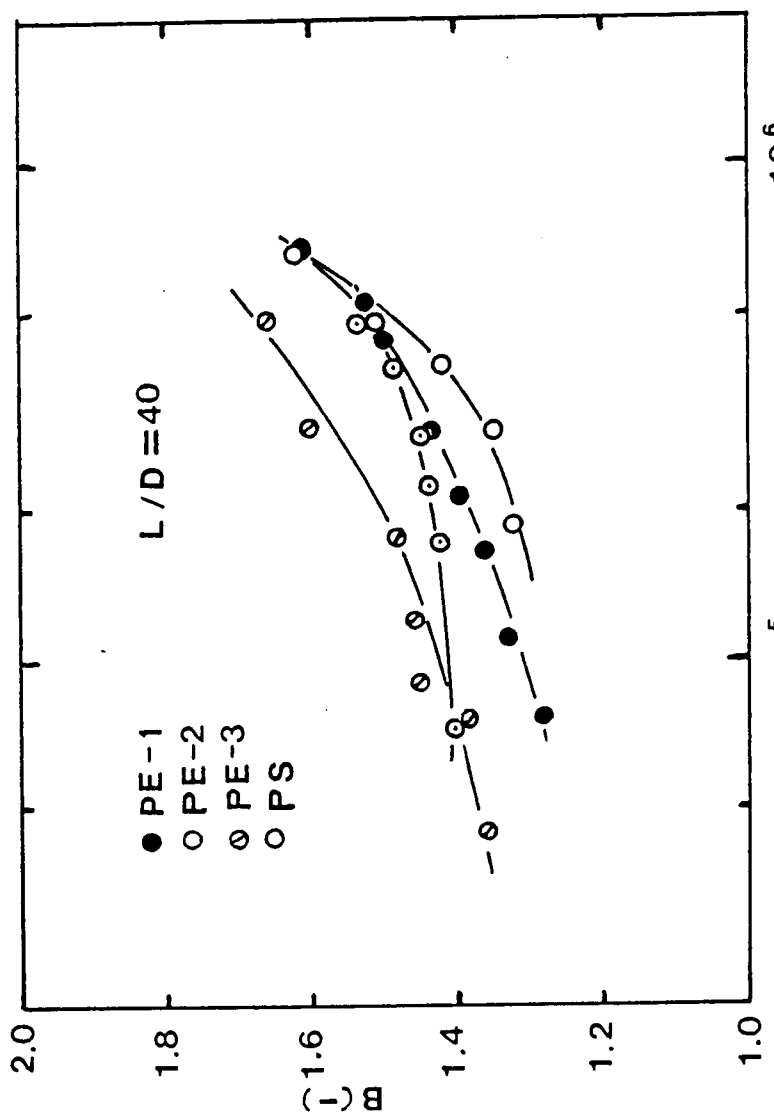


Figure VI-1. Extrudate swell (B) as a function of shear stress (σ_{12}) for PE-1, 2, 3 and PS.

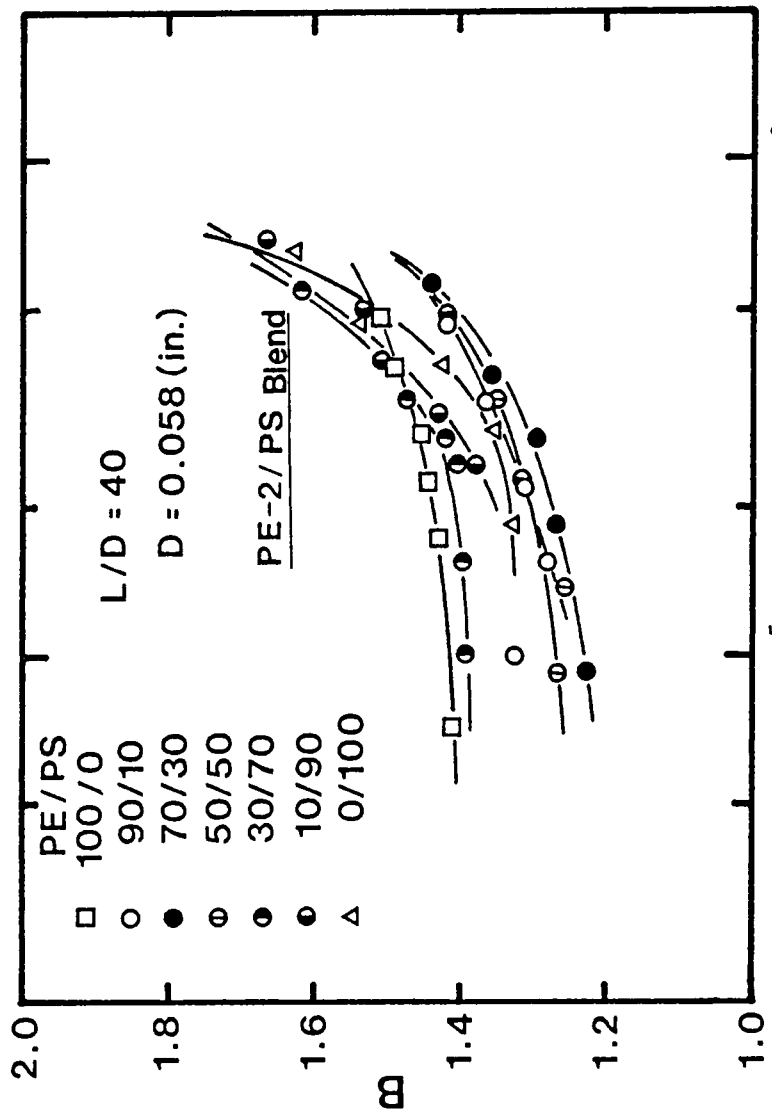


Figure VI-2. Extrudate swell (B) as a function of shear stress (σ_{12}) for PE-2/PS blends

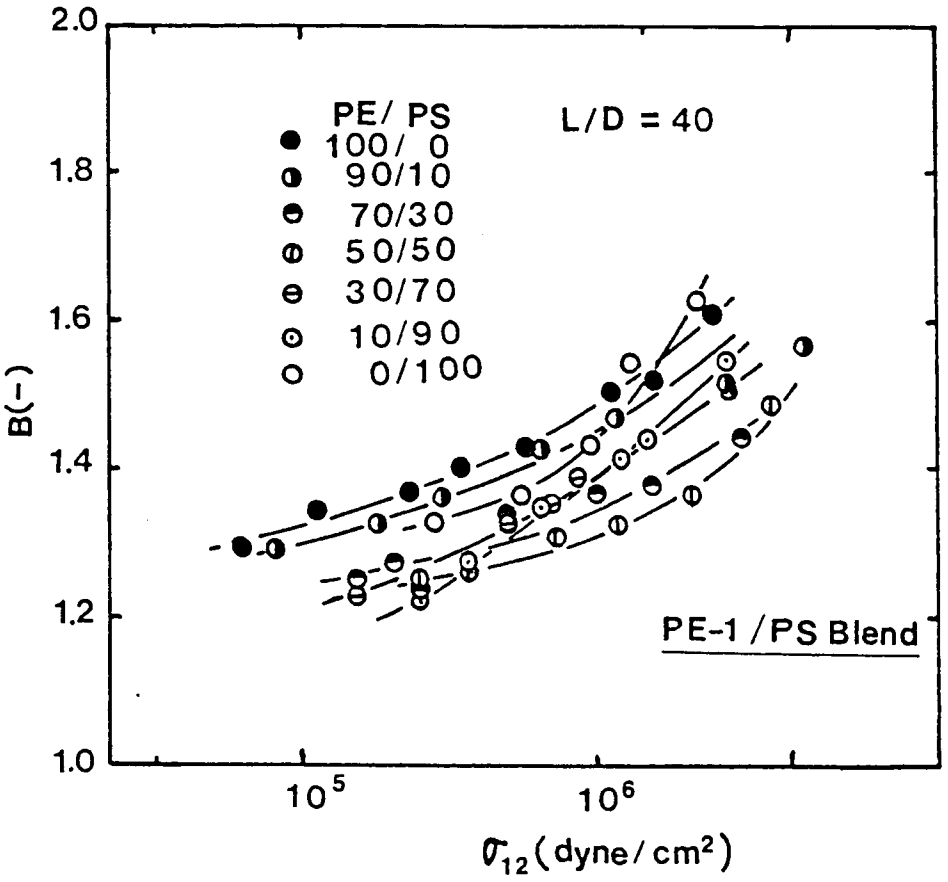


Figure VI-3. Extrudate swell (B) as a function of shear stress (σ_{12}) for PE-1/PS blend.

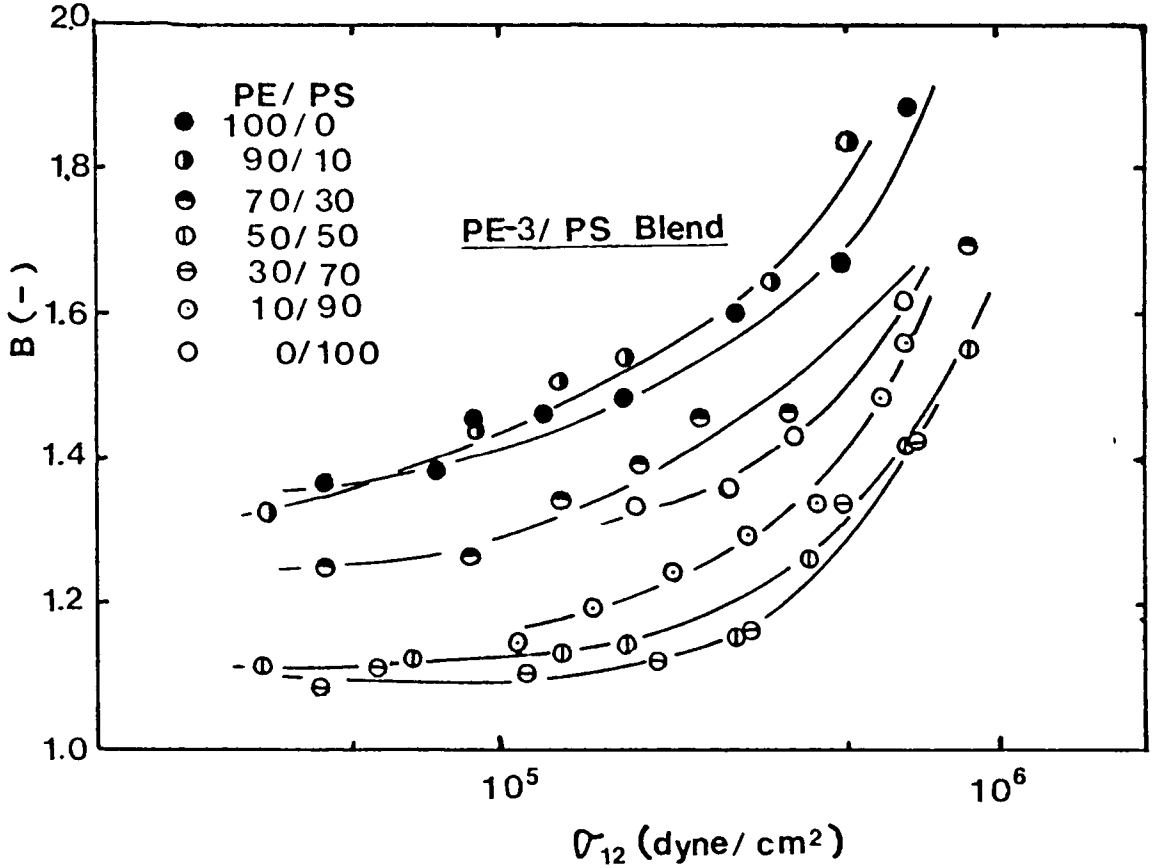


Figure VI-4. Extrudate swell (B) as a function of shear stress (σ_{12}) for PE-3/PS blend.

A.2. Discussion

Studies on extrudate swell of isotropic viscoelastic fluids have been investigated by many researchers. The view that extrudate swell is a result of unstrained recovery from fully developed Poiseuille flow is an old one and may be inferred from Dillon and Johnson (30) in the 1930's to Nakajima and Shida (107) among others in recent times. The first reasonably satisfactory treatment of the problem appears to be that of Tanner (159), who made use of unconstrained elastic recovery calculations by Lodge (92) for an integral Maxwell model with a Finger deformation measure. He found that the swell is specified by the dimensionless group, the Weissenberg Number, N_{ws}. Experimental studies of these and other extrudate swell theories have been reported by Vlachopoulos and his coworkers (182), Utracki, Baberkijan, and Kamal (176), White and Roman (192), Racin and Bogue (121), and Huang and White (67). Studies of die swell of polymer blends have been reported by Han and Yu (59) for PE/PS blends, Ablazova and Vinogradov (1) for POM/copolyamide systems, and Plochocki (118) for PE/PP systems. All of these investigators observe that the swell-composition curve exhibits a maximum when comparisons are made at fixed shear rate or shear stress. Swell-composition curves are plotted in Figures VI-5 to VI-7. These show a minimum. Figures VI-5 and VI-7 show a maximum. The swell-composition dependencies are not monotonic.

Results are now contrasted to the morphology found in the previous chapter. All of the blends exhibit a thin thread structure

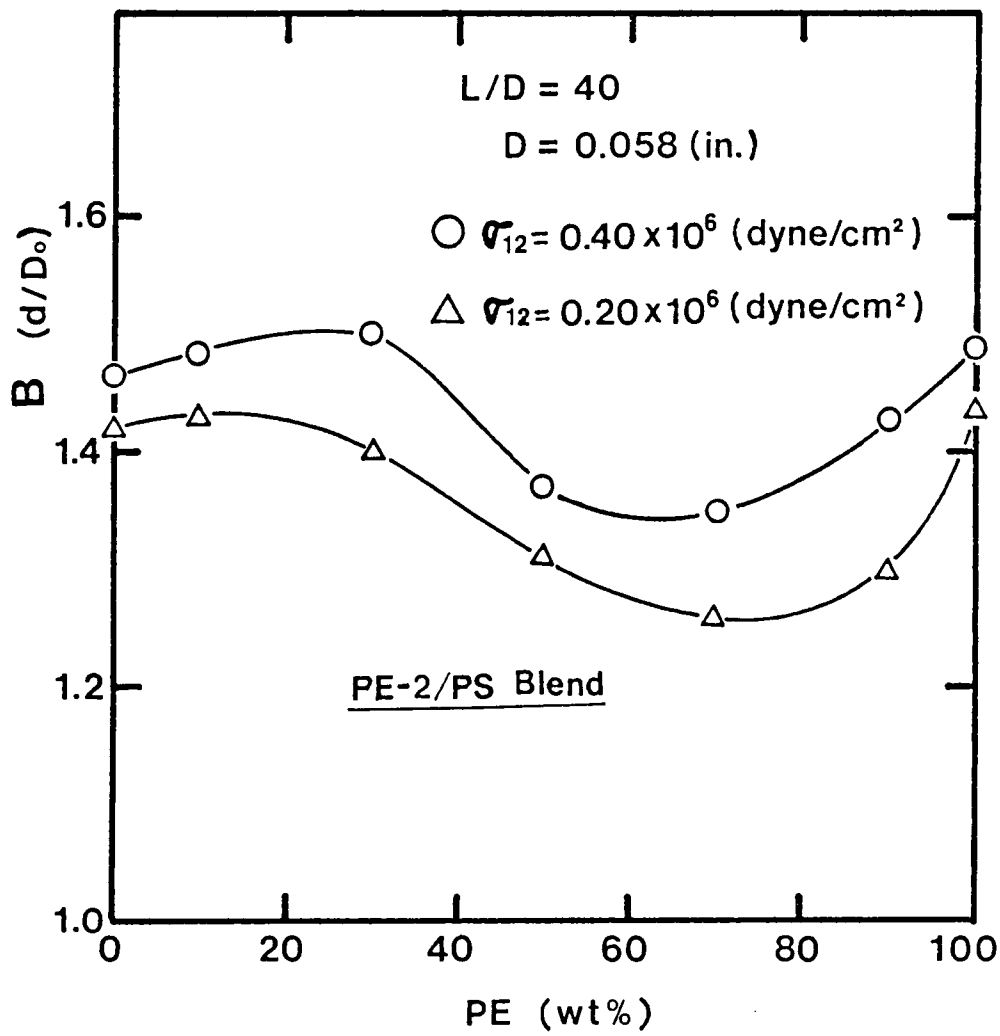


Figure VI-5. Composition dependence of extrudate swell (B) for PE-2/PS blends.

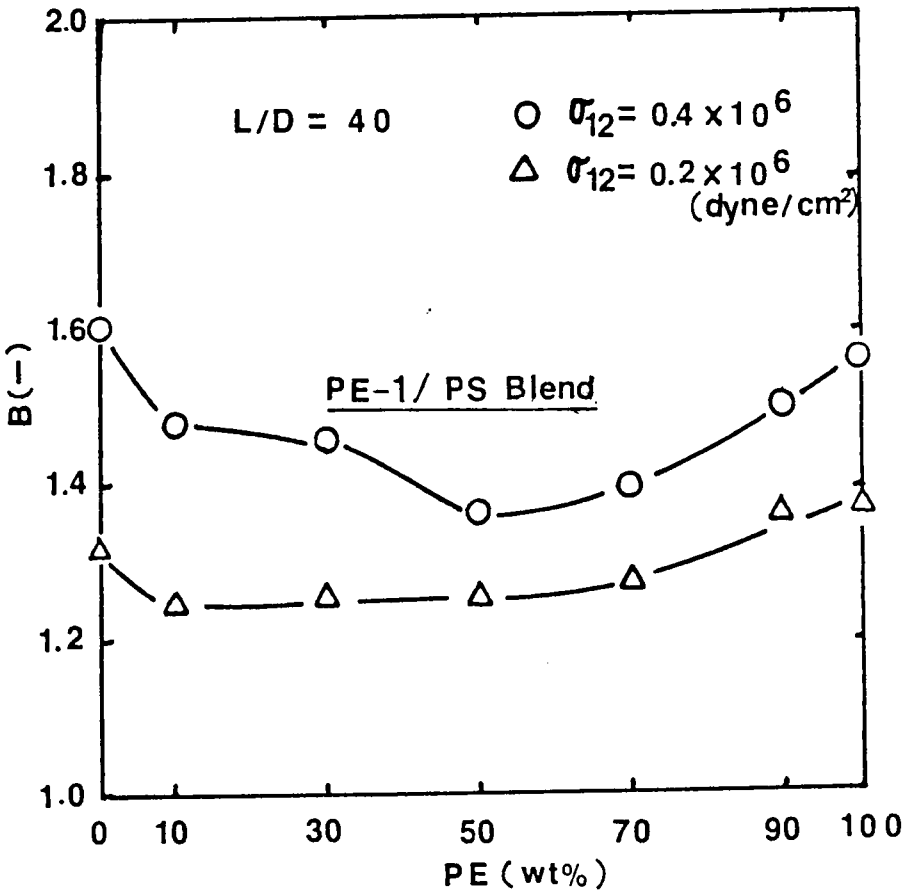


Figure VI-6. Composition dependence of extrudate swell (B) for PE-1/PS blends.

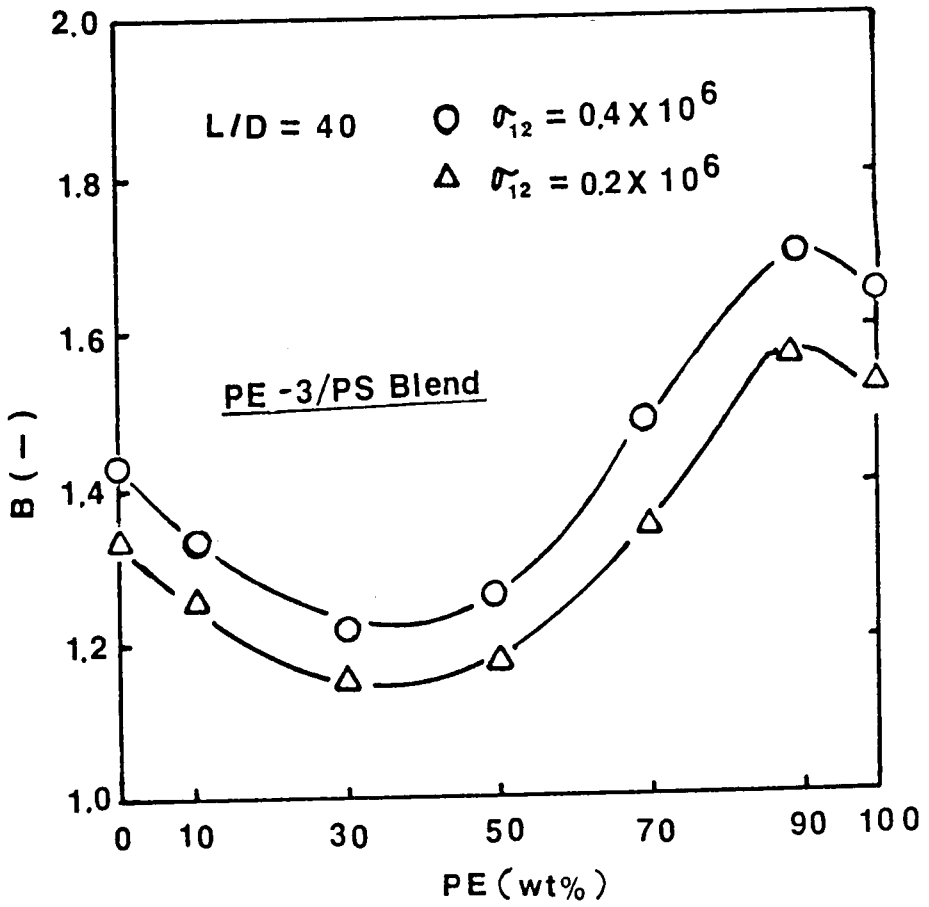


Figure VI-7. Composition dependence of extrudate swell (B) for PE-3/PS blends.

under high stress except the PE/PS-90/10 of PE-3/PS blends which are of polyethylene. A maximum is observed at this composition. This result contrasts with Vinogradov et al.'s work which show a maximum in the die swell-composition curves, corresponding to thin-fiber formation. In the case of PE-2/PS blends, N_1 vs. composition curve agrees well with the die swell-composition curve which has a maximum at PE-30/PE-70 and a minimum at PE/PS-70/30. However, in the case of PE-1/PE and PE-3/PS, the tendency of die swell-composition disagrees with the N_1 vs. composition and the shrinkage vs. composition curves. The PE-1/PS extrudate swell-composition curves exhibit only a minima (Figure VI-6), while the normal stress data show a maximum. This disagreement is certainly due to the complex mechanism of die swell of polymer blends which have heterogenious morphologies.

B. MELT SPINNING

B.1. Structure Development

B.1.1. Introduction. In this section, wide-angle x-ray diffraction studies of blend fibers were carried out using nickel filtered CuKα radiation. The crystalline orientation in the PE phase is discussed. Filaments were melt spun through air into a quench bath and then taken up in Figure III-3, p. 53.

B.1.2. Results. Diffractometer scans for PE/PS blends are shown in Figure VI-8, and WAXS film patterns at various $\frac{V_L}{V_o}$ are shown in Figure VI-9. A decrease in PE orientation is observed as PS contents increase. The x-ray photographs, shown in Figure V-10(a), p. 146, show the orientation of the crystals in as-spun filaments of polyethylene. With further melt drawing, the orientation along the fiber axis increased; the 020 reflection is first localized around the equator and then the 200 reflection tends to orient along the fiber axis.

B.1.3. Discussion. It is well established for both polyethylene and polypropylene that the crystalline orientation factors and morphology of melt spun fibers correlate with spin line stress (106). The behavior of the 200 reflection of the polyethylene spun filament is quite similar to that of many earlier studies of melt spinning polyethylene (79). They observed that the intensity distribution curve for the 200 reflection tends to split at the equator and to concentrate on the meridian. In comparison, the 020 reflection is rapidly localized around the equator with a melt draw-down ratio as low as 3.4. As the PS content increases, both of the 020 and 200 reflections of polyethylene phase in PE/PS blend fibers behave similarly to those of pure polyethylene fibers, but the localization of the 020 and equatorial concentration of the 200 are not observed until higher V_L/V_o. This contrasts with studies of the variation of crystalline orientation in polypropylene/nylon 6 blends (90). More specifically in Figure VI-10, the extrudates from the

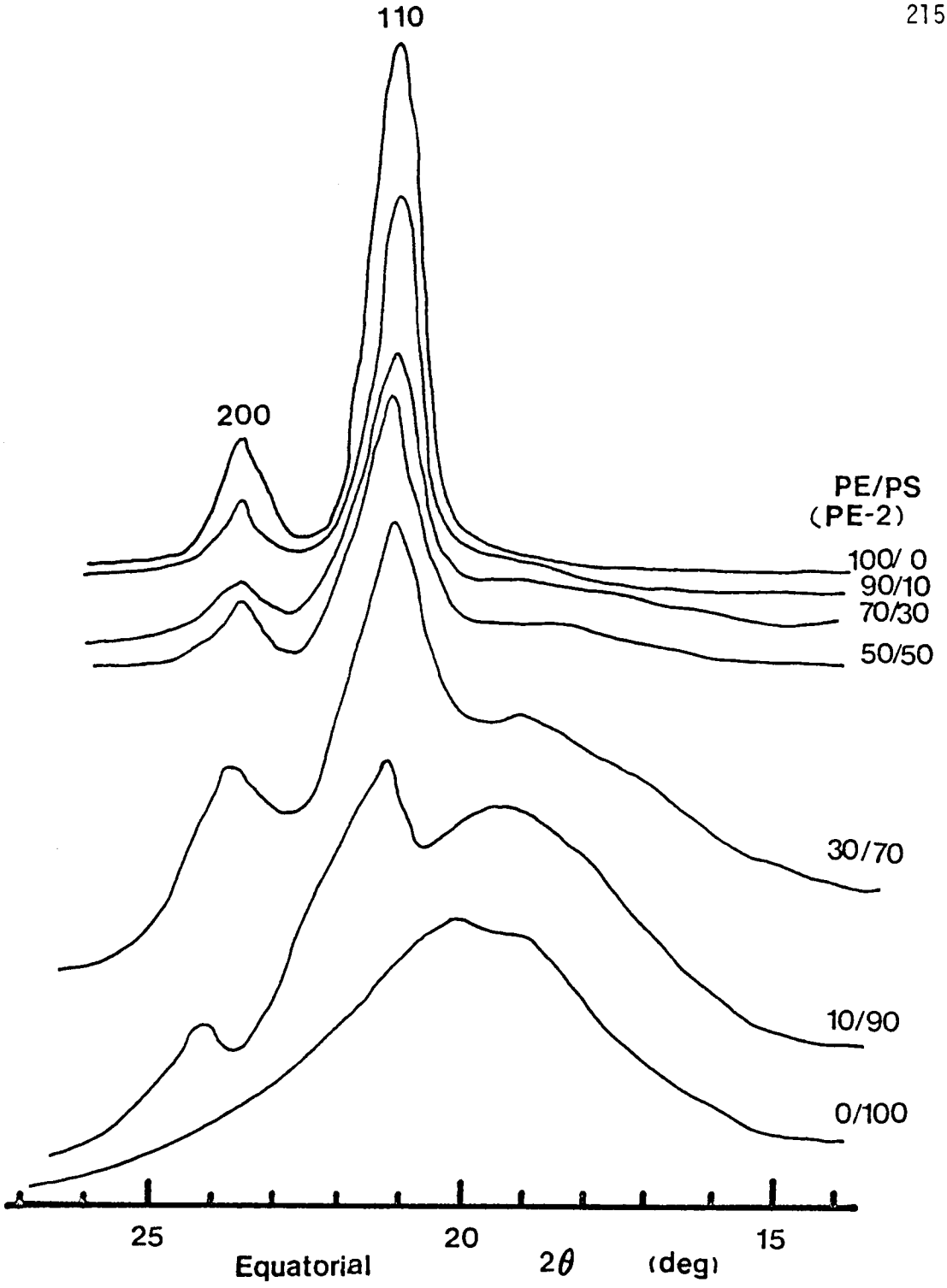


Figure VI-8. 2θ scan for polyethylene (PE-2), polystyrene (PS) and PE-2/PS blend melt spun fibers.

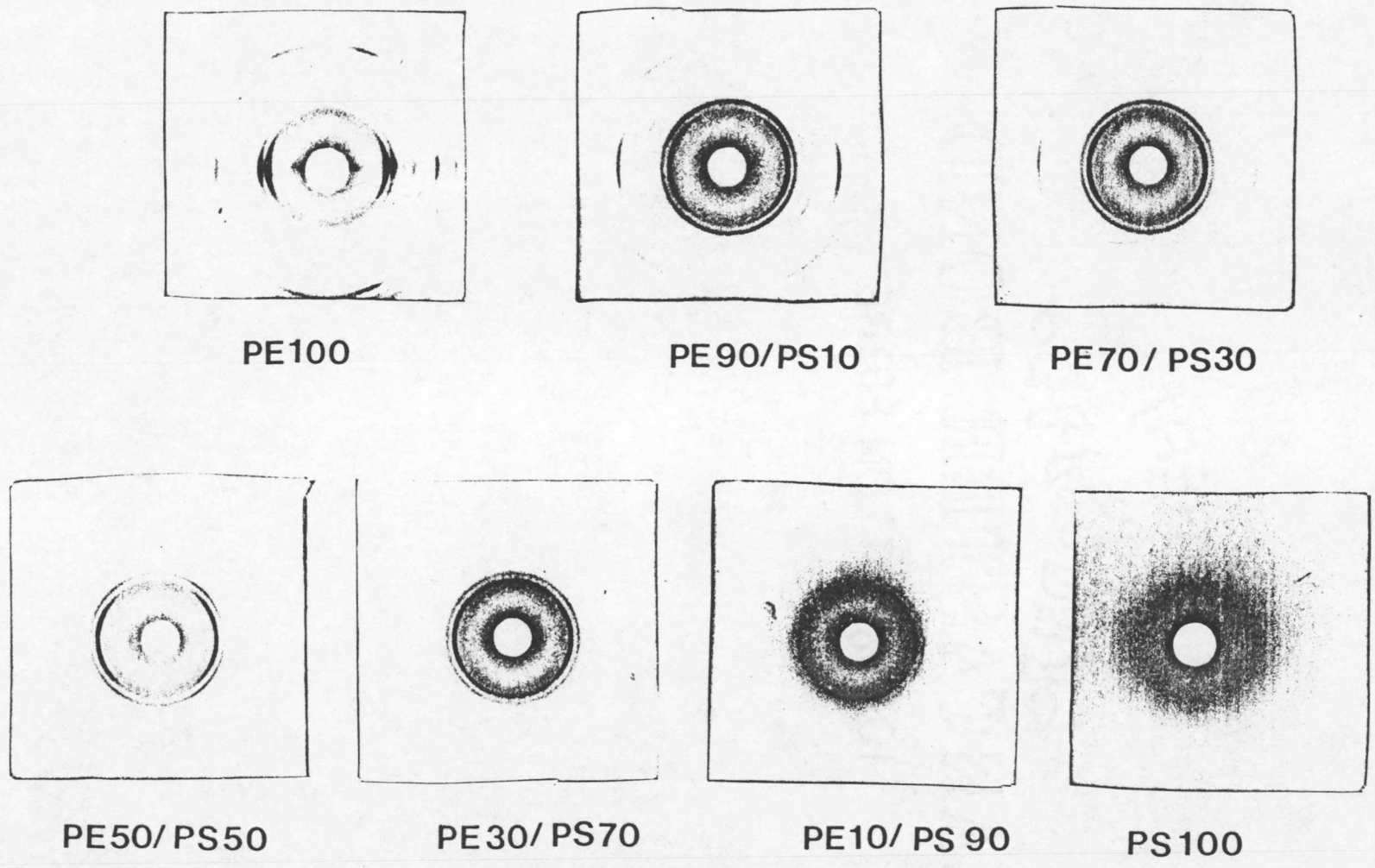


Figure VI-9. WAX film patterns for polyethylene (PE-2), polystyrene and PE-2/PS blend melt spun fibers.

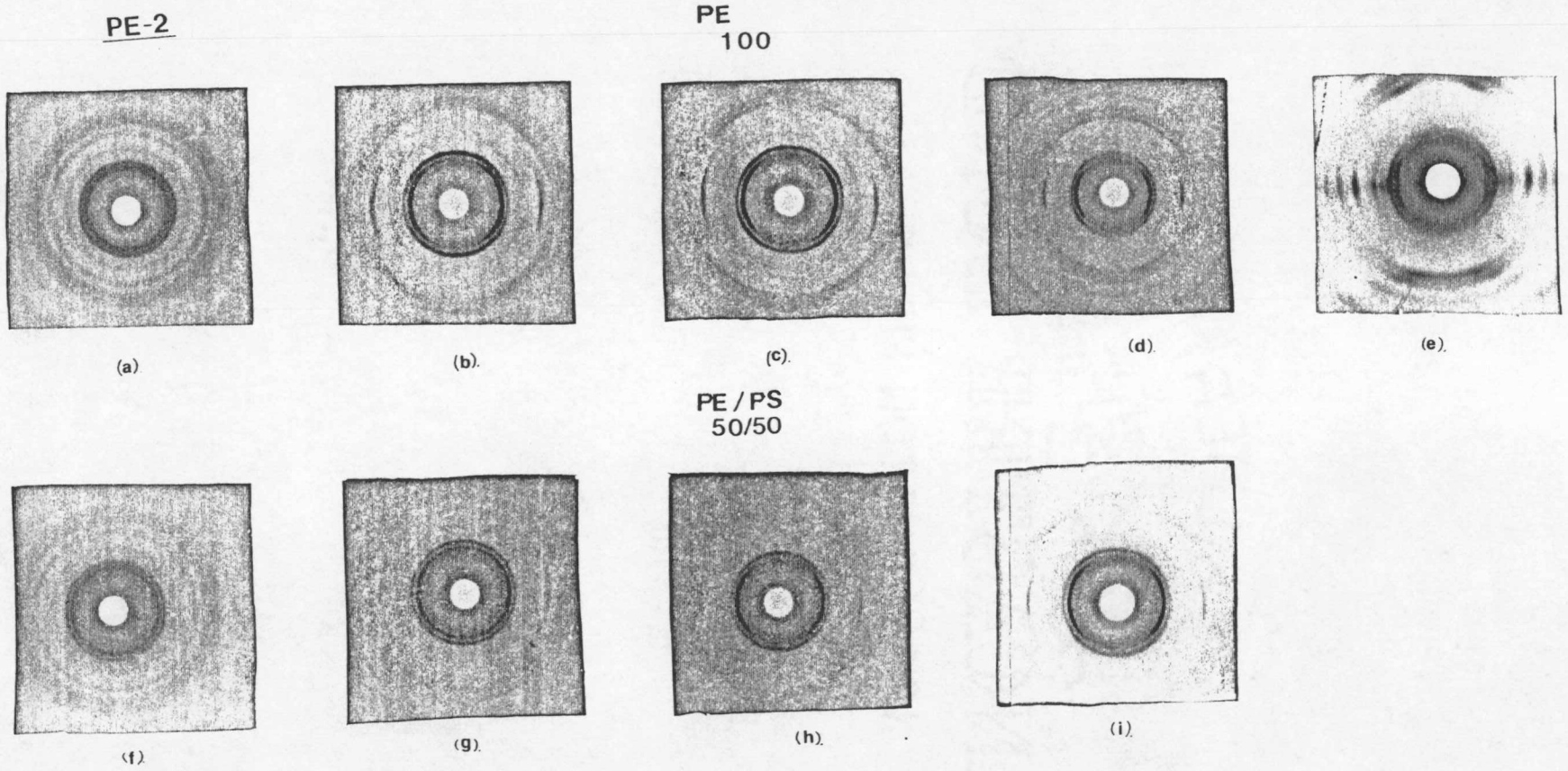


Figure VI-10. WAX film patterns for polyethylene (PE-2) and PE-2/PS blend melt spun fibers with different melt draw ratios: (a) 0; (b) 18.8; (c) 37.6; (d) 75.4; (e) .161; (f) 0; (g) 18.8; (h) 75.4; (i) 161.

capillary have no orientation. When melt draw is increased to 18.8, the 200 reflection is localized around the meridian. With increasing the draw ratio, the 200 reflection concentrates on the equator. At the same draw ratio $\frac{V_L}{V_o}$ = 75.0, the 200 reflection is localized on the equator and then at $\frac{V_L}{V_o}$ = 161.0 it shows the four spots. As the PS content increases, the shift of 200 reflection from the meridian to the equator increases.

The Herman-Stein orientation factors for PE crystalline regions were computed using equations (III-18) and (III-19) described in Chapter III and are plotted in Figures VI-11 to VI-16 as a function of spinline stress for PE, PS and PE/PS blends. At any stress, the c-axis and b-axis orientation factors decrease. f_a tends from negative to zero and to positive. In Figure VI-17, f_c is plotted against the composition of PE at a fixed spinline stress $\sigma = 6 \times 10^6$ dyne/cm^2. The decrease of the orientation factors with addition of PS contrasts with studies of the variation of crystalline orientation by Liang et al. (90) and Shimomura et al. (142), who made tubular film from polyethylene-polypropylene. However, a decrease of orientation of polyethylene phase is observed by Shimizu et al. (141) for polypropylene-polystyrene blends.

A possible reason for this behavior is the strong dependence of the viscosity of PS on temperature relative to that of PE. The stress exerted on the two phases may significantly redistribute itself in this case becoming higher in more viscous PS and lower in the PE. This is illustrated in the equation for the spinline tension F.

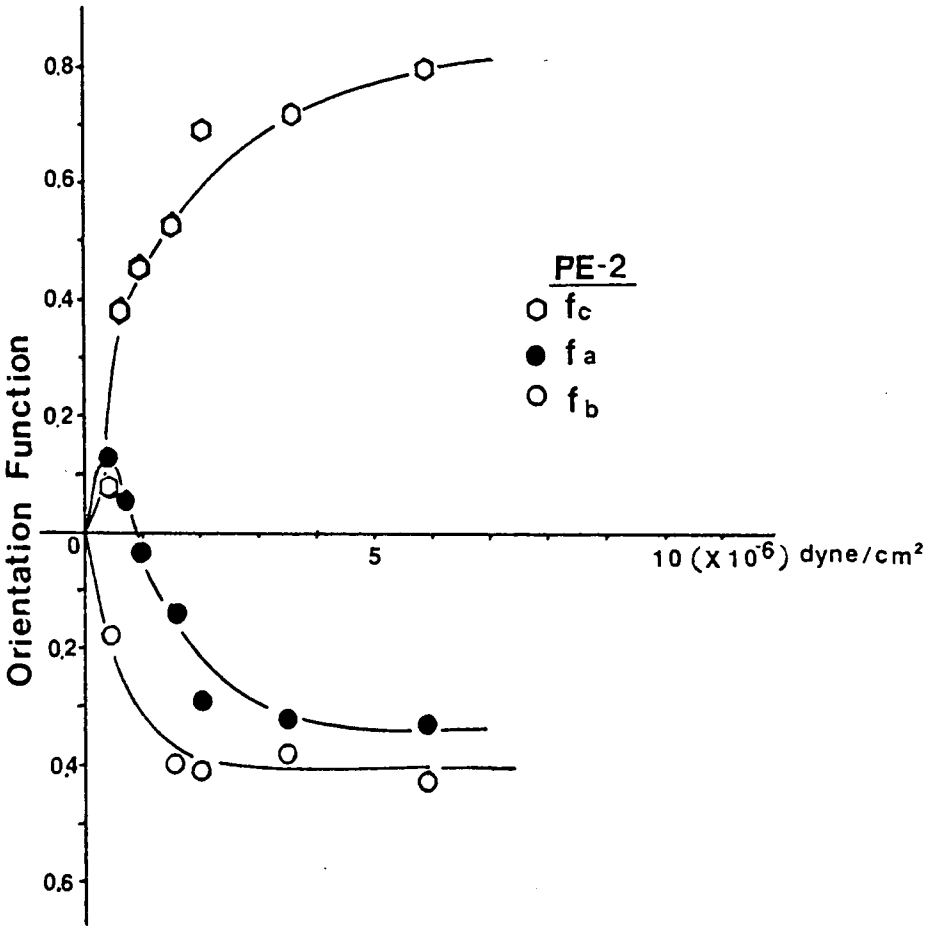


Figure VI-11. Herman-Stein orientation factors f_a, f_b and f_c as a function of spinline stress for PE-2.

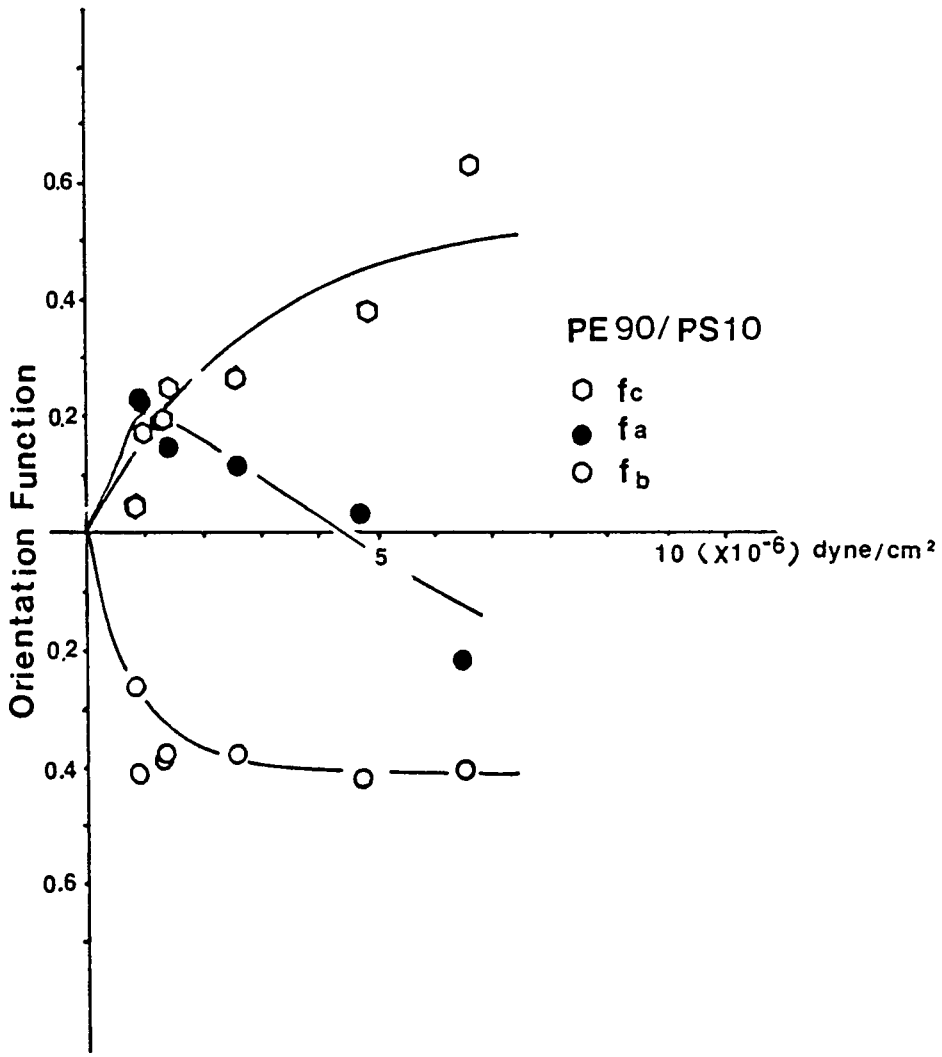


Figure VI-12. Herman-Stein orientation factors f_a, f_b and f_c as a function of spinline stress for PE-2/PS-90/10^c blend.

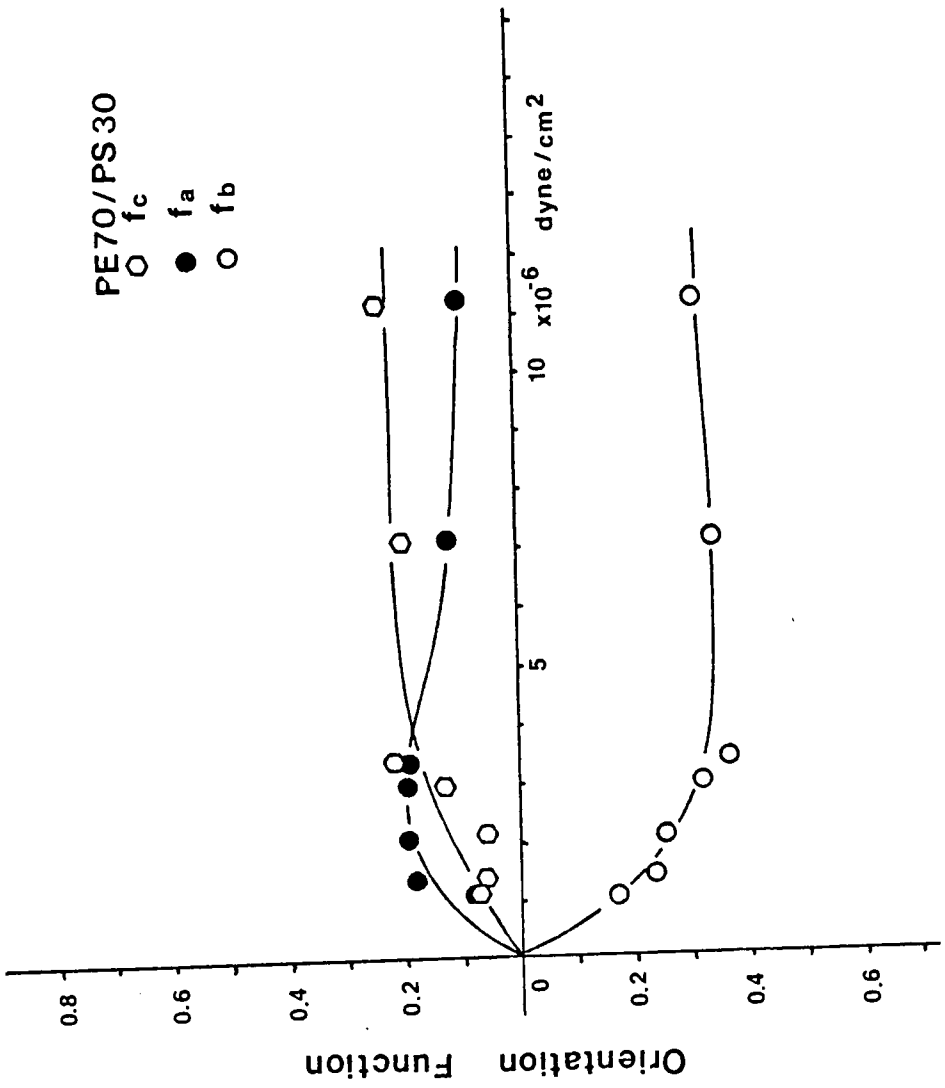


Figure VI-13. Herman-Stein orientation factors f_a, f_b and f_c as a function of spinline stress for PE-2/PS-70/30 blend.

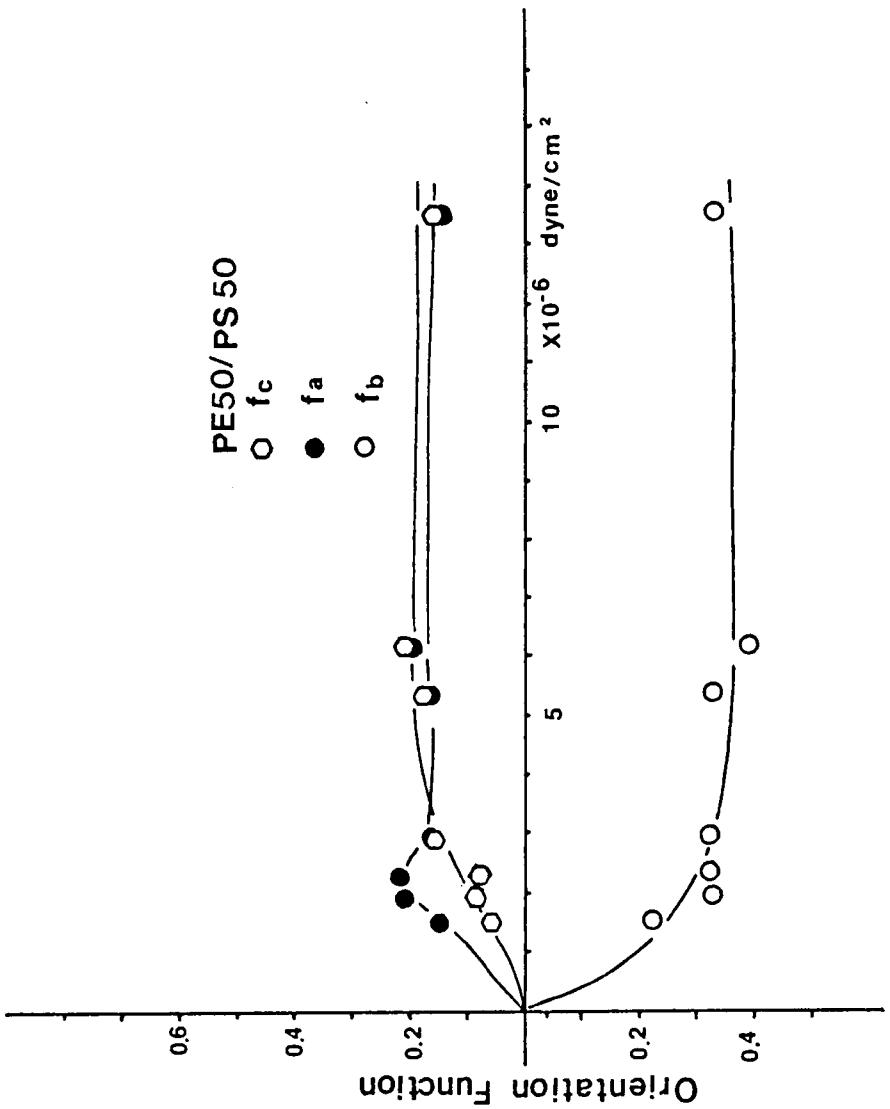


Figure VI-14. Herman-Stein orientation factors f_a, f_b and f_c as a function of spinline stress.

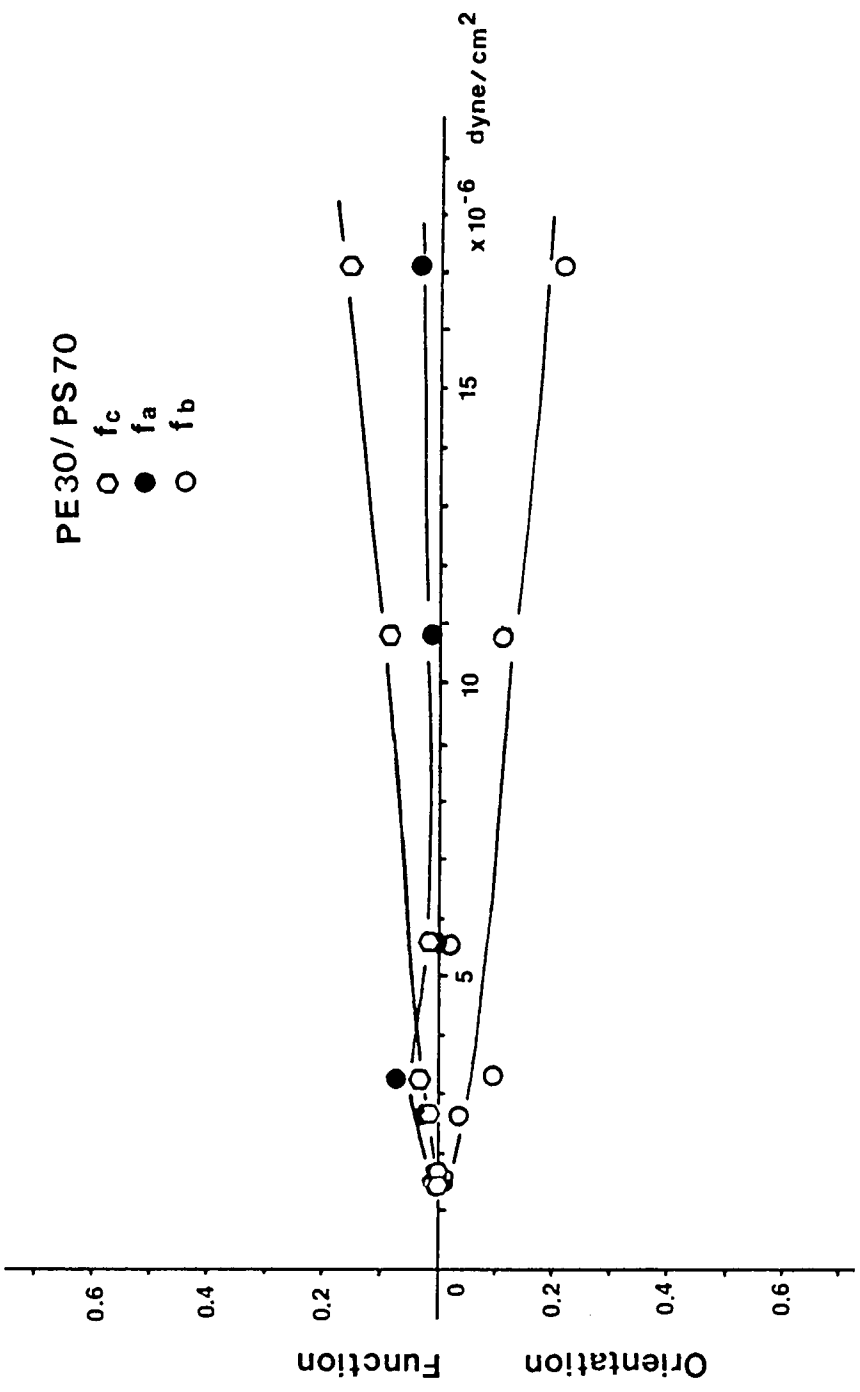


Figure VI-15. Herman-Stein orientation factors f_a, f_b and f_c as a function of spinline stress for PE-2/PS-30/70 blend.

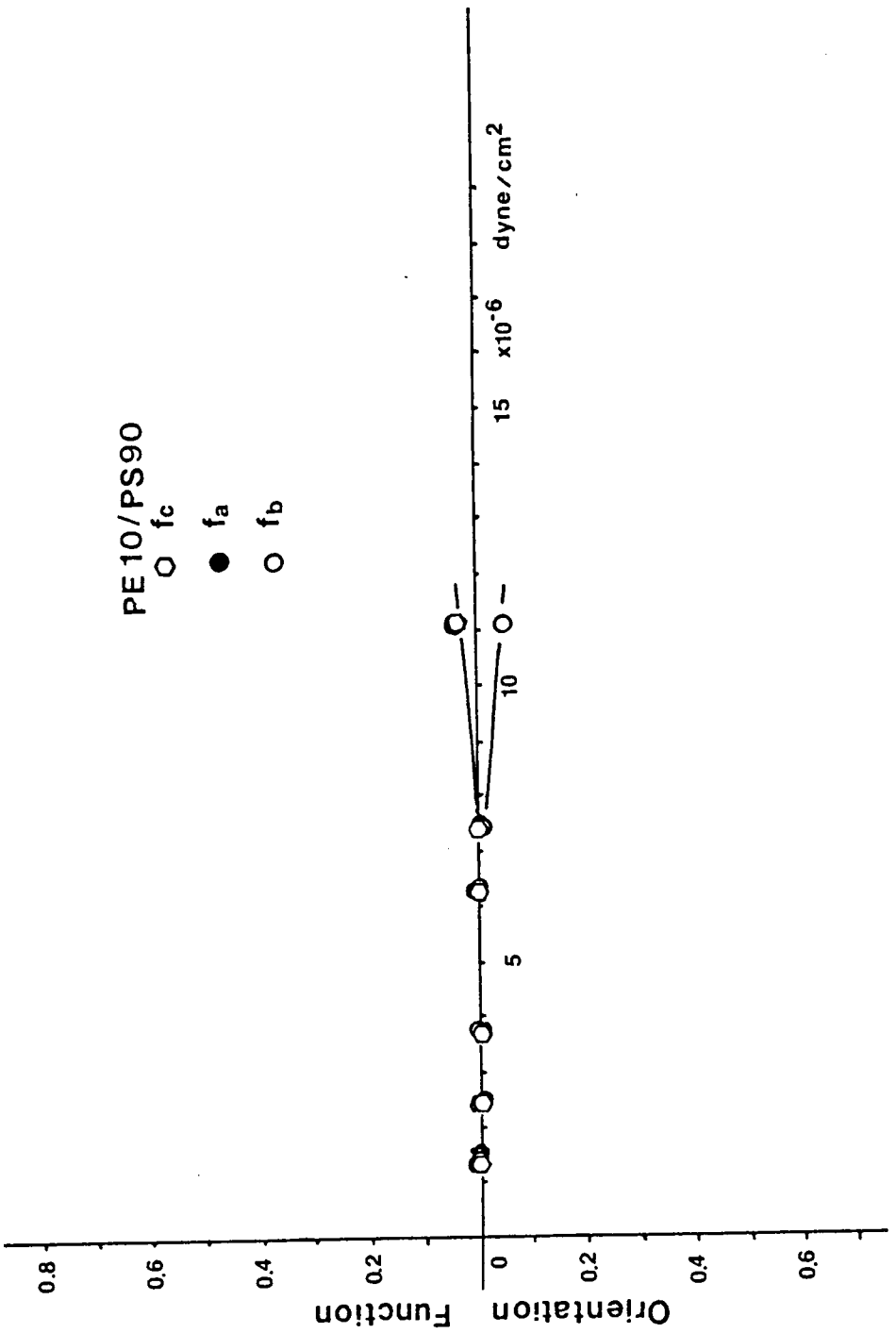


Figure VI-16. Herman-Stein orientation factors f_a, f_b and f_c as a function of spinline stress for PE-2/PS-10/90 blend.

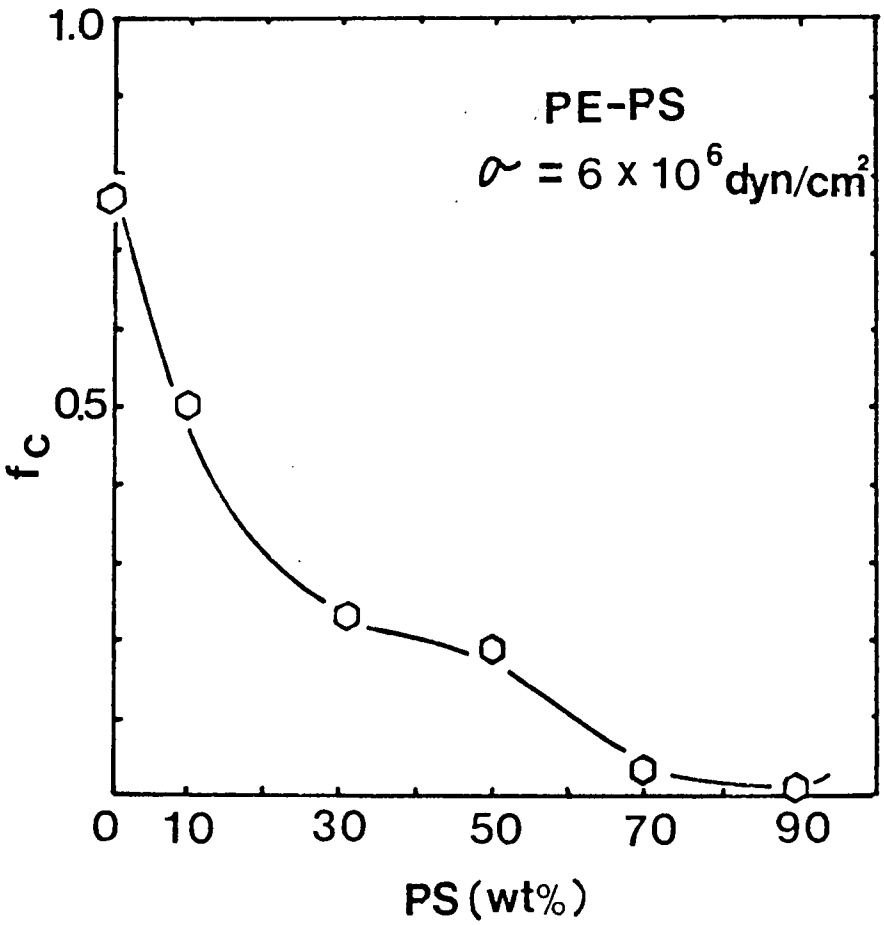


Figure VI-17. Composition dependence of Herman's orientation factors for PE-2/PS blends at a fixed spinline stress.

$$F \simeq \sigma_{PE} A_{PE} + \sigma_{PS} A_{PS} \qquad \text{(VI-1)}$$

$$= [\chi_{PE}^{SP} e^{E_{PE}/RT} A_{PE}(T) + \chi_{PS}^{SP} e^{E_{PS}/RT} A_{PS}(T)] \frac{dV_1}{dx_1}$$

The lower the temperature becomes, the larger the second term in the brackets and the smaller σ_{PE}.

B.2. Draw Resonance During Isothermal Melt Spinning

Isothermal melt spinning experiments were carried out for PS, PE, and PE/PS blend samples. Fluctuations of fiber diameter have been studied by many investigators. They may be classified into two types. There are what may be called forced oscillation fluctuations due to random fluctuations in spinline tension, output, cooling conditions, melt temperature, etc., and giving small irregularities in diameter fluctuations. The so-called "draw resonance phenomenon" occurs at a critical draw ratio dependent on the rheological properties of polymer melts during melt spinning. Draw resonance shows regular high amplitude diameter variations.

B.2.1. Results. Figure VI-18 shows typical diameter fluctuations of PE-2 fiber, PS, and PE/PS 50/50 blend fibers for unstable isothermal melt spinning conditions. Figure VI-19 gives the typical diameter fluctuations of PE-2/PS-50/50 fiber for both stable and unstable melt spinning conditions. Table VI-1 represents the critical draw ratio, the onset of draw resonance, for PS, PE, and PE/PS blend fibers during isothermal spinning. The data show that adding small amounts of polystyrene into polyethylene decreases the critical

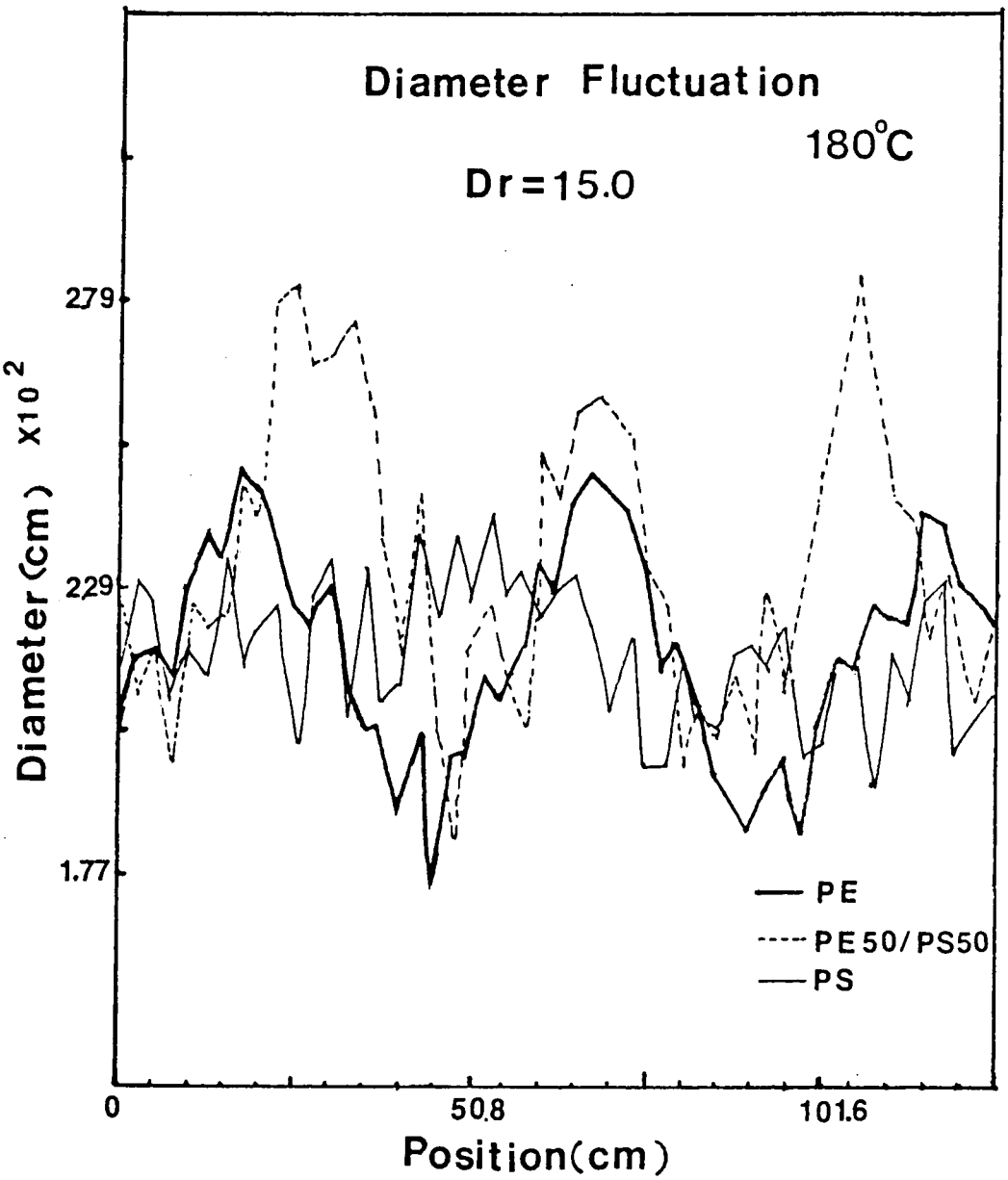


Figure VI-18. Diameter fluctuations of PE-2, PS and PE-2/PS-50/50 blend under the isothermal melt spinning after onset.

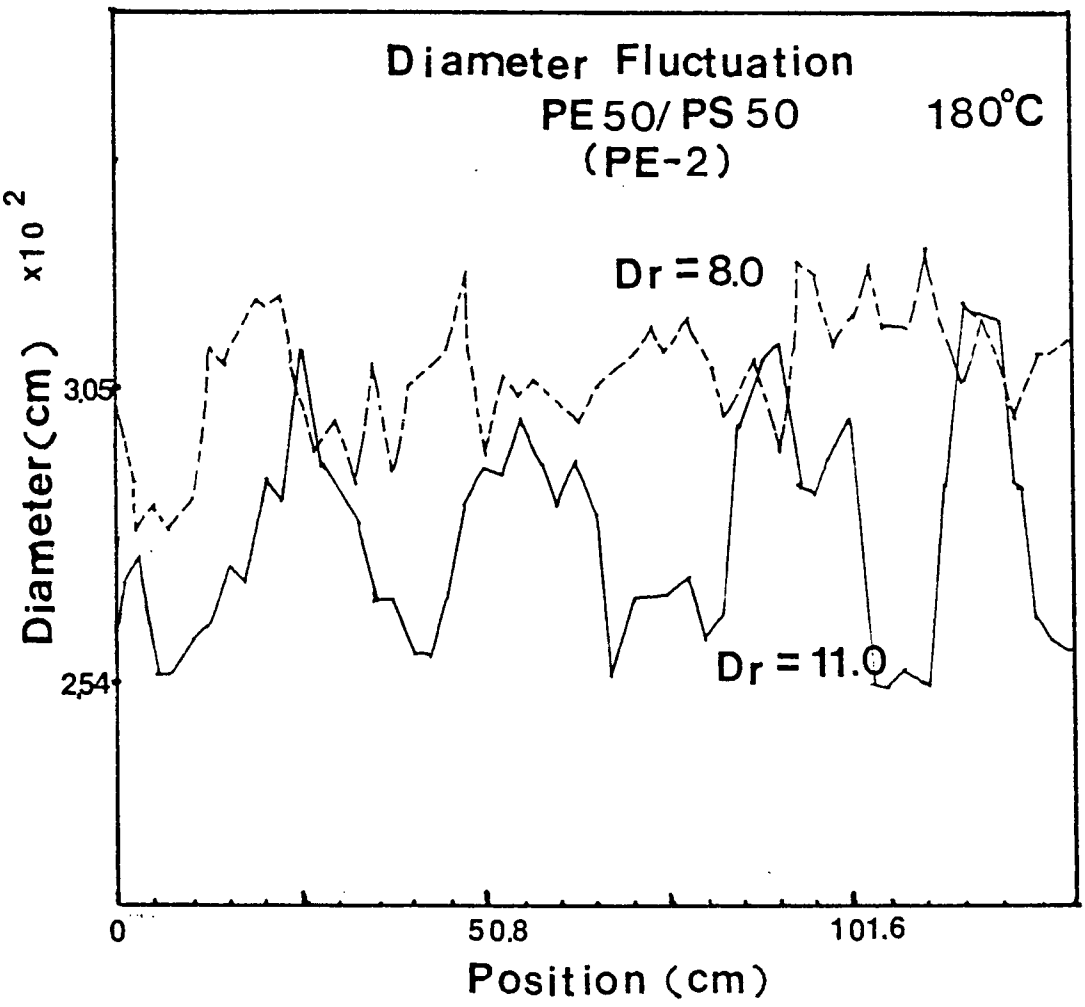


Figure VI-19. Diameter fluctuations of PE-2/PS-50/50 blend for stable and unstable conditions.

Table VI-1. Draw resonance of isothermal melt spinning

Polymers Composition PE-PS	Onset (V_L/V_0) PE-2	PE-1	PE-3
100 - 0	15.0	13.5	18.0
90 - 10	13.0	10.5	17.0
70 - 30	10.0	9.8	17.0
50 - 50	10.5	11.0	17.7
30 - 70	9.0	9.0	7.5
10 - 90	5.0	9.0	8.0
0 - 100	20.0	20.0	20.0

($V_0 = 8.45 \times 10^{-2}$ cm/sec)

$D_0 = 0.058$ in.

onset draw ratio. The onset draw ratio of polystyrene is about 20.0 and is 15.0 for PE-1, 13.5 for PE-1, and 18.0 for PE-2. The PE/SP-90/10 to 50/50 which have the polystyrene dispersed phase in the matrix of polyethylene have a lower draw ratio. The PE/PS-30/70 to 10/90 which may have polyethylene phase dispersed in the matrix of polystyrene also show much lower onset draw ratio. According to Figure VI-18, the amplitude of the diameter fluctuation increased with additional amounts of high density polyethylene, and the period of draw resonance became shorter. The PE/PS became less stable than the homopolymers.

B.2.2. Discussion. A similar tendency was observed by Han and Kim (53). Tanaka and White (158), in a study of the spinline diameter variation of PS/PE blend fibers containing a high viscosity PE and a low viscosity PS, showed these systems to be much more unstable than the pure PS melt. The critical draw ratio $\frac{V_L}{V_o}$ is less than 1.5 for PE/PS-10/90. Their result is much lower than our results. They used a 40 mg tensiometer because the diameter of the fibers were too thick, and the surfaces were too rough to use the former one.

The draw resonance results here correspond to the observations of elongation to break. Both tend to exhibit maxima as a function of composition. The latter experiments, however, indicate that homogeneous PS filaments are much more stable than the PE filaments. This is not found here.

C. MINI-FIBERS

C.1. Results

Toluene extracted PE-2/PS blend melt spun fibers are shown in Figure VI-20. Small diameter "mini-filaments" are obtained from the 10/90-PE/PS blends and 30/70-PE/PS and porous fibers from the 90/10 to 50/50 blends. These mini-filaments seem to be potentially infinitely long. Figure VI-21 shows the mini-filaments of extracted PE/PS-10/90 blends of three different polyethylenes. The PE-3 fibers from PE-3/PS-10/90 seem to be finest fibers. To get the diameters of these mini-fibers or the porous PE fibers from high PE content compositions, the cross-sections of the melt spun fibers were observed by SEM. Figures VI-22 to VI-29 show the microphotographs of cross-sections of solid blend fibers of varying drawdown ratios.

Most PE mini-fibers or holes in the extracted PE fibers became thinner and thinner with increasing drawdown ratios. Figures VI-20 and VI-28 show the finest mini-fibers of extracted PE-3/PS-10/90 blend. On the contrary, Figure VI-29 shows the largest mini-fibers of polystyrene of extracted PE-3/PS-90/10 blend.

C.2. Discussion

Similarly prepared mini-fibers have been reported by investigators in various laboratories (100)(103)(141)(172). Merriam and Miller (100)(103) reported mini-fibers of polyethylene having diameters from 0.2-100 microns and lengths from 1/32 to 1/2 inch. Shimizu and his coworkers (141) made the polystyrene-polypropylene

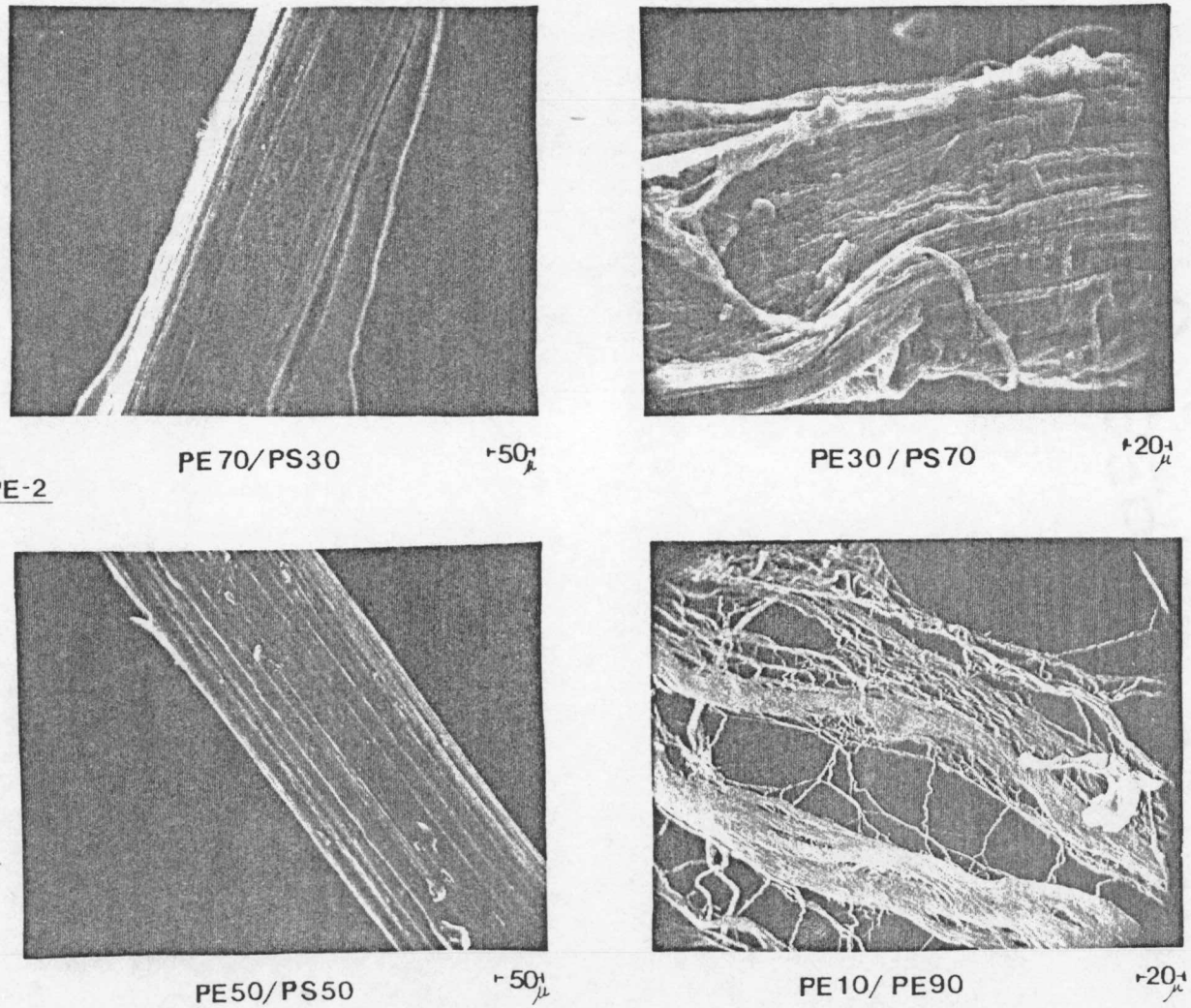
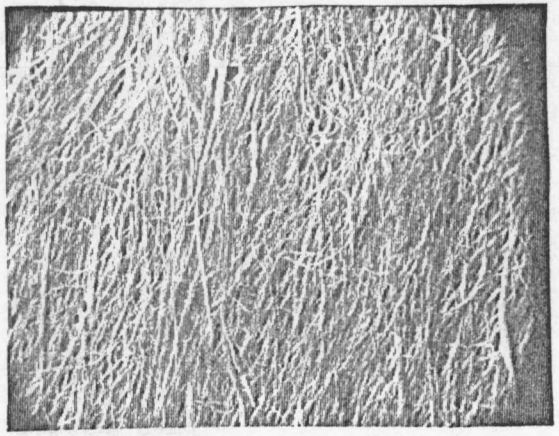
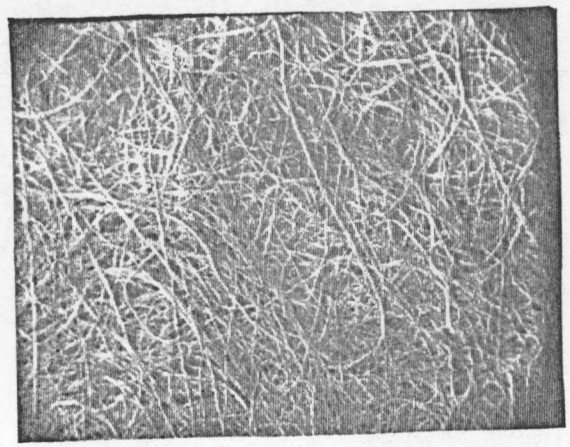
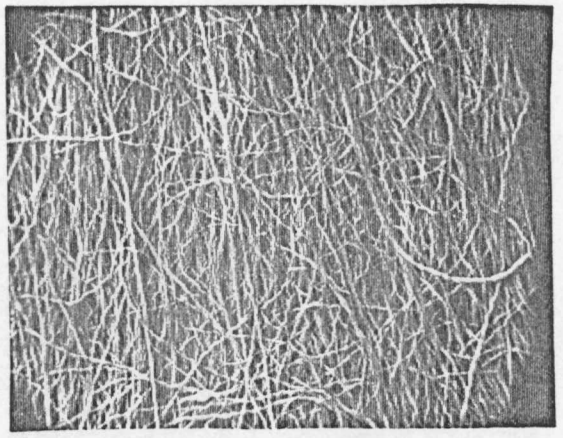


Figure VI-20. Toluene extracted PE-2/PS blend melt spun fibers at draw-down ratio V_L/V_0 = 215.







Toluene Extracted PE10/ PS90 Blend
Melt Spun Fibers

Figure VI-21. Toluene extracted various PE/PS-10/90 blend melt spun fibers at drawdown ratio V_L/V_0 = 18.8.

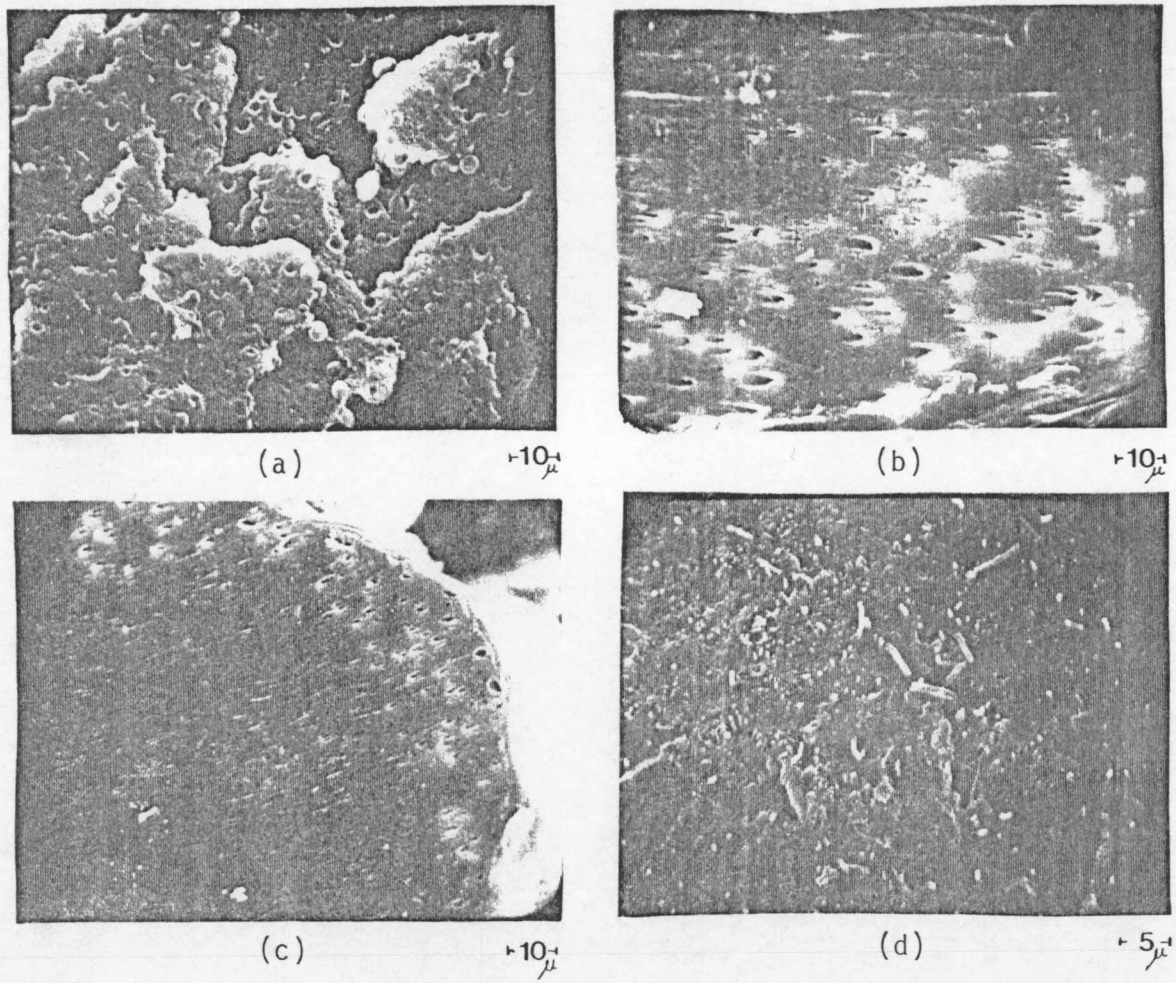


Figure VI-22. SEM microphotographs of PE-2/PS-90/10 blend melt spun fibers with different drawdown ratios: (a) 1; (b) 18.8; (c) 37.6; (d) 56.6; (e) 75.4.

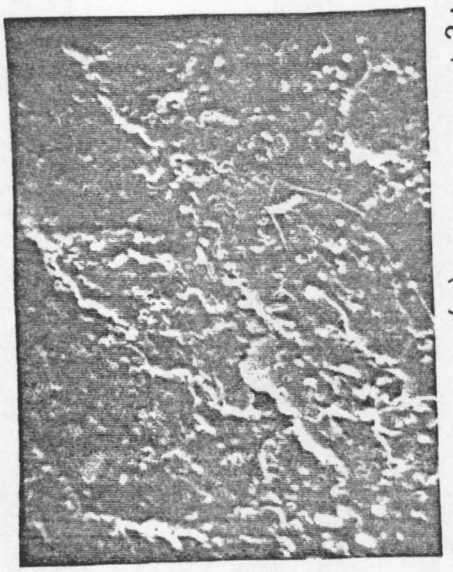


Figure VI-22 (continued)

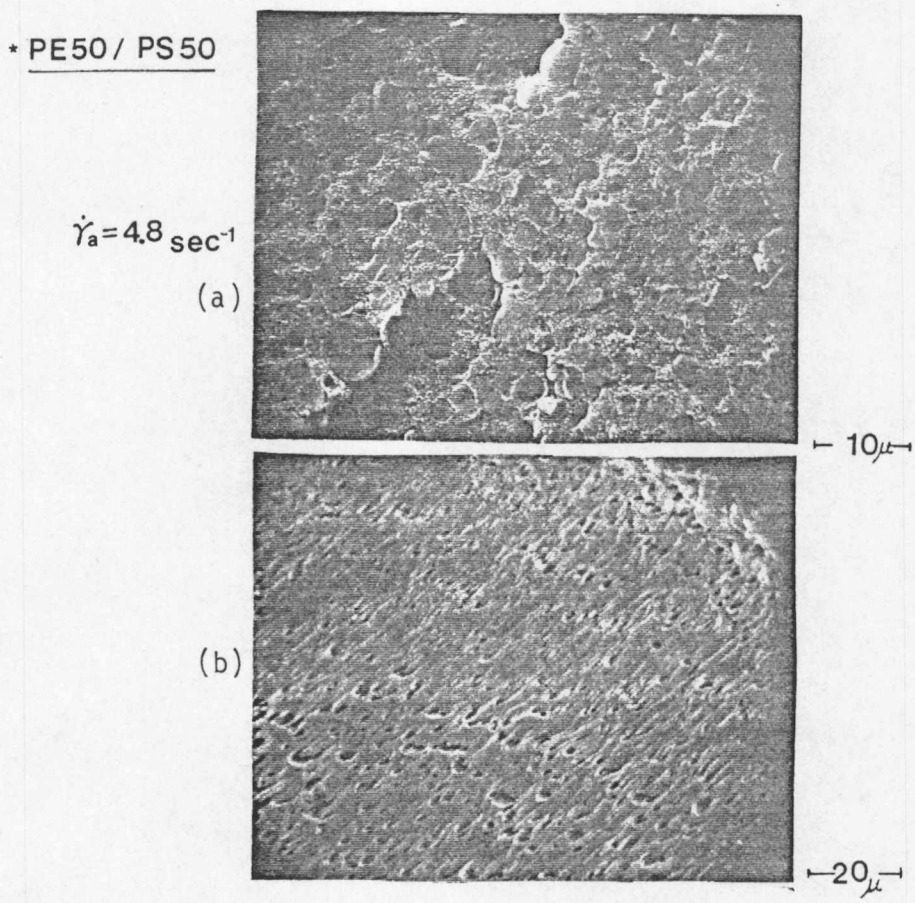


Figure VI-23. SEM microphotographs of PE-2/PS-50/50 blend melt spun fibers with different drawdown ratios: (a) 1; (b) 18.8; (c) 37.6; (d) 56.6.

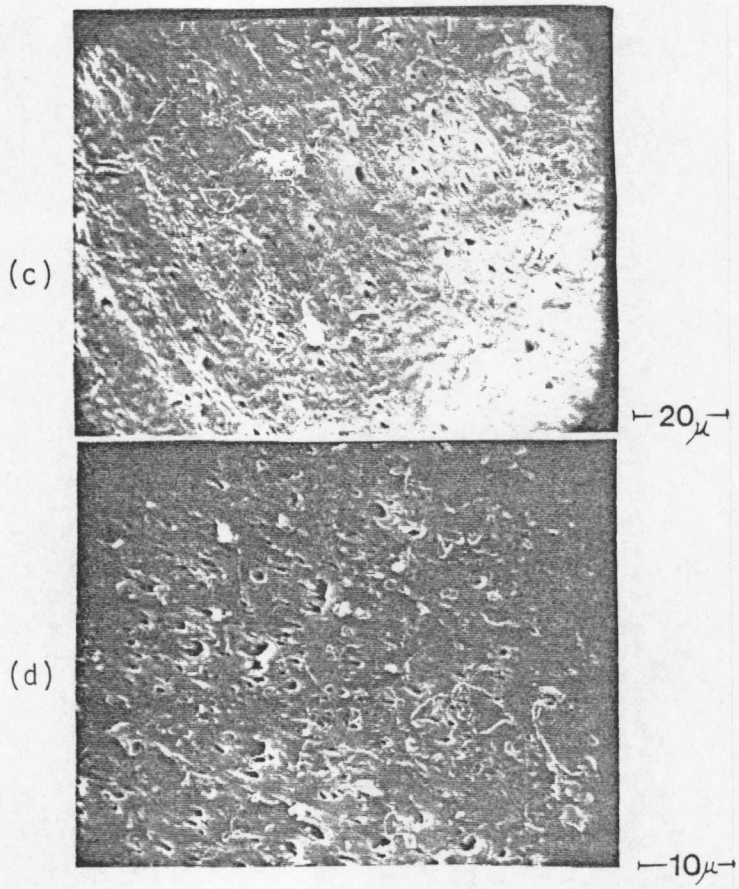


Figure VI-23 (continued)

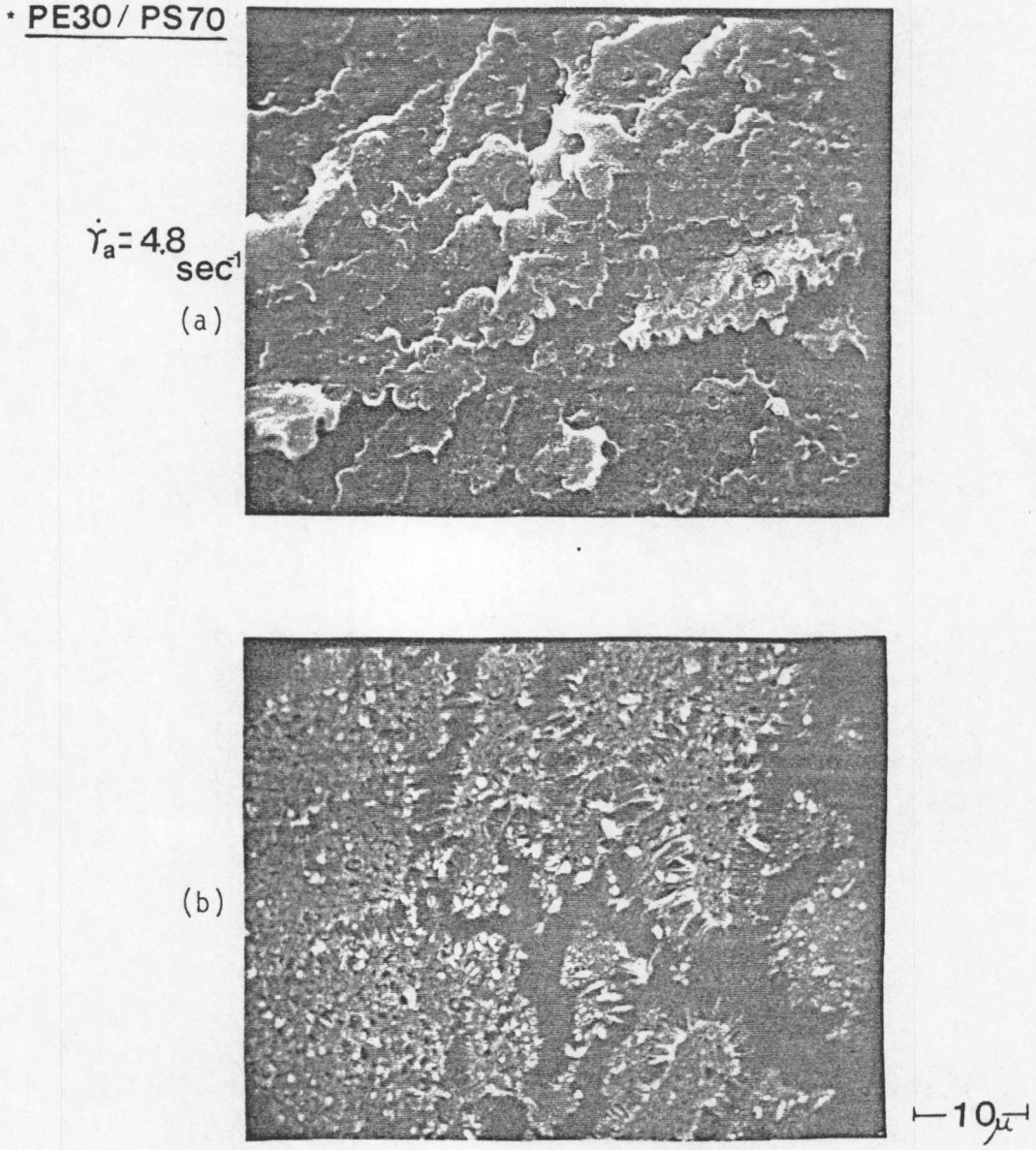


Figure VI-24. SEM microphotographs of PE-2/PS-30/70 blend melt spun fibers with different drawdown ratios: (a) 7; (b) 37.6.

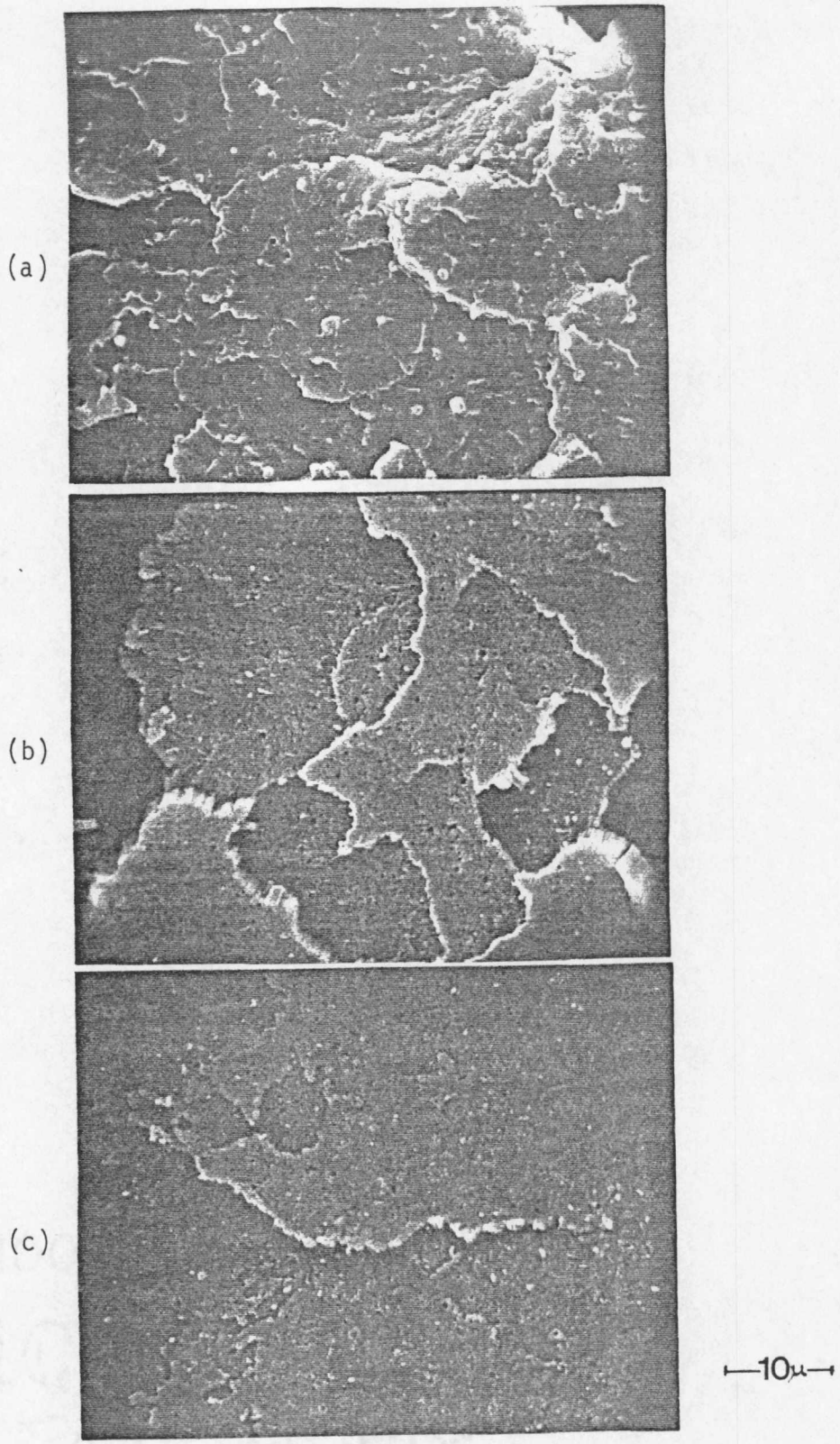


Figure VI-25. SEM microphotographs of PE-2/PS-10/90 blend melt spun fibers with different drawdown ratios: (a) 1; (b) 37.6; (c) 56.6.

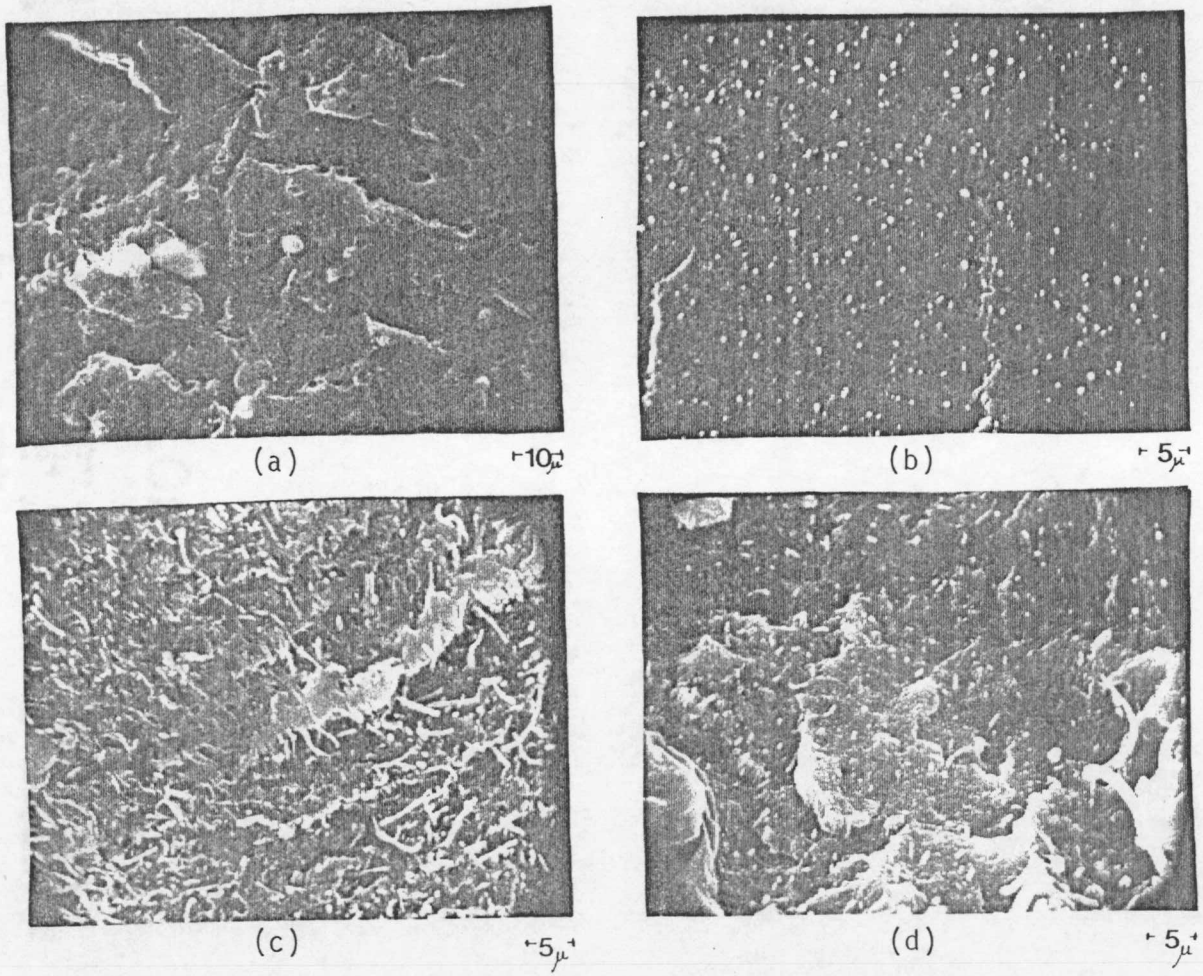
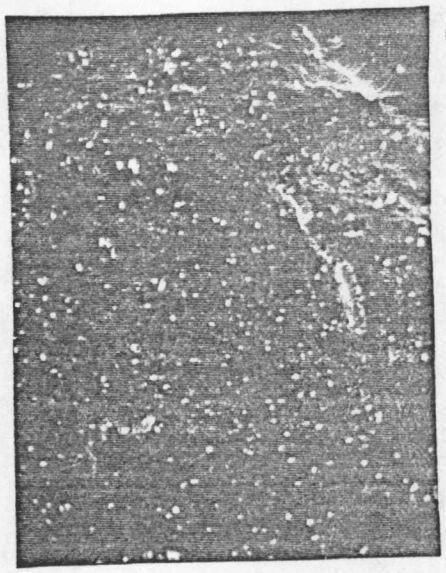


Figure VI-26. SEM microphotographs of PE-1/PS-90/10 blend melt spun fibers with different drawdown ratios: (a) 1; (b) 18.8; (c) 37.6; (d) 56.6; (e) 75.4.



(e)

Figure VI-26 (continued)

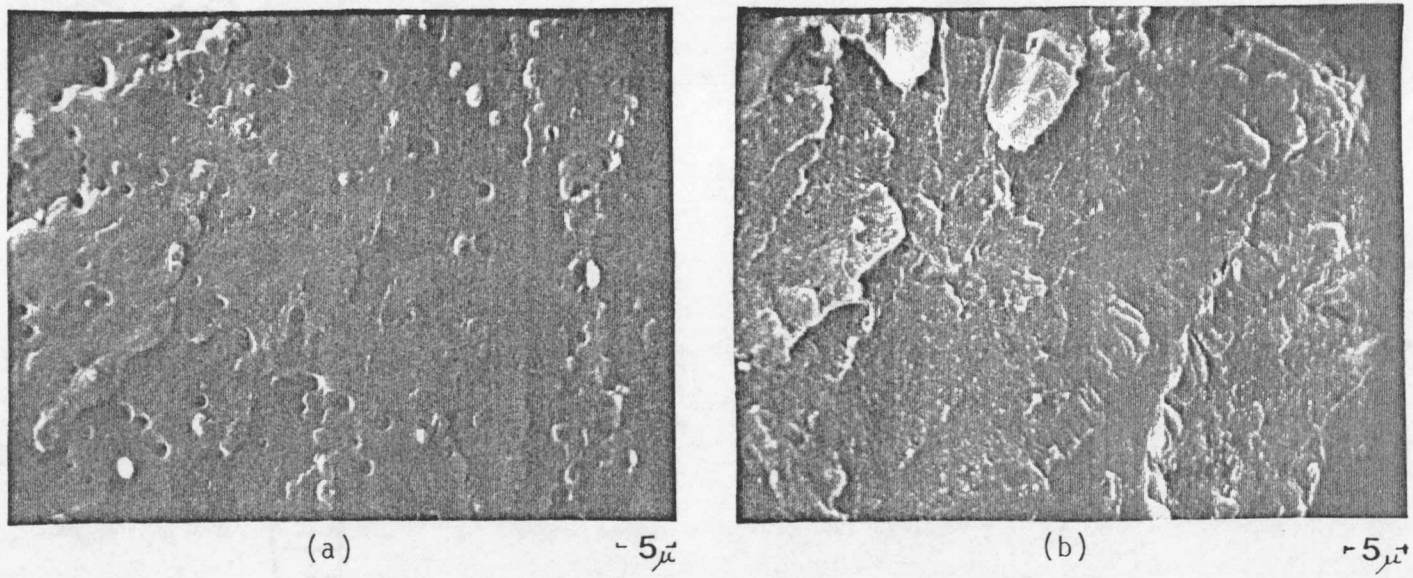
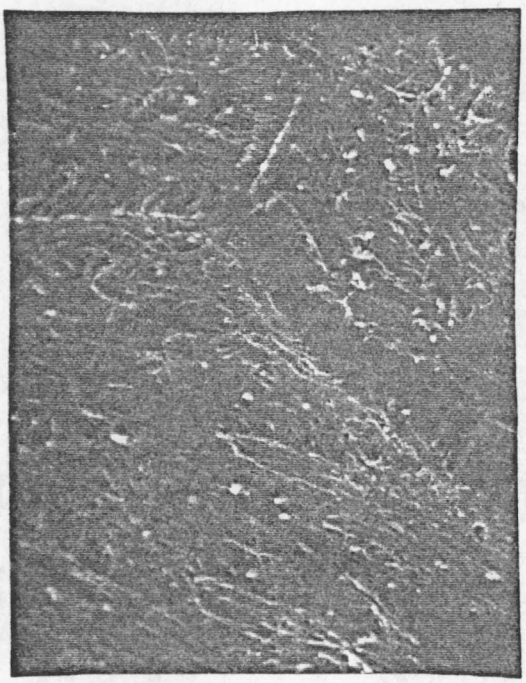


Figure VI-27. SEM microphotographs of PE-1/PS-90/10 blend melt spun fibers with different drawdown ratios: (a) 1; (b) 18.8; (c) 37.6.



(c)

Figure VI-27 (continued)

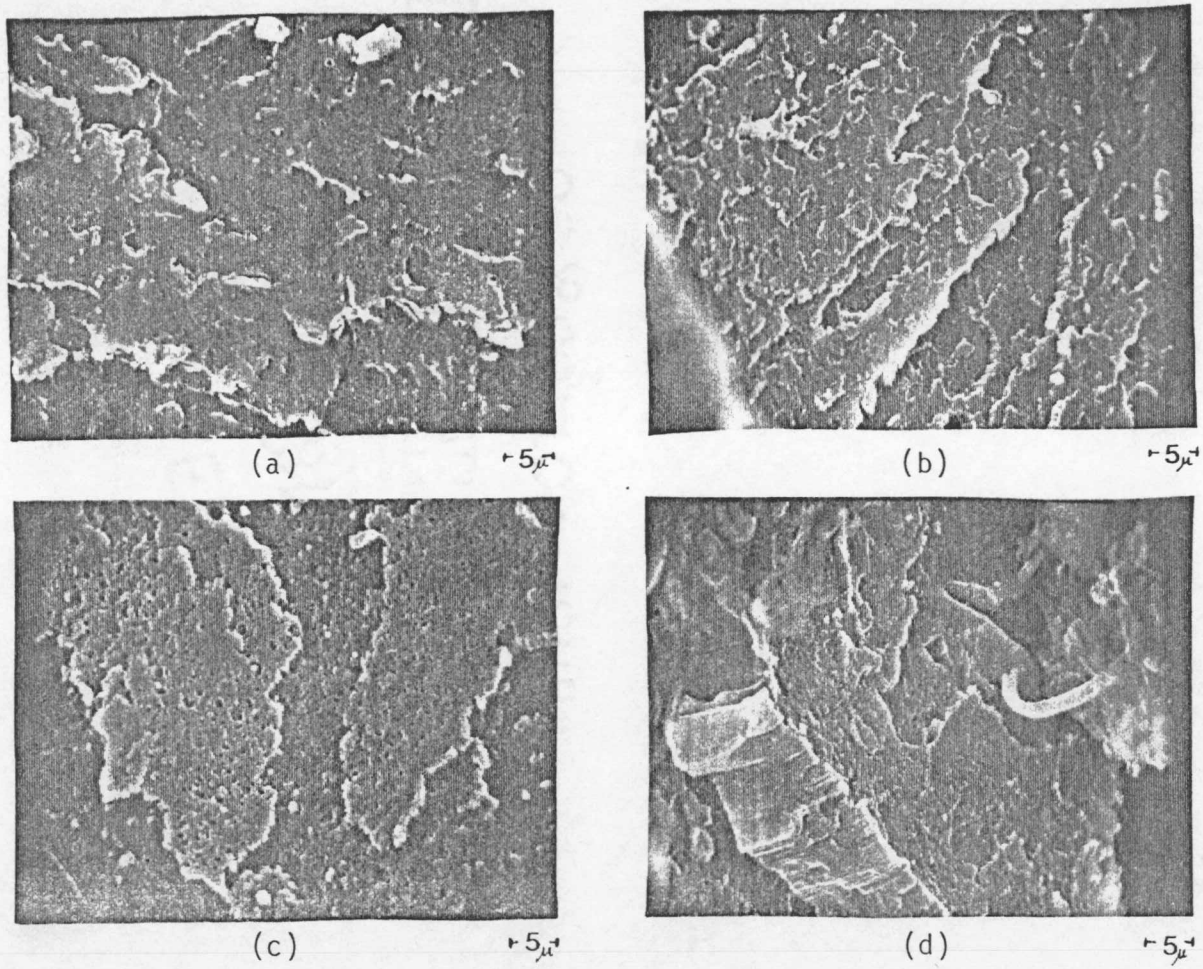


Figure VI-28. SEM microphotographs of PE-3/PS-10/90 blend melt spun fibers with different drawdown ratios: (a) 1; (b) 18.8; (c) 37.6; (d) 56.6; (e) 75.4.

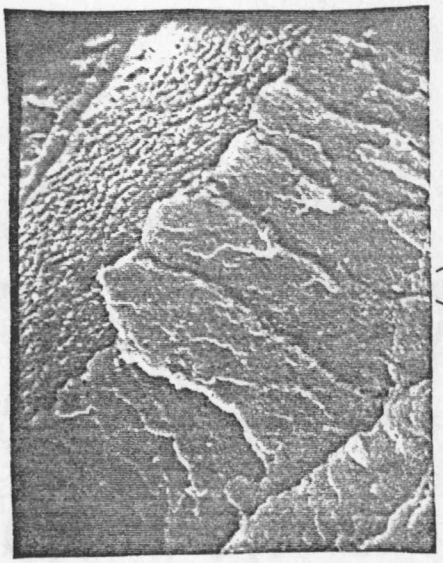


Figure VI-28 (continued)

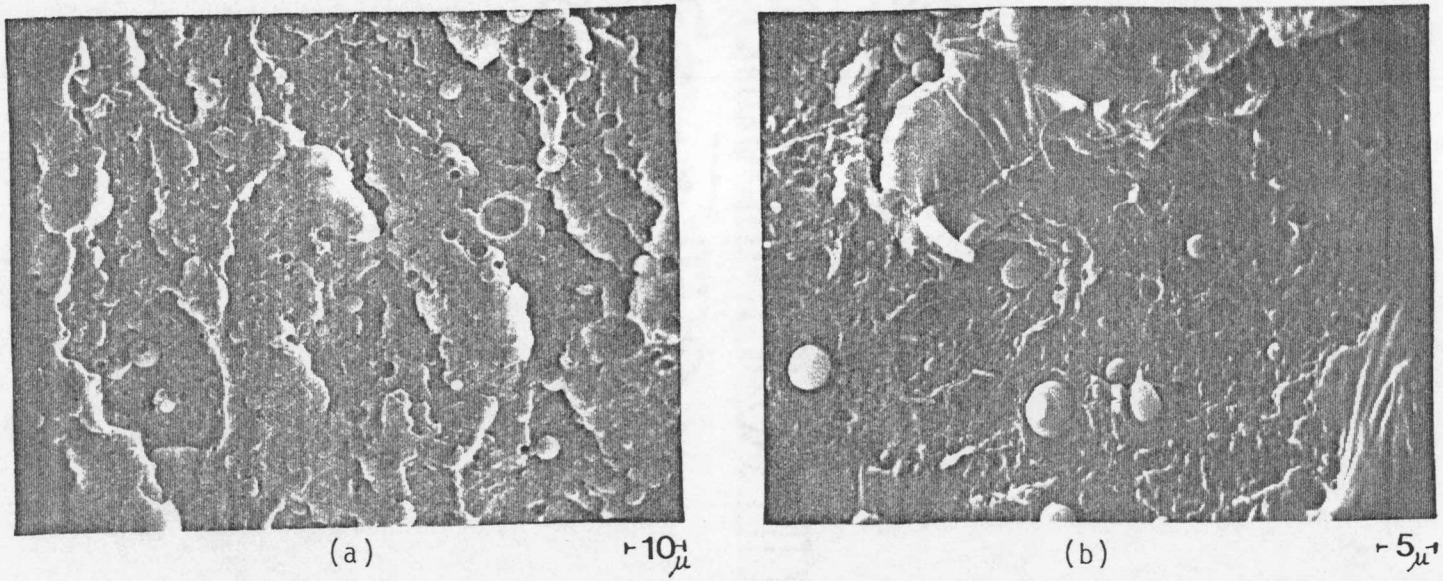


Figure VI-29. SEM microphotographs of PE-3/PS-90/10 blend melt spun fibers with different drawdown ratios: (a) 1; (b) 18.8; (c) 37.6; (d) 75.4.

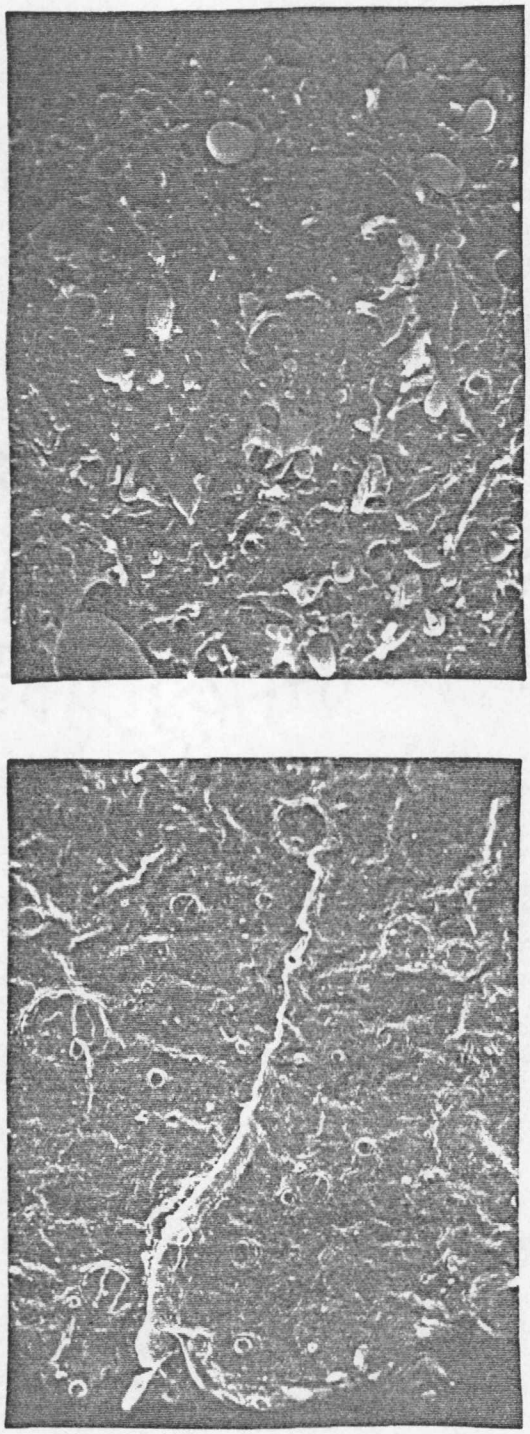


Figure VI-29 (continued)

blend fibers used by the high speed melt spun method. Liang et al. (90) reports the nylon 6-polypropylene blend fibers by using the same method as used here. They mentioned that small diameter mini-filaments that have diameters in a range from 0.5-5 microns are obtained from the formic acid extracted PP/N6-25/75 melt spun fiber.

The diameter of mini-fibers can be observed from samples which were embodied in the epoxy and fractured in liquid nitrogen. Figures VI-22 and VI-23 show the cross-section of PE/PS blends melt spun fibers. The diameters of the mini-filaments are listed in Tables VI-2 for PE-2/PS blend fibers and VI-3 for PE-1/PS, PE-2/PS, PE-3/PS-90/10 and.10/90 blend fibers.

If it is presumed that the diameter of the mini-fibers can be computed from the diameters of the "islands" in the extrudates by continuity, it may be written as follows, taking subscript "o" to represent the die and "L" the drawdown of the fiber at the take-up.

$$\frac{\pi d_o^2}{4} = V_o = \frac{\pi d_L^2}{4} V_L \qquad \text{(VI-2)}$$

$$d_L/d_o = \frac{1}{\sqrt{V_L/V_o}} \qquad \text{(VI-3)}$$

Equation (VI-3) and our experimental data are plotted in Figures VI-30 and VI-31. In the case of PE-2/PS blends, the deviation from affine deformation increases as PS content increases. The mini-fibers are larger than was expected from the above equations. The reduction

Table VI-2. The influence of drawdown ratios on the dimensions of mini-fibers of PE/PS, 10/90, 70/30, 50/50, 30/70 and 90/10 blend melt spun fibers

PE/PS Composition \ V_L/V_o	d_0	d_L			
	1	18.8	37.6	56.6	75.4
90/10	1.47	1.05	0.15	0.38	0.22
70/30	3.18	1.16	0.90	0.54	0.42
50/50	2.72	1.35	0.98	0.60	-
30/70	1.48	-	0.63	-	-
10/90	0.75	-	0.43	0.35	-

Table VI-3. The influence of drawdown ratios on the dimensions of mini-fibers of PE/PS, 10/90 and 90/10 blend melt spun fibers

PE/PS Composition \ V_L/V_o	d_o	d_L			
	1	18.8	37.6	56.6	75.4
PE-1	1.63				
90/10	1.63	0.24	0.23	0.20	0.18
10/90	0.67	0.39	0.29	-	-
PE-2					
90/10	1.47	1.05	0.50	0.38	0.22
10/90	0.75	-	0.43	0.35	-
PE-3					
90/10	5.44	1.91	1.88	1.75	-
10/90	0.48	0.34	0.27	0.25	0.16

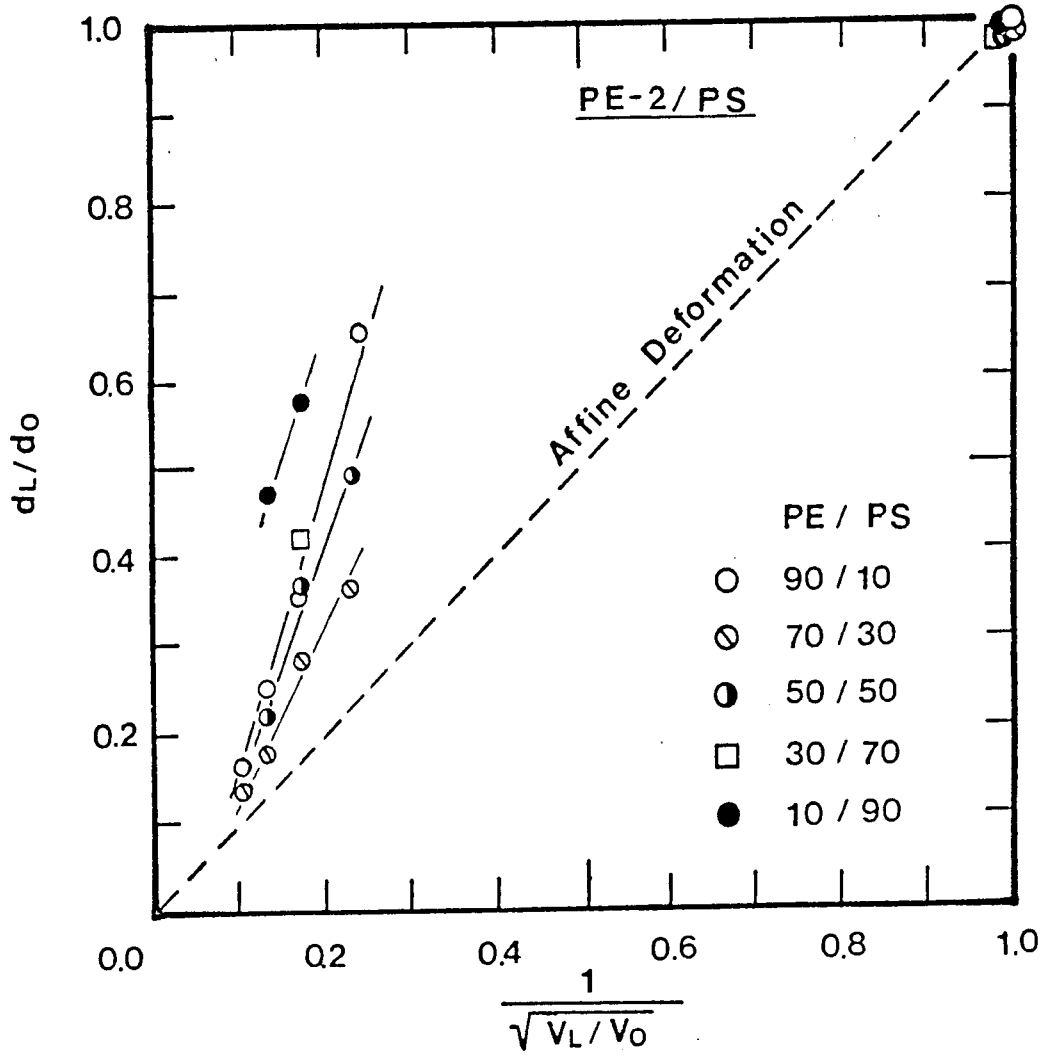


Figure VI-30. Comparison of affine-deformation of mini-fibers of PE-2/PS blend melt spun fibers.

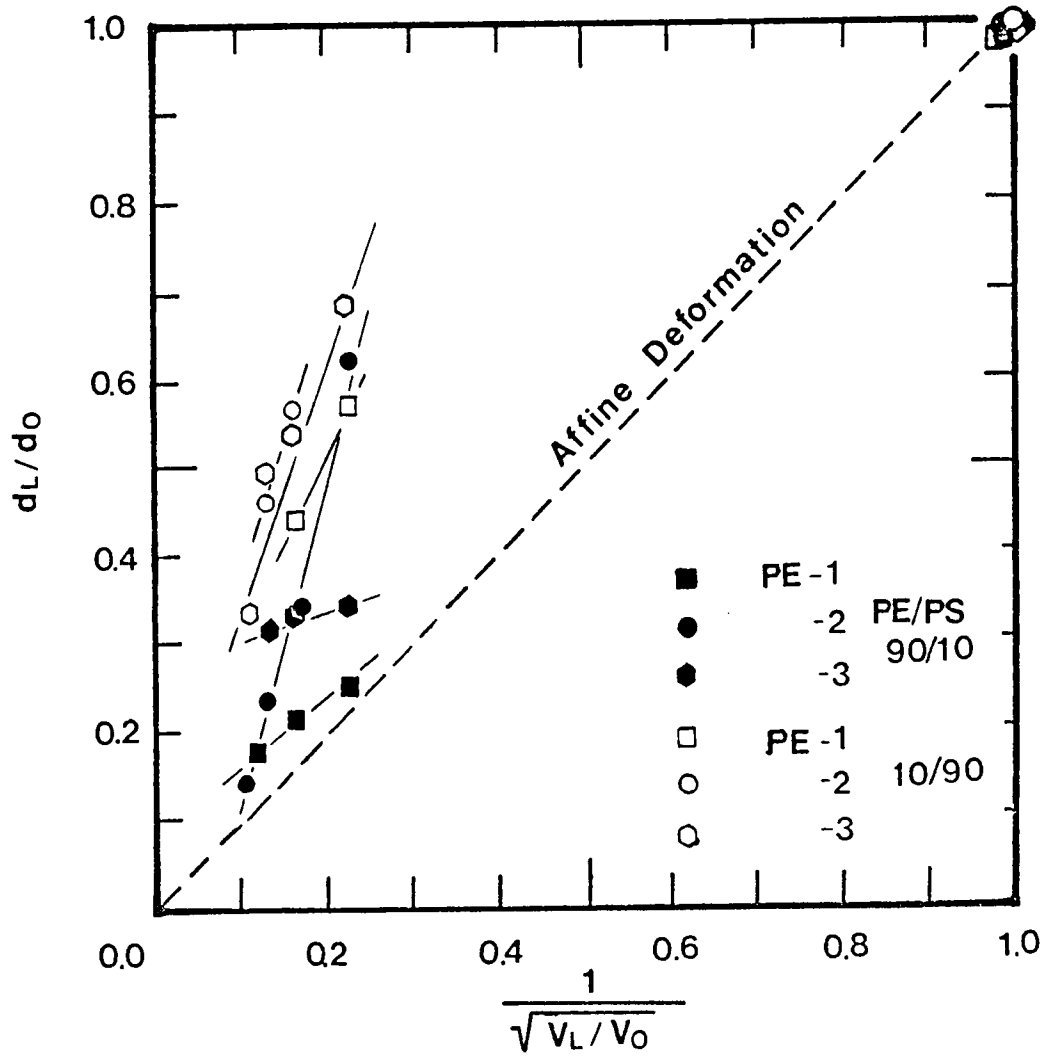


Figure VI-31. Comparison of affine-deformation of mini-fibers of PE-1, 2 and 3/PS-90/10 and -10/90 blend melt spun fibers.

seems strongly to depend on the viscosity, temperature and the initial size of the dispersed phase.

Diameter fluctuation of PE/PS mini-filaments is observed in Figure VI-32. The diameter of the mini-filaments around the boundary of fibers is larger than that of inside the fibers. This suggests non-affine kinematics during drawdown.

D. THE CHARACTER OF THE DISPERSED PHASE IN BIAXIALLY STRETCHED BLENDED FILMS

The studies on biaxial processing of mechanically dispersed polymer blends are very limited. In this section, the biaxially stretched films of polyethylene-polystyrene (PE-2/PS) blends are discussed for simultaneously stretched films at 130°C for 3 x 3 and 4 x 4. It was generally found to be very difficult to stretch the lower viscosity melt for PS because of sagging. 130°C was chosen as a proper temperature to process biaxially.

D.1. Results

Figures VI-33 to VI-37 show the fracture surface cross-section and the toluene extracted surface of biaxially stretched PE/PS blend films. The dispersed phase is stretched roughly biaxially according to the magnitude of stretching ratio. With increasing biaxial stretching, the polyethylene particles ($1 \simeq 6\mu$) were distorted to disks for PE-2/PS-90/10 blend. In the PE-2/PS-10/90 blend, the particles of polyethylene ($1.5 \simeq 3\mu$) spread to a flake shape with increasing biaxial stretch rates. In Figure VI-37, one can see that

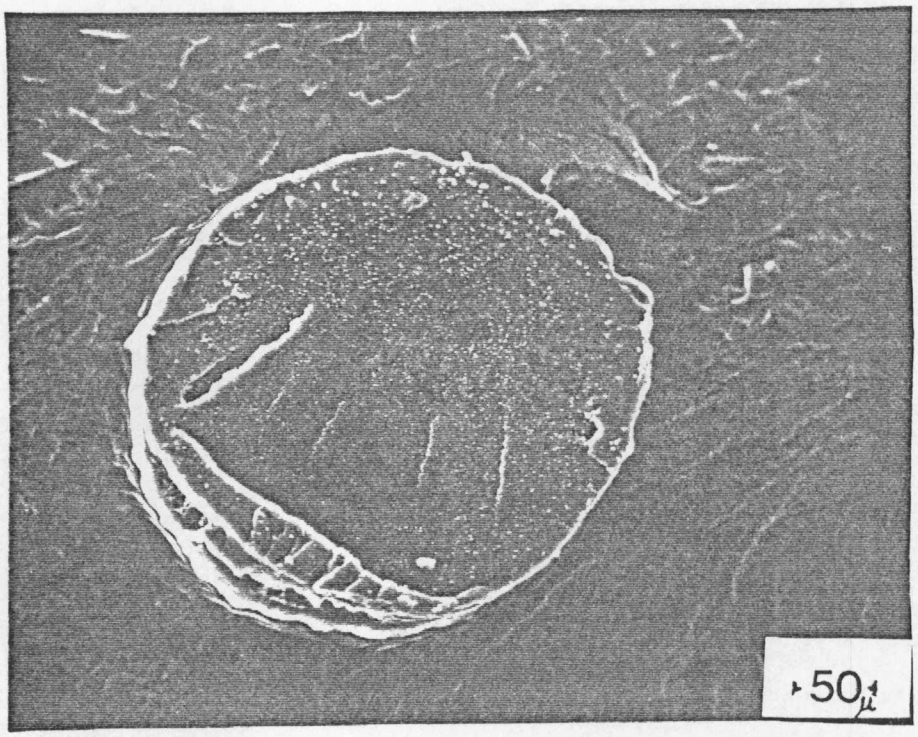


Figure VI-32. SEM microphotograph of PE-1/PS-90/10 blend melt spun fibers.

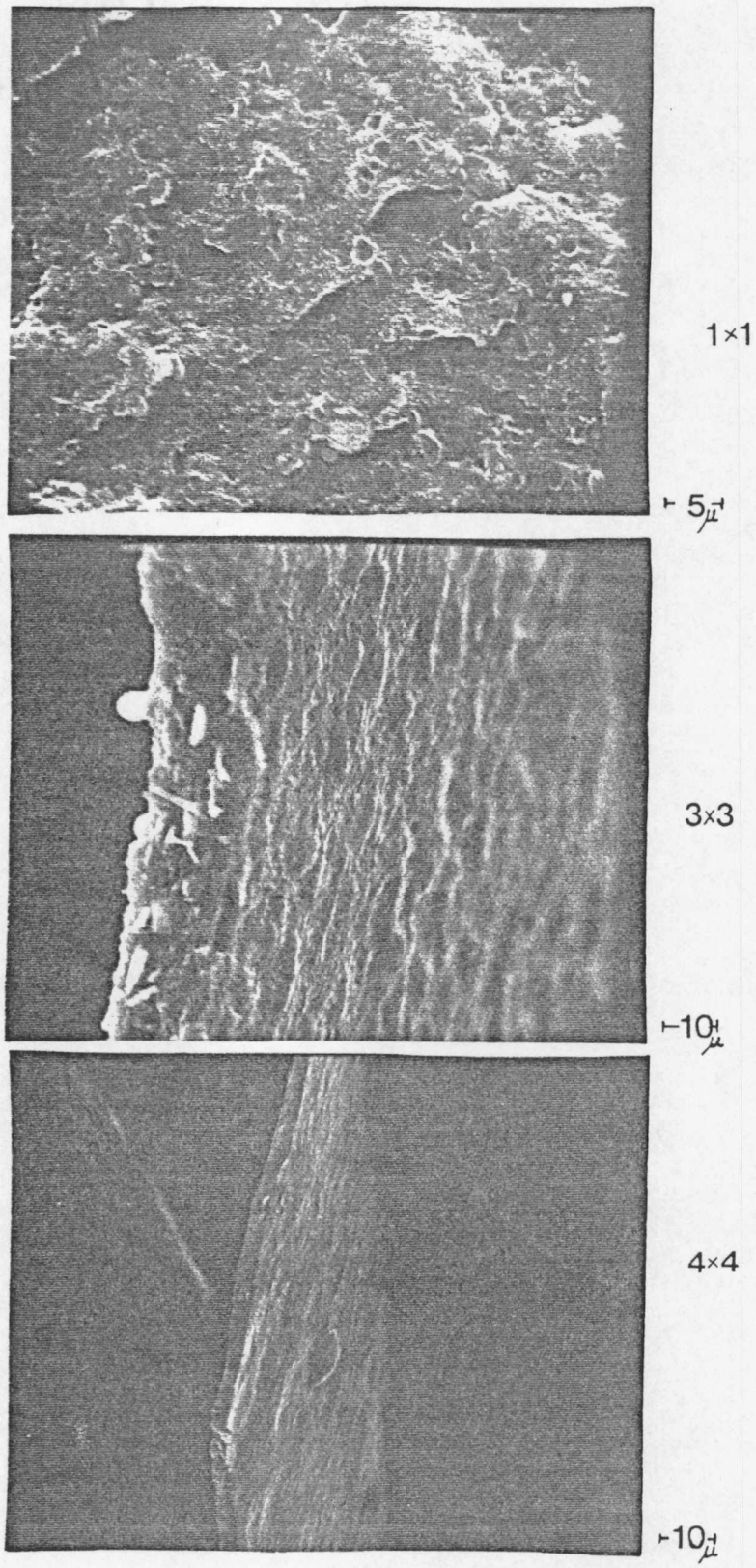


Figure VI-33. SEM microphotographs of biaxially stretched films of PE-2/PS-90/10 blend with different stretching ratios.

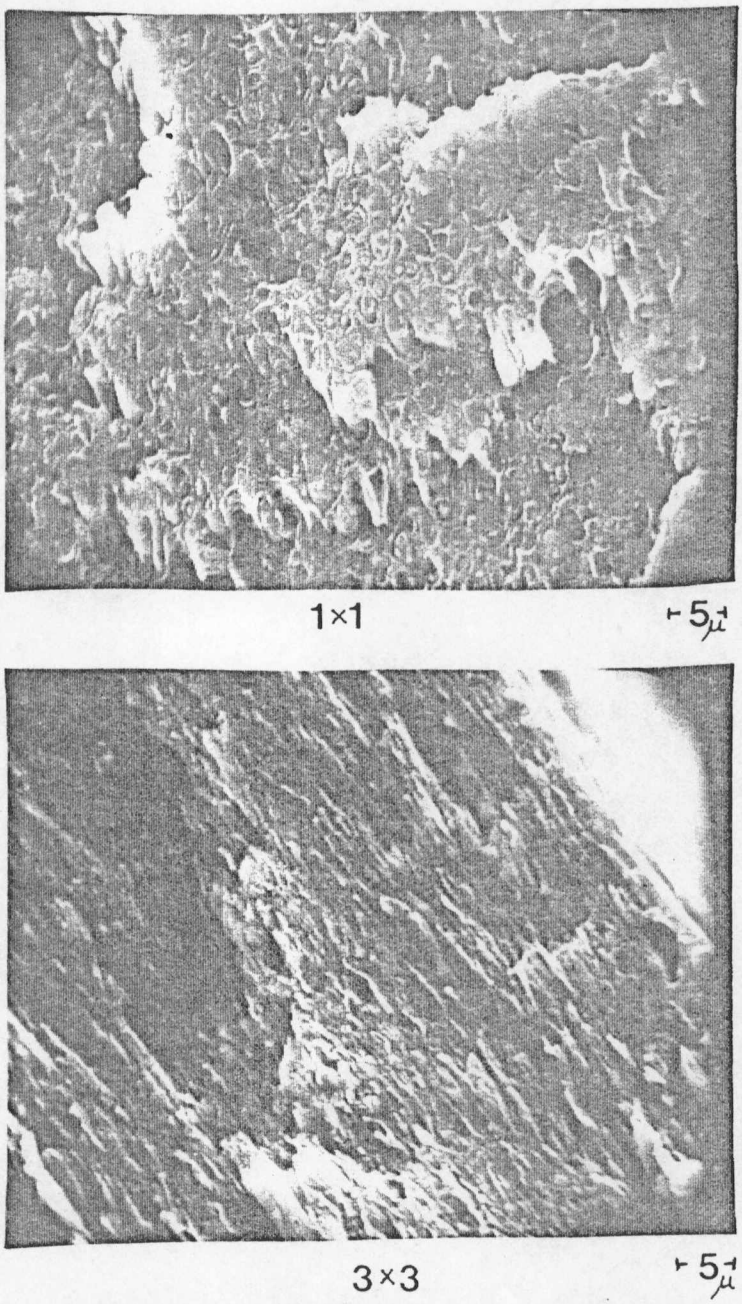


Figure VI-34. SEM microphotographs of biaxially stretched films of PE-2/PS-70/30 blend with different stretching ratios.

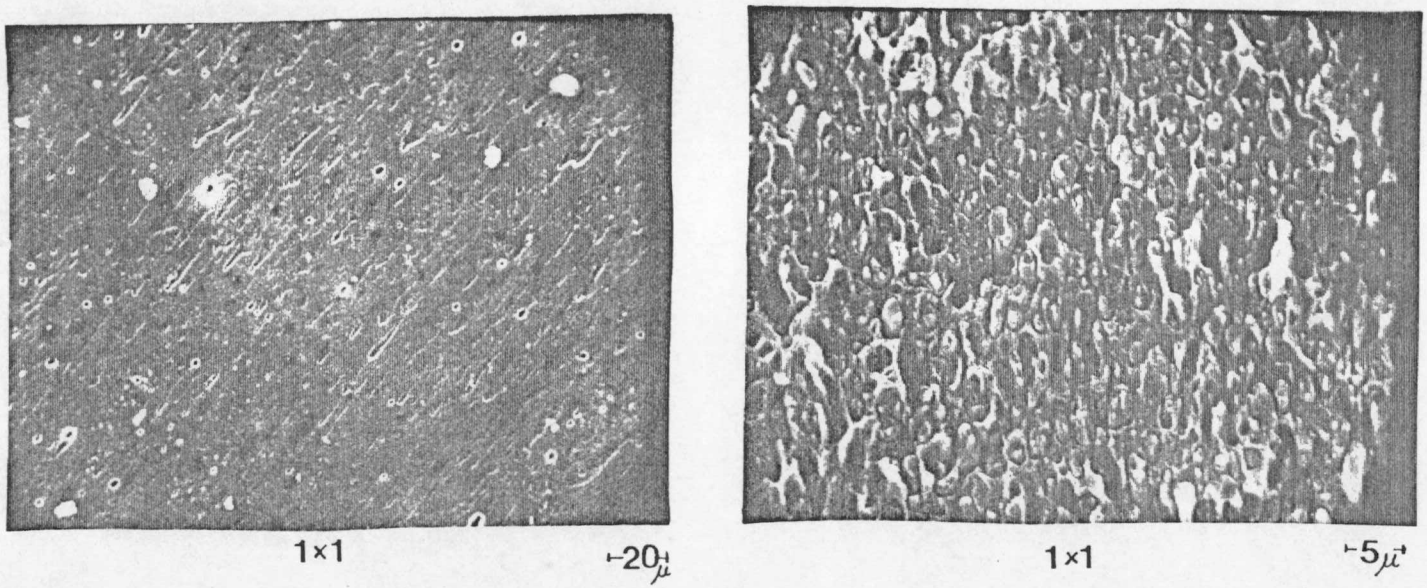


Figure VI-35. SEM microphotographs of PE-2/PS-90/10 blend with different stretching ratios.

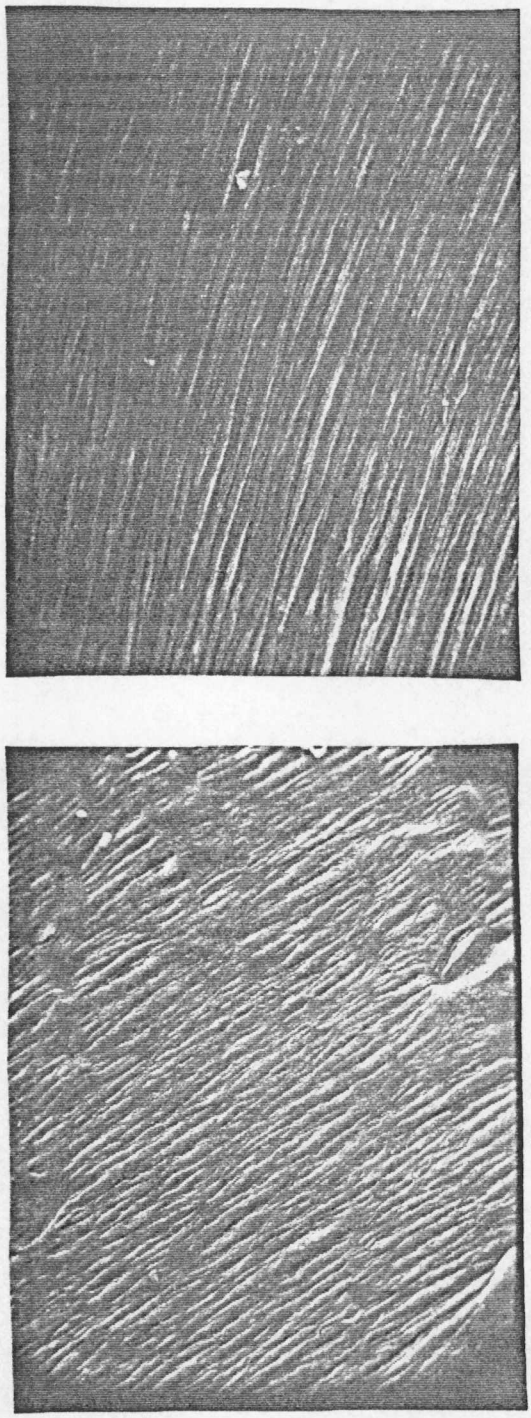


Figure VI-35 (continued)

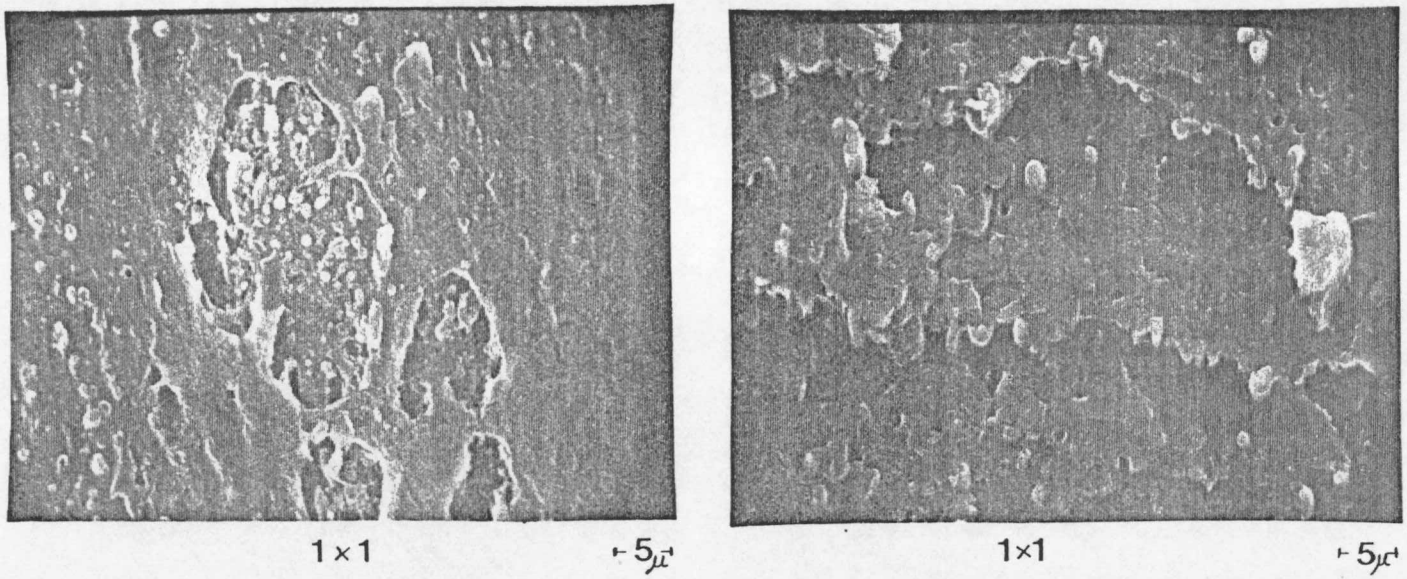


Figure VI-36. SEM microphotographs of biaxially stretched films of PE-2/PS-30/70 blend with different stretching ratios.

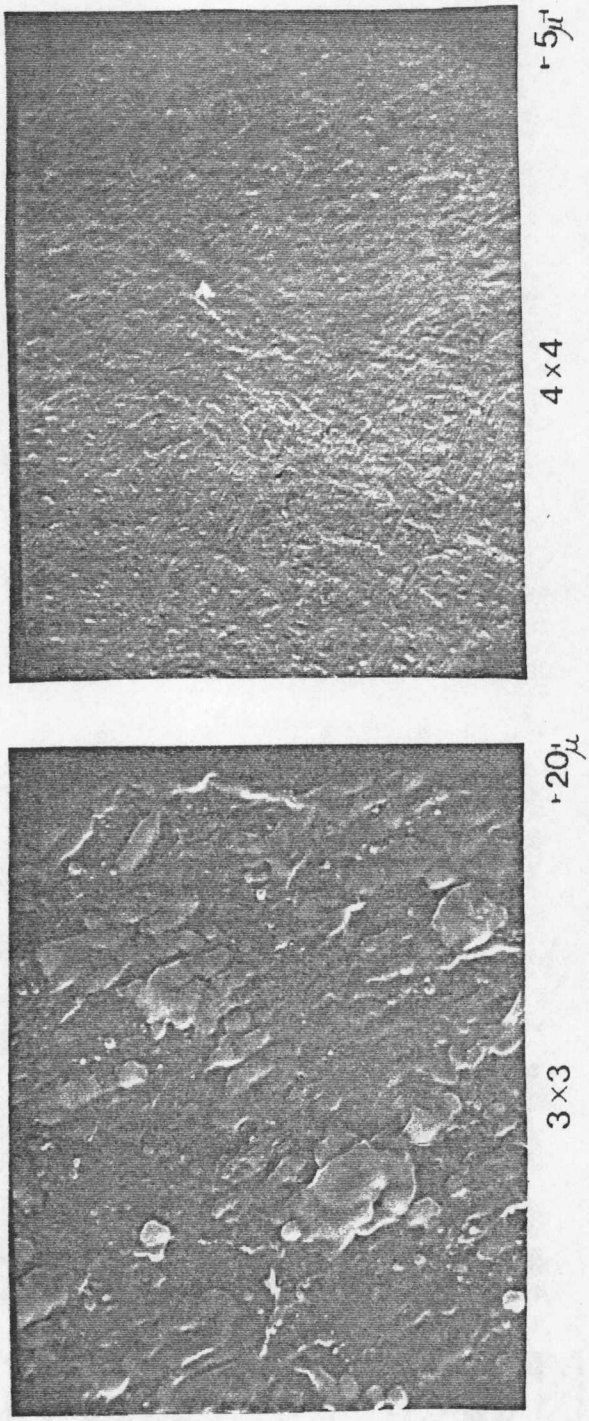


Figure VI-36 (continued)

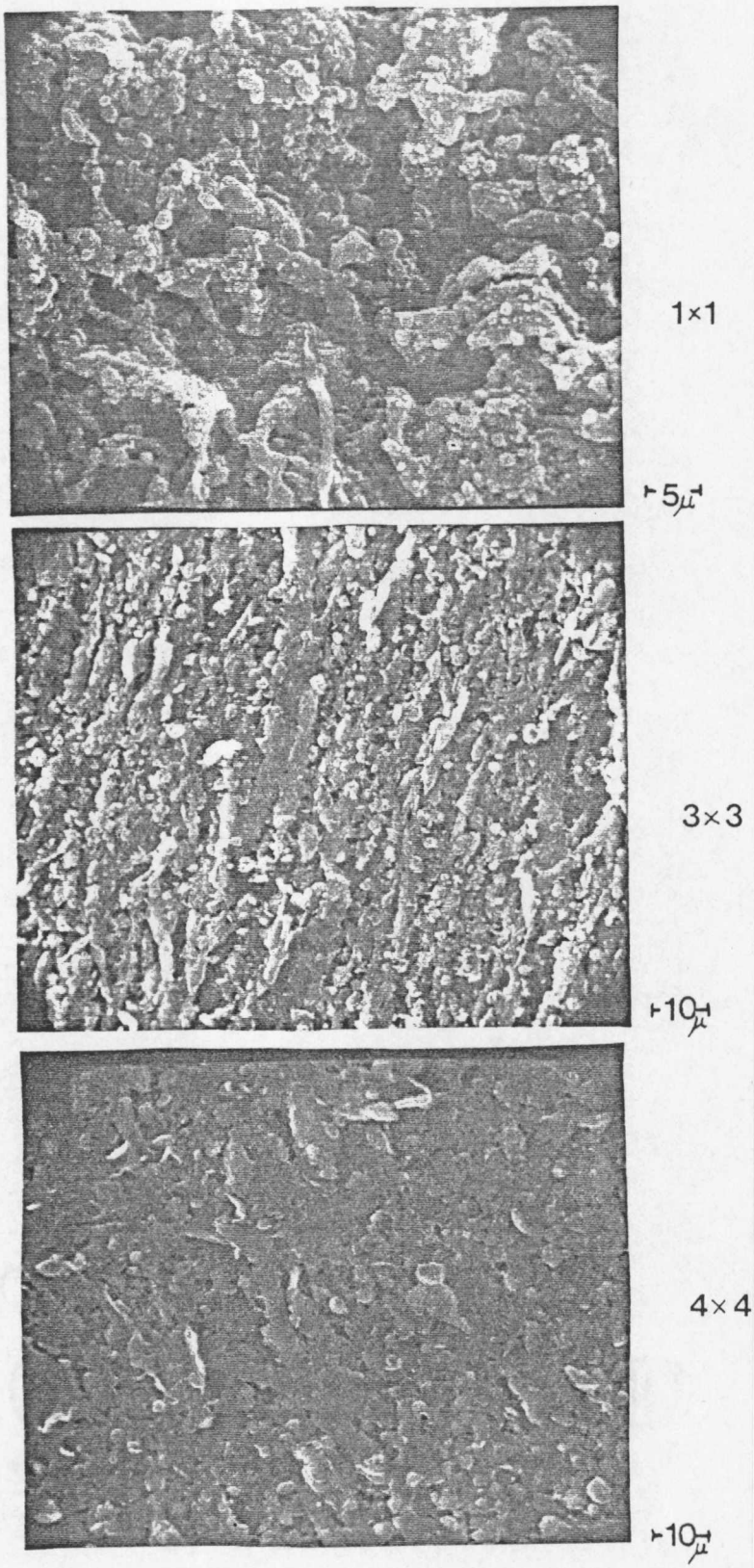


Figure VI-37. SEM microphotographs of biaxially stretched films of PE-2/PS-10/90 blend with different stretching ratios.

the flakes of polyethylene phase were tilted to one direction. In the PE-2/PS-50/50 blend, continuous rods of polyethylene appeared and arranged at angle ≈40° at 3 x 3 and then at 4 x 4. The continuous rods of polyethylene became mats. The cross-sections suggest a multilayered sheet at the higher levels of biaxial stretching. The mechanism of deformation of dispersed phase is explored in Figure VI-38.

D.2. Discussion

Thomas and Cleerman (162) have reported the biaxial stretching of HIPS to a biaxial stretch ratio of 3x by 3x at 128°C. They observed the cross-section of HIPS sheets using TEM. They reported that the rubber particle configuration in biaxially oriented HIPS showed that spherical particles ultimately flatten with increasing orientation, giving the appearance of multilayered sheet. In the present work, PE-2/PS-70/30, 30/70, and 10/90 show the appearance of multilayered sheet. The dispersed phase was stretched biaxially. The PE-2/PS-50/50 was initially a matrix of PS rods in a PE matrix. After stretching, it has continuous threads of polyethylene. The phenomenon must be considered in terms of fibrillation of polyethylene at high stretching rates. Initially, the polyethylene matrix was stretched biaxially. The response of the solid matrix with PS stress concentrates has to fibrillate.

The polyethylene sheets are stretched biaxially less uniformly than the polystyrene. It was observed that adding polystyrene

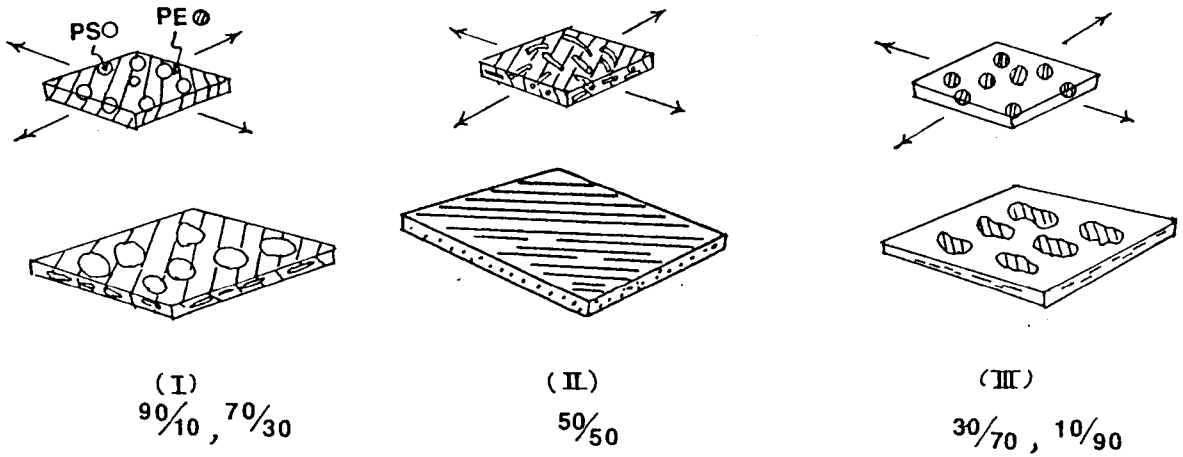


Figure VI-38. Schematic representation of biaxial deformation of discrete phase of PE-2/PS blend films.

into polyethylene creates more uniform sheets. Judging from SEM photomicrographs, one can see that the polystyrene phase of PE/PS blend sheets was stretched more than the polyethylene phase.

CHAPTER VII

CONCLUSIONS AND RECOMMENDATIONS

A. CONCLUSIONS

A broad-based study of the development of phase morphology, molecular orientation, rheological behavior, and processing of a high density polyethylene/polystyrene (PE/PS) blend, polyethylene/nylon 6 blend, and high density polyethylene/polycarbonate (PE/PC) systems has been reported. The most extensive studies were for polyethylene/polystyrene. Certain trends are clear:

1. The phase morphologies developed by a screw extruder/static mixer system generally involve phase dimensions of 1≃5μ except at 50/50 loadings where dimensions up to 10μ are obtained. Some reduction is obtained by subsequent shearing in viscometric instruments. Phase dimensions as fine as 0.6μ are obtained in a 10/90 PE/PS at higher shear rates in a capillary die. These diameters may be reduced even further by melt spinning. Small diameter mini-fibers may be produced by extracting the PS (with toluene). Mini-fibers of diameter of order 0.2 may be produced. The morphologies are much finer than in studies of the

polyethylene/nylon 6 system, polyethylene/polycarbonate system. This is presumably because of the lower interfacial tensions.

2. The phase morphologies of PE/PC and PE/N6 systems developed by a screw extruder/static mixer system are much coarser than those of PE/PS systems. With increasing shear stress, the dispersed phase becomes finer in the outer layer of the extrudate but remains coarser near the center line. This phenomenon would appear to be due to the higher interfacial tension and interpretable in terms of the dimensionless group $\eta\dot{\gamma}d/\kappa$. In these systems this is coupled with the fact that high stress occurs only in the outer regions of the capillary.
3. The fibrillation of extrudates was found to be influenced by the two dimensionless parameters, i.e., viscosity ratio λ and $\eta\dot{\gamma}d/\kappa$. If $\lambda > 2.2$ and $\eta\dot{\gamma}d/\kappa$ is small, the droplets are not transferred to fibers with shear flow. For $\lambda \leq 0.7$, the droplets evolve into thin fibers with increasing shear stress or $\eta\dot{\gamma}d/\kappa$.
4. The crystalline polyethylene orientation developed in melt spun PE/PS fibers is significantly reduced by the presence of polystyrene when comparisons are at the same spinline stress. This differs from observations made earlier on polypropylene/nylon 6 (90) and polyethylene/polypropylene (142) blends where crystalline orientation in the

polyethylene and polypropylene phase depends on the process stress in a manner equivalent to the pure phases. This is attributed to the greater temperature dependence on the viscosity of the PS on which the stress increasingly concentrates as the melt blends descends the threadline.

5. The shear viscosity and principal normal stress difference depend on the volume fractions of the individual polymers in a complex manner. Maxima and minima are observed as a function of composition. Interpretation of the shear viscosity is offered in terms of Taylor's and Choi-Schowalter's theory of emulsion (26) for dilute phases containing spheres and Lee's theory of lamellae flow for intermediate concentrations or dilute phases containing fibers.
6. Addition of PE to PS substantially increases the shrinkage of extrudates.
7. The extrudate swell for PE-2/PS of the blends correlate with the principal normal stress difference N_1. However, other systems show more complicated behavior.
8. The uniaxial elongation flow and melt spinning characteristics of the blends are dominated by the high density polyethylene. Addition of PE reduces the elongation to break and makes the spinline unstable. This may be due, in part, to non-homogeneities.

9. Films formed by biaxially stretching of PE/PS blends at 130°C show the appearance of multilayered sheets. The dispersed phase was stretched biaxially. At high stretching rates, fibrillation of PE has been observed.

B. RECOMMENDATIONS

The following studies on rheological, morphological characteristics and processing of polymer blends are recommended for future investigators:

1. More extensive studies of the effect of the influence of interfacial tension on the phase morphology.
2. The use of additives such as stearic acid and block copolymers to influence the morpology of polar and non-polar systems.
3. It is desirable to determine and analyze the mechanisms of elongation flow and elongation to break and its relationship to the deformation of the individual phases.
4. The development of orientation in two-phase blends needs further study. The results of the two components and the temperature dependence has a major effect.
5. More extensive studies of morphology variation in biaxially stretched sheets of blends are needed.

LIST OF REFERENCES

LIST OF REFERENCES

1. Ablazova, T. I., A. V. Judine, M. V. Tsebrenkz, B. V. Jarlykov, G. V. Vinogradov, Polymer, 16, 609 (1975).

2. Acrivos, A. and T. S. Lo, J. Fluid Mech., 86, 841 (1978).

3. Alle, N. and J. Lyngaal-Jorgensen, Rheol. Acta., 19, 104 (1980).

4. Amos, J. L., Polym. Eng. Sci., 14, 1 (1974).

5. Arrhenius, S., Zeitsch. für Phys. Chem. (i), 285 (1887).

6. Arrhenius, S., Nedd. Vetenskapsakad Nobelist, 2, 25 (1913).

7. Bank, M., J. Leffingwell and C. Thies, Macromolecules, 4, 43 (1971).

8. Ibid., J. Polym. Sci., A-2, 10, 1097 (1972).

9. Barensten, W. M., D. Heikens and P. Piet, Polymer, 15, 119 (1974).

10. Barensten, W. M. and D. Heikens, Polymer, 14, 579 (1973).

11. Bartow, J. W. and D. R. Paul, Polym. Eng. Sci., 21, 985 (1981).

12. Barthe's-Biesel, D. and A. Acrivos, J. Fluid Mech., 61, 1 (1973).

13. Bartok, W. and S. G. Mason, J. Colloid Sci., 13, 2936 (1958).

14. Bartok, W. and S. G. Mason, J. Colloid Sci., 14, 13 (1959).

15. Bartram, E., H. L. Goldsmith and S. G. Mason, Rheol. Acta, 14, 776 (1975).

16. Bonn, R. and J. Van Aarsten, Eur. Polym. J., 8, 1055 (1972).

17. Bunn, C. W., Trans. Faraday Soc., 35, 482 (1937).

18. Carley, J. F. and S. C. Crossan, Polym. Eng. and Sci., 21, 249 (1981).

19. Carley, J. F., R. S. Mallonk and J. M. McKevley, Ind. Eng. Chem., 45, 974 (1953).

20. Carley, J. F. and R. A. Strub, Ind. Eng. Chem., 45, 978 (1958).

21. Charles, M. E. and T. W. F. Russell, Canad. J. Chem. Eng., 37, 127 (1959).

22. Charles, M. E. and P. J. Redbenger, Canad. J. Chem. Eng., 40, 70 (1962).

23. Charles, M. E. and L. U. Lilleheht, J. Chem. Eng., 43, 110 (1965).

24. Chin, H. B. and C. D. Han, J. Rheol., 23, 557 (1979).

25. Chin, H. B. and C. D. Han, J. Rheol., 24 (1), 1 (1980).

26. Choi, S. J. and W. R. Schwalter, Phys. Fluids, 18, 420 (1975).

27. Cox, R. G., J. Fluid Mech., 37, 601 (1969).

28. Cruz, C. A., J. W. Barlow and D. R. Paul, Macromolecules, 12, 726 (1979).

29. Cruz, C. A., D. R. Paul and J. W. Barlow, J. Appl. Polym. Sci., 23, 589 (1979).

30. Dillon, J. H. and N. Johnson, Physics, 4, 225 (1933).

31. Einstein, A., Ann. Physik, 19, 289 (1906).

32. Einstein, A., Ann. Physik, 34, 591 (1911).

33. Everage, A. E., Jr., Trans. Soc. Rheol., 17:4, 629 (1973).

34. Everage, A. E., Jr., Trans. Soc. Rheol., 19:4, 509 (1975).

35. Fayt, R., R. Jerome and Ph. Jeyssie, J. Polym. Sci., 19, 198 (1981).

36. Flory, P. J., J. Chem. Phys., 9, 660 (1941).

37. Ibid., J. Chem. Phys., 10, 51 (1942).

38. Ibid., J. Chem. Phys., 13, 453 (1945).

39. Flory, P. J., in Principles of Polymer Chemistry, Cornell Univ. Press, Ithaca, NY (1962).

40. Flory, P. J., J. Am. Chem. Soc., 86, 1833 (1965).

41. Flumerfeld, R. W., Ind. Eng. Chem. Fundam., 11, 312 (1972).

42. Frankel, N. A. and A. Acrivos, J. Fluid Mech., 44, 65 (1970).

43. Fukushima, O., in Polymer Alloy, Kobunshi Gakkai, ed., Tokyo Kogaku Dogin (1980).

44. Gauthier, F., A. L. Goldsmith and S. G. Mason, Rheol. Acta, 10, 344 (1971).

45. Gemmel, A. R. and N. Epstein, Canad. J. Chem. Eng., 40, 215 (1962).

46. Gibbs, J. W., in The Scientific Papers of J. W. Gibbs, Vol. I, Dover, New York (1971).

47. Hadmard, M., Compt. Rend., 136, 299 and (1903).

48. Han, C. D., J. Appl. Polym. Sci., 17, 1289 (1973).

49. Han, C. D., Rheology in Polymer Processing, Academic Press, New York (1976).

50. Han, C. D. and K. Funatsu, J. Rheol., 22, 113 (1978).

51. Han, C. D. and H. B. Chin, Polym. Eng. Sci., 19, 1156 (1979).

52. Han, C. D., K. U. Kim, J. Parker, N. Siskovic and C. R. Huang, Appl. Polym. Symp., 20, 91 (1973).

53. Han, C. D. and Y. W. Kim, J. Appl. Polym. Sci., 18, 2589 (1974).

54. Han, C. D. and Y. W. Kim, Trans. Soc. Rheol., 19, 245 (1975).

55. Han, C. D., Y. W. Kim and S. J. Chen, J. Appl. Polym. Sci., 19, 2831 (1975).

56. Han, C. D. and R. G. King, J. Rheol., 24, 213 (1981).

57. Han, C. D. and R. Shetty, Polym. Eng. Sci., 16, 697 (1976).

58. Han, C. D. and R. Shetty, Polym. Eng. Sci., 18, 180 (1978).

59. Han, C. D. and T. C. Yu, J. Appl. Polym. Sci., 15, 1163 (1971).

60. Harris, J. E., Ph.D. Dissertation, Univ. of Texas at Austin (1981).

61. Hayashida, K., J. Takahashi and M. Matsui, Proc. 5th Int. Cong. Rheology, Kyoto (1968), 4, 525 (1977).

62. Heikens, D. and W. Barensten, Polym. 18, 69 (1977).

63. Heikens, D., H. Hoen, W. Batresten, P. Piet and H. Ladan, J. Polym. Sci. Polym. Symp., 62, 309 (1978).

64. Heiltmiller, R. F., R. Z. Naar and H. H. Zabusky, J. Appl. Polym. Sci., 8, 873 (1964).

65. Hildebrand, J. H. and R. L. Scott, in The Solubility of Non-electrolytes, pp. 94, 121, 425, Dover, New York (1948).

66. Hoy, K. L., J. Paint Technol., 42, 76 (1970).

67. Huang, D. and J. L. White, Polym. Eng. and Sci., 20, 182 (1980).

68. Huggins, K. L., J. Chem. Phys., 9, 440 (1940).

69. Ibid., J. Phys. Chem., 46, 151 (1942).

70. Ibid., Ann. N. Y. Acad. Sci., 43, 1 (1942).

71. Ide, Y. and J. L. White, J. Appl. Polym. Sci., 20, 2511 (1976).

72. Ide, Y. and J. L. White, J. Appl. Polym. Sci., 22, 1061 (1978).

73. Issacs, J. D. and J. B. Speed, U.S. Patent 2,533,878,

74. Kamar, R. and Y. Saradly, I.E.C. Fund., 11, 307 (1972).

75. Kanitz, A., Z. Physik. Chem., 22, 336 (1897).

76. Karam, H. and J. C. Bellinger, Ind. Eng. Chem. Fund., 7, 576 (1968).

77. Khambatta, F. B., F. Warner, T. Russell and R. S. Stein, J. Polym. Sci., 14, 1591 (1976).

78. Khan, A. A. and C. D. Han, Trans. Soc. Rheol., 20:4, 595 (1976).

79. Kitao, T., S. Ohya, J. Furukawa and S. Yamashita, J. Polym. Sci., 11, 1091 (1973).

80. Koenhen, D. M. and C. A. Smolders, J. Appl. Polym., 19, 1163 (1975).

81. Konstan, A. H. and W. R. Feairheller, Jr., AICHE J., 16, 837 (1960).

82. Kunori, T. and P. H. Geil, J. Macromol., B 18 (1), 93 (1980).

83. Launstein, C., Zeitsh. fur Phys. Chem., 9, 417 (1892).

84. Launstein, C., Zeitsh. fur Phys. Chem., 22, 336 (1897).

85. Lee, B. L. and J. L. White, Trans. Soc. Rheol., 18:3, 467 (1974).

86. Lees, C., Proc. Phys. Soc., 17, 460 (1900).

87. Leviton, A. and A. Leighton, J. Phys. Chem., 40, 71 (1936).

88. Li, C. H., Phys. Fluids, 12, 531 (1969).

89. Ibid., Phys. Fluids, 13, 1701 (1970).

90. Liang, Bo-Run, J. L. White, J. E. Spruiell and B. C. Gozuwami, J. Appl. Polym. Sci., 28, 2011 (1983).

91. Linebarger, C., Amer. J. Sci. Ser. 4 (11), 331 (1896).

92. Lodge, A. S., Elastic Liquids, Academic Press, New York (1964).

93. Lyttleton, D. V. and R. N. Traxler, Ind. Eng. Chem., 22, 1011 (1948).

94. Maclean, D. L., Trans. Soc. Rheol., 17:3, 385 (1973).

95. Maddock, B. H., SPE Journal, 15, 383 (1959).

96. Mark, H. and A. V. Tobolsky, in Physical Chemistry of High Polymeric Systems, p. 262, Wiley, New York (1950).

97. Martuscelli, E., et al., in Polymer Blends (1978).

98. Matsuo, M., C. Nozaki and Y. Jyo, Polym. Eng. Sci., 9, 197 (1969).

99. McMaster, L. P., Macromolecules, 6, 760 (1973).

100. Merriam, C. N. and W. A. Miller, U.S. Patent 3,099,067 (1963).

101. Meyer, K. H., E. Wolff and C. G. Boissonas, Helv. Chem. Acta, 23, 430 (1940).

102. Mikami, T., R. G. Cox and S. G. Mason, Int. J. Multiphase Flow, 2, 113 (1975).

103. Miller, W. A. and C. N. Merriam, U.S. Patent 3,097,991 (1963).

104. Minoshima, W., J. L. White and J. E. Spruiell, Polym. Eng. Sci., 20, 1166 (1980).

105. Mohr, W. D., R. L. Saxton and C. H. Jepson, Ind. Eng. Chem., 49, 1857 (1957).

106. Nadella, H. P., H. M. Henson, J. E. Spruiell and J. L. White, J. Appl. Polym. Sci., 21, 2003 (1977).

107. Nakagima, N. and M. Shida, Trans. Soc. Rheol., 10, 299 (1966).

108. Nawab, N. A. and S. G. Mason, Trans. Faraday Soc., 54, 1712 (1958).

109. Nelson, C. E. and G. N. Avegraplos, et al., Die Angev. Makromolekular Chemie, 60/61, 49 (Nr. 852) (1977).

110. Nishi, T., T. T. Wang and T. K. Kwei, Macromolecules, 8, 909 (1978).

111. Oda, K., J. L. White and E. D. Clark, Polym. Eng. Sci., 18, 25 (1978).

112. Olakishi, O., Macromolecules, 9, 316 (1975).

113. Olabishi, O., L. M. Robeson and M. T. Shaw, in Polymer-Polymer Miscibility, Academic Press, New Yrok (1979).

114. Olabishi, O. and R. Shimha, J. Appl. Polym. Sci., 21, 149 (1977).

115. Patterson, D. and A. Robard, Macromolecules, 11, 690 (1978).

116. Paxton, R., J. Appl. Polym. Sci., 7, 1499 (1963).

117. Paul, D. R., J. W. Balow, R. E. Bernstein and D. C. Wahrmund, Polym. Eng. Sci., 18, 1225 (1978).

118. Plochocki, A. P., J. Appl. Sci., 16, 987 (1972).

119. Plochocki, A. P., Trans. Soc. Rheol., 20:2, 287 (1976).

120. Pringogine, L., in The Molecular Theory of Solutions, North-Holland Pub., Amsterdam (1957).

121. Racin, R. and D. C. Bogue, Molecular Weight Effect in Die Swell and in Shear Rheology, University of Tennessee Report No. 115 (1976); J. Rheology, 23, 263 (1976).

122. Rayleigh, L., Proc. Lond. Math. Soc., 10, 4 (1879).

123. Rayleigh, L., Proc. Roy. Soc., 29, 71 (1879).

124. Reyer, G., Zeitsch. für Phys. Chem. (ii), 744 (1888).

125. Richardson, E. G., Kolloid. Z., 65, 32 (1933).

126. Richardson, E. G., J. Colloid Sci., 8, 367 (1958).

127. Roe, R. J., J. Phys. Chem., 69, 2809 (1965).

128. Roe, R. J., J. Phys. Chem., 72, 2809 (1968).

129. Roedink, E. and G. Challa, Polymer, 18, 173 (1978).

130. Rowell, H. S. and D. Finlayson, Engineering, 17, 606 (1922).

131. Rumscheidt, F. D. and S. G. Mason, J. Colloid Sci., 16, 238 (1961).

132. Russell, T. W. F. and M. E. Charles, Canad. J. Chem. Eng., 37, 18 (1959).

133. Sanchez, I. C. and R. H. Lacombe, Macromolecules, 11, 1145 (1978).

134. Scatchard, G., Chem. Rev., 8, 321 (1931).

135. Schott, N. R., B. Weisten and D. Lacomband, Chem. Eng. Prog., 71, 54 (1975).

136. Schonhorn, H., J. Phys. Chem., 43, 2041 (1965).

137. Schrenk, W. J., N. L. Bradley and T. Alfrey, Jr., Polym. Eng. Sci., 18, 620 (1978).

138. Schurer, J. W., A. deBoer and G. Challa, Polymer, 16, 201 (1975).

139. Scott, R. L., J. Chem. Phys., 17, 279 (1949).

140. Seefried, C. G., Jr. and J. V. Koleske, J. Test. Eval., 4, 220 (1976).

141. Shimizu, J., N. Okui, T. Yamamoto, M. Ishi and A. Takaku, Seni-i-Gakkaishi, 38, T-1 (1982).

142. Shimomura, Y., J. E. Spruiell and J. L. White, Polym. Eng. Rev., 2, 317 (1983).

143. Small, P. A., J. Appl. Chem., 3, 71 (1953).

144. Song, W. R. and D. W. Brownawell, Polym. Eng. Sci., 10, 222 (1970).

145. Southern, J. H. and R. L. Ballman, Appl. Polym. Sci., 20, 175 (1973).

146. Southern, J. H. and R. L. Ballman, J. Polym. Sci., 13, 863 (1975).

147. Sperling, L. H., Polym. Eng. Sci., 16, 87 (1976).

148. Spruiell, J. E. and J. L. White, Polym. Eng. Sci., 15, 660 (1975).

149. Starita, J. M., Trans. Soc. Rheol., 16:2, 339 (1972).

150. Stein, R. S., A. Misra, T. Yuasa and F. B. Khambatta, Pure Appl. Chem., 49, 915 (1977).

151. Stell, J. R., D. R. Paul and J. W. Balow, Polym. Eng. Sci., 16, 496 (1976).

152. Stoelting, J., F. E. Karaz and W. J. Mackweight, Polym. Eng. Sci., 10, 133 (1970).

153. Suetsugu, Y. and J. L. White, J. Appl. Polym. Sci., 28, 1481 (1983).

154. Sumner, O. G., Nature, 165, 182 (1950).

155. Tadmor, Z., Polym. Eng. Sci., 6, 185 (1966).

156. Tadmor, Z., D. I. Marshall and I. Klein, Polym. Eng. Sci., 6, 3 (1966).

157. Tadmor, Z. and I. Klein, in Principles of Plasticating Extrusion, Rheinhold, New York (1969).

158. Tanaka, H., M.S. Thesis, Univ. of Tennessee, Knoxville (1979).

159. Tanner, R. I., J. Polym. Sci., A-2, 9, 2067 (1970).

160. Taylor, G., Proc. Roy. Soc. London, A138, 41 (1932).

161. Taylor, G. I., Proc. Roy. Soc. London, A146, 501 (1934).

162. Thomas, L. S. and K. J. Cleerman, SPE J., 28, 39 (1972).

163. Thorpe, T. and J. Roger, Proc. Roy. Soc. London, 60, 152 (1896).

164. Ibid., Chem. News, 75, 152 (1897).

165. Ibid., Phil. Trans. London, A188, 71, 36 (1897).

166. Ibid., J. Chem. Soc., 71, 360 (1897).

167. Tomotika, S., Proc. Roy. Soc., A150, 322 (1935).

168. Ibid., Proc. Roy. Soc., A153 (1936).

169. Tompa, H., Trans. Faraday Soc., 45, 1140 (1949).

170. Torza, S., R. Cox and S. G. Mason, J. Colloid Sci., 38, 395 (1972).

171. Tsebrenko, M. V., M. Jakob, M. Ju. Kuchinka, A. V. Judin and G. V. Vinogradov, Inter. J. Polymeric Mater., 3, 99 (1974).

172. Tsebrenko, M. V., A. V. Yudin, T. I. Ablozova and B. V. Yarlykov, Polymer, 16, 609 (1975).

173. Tsebrenko, M. V., M. M. Rezanova and G. V. Vinogradov, Polymer, 20, 1023 (1980).

174. Uemura, Y. and M. Aoyagi, J. Appl. Polym. Sci., 19, 1029 (1975).

175. Uhland, E., Polym. Eng. Sci., 17, 671 (1977).

176. Utracki, L. A., Z. Bakerdijian and M. R. Kamal, J. Appl. Polym. Sci., 19, 431 (175).

177. Van Krevelev, D. W., in Properties of Polymer Correlations with Chemical Structure, p. 85, Elsevier, Amsterdam (1972).

178. Van Oene, H., J. Colloid and Interface Sci., 40, 448 (1972).

179. Van Oene, H., J. Polym. Sci., 10, 507 (1972).

180. Van Oene, H., in Polymer Blend, Vol. 1, Ch. 8, p. 295 (1978).

181. Vinogradov, G. V., B. V. Yarlykov, M. V. Tsebrenko, A. V. Yudin and T. I. Ablazova, Polymer, 16, 607 (1975).

182. Vlachopoulas, J. and T. W. Chan, J. Appl. Polym. Sci., 21, 1177 (1977).

183. Wagner, R., Zeitsh. für Phy. Chem. (V), 31 (1890).

184. Walters, K., Rheometry: Industrial Applications, edited by K. Walters, Wiley, New York (1980).

185. Wang, C. C. and M. M. Charles, Canad. J. Chem. Eng., 59, 668 (1981).

186. Week, J. Z. and F. E. Karaz, J. Appl. Phys., 48, 4068 (1977).

187. Wellinghoft, S. T., J. L. Koenig and E. Baer, Jr., J. Polym. Sci., Polym. Phys., 15, 1913 (1977).

188. Wenig, W., F. E. Karaz and W. J. Macknight, J. Appl. Phys., 46, 4194 (1975).

189. White, J. L., in Rheometry: Industrial Applications, edited by K. Walters, Wiley, New York (1980).

190. White, J. L. and B. Lee, Trans. Soc. Rheol., 19, 457 (1975).

191. White, J. L., A. P. Plochocki and H. Tanaka, J. Appl. Polym. Sci., 1, 217 (1981).

192. White, J. L. and J. F. Roman, J. Appl. Polym. Sci., 20, 1005 (1976); 21, 869 (1977).

193. White, J. L., R. C. Ufford, K. R. Dharod and R. L. Price, J. Appl. Polym. Sci., 16, 1313 (1972).

194. Wijkander, K., Wied. Beibl., 3, 8 (1879).

195. Wilchinsky, Z. W., J. Appl. Phys., 30, 792 (1959).

196. Wilchinsky, Z. W., J. Appl. Phys., 31, 1969 (1960).

197. Wilchinsky, Z. W., Adv. X-ray Anal., 6, 231 (1963).

198. Wolf, B. A., Macromol. Chem., 178, 1869 (1977).

199. Wu, S., J. Phys. Chem., 74, 632 (1970).

200. Yamane, H. and J. L. White, Polym. Eng. Rev., 2, 167 (1983).

201. Yu, H. S. and E. M. Sparrow, A.I.Ch.E.J., 13, 10 (1967).

202. Yu. T. C. and C. D. Han, J. Appl. Polym. Sci., 17, 1203 (1973).

203. Ziska, J. J., D. R. Paul and L. W. Balow, Polymer, 22, 918 (1981).

VITA

The author, Kyonsuku Min, was born in Kyoto, Japan, as the second daughter of Mr. and Mrs. Chungi Min. After completing her basic education, she was admitted to Kyoto University of Industrial Arts and Textile in April 1972. She studied Textile Engineering and received a Bachelor of Science degree in March 1976. She continued her education in graduate school at the same university. In her thesis, she investigated the domain structure of SIS, SI block copolymers. She received a Master of Science degree in March 1978.

She entered The University of Tennessee in the fall of 1979.